HAL
archives-ouvertes.fr

Neutrino physics with SoLid and SuperNEMO experiments

Delphine Boursette

To cite this version:

Delphine Boursette. Neutrino physics with SoLid and SuperNEMO experiments. High Energy Physics - Experiment [hep-ex]. Université Paris-Saclay, 2018. English. <NNT : 2018SACLS272>. <tel-01885274>

HAL Id: tel-01885274

https://tel.archives-ouvertes.fr/tel-01885274

Submitted on 1 Oct 2018

HAL is a multi-disciplinary open access archive for the deposit and dissemination of scientific research documents, whether they are published or not. The documents may come from teaching and research institutions in France or abroad, or from public or private research centers.

L'archive ouverte pluridisciplinaire **HAL**, est destinée au dépôt et à la diffusion de documents scientifiques de niveau recherche, publiés ou non, émanant des établissements d'enseignement et de recherche français ou étrangers, des laboratoires publics ou privés.

université PARIS-SACLAY

NNT: 2018SACLS272

Thèse de doctorat

Neutrino physics with SoLid and SuperNEMO experiments

Thèse de doctorat de l'Université Paris-Saclay
préparée à l'Université Paris-Sud
au sein du Laboratoire de l'Accélérateur Linéaire

École doctorale n° 576 PHENIICS
(Particules, Hadrons, Énergie, Noyau, Instru-
-mentation, Imagerie, Cosmos et Simulation)
Spécialité de doctorat : Physique des particules

Thèse présentée et soutenue à Orsay, le 13 septembre 2018, par

Delphine Boursette

Composition du jury :

Achille Stocchi Professeur Université Paris Sud — LAL	Président du jury
Corinne Augier Professeur Université Claude Bernard — IPNL	Rapporteuse
David Lhuillier Chercheur – CEA Saclay	Rapporteur
Christine Marquet Chercheuse – CENBG	Examinatrice
Nick van Remortel Professeur University of Antwerp	Examinateur
Mathieu Bongrand Chercheur – LAL	Co-Directeur de thèse
Laurent Simard Maître de conférence Université Paris Sud– LAL	Co-Directeur de thèse

n° LAL 18-014

Remerciements

Cette thèse sur les neutrinos fut une expérience extrêmement enrichissante, qui m'a permis de rencontrer des personnes passionnantes que je souhaite remercier.

Je remercie tout d'abord les membres de mon jury de thèse pour le temps qu'ils ont consacré à la lecture de mon manuscrit: les rapporteurs Corine Augier et David Lhuillier ainsi que Christine Marquet et Nick Van Remortel avec qui j'ai eu la chance de travailler sur SuperNEMO et SoLid. Merci à Achille Stocchi, président du jury, qui a été d'un grand soutien pour l'expérience SoLid.

Je suis infiniment reconnaissante à Mathieu Bongrand, mon directeur de thèse. Tu as toujours été très présent tout en me laissant la liberté d'explorer les sujets qui m'intéressaient le plus. J'ai compris grâce à toi qu'on peut toujours trouver une solution, même aux problèmes d'instrumentation sur le banc de test. J'ai aussi appris l'importance des détails, que ce soit dans l'analyse de données ou dans les présentations. Merci de m'avoir appris le métier de chercheur.

Je remercie également tous les autre membres du groupe neutrino du LAL. Laurent Simard, mon co-directeur de thèse, merci pour ta disponibilité, tes conseils et pour ta relecture attentive de mon manuscrit. Xavier Garrido et Steven Calvez, votre aide a été précieuse pour l'installation et l'utilisation de Falaise, avec toujours une blague en prime. Merci Luis Manzanillas pour ton aide sur SoLid, surtout sur la fin de la thèse et l'analyse IBD. Les discussions passionnantes lors des déjeuners avec Serge Jullian, Xavier Sarazin, Pia Loaiza, Carla Macolino vont me manquer. Je souhaite bon courage à Cloé et Noë pour la suite, vous êtes entre de bonnes mains !

L'aide du groupe mécanique du LAL a été très précieuse pour construire le banc de test. Merci beaucoup à Stéphane Jenzer et Aurélien Blot. Les heures à clipser des milliers de miroirs pour le détecteur SoLid sont finalement passées vites en votre compagnie ! Merci également à Dominique Breton et Jihane Maalmi pour l'aide sur l'électronique du banc de test.

J'ai pu effectuer ma thèse dans d'excellentes conditions grâce à tout le personnel du LAL, que ce soit la direction, le service mission, Geneviève Gilbert... Merci beaucoup pour votre accueil.

Je souhaite une bonne continuation aux thésards du LAL. Je veux remercier en particulier Victor Renaudin et Valentin Frey, ainsi que Mathilde et Sylviane, pour tous les déjeuners et dîners partagés, à discuter de notre expérience de thésard, de notre avenir et à refaire le monde.

Durant cette thèse, j'ai eu la chance de travailler au sein de deux collaborations différentes avec des personnes passionnantes. Je remercie donc tous ceux avec qui j'ai pu travailler sur les expériences SoLid et SuperNEMO. Frédéric Yermia, Benoît Viaud et Petra Van Mulders, vous m'avez beaucoup aidée dans l'analyse des données de SoLid avec vos conseils avisés! Je souhaite une bonne route aux thésards des 2 collaborations, il y en a beaucoup, avec qui j'ai partagé cette aventure et des supers moments en réunions de collaborations ou en conférences, en particulier Simon et Céline, mes comparses de la task-force proto-analyse.

Je voudrais également remercier tous les membres du CA de l'association D2I2. M'investir dans cette association de doctorants des deux infinis a été particulièrement enrichissant. L'après-thèse peut parfois être inquiétant mais pouvoir en discuter au sein de l'association et rencontrer des gens aux parcours inspirants m'a permis d'appréhender sereinement la suite et de savoir ce que je souhaitais faire.

Beaucoup de gens dans mon entourage ont rendu ces 3 années de thèse et les années d'études précédentes particulièrement épanouissantes et heureuses.

Il y a d'abord les amis de toujours, rencontrés au primaire ou en option musique au lycée, avec qui j'ai grandi et que la distance ne peut pas séparer : Adèle, Camille, Colette, Julie, Juliette, Micka. Merci d'avoir toujours été là, vivement tous les prochains week-ends aux quatre coins de la France !

Je remercie également les amis rencontrés à l'ENS Cachan qui ont aussi fait de ces années d'études des années de réjouissances et de voyages, en particulier Clémentine, Amélie et JN pour tous les brunchs à partager nos premières expériences professionnelles.

Karine et Alicia, merci pour tous les supers moments partagés ensemble qui m'ont permis de décompresser.

Amélie, j'ai de la chance de t'avoir comme soeur. Avec ta détermination et ta joie de vivre, tu te crées un parcours admirable.

Je dois énormément à mes parents qui m'ont soutenue pendant ces longues années d'études. Merci pour tout ce que vous m'avez transmis comme la curiosité, la persévérance ou l'importance du travail pour s'épanouir. Vous avez toujours été là pour m'écouter et m'aider et c'est une énorme force de savoir que je peux toujours compter sur vous.

Enfin je remercie Grégory : merci de me pousser à toujours donner le meilleur de moi-même, d'être aussi ambitieux pour moi que je le suis. Merci d'avoir rendu ces 3 années de thèse à tes côtés merveilleuses et de continuer à me rendre heureuse.

Contents

Introduction **11**

1 Neutrino physics **13**
1.1 Neutrinos: what is established 13
1.1.1 Discovery of neutrinos 13
1.1.2 Neutrino spin and helicity 17
1.1.3 Neutrino and anti-neutrino 17
1.1.4 Discovery of neutrino flavours 18
1.1.5 Neutrino Oscillations 19
1.1.6 Conclusion: recap of which neutrino properties are established 26
1.2 Neutrino mysteries 26
1.2.1 Questions about neutrinos 26
1.2.2 Neutrino nature: Dirac, Majorana 30
1.2.3 Sterile neutrinos 41
1.2.4 Sterile neutrinos influence on $\beta\beta$ decay search 57
1.2.5 Conclusion 60

I SuperNEMO **61**

2 The SuperNEMO demonstrator **63**
2.1 SuperNEMO technology 63
2.1.1 Detection principle 63
2.1.2 Mechanical design 64
2.1.3 The source foils 65
2.1.4 The tracker 66
2.1.5 The magnetic field 66
2.1.6 The calorimeter 67
2.1.7 The calibration system 68
2.1.8 Expected sensitity 70
2.2 Backgrounds 70
2.2.1 Types of background 70
2.2.2 Background reduction 73
2.3 Simulation and analysis tools 75
2.3.1 Monte-Carlo simulation 75
2.3.2 Analysis chain 76
2.4 Conclusion 78

3 External background analysis **79**
3.1 Simulation to study the external background 79
3.1.1 Motivations of the study 79
3.1.2 Simulations and estimation of the expected backgrounds . . 79
3.2 External background expected in the 2 electron channel 84
3.2.1 Contributions to the external background 84
3.2.2 External and internal probability cuts 85
3.3 External background measurement 86
3.3.1 The crossing electron channel 87
3.3.2 The γe-ext channel 88
3.3.3 Impact of the external background of the Se $2\nu\beta\beta$ half-life measurement 90
3.4 Control of the external background with copper foils 92
3.4.1 Events expected in the two electrons channel in copper foils 93
3.4.2 Copper foil thickness study 94
3.5 Conclusion 95

II SoLid **99**

4 The SoLid experiment principle and SM1 prototype results **101**
4.1 Introduction 101
4.2 Antineutrino source: the BR2 reactor 101
4.2.1 Antineutrinos from nuclear reactors 101
4.2.2 The BR2 reactor 103
4.3 The IBD reaction 103
4.4 The backgrounds 105
4.4.1 Cosmic background 105
4.4.2 Reactor background 106
4.4.3 Natural radioactivity 106
4.4.4 Background measurement 106
4.5 SoLid technology 107
4.5.1 Scintillator detection principle 107
4.5.2 Wavelength shifting optical fibers 109
4.5.3 Silicon photomultipliers 109
4.6 SoLid sensitivity 111
4.7 SM1 prototype 111
4.7.1 SM1 mechanical design 111
4.7.2 SM1 electronics readout 112
4.7.3 Event reconstruction 114
4.8 SM1 results 115
4.8.1 Neutron detection study 115
4.8.2 Light yield and energy resolution 118
4.8.3 Detector response 119
4.8.4 IBD search 121
4.9 Conclusion 123

5 Optimization of the light yield for SoLid phase I 125
5.1 Introduction . . . 125
5.2 Test bench setup . . . 125
5.2.1 The ^{207}Bi source . . . 126
5.2.2 The external trigger system . . . 127
5.2.3 The scintillator detector . . . 129
5.2.4 Electronics and Acquisition . . . 130
5.2.5 Simulation of energy losses of the electrons . . . 131
5.3 Data measurement processing . . . 134
5.3.1 Correction from temperature . . . 135
5.3.2 Correction of pedestal . . . 135
5.3.3 Correction from cross-talk . . . 135
5.3.4 Pulse reconstruction . . . 136
5.3.5 Conversion from pulse charge to photo-avalanches . . . 138
5.3.6 Fit of the conversion electron peak . . . 138
5.3.7 Measurement uncertainties . . . 139
5.4 Light collection study . . . 140
5.4.1 Scintillating material . . . 141
5.4.2 Cubes wrapping . . . 142
5.4.3 ^{6}LiF:ZnS(Ag) neutron screens . . . 143
5.4.4 Optical fibers . . . 145
5.4.5 Mirrors . . . 146
5.5 Configuration study . . . 147
5.5.1 Optical fiber configuration . . . 147
5.5.2 Comparison between SM1 and SoLid configurations . . . 148
5.6 SoLid cube production performance . . . 151
5.7 Conclusion . . . 151

6 SoLid phase I detector 153
6.1 Introduction . . . 153
6.2 Mechanical design . . . 153
6.3 Electronics and trigger . . . 155
6.4 Construction planning . . . 157
6.5 Individual cube calibration . . . 158
6.5.1 Calibration at Ghent with Calipso . . . 160
6.5.2 Calibration on site with CROSS . . . 164
6.6 Data taking campaigns . . . 166
6.7 Conclusion . . . 167

7 SoLid phase I data analysis 169
7.1 Introduction . . . 169
7.2 SoLid phase I data taking . . . 169
7.3 Object reconstruction . . . 170
7.3.1 Saffron analysis software . . . 170
7.3.2 Neutron reconstruction . . . 170
7.3.3 Muon reconstruction . . . 171
7.3.4 EM cube reconstruction . . . 172

7.4 EM cubes reconstruction cuts 174
7.4.1 Cube reconstruction performance 174
7.4.2 Asymmetry cut 176
7.4.3 Multiplicity cuts 177
7.4.4 Validation of the cuts with AmBe data 177
7.5 IBD cuts study with simulation data 178
7.6 BiPo background study 181
7.6.1 BiPo search 181
7.6.2 BiPo removal 185
7.7 Study of background from after-muon events 185
7.8 Search for IBD events 185
7.9 Conclusion 187

Conclusion **191**

Résumé **193**

Introduction

Neutrinos are fundamental particles that keep challenging our knowledge about the Universe. They are the most abundant particles of matter and yet many mysteries remain about them. In the last 60 years, since they were first observed, many experiments have provided knowledge about their properties, but they have also added more questions about them and the Standard Model of particle physics. For example, it has been demonstrated that they can oscillate between three lepton flavours and thus that they have a mass, but this raised many questions: what mechanism gives such small masses to neutrinos? What is their nature? Could they oscillate toward sterile neutrinos? During this thesis, I have worked on two different experiments that investigate these issues: SuperNEMO and SoLid.

The Majorana mass mechanism could explain the smallness of neutrino masses, but it implies that they should be their own antiparticle. This can be investigated by looking for neutrinoless double beta decay which is the purpose of the SuperNEMO experiment. A demonstrator, composed of a tracker and a calorimeter, is being assembled at the Modane Underground Laboratory. Six kilograms of the double beta emitter ^{82}Se will be placed at the center of the detector. The search for $0\nu\beta\beta$ decays is very challenging as this process, if it exists, is very rare so the backgrounds have to be reduced and controlled with high precision.

The SoLid experiment searches for sterile neutrinos close to the BR2 nuclear reactor in Belgium. The first prototype, SM1, has demonstrated that the very segmented technology used for this experiment is efficient to reject backgrounds. A lot of R&D has been conducted to improve the energy resolution of the detector. The SoLid phase I detector has been built in 2017 and is now taking data. The hunt for sterile neutrinos has started.

This thesis is divided in two parts. The first part is about the SuperNEMO experiment and the search for neutrinoless double beta decay. The second part concerns the SoLid experiment and the search for sterile neutrinos.

The first chapter describes our current knowledge and questions about neutrino physics. It explains why the search for neutrinoless double decay and sterile neutrinos is important and describes the experimental status of these fields of research.

The second chapter is about the SuperNEMO experiment. A description of the demonstrator is given as well as the different backgrounds it will have to fight

against.
The third chapter focuses on the work done during this thesis to understand the impact of the external background on the SuperNEMO experiment. It also shows a study of the utility to use copper foils in the detector to control this background.

In the fourth chapter, the principle of the SoLid experiment is given. The detector technology is explained, then the results of the first prototype SM1 are discussed.
The fifth chapter shows the work done during this thesis to increase the light yield in order to improve the energy resolution of SoLid phase I. The test bench built at LAL is described and the results of the different tests are presented.
The sixth chapter is dedicated to the SoLid phase I experiment. The detector design and performance and the calibrations are described.
The seventh chapter provides a preliminary reactor neutrino search with the first SoLid phase I data.

Chapter 1

Neutrino physics

1.1 Neutrinos: what is established

In a century, we have discovered and learnt a lot about a whole new world: the world of the infinitesimally small, the world of particles. While physicists have managed, with giant detectors and accelerators, to create a standard model of particle physics which seems to work well, there is a particle whose properties are still elusive because it interacts very weakly with matter: the neutrino. It is very important to learn more about it because it could help us to improve or even go beyond the Standard Model.

1.1.1 Discovery of neutrinos

The beginning of the XXth century was the beginning of particle physics. In 1896, H. Becquerel discovered radioactivity by showing almost accidentally that uranium emits a radiation that exposes photographic plates [80]. He did not know what this radiation was. By investigating cathode rays, J. J. Thomson and other physicists discovered the electron the following year. In 1899, E. Rutherford showed the existence of α and β rays while P. Villard detected in 1900 a third type of radiations: γ rays. At the same time, several physicists, including P. and M. Curie, or W. Kaufmann, demonstrated that β rays and cathode rays were the same particle: electrons [69]. This was the knowledge physicists had at the beginning of the history of neutrinos: they had just discovered a new physics phenomenon, radioactivity, and they had started to distinguish some particular radiations.

The history of the neutrino starts with the controversy on the β spectrum continuity. After the recent and very exciting discoveries of radioactivity and electrons, some physicists, like Kaufmann or Becquerel, started to study the electrons emitted in β decays. They saw that these electrons had a wide energy spectrum which seemed continuous. It surprised the physicists at that time as they had seen that the α and γ radiations had discrete lines in their spectrum. The argument lasted for a few years even after J. Chadwick's experiment in 1914: instead of detecting electrons with photographic plates as it used to be done, he started to use newly developed Geiger counters [57]. With his apparatus, he demonstrated the conti-

nuity of the β spectrum. Still, some physicists like Lise Meitner asked for more evidence. Chadwick's result was confirmed in 1927 by C. Ellis and W. Woodster with a calorimetric measurement of the electron energy [67].

However, this discovery lead to another polemics: why is the β spectrum continuous? N. Bohr thought that the energy conservation was violated in single interactions, and conserved only statistically. This idea was first suggested by W. Nernst in 1916 and several physicists, like G. C. Darwin or A. Sommerfeld, used it in an attempt to explain the young quantum theory. However, W. Pauli who did not like this idea, proposed another "desperate way out" in his famous letter to "radioactive ladies and gentlemen" [105] : the existence of a new neutral particle with spin 1/2 emitted at the same time as the electron that he called the neutron. He also wrote that this neutron should "satisfy the exclusion principle" and its mass "should be of the same order of magnitude as the electron mass". Although he admitted that his idea "may not seem very probable", it was quite attractive as it explained why the electron did not have always the same energy in the β decay (the neutrino could take on a variable part of the decay energy) and it also solved the problem of nuclear statistics and spin considering that the neutrino was part of the nucleus. This last problem was actually solved by the discovery of the neutron by J. Chadwick in 1932, which was tied to the belief in the conservation of the energy. E. Fermi's theory, published in 1934, gave a satisfying answer to all these issues. He assumed that the nucleus was composed of protons and neutrons, and that W. Pauli's neutrons, which he called "neutrinos" were created in the β decay. In his theory, β decay consisted of a neutron decay inside a nucleus into a proton, an electron and a neutrino. As it will be seen later, the neutrino emitted is actually an antineutrino (1.1):

$$\mathrm{n} \rightarrow \mathrm{p} + \mathrm{e} + \overline{\nu} \tag{1.1}$$

This solution preserved the conservation laws. This theory also shows that the neutrino mass was nearly zero because of the form of the tail of the β energy spectrum.

As A. Franklin explains, at that time physicists seem to have accepted the existence of the neutrino and Fermi's theory, but "there is something a little troubling about the argument. The conservation laws support the neutrino, but the neutrino saves the conservation laws." [69]. This is why other experimental proofs of the existence of the neutrinos were needed.

In 1936, using E. Fermi's theory, H. Bethe and R. Bacher explained that "there is only one process in which neutrinos can certainly cause. That is the inverse β-process" [52]. This process, also called inverse beta decay (IBD), is the following (1.2):

$$\overline{\nu} + \mathrm{p} \rightarrow \mathrm{n} + \mathrm{e}^{+} \tag{1.2}$$

This process is very important because it is still used nowadays to learn more about neutrinos. However, like all neutrino processes, its cross-section is very small which makes it very difficult to be observed. H. Bethe and R. Bacher explained that "a neutrino has to go, in the average, through 10^{16} km of solid matter before it causes such a process. The present method of detection must be improved at least by a

factor 10^{13} in sensitivity before such a process could be detected" [52]. It seemed almost impossible to detect neutrinos at that time. However, 12 years later, H. Crane moderated this sentence as he calculated that the increase in sensitivity needed was 10^7 and the use of a chain-reacting pile to get a high neutrino flux could help the detection.

The detection of neutrinos using the IBD process finally happened 20 years later. To detect this particle which has a low probability to interact, physicists needed an intense source of neutrinos and a big neutrino target. F. Reines, who had taken part to the Manhattan project and nuclear trials in the Pacific ocean, imagined with C. Cowan, his colleague at the Los Alamos laboratory, that they could use the explosion of a nuclear bomb as a source of neutrinos. They calculated that by installing their detector at 50 m from the bomb, they needed several tons of scintillation liquid. They called such a big neutrino detector "El Monstro". Its construction started in 1951 but in 1952, they considered they could use a nuclear reactor as the neutrino source instead of a bomb. Despite obvious security reasons, an advantage was that they could let their experiment run for a long time to detect more IBD events, although the flux was much lower than the one of an atomic bomb. Their detector was composed of 2 tanks of 400 l of a mix of water and cadmium chlorure. When a $\overline{\nu}$ entered the detector, it interacted with a proton to create a positron and a neutron. The positron immediately annihilated with an electron by emitting 2 back-to-back gammas of 511 keV (the prompt signal). After a few microseconds, the neutron was captured by a cadmium atom emitting other gamma rays (the delayed signal). To detect these gamma rays, there were liquid scintillation tanks around the water and cadmium tanks and they built an electronic circuit to detect the 2 gamma signals of the positron and the neutron in time delay coincidence.

They ran a first experiment in 1953 at the Hanford reactor without enough shielding. They had several complications due to cosmic background with a first signal over background ratio (S/B) of 1/20 so only a vague signal was observed [108]. They improved their experiment at Savannah River with a better segmentation using more tanks to distinguish more easily muon tracks (figure 1.1). They could define a prompt signal if scintillation signals were found in 2 tanks, as a positron creates 2 gammas of opposite direction, but no more than 2 tanks as a scintillation signal in 3 tanks would sign a crossing atmospheric muon interaction (figure 1.2). This segmentation idea to reject backround is important and has been used a lot in other experiments (including SoLid). They improved their S/B to 3/1. To calibrate in energy their detector, they used atmospheric muons and radioactive sources. In 1956, F. Reines and C. Cowan managed to detect a signal depending on the reactor power in agreement with the predicted cross-section at 4 σ [108].

The neutrino was first postulated theoretically to explain an experimental problem: the continuity of the β spectrum. However, to get the status of a well accepted particle in the physicists community, it still had to be detected directly. This was done by F. Reines and C. Cowan in 1956. A very similar process will happen several

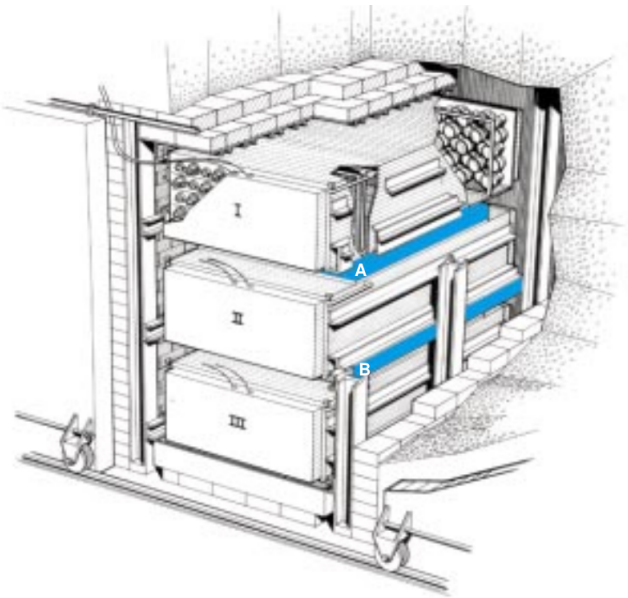

Figure 1.1: F. Reines and C. Cowan neutrino detector at Savannah River. The protons in the water in blue are the neutrino target. The scintillation signal from the positron and then the neutron are detected in the tanks I, II and III.

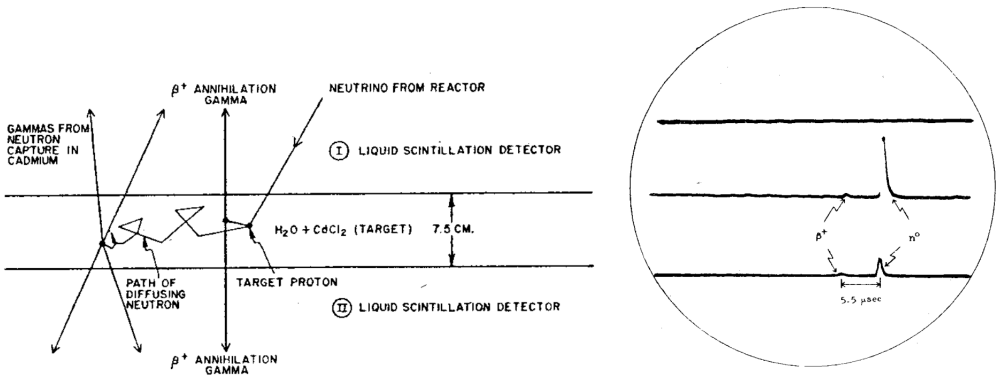

Figure 1.2: *Left:* schematic diagram of the neutrino detector. *Right:* a characteristic signal of an IBD record by F. Reines and C. Cowan [108].

times in neutrino history. While several particles were first detected directly and then included in the theory of particle physics, neutrinos, and later sterile neutrinos (if they exist), have first been imagined by theoreticians to explain experimental issues and will (or may) then be detected directly.

1.1.2 Neutrino spin and helicity

In Fermi's theory, the neutrino is a spin 1/2 particle, so it is a fermion. In 1956, T. Lee and C. Yang [91] suggested parity non conservation in weak interaction. C. Wu [113] and her colleagues demonstrated it by studying the angular distribution of the electron in the ^{60}Co decay after polarizing the ^{60}Co atoms.

This demonstration was very important for theorists. Some of them had already assumed parity non conservation, like T. Lee and C. Yang or L. Landau in 1957. It led them to propose a theory of neutrino with 2 components instead of 4 components usually required for fermions (2 particle and 2 antiparticles with a spin +1/2 or a spin -1/2). This meant that the neutrino should have only a spin antiparallel to its momentum (we call this a left-handed neutrino, meaning that its helicity is -1) and the antineutrino should have only a spin parallel to its momentum (we call this a right-handed neutrino, meaning that its helicity is +1).

M. Goldhaber and others proved indeed in 1958 that the helicity of the neutrino is always -1 using the electron capture of ^{152}Eu and measuring the gamma helicity from ^{152}Sm* deexcitation which was the same as the emitted neutrino helicity [94].

By measuring the neutrino helicity in agreement with the 2-component theory, this experiment established that parity violation was maximal in β decay. However, the 2-component theory also predicted that the neutrino mass should be zero. We will see later that this is a problem.

1.1.3 Neutrino and anti-neutrino

In 1955, R. Davis demonstrated that ν_e have different behaviour from $\overline{\nu}_e$ by showing that their cross-section when interacting with neutrons are different. To show this, he used a radio chemical experiment, the same principle as the one used to detect the first solar neutrinos. In 1948, B. Pontecorvo proposed radiochemical detection methods to study neutrinos based on the reaction:

$$\nu_e +^{37} Cl \rightarrow^{37} Ar + e^- \tag{1.3}$$

R. Davis used the Brookhaven reactor, in the USA, as a source of neutrinos. To detect their interaction with neutrons of ^{37}Cl, he detected the produced ^{37}Ar which he extracted by flooding He through the detector and then trapped. The ^{37}Ar decays were then counted. He did not see any $\overline{\nu}_e$ interacting with neutrons while it was proven that ν_e did interact with neutrons (this detection principle with ν_e was

used later to detect solar neutrinos). It was deduced from this experiment that ν_e and $\overline{\nu}_e$ are different particles. However, the discovery of parity violation and the different helicities for neutrinos and antineutrinos could explain the different cross-sections for neutrino and antineutrino weak interaction. It means that Davis experiment was discriminating between left-handed and right-handed particles but did not prove that neutrinos and antineutrinos were different particles. Similar results concerning the weak interaction cross-sections were obtained later at CERN for ν_μ and $\overline{\nu}_\mu$.

This is not the end of the story for the comparison of neutrinos and antineutrinos. As we will see, whether neutrinos and antineutrinos are the same particle is still an open question.

1.1.4 Discovery of neutrino flavours

After the detection of the first neutrinos, many questions arose. One of these questions was: are there different neutrinos? Although several physicists thought it was useless to introduce more complexity with different neutrinos, the failure to observe the decay: $\mu \rightarrow e + \gamma$ which would be possible if the muon decay was $\mu \rightarrow e + \nu + \overline{\nu}$ lead theoreticians to propose the existence of 2 neutrinos: the electron neutrino (ν_e) and the muon neutrino (ν_μ) with two different lepton flavors. To answer this question, B. Pontecorvo proposed to try to detect the reaction: $\overline{\nu}_\mu + p \rightarrow e^+ + n$ which had already been detected by Reines and Cowan with $\overline{\nu}_e$ (the IBD reaction) [107]. In the 1960's, L. Lederman, M. Schwartz et J. Steinberger used the Brookhaven AGS accelerator which produced pions to check if neutrinos emitted in β-decay were the same as the one emitted in pion decay. As they saw less electrons than muons after these neutrinos interacted with the protons and neutrons of their detector, it meant that neutrinos emitted from pion decay (or ν_μ), did not have the same cross-section as the one emitted in beta decay which were observed in nuclear reactors. This was the discovery of ν_μ and it also seemed to imply the conservation of the lepton number.

In 1989, the number of active (not sterile) light neutrinos have been measured with the width of the Z^0 boson at LEP and was in agreement with the existence of 3 neutrinos. This third neutrino was then thought to be the tau neutrino (ν_τ) as the τ particle was a lepton discovered in the 1970's. This ν_τ was detected in 2000 at Fermilab by the DONUT experiment. It used ν_τ produced by protons from the Tevatron accelerator which decayed into charmed mesons. The ν_τ interactions were then detected in an emulsion cloud chamber. Four events of ν_τ were found which was a clear signal compared to their background [89].

We have seen that several types of neutrinos have been discovered corresponding to the 3 lepton flavours. The study of this flavour neutrino fluxes will lead to the discovery of another intriguing property of neutrinos. Indeed, we are going to see that some anomalies in the neutrino fluxes have bothered physicists for some time.

1.1.5 Neutrino Oscillations

Experimental discovery of oscillations: the solar neutrinos issue

Solar neutrinos are a very important source of information to understand the energy process which take place in the sun. Indeed, as neutrinos interact very weakly, the ones which are produced inside the sun can get to us very quickly while photons scatter a lot in the core of the sun. R. Davis decided to search for interactions of solar neutrinos with Cl using the reaction 1.3. In the 1960's, after several failures, he installed a tank of 600 t of C_2Cl_4 in the Homestake gold mine in Dakota. Detecting ν_e appeared to be more difficult than not detecting $\overline{\nu}_e$. His detector was based on the same principle as the one he used previously. He installed this solar neutrino experiment in a mine to decrease the backgrounds, like atmospheric muons. After letting the Ar atoms accumulating during several months, he detected a very low neutrino flux. In 1968, the first published results showed a deficit of solar neutrinos [62]. After several years of data taking, different experiments and more precise calculations of the solar neutrino flux, the problem remained. There were 3 possible explanations to this result: either the solar model used for calculations was wrong, or Davis had made some mistakes in his experiment, or neutrinos could have a flavour that changes with time and Davis experiment would be sensitive to only one type of flavour.

Other radiochemical experiments were conducted with gallium including the Gallex [8] and SAGE [9] experiments, which will be very important later for the sterile neutrino problem. Both experiments detected a neutrino flux lower than the predicted one. However, it was hard to conclude with all these radiochemical experiment as they did not give much information on the neutrinos: neither their energy nor their capture time.

In 1996, the Super-Kamiokande experiment [11], in the Kamioka mine in Japon, started operation. This experiment used the Cherenkov effect produced by electrons and muons in water interacting via neutral or charged current with neutrinos. It has the advantage to give information on the direction, time and energy of the neutrinos. Solar ν_e could be detected via ν_e scattering on electron. The observed solar neutrino flux was about 45% of the flux predicted by the solar standard model. Atmospheric ν_e and ν_μ could also be detected as atmospheric ν_μ have higher energy which allows them to produce muons. ν_e and ν_μ could be differentiated with the form of the Cherenkov light pattern. This experiment showed that atmospheric ν_μ travelling across the earth seemed to disappear while it was not the case for ν_e. A deficit of neutrinos was observed for both atmospheric and solar neutrinos.

The conclusive experiment on the solar neutrino issue was the SNO experiment [24]. It started to take data in 1999. It worked on the same principle as Super-Kamiokande but instead of water (H_2O), heavy water (D_20) was used. It has the advantage to be sensitive to the total neutrino flux (ν_e, ν_μ and ν_τ fluxes) and not only to the ν_e flux. Indeed, it could also detect flavor-blind neutral currents while previous experiments like Super-Kamiokande could only detect ν_e scattering via

charged current and elastic scattering. The SNO experiment could detect the ratio of solar ν_e over the total solar neutrino flux independently of the solar model. The measured total solar neutrino flux was in good agreement with the predicted flux from the solar model. However, the ν_e flux was much lower. This was a proof that ν_e produced in the sun arrived at earth with a different flavour: neutrinos oscillate.

These last two experiments received a Nobel Prize in 2015 "for the discovery of neutrino oscillations, which shows that neutrinos have mass".

Phenomenology of oscillations

A formalism has been introduced to explain how neutrinos can oscillate. This formalism will be introduced here to understand how oscillation can imply that neutrinos have masses. The study will be simplified considering oscillations in vacuum.

The oscillation mechanism comes from the fact that the flavour eigenstates (ν_e, ν_μ, ν_τ) are different from the mass eigenstates (ν_1, ν_2 and ν_3). The mixing between flavour and mass is described by the Pontecorvo-Maki-Nakagawa-Sakata (PMNS) matrix [114]:

$$\begin{pmatrix} \nu_e \\ \nu_\mu \\ \nu_\tau \end{pmatrix} = \begin{pmatrix} U_{e1} & U_{e2} & U_{e3} \\ U_{\mu 1} & U_{\mu 2} & U_{\mu 3} \\ U_{\tau 1} & U_{\tau 2} & U_{\tau 3} \end{pmatrix} \begin{pmatrix} \nu_1 \\ \nu_2 \\ \nu_3 \end{pmatrix} \tag{1.4}$$

This unitary PMNS matrix which has 9 parameters can also be written with 3 mixing angles (θ_{12}, θ_{13}, θ_{23}) and 3 CP violation phases: 1 Dirac phase (δ) and 2 Majorana phases (α, β):

$$U_{PMNS} = \begin{pmatrix} 1 & 0 & 0 \\ 0 & c_{23} & s_{23} \\ 0 & -s_{23} & c_{23} \end{pmatrix} \begin{pmatrix} c_{13} & 0 & s_{13}e^{-i\delta} \\ 0 & 1 & 0 \\ s_{13}e^{i\delta} & 0 & c_{13} \end{pmatrix} \begin{pmatrix} c_{12} & s_{12} & 0 \\ -s_{12} & c_{12} & 0 \\ 0 & 0 & 1 \end{pmatrix} \begin{pmatrix} i & 0 & 0 \\ 0 & e^{i\alpha} & 0 \\ 0 & 0 & e^{i\beta} \end{pmatrix} \tag{1.5}$$

where $c_{ij} = \cos(\theta_{ij})$ and $s_{ij} = \sin(\theta_{ij})$. We will see later that this description is useful to discriminate between the different types of oscillations observed experimentally.

To determine the evolution of the mixing with time, quantum mechanics is required. A neutrino of a certain flavour ν_α (ν_e, ν_μ or ν_τ) can be described as a superposition of different mass eigenstates ν_i. These mass eigenstates evolve according to the Schrödinger equation. As the neutrino masses are very small and their speed is relativistic, their energy calculation can be simplified:

$$E_i = \sqrt{p_i^2 + m_i^2} \approx p_i + \frac{m_i^2}{2p_i} \tag{1.6}$$

Using the fact that neutrinos propagate almost at the speed of light ($t \approx L$ with L the travelling distance of neutrinos), the Schrödinger equation describing the evolution of a mass eigenstate becomes:

$$|\nu_i(t)\rangle = e^{-i(E_i t - p_i L)} |\nu_i(0)\rangle = e^{-i(m_i^2/2p_i)L} |\nu_i(0)\rangle \tag{1.7}$$

It leads to a desciption of a neutrino of flavour ν_α:

$$|\nu_\alpha(L,E)\rangle = \sum_i U^*_{\alpha i} e^{-i(m_i^2/2E)L} |\nu_i\rangle = \sum_\beta \left(\sum_i U^*_{\alpha i} e^{-i(m_i^2/2E)L} U_{\beta i} \right) |\nu_\beta\rangle \tag{1.8}$$

with $E \sim p$ the average energy of the different mass eigenstates. The probability to detect a neutrino of flavour ν_β when the source neutrino had a flavour ν_α is then:

$$P_{\nu_\alpha \to \nu_\beta}(L,E) = |\langle \nu_\beta | \nu_\alpha(L,E)\rangle|^2 = \sum_{i,j} U^*_{\alpha i} U_{\beta i} U_{\alpha j} U^*_{\beta j} e^{-i(\Delta m^2_{ij}/2E)L} \tag{1.9}$$

where $\Delta m^2_{ij} = m_i^2 - m_j^2$.

We can either look for appearance of ν_β in the ν_α flux ($P_{\nu_\alpha \to \nu_\beta}$) or for disappearance of ν_α in the ν_α flux ($1 - \sum_{\beta \neq \alpha} P_{\nu_\alpha \to \nu_\beta}$).

If all the ν_i mass eigenstates were null, then Δm^2_{ij} would be null and we would not observe any oscillation between flavours. It shows also that the oscillations are only sensitive to the square mass difference, this is why the absolute ν mass can not be determined with oscillations in vacuum. The amplitude of the oscillations is given by the PMNS matrix terms ($U^*_{\alpha i} U_{\beta i} U_{\alpha j} U^*_{\beta j}$) that are determined experimentally. From 1.9, we see that the observed oscillation phase $(\Delta m^2_{ij}/2E)L$ depends on the distance between the source and the detector (L), and the neutrino energy (E). To be sensitive to a particular square mass difference and be able to determine it, the observed oscillations must be sensitive to a particular phase (so equal to 2π):

$$\frac{\Delta m^2_{ij}}{2E} L_{ij} = 2\pi \to L_{ij} = \frac{4\pi E}{\Delta m^2_{ij}} \tag{1.10}$$

This is why neutrino oscillations observed at different distances and energies are required to determine the different square mass differences and PMNS matrix terms.

Natural neutrinos, created in the sun or in the atmosphere, have led to the discovery of oscillations. To study this phenomenon in more detail, artificial neutrinos from reactors and accelerators were also needed. Specific oscillations corresponding to particular square mass differences or mixing angles in 1.5 have been observed:

- the solar (and reactor) sector: sensitive to Δm^2_{21} and θ_{12}
- the atmospheric (and accelerator) sector : sensitive to $\Delta m^2_{23} \approx \Delta m^2_{31}$ and θ_{23}
- the reactor and accelerator sector: sensitive to Δm^2_{31} and θ_{13}

For example, θ_{12} and θ_{13} can be studied with the $\overline{\nu}_e$ survival probability (equation 1.11) which can be deduced from 1.9:

$$\begin{aligned} P_{\overline{\nu}_e \to \overline{\nu}_e} =& 1 - \cos^4\theta_{13}\sin^2(2\theta_{12})\sin^2(\Delta m^2_{12}\frac{L}{4E}) \\ & - \sin^2(2\theta_{13})\left(\cos^2\theta_{12}\sin^2(\Delta m^2_{13}\frac{L}{4E}) + \sin^2\theta_{12}\sin^2(\Delta m^2_{23}\frac{L}{4E})\right) \end{aligned} \tag{1.11}$$

For solar experiments, as θ_{13} is small but L/E is large enough to compensate the smallness of Δm^2_{12}, the last term can be neglected and $P_{\overline{\nu}_e \to \overline{\nu}_e}$ is approximated as:

$$P_{\overline{\nu}_e \to \overline{\nu}_e (solar)} \approx 1 - \sin^2(2\theta_{12})\sin^2(\Delta m^2_{12}\frac{L}{4E}) \tag{1.12}$$

Solar neutrinos are thus sensitive to $|\Delta m^2_{21}|$ and θ_{12}.

For reactor neutrino experiments, L/E is much smaller and as $\Delta m^2_{21} << \Delta m^2_{13} \approx \Delta m^2_{23}$, in eq. 1.11, the second term can be neglected.

By defining an effective mass splitting m_{ee} such that:

$$\Delta m^2_{ee} = \cos^2\theta_{12}\sin^2(\Delta m^2_{13}\frac{L}{4E}) + \sin^2\theta_{12}\sin^2(\Delta m^2_{23}\frac{L}{4E}) \tag{1.13}$$

it can be shown that a very good approximation leads to [104]:

$$P_{\overline{\nu}_e \to \overline{\nu}_e (reactor)} = 1 - \sin^2(2\theta_{13})\sin^2(\Delta m^2_{ee}\frac{L}{4E})) \tag{1.14}$$

This shows that reactor neutrinos allow the determination of θ_{13} and $|\Delta m^2_{ee}|$.

θ_{12} sector: solar and reactor neutrinos

As seen previously, solar neutrinos have led to the discovery of neutrino oscillations because of the solar ν_e disappearance. This effect is actually not due to oscillations in vacuum but to oscillations in matter: the Mikheïev-Smirnov-Wolfenstein (MSW) effect [114]. It takes into account the interaction between ν_e and electrons in matter via charged currents by adding a new energy to the Shrödinger equation for ν_e from which we deduced the oscillation probabilities. The Sun produces only ν_e but because of the electrons present in its plasma, their probability to be detected as ν_μ or ν_τ increases. These oscillations depend mostly on Δm^2_{21} and θ_{12}.

Solar neutrino experiments which look for the value of θ_{12} include Homestake, Gallex, SAGE, SNO and Super-Kamiokande.

Long baseline reactor experiments are also sensitive to these parameters. The KamLAND experiment [12] detected $\overline{\nu}_e$ from 55 reactors in Japon at an average distance of 180 km. It used liquid scintillator and photomultiplier tubes (PMT) to detect $\overline{\nu}_e$ via inverse beta decay. Neutrons from IBD were detected via capture on free protons which produces 2.2 MeV gammas.

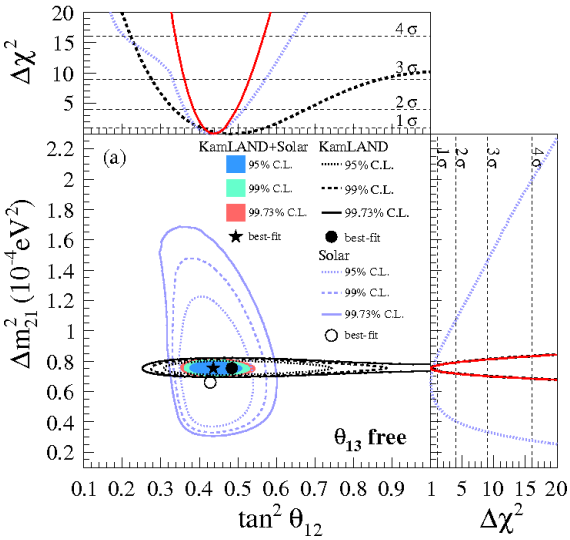

Figure 1.3: Allowed region for neutrino oscillation parameters from KamLAND and solar neutrino experiments. The side-panels show the $\Delta\chi^2$ profiles projected on the axis [71]

With current data from different experiments (figure 1.3), the values for the parameters are [1]:

$$\Delta m^2_{21} = 7.53 \pm 0.18 \times 10^{-5}\ \text{eV}^2 \tag{1.15}$$

$$sin^2\theta_{12} = 0.307 \pm 0.013 \tag{1.16}$$

θ_{23} sector: atmospheric and accelerator neutrinos

When cosmic rays enter the atmosphere, they produce mesons and muons which decay into neutrinos or antineutrinos of electronic or muonic flavour. Some experiments, like the IMB experiment, had shown issues with atmospheric neutrinos due to oscillations by comparing the fluxes of ν and $\overline{\nu}$ of electronic and muonic flavours [50]. The Super-Kamionande experiment had seen a ν_μ disappearance depending on the azimuthal angle of the neutrino. All these were hints of atmospheric neutrino oscillation. These ones have the baseline and energy which allow computing Δm^2_{31} ($\approx \Delta m^2_{32}$) and θ_{23}.

Current experiments which study atmospheric neutrinos can use the Cherenkov effect in water like Antares [83] or in ice like IceCube [6]. They installed strings of optical modules with PMTs in the Mediterranean Sea or the South Pole, respectively, to detect the Cherenkov light created by charged particles induced by neutrino interactions.

Experiments with accelerators which create ν_μ beams allow also to study these parameters and are the most constraining ones. The ν_μ beam is created from a proton beam which produces pions and kaons when hitting a target. These pions and kaons can then decay into ν and $\overline{\nu}$. Some experiments like NoνA [59], Minos

[19] and T2K [20] are very competitive in the determination of the atmospheric neutrino oscillation parameters. NOνA is the longest baseline experiment with a 810 km baseline in the USA. It searches for ν_μ disappearance and ν_e appearance from a ν_μ beam of Fermilab. The neutrinos that travel through the Earth are very sensitive to matter effects. T2K (The Tokai to Kamioka experiment) looked for ν_τ or ν_e appearance from the ν_μ beam of the J-PARC accelerator facility in Tokai. The detector used is the Super-Kamiokande detector described previously that also detects atmospheric neutrinos.

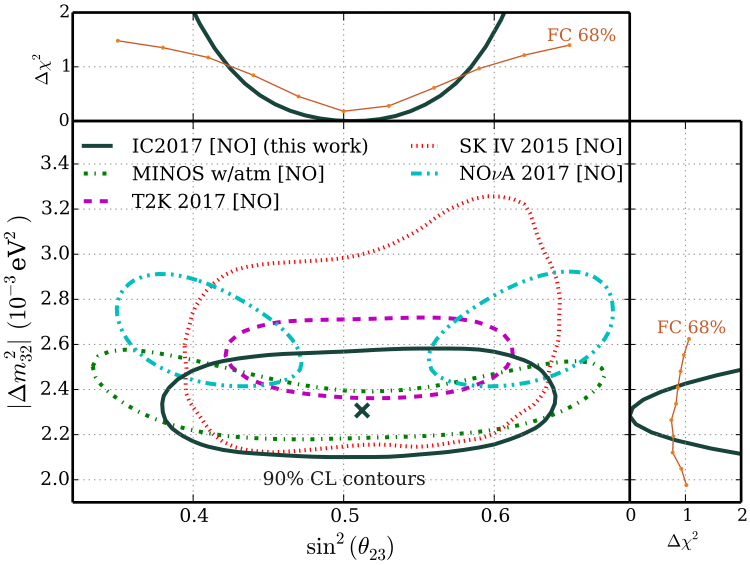

Figure 1.4: Allowed region at 90 % C.L. for atmospheric neutrino oscillation parameters from IceCube, MINOS, T2K, Super-Kamiokande and NOνA [5]

With current data from different experiments (figure 1.4), the values for the θ_{23} sector parameters are [1]:

$$\Delta m^2_{23}(\approx \Delta m^2_{31}) = 0.00251 \pm 0.00005 \text{ eV}^2 \tag{1.17}$$

$$sin^2\theta_{23} = 0.417 \pm 0.028 \tag{1.18}$$

θ_{13} sector: reactor and accelerator neutrinos

θ_{13} is the smallest angle of the PMNS matrix, thus it is more difficult to measure it. In 2011, the accelerator experiment T2K was the first one to prove that θ_{13} is non zero [10]. Dedicated experiments have since measured with more precision this mixing angle. To do so, they used neutrinos from reactors as their energies and accessible baselines can correspond to oscillations associated to θ_{13}.

A first reactor experiment has already been described: the one of F. Reines and C. Cowan which led to the first detection of neutrinos. Indeed, contrary to the solar or atmospheric experiments, reactors have a big neutrino flux (10^{20} $\overline{\nu}_e$ GW$_{th}$

$^{-1}$ s^{-1} for fission reactors), bigger than backgrounds which make the neutrino detection easier with more compact detectors. Most of these oscillation experiments use 2 detectors: a near one to measure the neutrino flux and a far one to study the oscillations. The oscillation phenomenum observed is $\overline{\nu}_e$ disappearance. The detectors are based on the detection of IBD reactions, i.e. a detection in delay time coincidence of a positron and a neutron via radiative capture which sign the interaction of a $\overline{\nu}_e$ with a proton of the detector (eq. 1.2).

The Double Chooz experiment, located in France, detected IBD events with Gd-doped liquid scintillator [15]. Neutrinos originated from 2 reactor cores of 4.25 GW$_{th}$ at 1.05 km from the detector. The prompt signal is the positron annihilation and the delayed signal is the neutron capture on H or Gd which produces 2.2 MeV or 8 MeV gamma rays respectively.

In 2012, the Double Chooz experiment confirmed that θ_{13} is non-zero [15] and the Daya Bay [31] and RENO[110] experiments have since improved this measurement.

Daya Bay, in China, has done the most precise measurement of the reactor mixing angle. It observes neutrinos from six 2.9 GW$_{th}$ reactors with eight detectors located at different baselines. The detector technology used is Gd-doped liquid scintillator to detect IBD events. The RENO experiment in Korea works on the same principle with 6 reactor cores and 2 detectors: a near one and a far one.

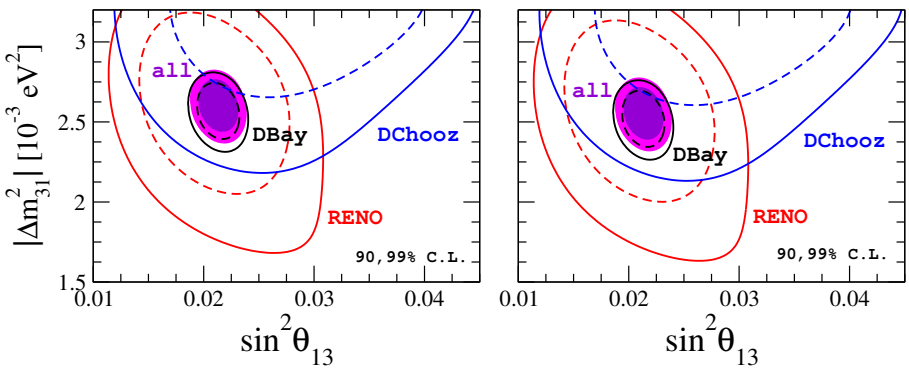

Figure 1.5: Allowed region at 90 and 99% C.L. for θ_{13} sector from Daya Bay, RENO and Double Chooz reactor experiments for normal hierarchy (left) and inverted hierarchy (right) (see section 1.2.1) [109]

With current data from different experiments, the value for the θ_{13} parameter is [1]:

$$sin^2\theta_{13} = 0.0212 \pm 0.0008 \tag{1.19}$$

1.1.6 Conclusion: recap of which neutrino properties are established

A picture of our admitted knowledge on neutrinos from experimental data has been established. We know that neutrinos are fermions with no charge and spin 1/2. Neutrinos are left-handed and antineutrinos are right-handed. There are 3 different leptonic flavours of neutrinos (ν_e, ν_μ and ν_τ) which are different from the 3 mass eigenstates (ν_1, ν_2 and ν_3). This allows neutrinos to oscillate from a flavour to another. They interact only via weak interaction. They can interact with matter via the exchange of a W-boson, i.e. via charged-current interaction, and are converted to a charged lepton of the same flavor:

$$\nu_l + X \rightarrow l + X' \tag{1.20}$$

Neutrinos can also interact with matter via the exchange of a Z-boson, i.e. via neutral-current interactions:

$$\nu_l + X \rightarrow \nu_l + X' \tag{1.21}$$

This process can be tagged by observing the system against which the neutrino is recoiling.

However, this is not the end of the story. With this picture of the neutrino, there are several inconsistencies and anomalies like the small masses of neutrinos which disagree with the Standard Model of particle physics. These issues are very important to solve as they are currently one of the most promising path towards new physics.

1.2 Neutrino mysteries

1.2.1 Questions about neutrinos

The existence of neutrinos has been demonstrated sixty years ago. However, as they are difficult to detect, they remain the most mysterious particles of the standard model. Indeed, there are still many questions about them that are not answered:

- What is the absolute neutrino mass scale?
- What is the neutrino mass hierarchy?
- What are the precise values of all the PMNS matrix parameters? Why is this matrix so different from the CKM matrix (the quark flavor mixing matrix which is almost proportional to the identity matrix)?
- Do neutrinos violate CP? What are the CP violating phases in the PMNS matrix? More broadly, is there CP violation in the lepton sector?
- What is the neutrino nature: Majorana or Dirac (i.e. are neutrino and antineutrino states equivalent)?

- Are there only 3 types of neutrinos? Could there be sterile neutrinos?

In the following, these issues will be developed along with the description of current experiments trying to solve them. In my thesis, I have worked on two of these experiments, SuperNEMO and SoLid, which try to answer questions concerning the nature of neutrinos.

Absolute neutrino mass

Before discovering neutrino oscillations, physicists thought neutrino masses were null. Although it was proven that it is false, their masses are very small, at least six orders of magnitude smaller than the electron mass. This is why finding the absolute neutrino mass scale is very difficult. Oscillation experiments give many informations on neutrinos but they can not bring any information on the absolute neutrino masses. Measurements of the end-point on the β decay spectrum have always been the most sensitive and model-independent experiment to find neutrino masses. The end of the energy spectrum is cut off m_ν before the zero-mass end-point so the absolute neutrino mass can be known from the shape of the β energy spectrum.

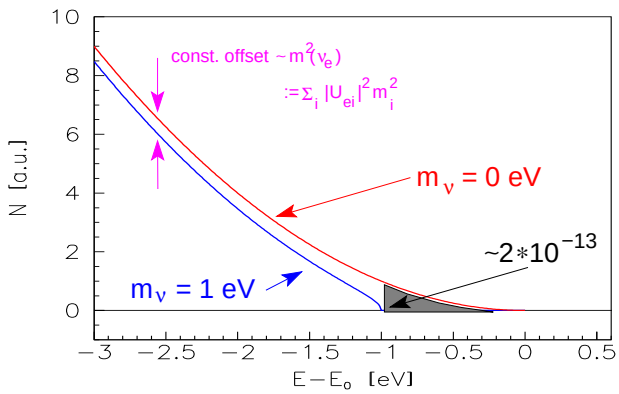

Figure 1.6: The end-point of the β decay energy spectrum in case neutrino have a zero mass or a 1 eV mass [64].

As β decay spectrum measurements are done with only one flavor, ν_e, which is a superposition of at least three mass eigenstates ν_1, ν_2 and ν_3 whose weight depends on the mixing matrix elements, the spectrum observed is a superposition of three spectrum whose endpoint cutoffs are the three mass eigenstates. A neutrino effective mass is defined: $m_\beta = \sum_i |U_{e_i}|^2 m_i$ and the β decay spectrum can be approximated as a single neutrino spectrum. To measure such a small effect (figure 1.6), dedicated experiments must have a very high energy resolution. A β decay nuclide used a lot for these experiments is tritium because it has a low energy end-point ($Q_\beta = 18.6$ keV) and a high decay rate. Tritium experiments have already put limit on the neutrino mass: $m_\beta < 2$ eV [40]. The current most ambitious experiment is KATRIN. It aims at a precision study of the tritium beta decay and may

start to be sensitive to the mass hierarchy if it achieves a sensitivity of 200 meV. Some R&D is also conducted to improve the energy resolution of neutrinos mass experiments using bolometers or cyclotron radiation emission spectroscopy like in Project 8 [43].

Cosmology and $0\nu\beta\beta$ experiments can also put constraints on the absolute neutrino mass but they are much more model dependent. Current cosmological constraints are the most stringent and consider the sum of neutrino masses to be below tenths of an eV [78].

Mass hierarchy

The pattern of the neutrino masses is still unknown. We have a good idea of the value of 2 square mass differences thanks to neutrino oscillations, but it does not tell how neutrino masses are ordered. As we have seen, $\Delta m^2_{12} << \Delta m^2_{13} \approx \Delta m^2_{23}$. So there could be either a "normal hierarchy" consisting of two light and one heavy neutrino, or an "inverted hierarchy" with two heavy and one light neutrino (figure 1.7). Resolving the issue of the neutrino mass hierarchy would have impacts on the search for CP violation, the absolute neutrino mass and the search for neutrinoless double beta decay to discover the neutrino nature.

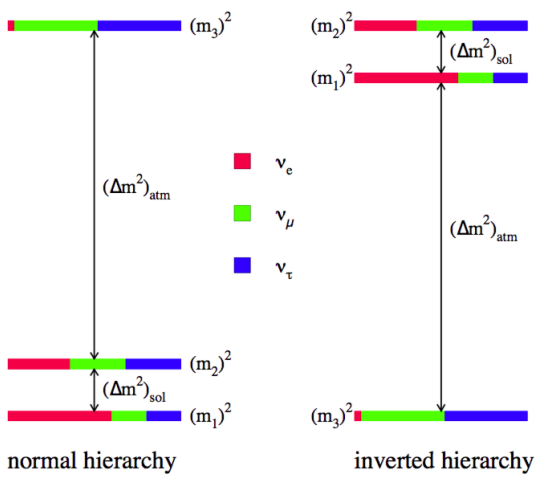

Figure 1.7: The two possible neutrino mass hierarchies

The mass hierarchy can be determined thanks to oscillation effects. Indeed, oscillation probabilities (equation 1.9) depend on the different Δm^2_{ij} as long as the different U_{ij} are non-zero and distinct. By measuring these probabilities and knowing the U_{ij} parameters, one can have a measurement of Δm^2_{13} and Δm^2_{23} which allows distinguishing which one is the largest if the measurement is precise enough. This is a challenging measurement as $\Delta m^2_{12} << \Delta m^2_{13}$ and $\sin^2\theta_{13} << 1$ so it requires a very good energy resolution. However, the mass hierarchy could also be determined thanks to matter effects in oscillations.

Accelerator experiments like NOνA and T2K are trying to solve this issue. Other sources of neutrinos can be used like reactor neutrinos (JUNO in China and RENO50 in South Korea will tackle this issue) or atmospheric neutrinos (with Cherenkov detectors like Hyper-K, MEMPHYS, PINGU and ORCA for example). Current data seem to favor normal hierarchy mostly because NOνA and T2K have a better agreement in the value of θ_{23} with normal hierarchy [109] but this is preliminary. Future accelerator experiments like DUNE in the USA or Hyper-Kamiokande in Japan will have a better sensitivity to the mass hierarchy.

If we were lucky enough to observe a supernova, it could also help to determine the mass hierarchy as their matter effects are quite different from the one which happen on earth. They are a big source of neutrinos but are not frequent and can not be predicted, plus there are model-dependant effects to take into account. Experiments aiming at detecting supernovae neutrinos include Super-K, IceCube, ORCA, KamLAND, Borexino, Daya Bay or JUNO.

To solve this problem of mass hierarchy, other observables than neutrino oscillation can also be used like measurements of absolute neutrino masses, $0\nu\beta\beta$ or cosmology, which would be sensitive to the mass hierarchy if the sum of neutrino masses is less than 0.1 eV ([7], see figure 1.8).

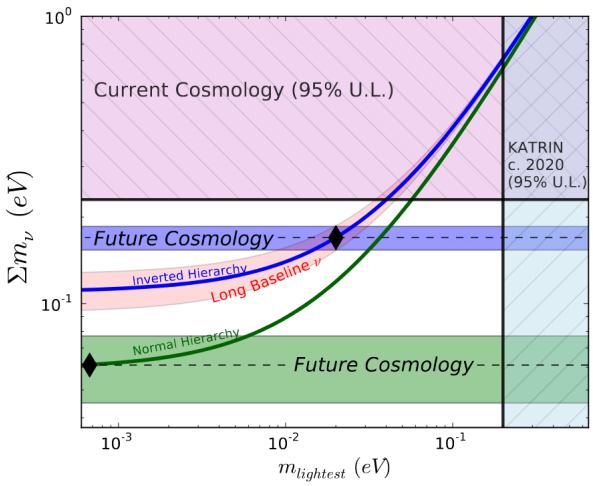

Figure 1.8: Constraints on the neutrino mass hierarchy by cosmology, long baselines and direct neutrino mass (KATRIN) measurements [7]. $m_{lightest}$ is the smallest neutrino mass.

CP violation

CP violation plays a crucial role in the history of the universe as it could be responsible for the asymmetry between matter and antimatter. It has first been observed in kaon systems in 1964 [58]. It comes from the CP-odd phase parameter in the CKM quark mixing matrix. If it exists in neutrino oscillations (via the CP-odd phase δ), it would be a completely new source of CP violation which would be

really interesting to observe.

The CP conjugate of $\nu_\alpha \to \nu_\beta$ is $\overline{\nu}_\alpha \to \overline{\nu}_\beta$ so CP violation implies that:

$$P(\nu_\alpha \to \nu_\beta) \neq P(\overline{\nu}_\alpha \to \overline{\nu}_\beta) \tag{1.22}$$

with $\alpha \neq \beta$ else the equality is guaranteed by CPT invariance. To measure these oscillation probabilities, beams of neutrinos and anti-neutrinos are needed. CP-violation in the lepton sector can also be searched with a precise determination of the neutrino mixing matrix elements. In the PMNS matrix (equation 1.5), there are 3 phases which can be sources of CP violation: one Dirac phase δ and two Majorana phases α and β. The two Majorana phases are physical only if neutrinos are Majorana fermions but the nature of the neutrino is still unknown and these phases do not affect oscillations. However, the Dirac phase can be explored in oscillation experiments. If it is different from 0 or π, then neutrino oscillation probabilities violate CP invariance.

Atmospheric neutrinos and antineutrinos can be used to study CP violation but they require huge statistics to contain the uncertainties on their baseline and energy distributions.

CP violation can also be searched with long-baseline experiments using accelerators which can produce either neutrinos or antineutrinos. Although there is no statistical evidence, there are hints from accelerators experiments for the value of δ from T2K, NOνA or MINOS. The current best fit value for the Dirac CP phase, which is dominated by T2K results, is $\delta_{CP} \simeq 3\pi/2$ [109].

1.2.2 Neutrino nature: Dirac, Majorana

The mechanism responsible for the generation of neutrino mass is still unknown. Neutrino masses are so small, particularly compared to other known fermion masses, that they rise lots of questions. Indeed, neutrino masses are at least six orders of magnitude smaller than the electron mass, so there is a surprising energy gap between neutrino masses and other fermions masses which may indicate that the neutrino mass mechanism is different from the other fermions.

Currently, we consider two different mechanisms which can occur: the Dirac mass mechanism or the Majorana mass mechanism. Proving that the neutrino is a Majorana or Dirac particle would have a huge impact on neutrino physics and particle physics. Indeed, a Majorana neutrino would violate lepton number conservation, which has never been observed, and neutrino masses would come from a new fondamental energy scale in physics.

Dirac mass

A natural way to give a mass to neutrinos is to copy the way quarks and charged leptons acquire their mass through Yukawa coupling to the Higgs field. The Dirac

mass can be defined as: $m_D = g_Y \frac{v}{\sqrt{2}}$ where g_Y is the Yukawa coupling constant and v the expected vacuum value.

In the case of a free field without interaction, the Lagrangian which describes the evolution of the neutrino wave function ψ can be written:

$$L = \overline{\psi}\left(i\gamma^\mu \frac{\delta}{\delta x^\mu} - m_D\right)\psi \tag{1.23}$$

It is composed of a first term which corresponds to the kinetic energy and a second term which is the Dirac mass term of the neutrino.

The chirality operators $P_L = \frac{1}{2}(1-\gamma_5)$ and $P_R = \frac{1}{2}(1+\gamma_5)$ can be used to decompose the neutrino wave function:

$$\psi = P_L\psi + P_R\psi = \psi_L + \psi_R \tag{1.24}$$

This definition of the chirality operators implies :

$$\overline{\psi}_L\psi_L = \overline{\psi}P_R P_L\psi = 0 \tag{1.25}$$

It follows that the Dirac mass term of the lagrangian is given by:

$$L_D = -\overline{\psi}m_D\psi = -m_D(\overline{\psi}_L + \overline{\psi}_R)(\psi_L + \psi_R) = -m_D(\overline{\psi}_L\psi_R + \overline{\psi}_R\psi_L) \tag{1.26}$$

This solution to give a mass to neutrinos requires that there exists both left-handed and right-handed neutrinos. But as we have seen, only left-handed neutrinos have been detected. This would mean that if it is the right way to create neutrino mass, there should exist right-handed neutrinos which do not interact weakly to explain why they have not been detected yet. Another issue is that the Yukawa coupling constant should be very small for neutrinos as their mass are so small compared to other fermions. Taking the upper limit from tritium experiments, a neutrino mass of 2 eV requires a Yukawa coupling of the order of 10^{-12}. This mass mechanism does not give any explanation for this smallness.

Majorana mass

In 1937, Ettore Majorana proposed the idea that ψ_L and ψ_R may not be independant. The Majorana relation between ψ_L and ψ_R would be:

$$\psi_R = \xi C\overline{\psi}_L^T \tag{1.27}$$

With ξ an arbitrary phase factors which can be absorbed by defining $\psi \to \xi^{1/2}\psi$ and C the charge conjugation matrix. This way the neutrino wave function (eq. 1.24) can be written:

$$\psi = \psi_L + \psi_R = \psi_L + C\overline{\psi}_L^T \tag{1.28}$$

which implies:

$$\psi^C = C\overline{\psi}^T = \psi \tag{1.29}$$

This means that the charge conjugate of the neutrino, the antineutrino, is the same particle as the neutrino. This is possible for neutrinos because they are neutral. The only difference is the helicity as in this description if neutrinos are left-handed then antineutrinos are right-handed.

As the observed neutrinos are only left-handed, a mass term should be generated in the Lagrangian from equation 1.26 with only ψ_L. The Majorana relation allows doing so since one can prove with eq. 1.27 that ψ_L^C is right-handed.
Thus a Majorana mass term m_M can be generated in the Lagrangian by using ψ_L^C in place of ψ_R in equation 1.26:

$$L = -\frac{1}{2} m_M (\overline{\psi}_L \psi_L^C + \overline{\psi^C}_L \psi_L) \tag{1.30}$$

The factor 1/2 avoids double counting. The advantage of this mechanism is that neutrinos can acquire their mass through this Majorana mass term which does not require a Yukawa coupling.

Seesaw mechanism

A possible explanation to the smallness of neutrino masses has been found with the seesaw mechanism involving both Dirac and Majorana mass mechanisms. A general Lagrangian can be defined including the Dirac mass term m_D of equation 1.26, another Dirac mass term (same m_D) with the charge conjugate fields, and the Majorana mass terms from equation 1.30 for left-handed and right-handed neutrinos with masses m_L and m_R respectively:

$$\begin{aligned} L_{M+D} &= -\frac{1}{2}(m_D \overline{\psi}_R \psi_L + m_D \overline{\psi^C}_L \psi_R^C + m_L \overline{\psi^C}_L \psi_L + m_R \overline{\psi^C}_R \psi_R) + h.c. \\ &= -\frac{1}{2} \begin{pmatrix} \overline{\psi^C}_L & \overline{\psi}_R \end{pmatrix} \begin{pmatrix} m_L & m_D \\ m_D & m_R \end{pmatrix} \begin{pmatrix} \psi_L \\ \psi_R^C \end{pmatrix} + h.c. \end{aligned} \tag{1.31}$$

Here ψ are not mass eigenstates as the mass matrix is not diagonal. The mass matrix can be diagonalised with the mass eigenstates ψ_+ and ψ_- to determine the mass eigenvalues m_+ and m_-:

$$m_\pm = \frac{1}{2}\left(m_L + m_R \pm \sqrt{(m_L - m_R)^2 + 4m_D^2}\right) \tag{1.32}$$

The mixing angle θ which describes the mass eigenstates ψ_+ and ψ_- as a mixing of ψ_L and ψ_R is then:

$$\tan 2\theta = \frac{2m_D}{m_R - m_L} \tag{1.33}$$

For the seesaw mechanism, one considers that $m_L = 0$ and $m_D \ll m_R$. In this case, the two mass eigenstates and the mixing angle become:

$$m_+ \approx m_R \qquad m_- \approx \frac{m_D^2}{m_R} \tag{1.34}$$

$$\tan 2\theta = \frac{2m_D}{m_R} \ll 1 \tag{1.35}$$

This would imply the existence of a heavy sterile neutrino ψ_+ of mass m_R and a light neutrino ψ_- of mass $\frac{m_D^2}{m_R}$. As the mixing angle is very small, ψ_- is almost entirely composed of ψ_L so it corresponds to the observed left-handed light neutrino while ψ_+ is almost entirely composed of ψ_R which would be a right-handed heavy neutrino not observed yet. This seesaw mechanism could explain the smallness of the observed neutrino mass independently from the value of the Yukawa coupling with the existence of a heavy neutrino. This model could be real if neutrinos are Majorana particles but this has to be proven.

$\beta^-\beta^-$ phenomenology

Oscillation experiments can not distinguish the nature of the neutrinos. The best way to know if neutrinos are Majorana or Dirac particles is to search for lepton number violation. Indeed, if they are Dirac particles, neutrinos have a lepon number L = 1 and antineutrinos have a lepton number L = -1, just like other leptons according to the Standard Model. However if they are Majorana particles, neutrinos and antineutrinos must have the same lepton number so lepton number is violated. It can be shown [79] that the Majorana mass term generates transitions with ΔL= $\pm$2.

The most sensitive experiments to lepton number violation we can think of is the search for neutrinoless double beta decay ($0\nu\beta\beta$). Neutrinoless double beta decay would imply lepton number violation by 2 units. The detection of such process would have a huge impact in particle physics because lepton number violation has never been observed for any force although we do not know any symmetry that could explain this conservation law.

The first idea of the existence of $2\nu\beta\beta$ (1.36) was formulated by Goeppert-Mayer in 1935. A nucleus (A, Z) could emit two electrons and two neutrinos in one decay when a simple beta decay is energetically disfavored for nucleus with an even number of protons and neutrons.

$$(A, Z) \rightarrow (A, Z + 2) + 2e^- + 2\overline{\nu}_e \tag{1.36}$$

Observing $2\nu\beta\beta$ decay is very challenging. This process is extremely rare with half-lives bigger than 10^{19} years. Only a few nuclei are concerned as it requires that $Q_{\beta\beta}$ is positive and that the nucleus can not decay via simple β decay, else the half-life of β decay is much smaller that the one of $2\nu\beta\beta$ decay (figure 1.9). There are only 35 nuclei in nature that undergo $2\nu\beta\beta$ decay.

In 1939, Furry considered the idea of $0\nu\beta\beta$ (reaction 1.37): no neutrino would be emitted in the $\beta\beta$ decay process if neutrinos and antineutrinos are the same particle. A virtual $\overline{\nu}$ which is emitted in the decay of the nucleus toward an intermediate state is absorbed by this intermediate nucleus while decaying and emitting

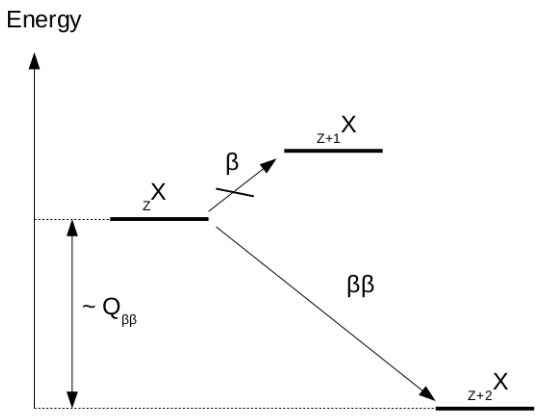

Figure 1.9: Allowed $\beta\beta$ transition

a second electron. This process is forbidden by the Standard Model and could be possible only if neutrinos and antineutrinos are the same Majorana particle. Although several theories exist to explain $0\nu\beta\beta$, they all impose neutrinos to be Majorana particles.

$$(A, Z) \rightarrow (A, Z + 2) + 2e^- \tag{1.37}$$

An experimental way to identify $2\nu\beta\beta$ from $0\nu\beta\beta$ is to look at the energy spectrum of the two final electrons (figure 1.10). For $2\nu\beta\beta$, there are 4 leptons in the final state so the energy sum spectrum of the two electrons is continuous from 0 to $Q_{\beta\beta} = M_i - (M_f + 2m_e)$ with M_i and M_f the masses of the initial and final nucleus and m_e the electron mass. However in the $0\nu\beta\beta$, the only light particles of the final states are the 2 electrons so their energy sum spectrum should be a peak at the value $Q_{\beta\beta}$.

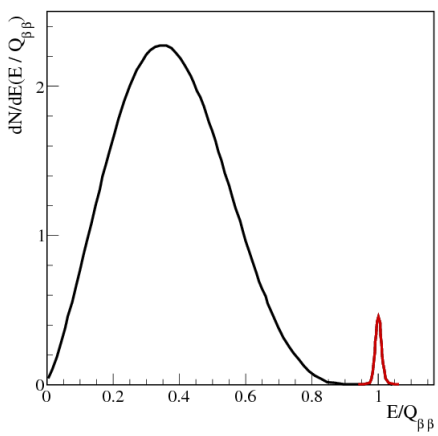

Figure 1.10: Energy spectrum expected for $2\nu\beta\beta$ in black and $0\nu\beta\beta$ in red. The $0\nu\beta\beta$ peak is smeared by the detector energy resolution.

The half-life of the $0\nu\beta\beta$ decay can be calculated:

$$(T_{1/2}^{0\nu\beta\beta})^{-1} = G_{0\nu\beta\beta} \times (M_{0\nu\beta\beta})^2 \times \left(\frac{m_{\beta\beta}}{m_e}\right)^2 \tag{1.38}$$

With $G_{0\nu\beta\beta}$ the two particle phase space factor, $M_{0\nu\beta\beta}$ is the nuclear matrix element and $m_{\beta\beta}$ the effective Majorana neutrino mass which takes into account the neutrino mixing.

- The phase space factor $G_{0\nu\beta\beta}$ depends on $Q_{\beta\beta}$ and details of the kinematics. It is known with good precision today.

- The nuclear matrix element $M_{0\nu\beta\beta}$ is difficult to calculate because of the high number of nuclei which requires precise many-body nuclear models. Different models are developped and tested like the Nuclear Shell Model or the Quasiparticle Random Phase Approximation. The nuclear matrix elements are different for $2\nu\beta\beta$ and $0\nu\beta\beta$. Measuring the half-life of $2\nu\beta\beta$ is a good way to check the model predictions but is not sufficient to predict unambiguously the $0\nu\beta\beta$ ones.

- The effective Majorana neutrino $m_{\beta\beta}$ is defined as:

$$m_{\beta\beta} = |\sum_i U_{ei}^2 m_i| \tag{1.39}$$

  It depends on the PMNS parameters including the Dirac and Majorana CP violation phases. We see that observing $0\nu\beta\beta$ could constrain the PMNS matrix elements and the absolute neutrino mass. This effective Majorana mass also depends on the neutrino mass hierarchy as it can be written as a function of the different square mass differences. Figure 1.11 shows that knowing the minimum neutrino mass would help to know which region of $m_{\beta\beta}$ has to be reached in order to search for $0\nu\beta\beta$.

Double beta decay experiment status

The observation of $0\nu\beta\beta$ requires the detection of 2 electrons emitted at the same time whose sum energy is equal to $Q_{\beta\beta}$. Double beta decay experiments try to optimize three factors: the biggest exposure (mass×time), the best radiopurity and the best background rejection. No signal has been observed yet although several experimental techniques have been developed to tackle this issue.

These experiments require a very low background environment as the signal they are seeking is very rare. This is why the detectors are placed underground to be shielded against cosmic rays. The source and all the materials in the detector have to be purified to tremendously lower radioactivity. The isotopes with high $Q_{\beta\beta}$ are more suited as the background from natural radioactivity decreases with energy.

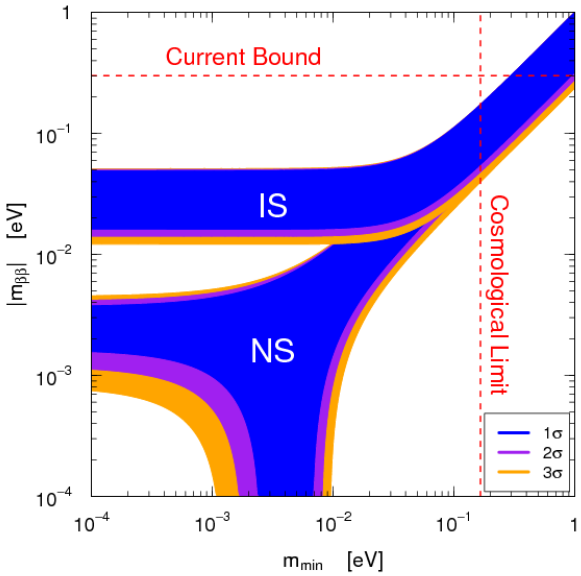

Figure 1.11: The effective Majorana neutrino mass as a function of the minimum neutrino mass for both hierarchies. Observing a $0\nu\beta\beta$ signal could determine the mass hierarchies. However, if the hierarchy is normal, $0\nu\beta\beta$, even if it exists, may never be observed.

The choice of the $\beta\beta$ isotope is very important to get a good sensitivity to $0\nu\beta\beta$. $\beta\beta$ decay experiments prefer isotopes with a high transition energy $Q_{\beta\beta}$ and a high $2\nu\beta\beta$ half-life to avoid backgrounds in the region of interest, large phase space factors and nuclear matrix elements to expect more signal, a high natural abundance to facilitate the enrichment.
Various types of experiments searching for $0\nu\beta\beta$ have to be considered.

Germanium experiments

Germanium semiconductor diodes can be both the source and the detector with excellent detection efficiency and energy resolution (down to a few keV) when cooled to low temperature. In this calorimetric approach, the charge carriers (electrons and holes) created by a particle interaction in the semiconductor are collected by electrodes and converted into a voltage pulse by preamplifiers. Pulse shape discrimination techniques are used to discriminate multi-sites (more likely γ signals) and single-site events (including $\beta\beta$ signals). These diodes are enriched in the $\beta\beta$ emitter ^{76}Ge. Its low $Q_{\beta\beta}$ of 2039 keV makes them sensitive to natural radioactive backgrounds like ^{208}Tl.

Previous germanium experiments like Heidelberg-Moscow or IGEX have already put constrains on the $0\nu\beta\beta$ half-life of more than 10^{25} years.

GERDA is a germanium experiment located in Italy at the Gran Sasso underground laboratory (LNGS). It reprocessed coaxial germanium detectors from Heidelberg-Moscow and IGEX experiments. It achieved a mass of 17.67 kg of ger-

manium enriched at 86% in phase I. It is cooled down with ultra-pure liquid argon which also acts as an external γ shield and an active muon veto. For phase II, GERDA has used new broad energy germanium (BEGe) that doubled its mass (figure 1.12). BEGe allow better pulse-shape discrimination leading to a better background rejection. GERDA aims to become the first background-free experiment searching for $0\nu\beta\beta$ with less than 1 count expected in the energy region of interest (figure 1.13). When combining data from phase I and phase II, GERDA reaches a lower limit for $0\nu\beta\beta$ half-life of 5.3×10^{25} years [21].

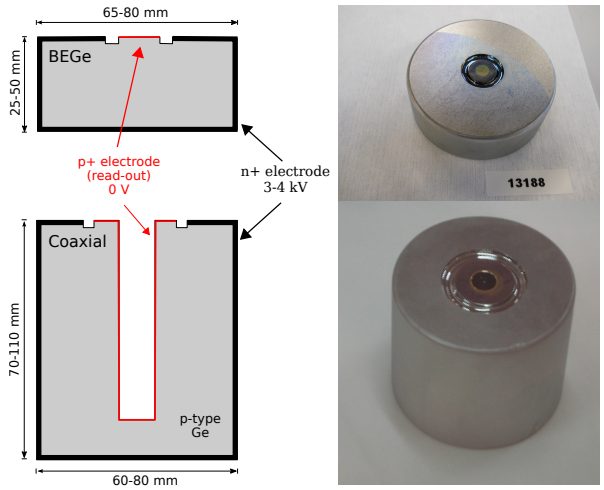

Figure 1.12: Two types of germanium detectors from GERDA: BEGe and Coaxial with their corresponding photos on the right.

The MAJORANA demonstrator located in the Sanford Underground Research Facility in Lead, South Dakota is also a germanium detector with 44.8 kg of Ge. It was built to establish the feasibility of a Ge-based ton-scale experiment with the GERDA collaboration by showing the expected background will be low enough [66]. To do this, they use ultra-low background electroformed copper for the construction of the cryostat and other detector components.

Bolometer experiments

Bolometers can measure the heat increase generated by a particle interacting in its crystal. They work at very low temperature (around 10 mK) to detect phonons with semiconductor thermistors. The crystals are both the source and the detector. They have a great energy resolution and low intrinsic background but there can be issues with signal pile-up as they have slow response and backgrounds from surface contamination due to limits of the crystal geometry.

The CUORE experiment (Cryogenic Underground Observatory for Rare Events) is also located at LNGS. It is a ton scale experiment that uses the isotope ^{130}Te with TeO_2 crystals. It is the successor of the CUORICINO and CUORE-0 experiments and is currently in its commissioning phase. The CUORE detector is composed of

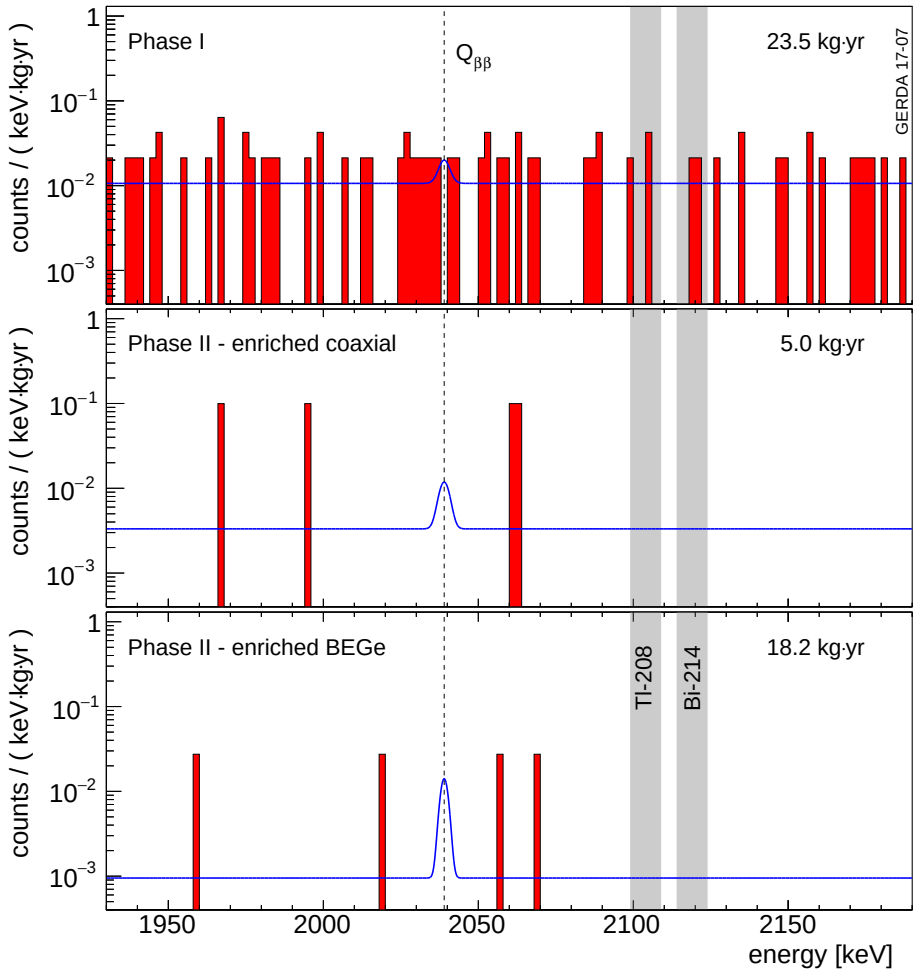

Figure 1.13: Results of the GERDA experiment with combined Phase I data (top), Phase II coaxial (middle) and BEGe detector spectra (bottom) in the analysis window with their exposure. The red histogram is the final spectrum. The grey bands indicate intervals excluding known γ lines. The blue line is the hypothetical signal for $T_{1/2}^{2\beta0\nu} = 8.0 \times 10^{25}$ years. [21]

988 TeO_2 cubic crystals of 750 g [27]. With CUORICINO and CUORE-0, a limit on the $0\nu\beta\beta$ half-life of 4.0×10^{24} years had been set. With CUORE, the expected limit is 9×10^{25} years [27].

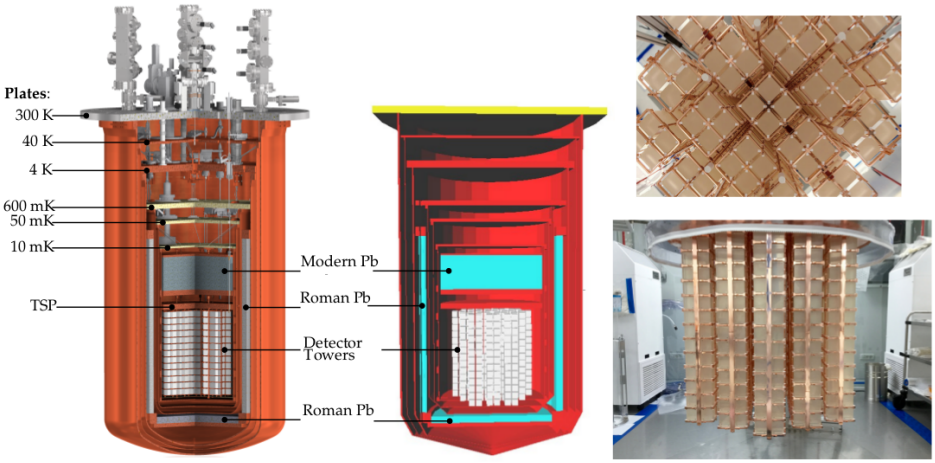

Figure 1.14: Schematic view of the CUORE detector (left) and its photo (right) [27]

CUPID is a project of CUORE upgrade to use scintillating bolometers. The first stage is LUCIFER (Low-background Underground Cryogenics Installation For Elusive Rates) with 15 kg of ZnSe. LUMINEU (Luminescent Underground Molybdenum Investigation for NEUtrino mass and nature) uses $ZnMoO_4$ crystals to search for double beta decay of ^{100}Mo [34]. Scintillating bolometers can measure both light pulses and heath pulses. With scintillation light, a better background rejection can be achieved. However, scintillating bolometers are not used for Te crystals because of their low light yield.

Time projection chamber

Time projection chambers (TPC) using gas provide a 3-dimensional reconstruction of particle trajectories. Electrons from ionization of the medium by a charged particle, drift in an electric field towards an anode with a readout system.

Exo-200 is located in a salt mine in the USA and uses 200 kg of xenon enriched at 81% in ^{136}Xe. It has a cylindrical liquid xenon TPC detector with the cathode at the center. The scintillation light in the TPC is registered by avalanche photodiodes (APD) and the signal charge is registered by anode wire grids. It can discriminate between single-sites and multiple-sites. As shown in figure 1.16, there are still several backgrounds in the energy region of interest. Exo-200 found a lower limit for the $0\nu\beta\beta$ half-life of 1.8×10^{25} years [26]. Their half-life sensitivity should be improved to 10^{28} years with nEXO, a ton-scale liquid xenon TPC detector.

NEXT-100 will be a high-pressure gaseous xenon TPC detector at the Canfranc underground laboratory in Spain [68]. Particle tracks will be longer than in liquid

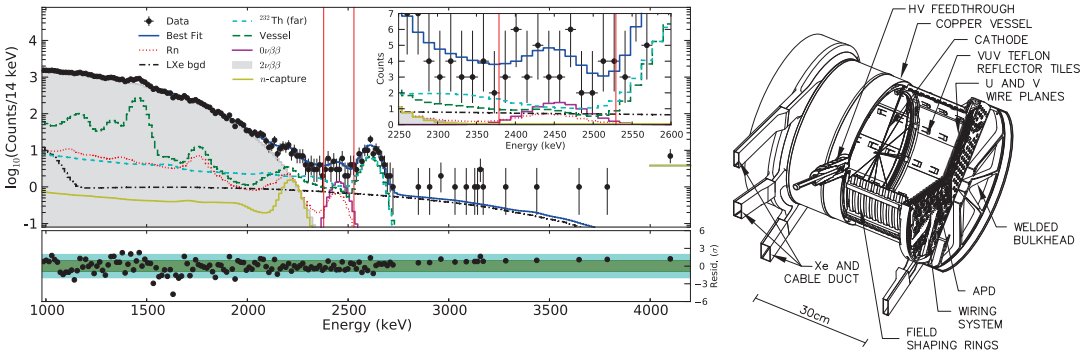

Figure 1.15: Left: energy spectrum of single-site events for EXO-200 experiment with a zoom in the energy region of interest. Right: schematic view of the EXO-200 TPC detector. [55]

xenon detector and background rejection with tracks topology will be easier. It will also have a better energy resolution but as gas have lower density than liquids, reaching a large exposure will be more difficult. NEXT-100 aims to reach a lower half-life limit of 6.0×10^{25} years for an exposure of 275 kg.years.

Liquid scintillator experiments

Liquid scintillator experiments introduced here are very large detectors. KamLAND and SNO have already been presented. Although they were originally built to study neutrino oscillations, they can look for double beta decay by adding $\beta\beta$ isotopes in their detectors. They both use PMTs to detect the scintillation light. The inconvenience of this kind of experiments is the lower energy resolution and absence of event topology information but they have the largest amounts of isotopes.

KamLAND-ZEN, located under mount Ikenoyama in Japan [72], is a liquid scintillator experiment with xenon. It uses the existing KamLAND detector where a balloon of 13 ton of Xe-loaded liquid scintillator is suspended at the center. The main liquid scintillator (1 kton) is used as a shield against cosmic rays and as a detector for internal radiation from the xenon liquid scintillator in the balloon. Despite an issue with ^{110m}Ag background on the balloon and ^{214}Bi contamination, they put the best lower limit so far on the $0\nu\beta\beta$ half-life of 1.07×10^{26} years.

SNO (Sudbury Neutrino Observatory) located in SNOLAB, in a nickel mine in Canada, is the world's largest liquid scintillator experiment. The SNO+ detector will be filled with 780 tons of liquid scintillator and 800 kg of ^{130}Te in 2018 and 2019. The projected lower limit on the $0\nu\beta\beta$ half-life is 9×10^{25} years after 5 years.

Tracker-Calorimeter experiments: NEMO

One series of experiments, called NEMO (Neutrino Ettore Majorana Observatory), uses both a tracker and calorimeter technology with a passive source. The tracker can reconstruct full topology of events, including tracks of individual electrons and the calorimeter can measure the particle energies. This way electrons and

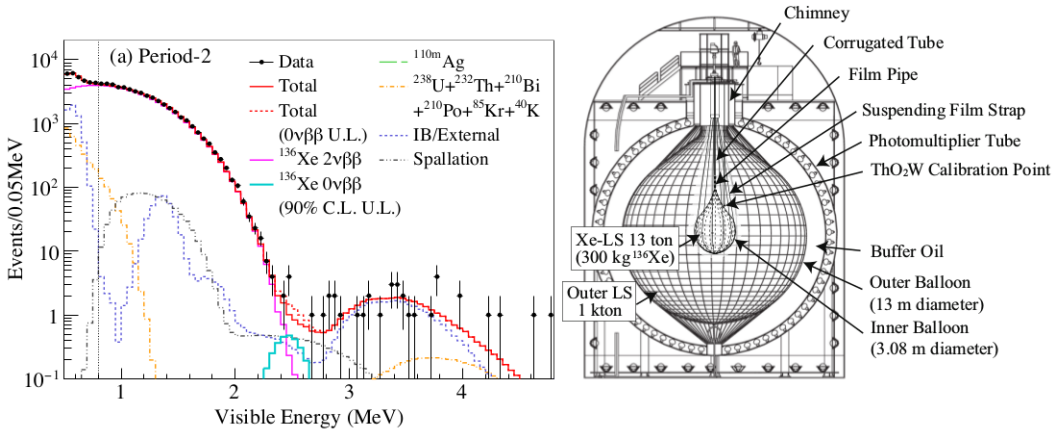

Figure 1.16: *Left:* KamLAND-Zen energy spectrum of selected $0\nu\beta\beta$ candidates within a 1 m radius spherical volume in Period-2 drawn together with best-fit backgrounds, the $2\nu\beta\beta$ decay spectrum, and the 90% C.L. upper limit for $0\nu\beta\beta$ decay. *Right:* schematic view of the KamLAND-Zen detector. [55]

γ are easily distinguished. A magnetic field in the tracker allows the discrimination of positrons from electrons. This technology offers a great background rejection and could also allow to distinguish between different mechanisms of $0\nu\beta\beta$ decay. However, it brings several challenges: the smallness of target foils, a modest energy resolution or a reduced detection efficiency.

The NEMO-3 detector was located in the Modane underground laboratory (LSM) in the Frejus tunnel [38]. It was made of several sectors with thin source foils containing 7 different $\beta\beta$ isotopes. The source foils were suspended between two trackers made of drift cells operating in Geiger mode in a concentric cylindrical volume. The tracker was surrounded by plastic scintillator calorimeters with low radioactivity PMTs. The NEMO-3 experiment took data from February 2003 to January 2011 with seven isotopes. After reducing the radon background thanks to the installation of a radon reduction factory in October 2004, it has set limits on the $0\nu\beta\beta$ half-life of these 7 isotopes between 0.9×10^{19} and 1.1×10^{24} years [54] [39] [36] [37].

The next experiment, SuperNEMO, aims to reach a total mass of ^{82}Se of 100-200 kg [46]. The detector will be composed of about twenty modules housing 5-7 kg of isotopes each. The first module, the SuperNEMO demonstrator, is being built at Modane. More information on this experiment is given in chapter 2.

1.2.3 Sterile neutrinos

Anomalies in the neutrino flux

Sterile neutrinos have already been introduced in 1.2.2. If right-neutrinos exist, which can be required for the Dirac mass mechanism, they would have no weak

interactions except through mixing with left-handed neutrinos. The seesaw mechanism implies also the existence of heavy sterile neutrinos to explain the smallness of neutrino masses.

The existence of sterile neutrinos is not only suggested by possible mass mechanisms. Some experimental anomalies in neutrino oscillations are also indications that new types of neutrinos may exist with a mass at the eV scale. Three types of anomalies have been detected in different experiments: an excess of $\overline{\nu}_e$ with LSND, excess of ν_e and $\overline{\nu}_e$ with MiniBooNE, a deficit of ν_e in SAGE and GALLEX source calibrations and a deficit of $\overline{\nu}_e$ in reactor neutrino experiments.

LSND and MiniBooNE

The LSND experiment [22] detected neutrinos created from a proton beam interacting on a target. It was located at Los Alamos LAMPF accelerator National Laboratory and took data between 1993 and 1998. Neutrinos traveled over 30 m before reaching the detector which was made of a cylindrical tank filled of 167 tons of scintillating liquid (mineral oil doped with scintillator) and covered of 1220 PMTs. The goal was to detect both the scintillation and Cherenkov lights.
The first type of oscillations searched was $\overline{\nu}_\mu \rightarrow \overline{\nu}_e$ with energies between 20 and 200 MeV. The $\overline{\nu}_e$ were detected via IBD interactions. The positron signal is associated to a first Cherenkov and scintillation light. The neutron signal was the detection of a 2.2 MeV γ from neutron capture on hydrogen.
LSND observed an excess of 87.9 $\overline{\nu}_e$ (3.8 σ) which could correspond to oscillations with Δm^2 between 0.2 and 2 eV^2 or around 7 eV^2. The KARMEN experiment, which also studied accelerator neutrinos with a segmented liquid scintillation calorimeter did not observe such an excess and set limits compatible with LSND results for oscillations with $\Delta m^2 < 10$ eV^2.

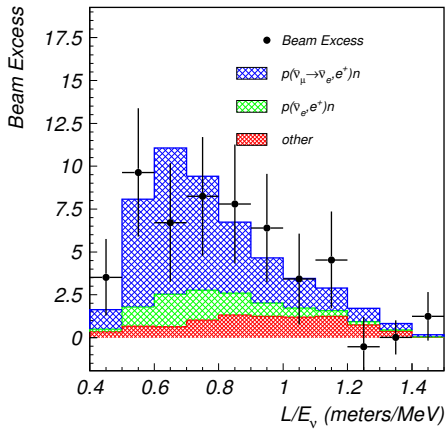

Figure 1.17: The LSND excess indicating possible ν_μ and $\overline{\nu}_e$ appearance. The shaded region shows the expected distribution from a combination of neutrino background plus neutrino oscillations at low Δm^2 [22].

The SCiBooNE/MiniBooNE experiment used a FERMILAB beam which can produce both ν_μ and $\overline{\nu}_\mu$ [60]. Its goal was to verify the LSND oscillations for the same Δm^2 but at different distance and energy. It was a two detector experiments as the flux is not predicted well enough. The SciBooNE detector used 10.6 tons of scintillator strips at 100 m from the proton target which produced the beam. The MiniBooNE detector was located at 540 m from the proton target. It was filled with 800 tons of mineral oil and covered by 1280 PMTs. As the oil was not doped with scintillator, the particles were detected via their Cherenkov light. The ν_e and $\overline{\nu}_e$ interact via charged current quasi elastic scattering. An excess of 381.2 ± 85.2 ν_e events (4.5σ) was observed. Combining it with the $\overline{\nu}_e$ appearance data, a total ν_e plus $\overline{\nu}_e$ event excess of 460.5 ± 95.8 events ($4.8\ \sigma$) is found. The MiniBooNE data are consistent in energy and magnitude with the excess of events reported by LSND, and the combined LSND and MiniBooNE excesses have a significance of $6.1\ \sigma$. The best fit of these data occurs for neutrino oscillations at $\Delta m^2_{new} = 0.041$ eV^2 and $\sin^2 2\theta_{new} = 0.958$ [23].

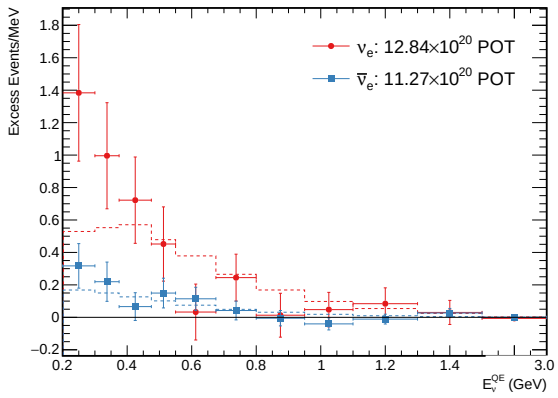

Figure 1.18: The MiniBooNE total event excess as a function of neutrino energy in both neutrino (in red) and antineutrino (in blue) mode. The dashed curve show the best fits assuming standard two neutrino oscillations [23].

SAGE and GALLEX

Other neutrino flux anomalies come from the SAGE (USA, Russia) and GALLEX (Europe) experiments which have both searched for solar neutrinos with great volumes of liquid gallium. To perform their calibration, they used intense artificial radioactive sources, ^{51}Cr and ^{37}Ar, placed inside their detectors. These sources produced monoenergetic ν_e via electron capture. The emitted neutrinos were detected via the reaction:

$$^{71}Ga + \nu_e \rightarrow ^{71}Ge + e^- \tag{1.40}$$

.

The produced germanium was then extracted and the counting of Ge nuclei was made via electron capture decays, inverse reaction of reaction 1.40, which produces

Auger electrons and X-rays detected with proportional counters.

GALLEX, the European experiment, had a detector of 101 tons of $GaCl_3$ at the LNGS and recorded data between 1991 and 1996. The Soviet-American experiment SAGE had twice more gallium than GALLEX and was operated in the Baksan underground laboratory.

These experiments measured a ratio of observed number of neutrinos over predicted number of neutrinos for their calibrations R = 0.86 ± 0.05. It represents a neutrino deficit of 2.9 σ [76]. The gallium anomaly could be explained by oscillations toward sterile neutrinos at very short distance with $\Delta m^2_{new} > 0.35$ eV^2 and $\sin^2(2\theta_{new}) > 0.07$ [76].

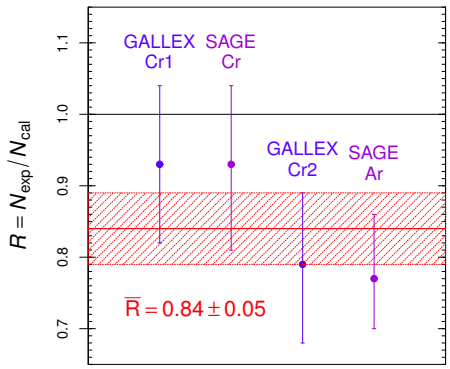

Figure 1.19: Ratios of the measured over calculated number of number of ν_e events in the GALLEX and SAGE radioactive source experiments. The horizontal shadowed red band shows the average ratio and its uncertainty [73].

Reactor antineutrino spectrum

The search for neutrino oscillations in reactor experiments is based on disappearance measurements of the $\overline{\nu}_e$ via IBD reactions. Experiments which use nuclear reactors at very short baseline (< 100 m) such as ILL-Grenoble, Bugey, Goesgen, Rovno, Krasnoyarsk or Savannah River have only one detector contrary to oscillation experiments with longer baseline which often use 2 detectors: a near and a far one to have a precise measurement of the neutrino flux. The calculation of neutrino flux and spectrum emitted by nuclear reactors rely thus on precise theoretical predictions instead of detector measurements. Until the end of 2010, results of these experiments were in agreement with the 3 neutrinos oscillation model: their ratio of observed event rate over predicted was 0.976 ± 0.024 [99].

However, for the Double Chooz experiment preparation, the Saclay and Subatech-Nantes neutrino groups have reevaluated the reactor neutrino spectrum for ^{235}U, ^{239}Pu, ^{241}Pu and ^{238}U. They have improved the conversion of electron to neutrino data with a better treatment of nuclear data and corrections to Fermi theory. The previous model used a simpler conversion procedure. At the ILL-Grenoble reactors,

thin targets of ^{235}U, ^{239}Pu and ^{241}Pu had been irradiated with thermal neutrons. Their electron spectrum had been converted to $\overline{\nu}_e$ spectrum using 30 effective beta branches. The new conversion method used the ILL spectrum but it took into account decays of thousands of fission products.

They published their results in 2011 showing that for reactor experiments with a baseline smaller than 100 m, the ratio of observed over predicted event rate is 0.943 ± 0.023 [99]. There are several reasons for this deficit. First, the reevaluation of the conversion of the β spectrum to $\overline{\nu}_e$ spectrum measured at ILL increased the predicted flux by 3.5 %. This shift comes from two main systematic effects. The first one is the use of Coulomb and weak magnetism corrections from Fermi theory which has an effect at low energies below 4 MeV. The second one is the use of the complete distribution of the charge of the nucleus which contributes to the total spectrum and have an important effect at high energy above 4 MeV. Moreover, off equilibrium effects due to long-lived isotopes have been taken into account and increased the predicted flux by 1 %. In addition, the reevaluation of the neutrino detection cross section via IBD that depends on the neutron life-time whose measured value decreased in the past years led to a shift of the predicted detected $\overline{\nu}_e$ flux by 1.5 %.

The data of the previous experiments have been reworked and show a deficit of $\overline{\nu}_e$ that could correspond to an oscillation with $\Delta m^2 > 1.5$ eV^2 [99].

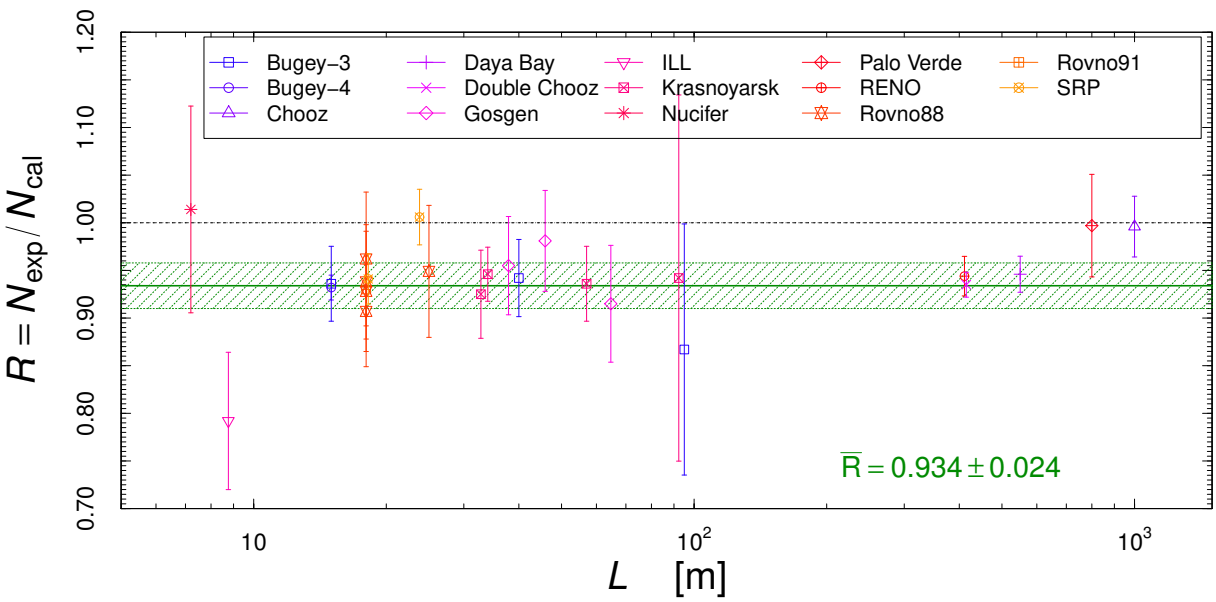

Figure 1.20: Ratios R of reactor experiments as a function of the reactor-detector distance L. The horizontal band shows the average ratio $\overline{R}$ and its uncertainty. The error bars show the experimental uncertainties [74].

Some solutions to the reactor antineutrino anomaly could be a systematic error of the reactor neutrino experiments or an error in the spectrum evaluation. How-

ever, as it happened several times in the neutrino history, rate anomalies can be hints for new types of neutrino oscillations so it has to be investigated.

Combining the reactor data with those of the gallium and MiniBoone experiments, new oscillation parameters can be found, compatible with $|\Delta m^2_{new}| > 1.5$ eV^2 and $\sin^2(2\theta_{new}) = 0.14 \pm 0.08$ at 95% [99]. This Δm^2_{new} is much larger than the ones already presented so this could be a hint for oscillations toward a new sterile neutrino.

Another anomaly has also been found with reactor neutrinos: the 5 MeV bump. Experiments like Daya Bay, RENO and Double Chooz have all reported an excess of events for prompt energies around 5 MeV. The Double Chooz experiment has shown that this excess is correlated with the reactor power [14].

Sterile neutrinos would be neutral with no known weak interaction except those induced by mixing. However, they could interact through new physics interactions beyond the Standard Model.

Status of first generation of sterile neutrino experiments

Several possibilities exist to investigate the existence of sterile neutrinos at the eV scale.

For example, the SOX experiment (Short distance neutrino Oscillations with BoreXino) [51] aimed to use the solar neutrino detector BOREXINO to search for new oscillations of neutrinos coming from an artificial radioactive source [51]. Using artificial radioactive neutrino source allows one to have a very short baseline and to put the detector underground with a large overburden to shield against cosmic rays. However, the large gamma ray background from the source and the low event rate compared to nuclear reactors are challenging. The detector supposed to be used for the SOX experiment, Borexino, is a liquid scintillator detector that detects $\overline{\nu}_e$ via IBD. The SOX experiment was supposed to deploy a ^{51}Cr ν_e source and a ^{144}Ce-^{144}Pr $\overline{\nu}_e$ source in the detector. With this technology, they intended to cover most of the reactor anomaly region. However, because of difficulties to produce the radioactive source, the experiment has been cancelled.

As several hints come from reactor neutrinos, it is a natural idea to search for sterile neutrinos near a nuclear reactor. To cover the Δm^2 around 1 eV searched for oscillations toward a new sterile neutrino, constraints are put in the L/E parameter. As it has been seen, reactor antineutrinos ($\overline{\nu}_e$) are most of the time detected via IBD interaction. The energy spectrum of neutrinos interacting via IBD is smoothly peaked around 3 MeV. This imply that L, the baseline, must be very short (only a few meters) to be sensitive to this Δm^2. There are several other requirements for this type of experiments:

- Experiments need a very compact reactor core to keep a low systematic error on the baseline. It is also a good point to have a simple fuel composition (only

^{235}U) as flux and energy spectrum evaluation become simpler.

- To install a detector as close as a few meters to a reactor core, materials must be chosen carefully with safety considerations (no flammable liquids...).

- A good sensitivity to the IBD vertex position is also required. This can be achieved with a good segmentation of the detector.

- To create efficiently IBD events, the neutrino target must contain a lot of free protons. This is why plastic or liquid scintillators are favoured.

All these reactor neutrino experiments at very short baseline face several challenging backgrounds. There are fast neutrons and γ coming from the reactor but also cosmogenic muons as they do not have a high overburden. Thermal and epithermal neutrons are often removed with polyethylene or water shielding. Lead (Pb) is used to protect the detector against γ rays. Moreover, active muon vetos made with scintillators are often used.

Different technics are used to detect the IBD signal (a positron and a neutron in delayed time coincidence). The energy threshold of the IBD reaction is 1.804 MeV. This is why low energy neutrinos which are specially emitted by long-lived part of the fission products can not be detected. By detecting only IBDs, the spent fuel or radioactive waste can not be studied. However IBD detectors are useful to monitor the fission processes.

Most of the neutrino energy after subtraction of the threshold energy is transferred to the positron which annihilates with an electron creating 2 γ of 511 keV. The isotopes used to detect neutrons need to have a high neutron capture cross-section and be detected easily. The most commonly used are gadolinium (Gd), hydrogen (H) or lithium (Li). Neutron capture on Gd creates a γ ray cascade of 8 MeV. Neutron capture on H releases a 2.2 MeV gamma. Gadolinium is widely used but the emitted γ rays are similar to the ones emitted by neutron capture on iron so it can be an issue because of the high neutron background in the environment of a reactor. Neutron capture on lithium produces an alpha and a tritium with a total energy of 4.78 MeV. The advantage of this reaction is that it can be localised with precision as alpha and tritium are ionising particles so they do not travel a lot in materials (contrary to γ which can cross several tenth of cm of material).

A first generation of very short baseline reactor experiments has taken data recently. These experiments are Nucifer and NEOS. However they were not segmented detectors so they could measure the neutrino flux at one location only. They were followed by several new experiments in different countries that look for oscillations toward a new sterile neutrino by searching for different patterns in the neutrino spectrum. To do so, they are very segmented experiments. These new experiments are numerous. They include DANSS, Prospect, Stereo or SoLid which will be described in the following.

First generation of very short baseline reactor experiments

The Nucifer experiment [53] has been built for online monitoring of nuclear reactors. The detection of antineutrinos from a reactor can help to assess its thermal power and its fissile content. The advantage of this type of detector is that they can monitor the reactor in real-time from outside the reactor containment.

The Nucifer detector was located at the Osiris research reactor in Saclay, France, at 7.2 m from the core. The maximal thermal power of the reactor is 70 MW_{th} and its volume is $80 \times 70 \times 70$ cm^3. Its fuel is enriched at 19.75 % in ^{235}U. The Nucifer detector was a liquid scintillator tank of 0.847 m^3 coated with reflective Teflon. The liquid scintillator was doped with gadolinium (Gd). Antineutrinos were detected via IBD reactions. The neutron were captured by Gd or H. The light was detected by 16 PMTs at the top of the detector vessel. Its overburden was around 12 meters water equivalent (m.w.e.) but it used also more than 50 tons of passive shielding. Polyethylene (PE) was used as a neutron shielding and lead layers protected the detector against gamma rays. An active veto made of plastic scintillator was also installed to tag muons.

The Nucifer experiment detected 281 ± 7 $\overline{\nu}_e$ per day for 272 ± 23 $\overline{\nu}_e$ per day predicted which allows reactor monitoring. However, because of large backgrounds and uncertainties on the reactor neutrino flux predictions, it could not reach a conclusion concerning the reactor neutrino anomaly as the detector was not segmented.

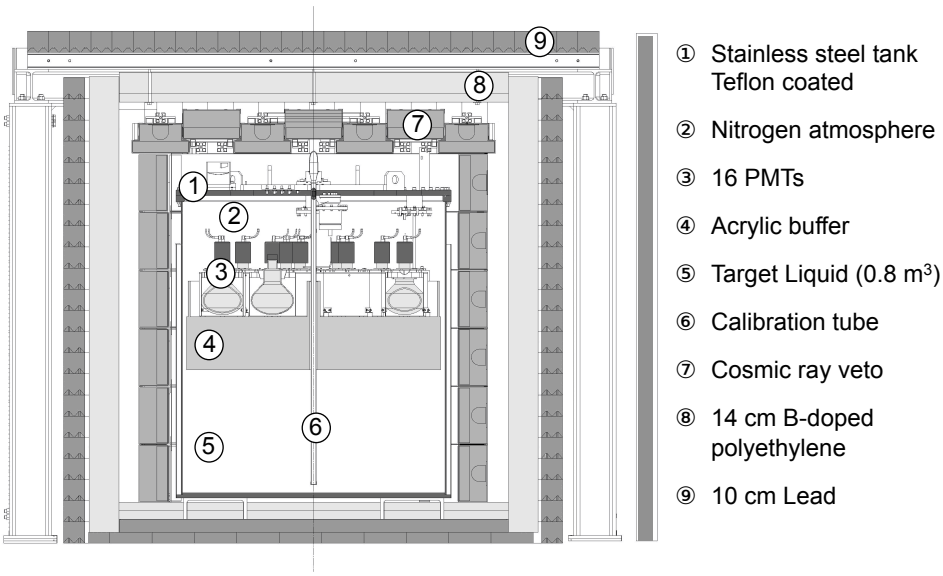

Figure 1.21: The Nucifer detector [53]

The NEOS experiment (Neutrino Experiment for Oscillation at Short baseline) [87] was built to search for new oscillations towards a sterile neutrino. It is a Korean experiment deployed at the Hanbit nuclear power complex at 24 m from a 2.8 GW_{th} reactor core. It is the same reactor complex as the one used for the RENO experiment. The active core size is 3.1 m in diameter and 3.8 m in height. NEOS

detector (figure 1.22) is filled with 1008 L of 0.5 % Gd-loaded liquid scintillator. The light is readout by 19 PMTs at each end of the target vessel. As the detector is located 10 m below ground level and is under the wall of containment building, the minimum overburden is 20 m.w.e. The detector is protected from neutrons with borated PE and from gamma rays thanks to lead layers. Plastic scintillator surround the detector to act as muon counters.

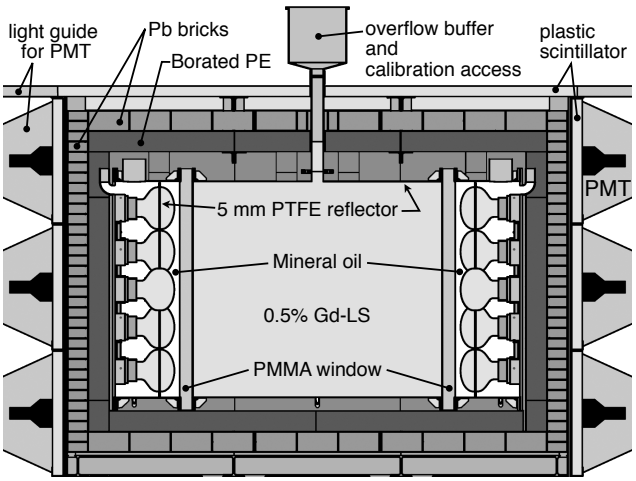

Figure 1.22: The NEOS detector from [87]

The NEOS experiment has measured a rate of 1976 antineutrinos per day and a signal to background ratio of 22 [88]. The IBD energy spectrum can be seen in figure 1.23. No evidence of a new oscillation toward sterile neutrino was found. A limit on θ_{new} for $\Delta m^2_{new} \approx 1$ eV^2 was set: $\sin^2(2\theta_{new}) < 0.1$. The exclusion curves in the $\sin^2 2\theta_{14} - \Delta m^2_{41}$ parameter space are shown in figure 1.24. This is a model-dependent result, however, as Daya Bay result has been used to study the oscillations while it has different systematics. Like in Double Chooz, Daya Bay and RENO, an excess around 5 MeV has been observed.

Status of new generation of sterile neutrino experiments

Many new reactor neutrino experiments at very short baselines have been built in the past few years and are currently taking data. They are segmented detectors to make a relative measurement of the antineutrino flux.

STEREO

STEREO installed its detector at 10 m from the core of the ILL researched reactor at Grenoble (France) [96]. The reactor is highly enriched at 93% in ^{235}U. The detector is made of six cells, placed between 9 and 11 m from the reactor core, filled with Gd-loaded liquid scintillator. The light is readout by 24 PMTs placed on top of the cells (figure 1.25). A gamma catcher is built around the detector

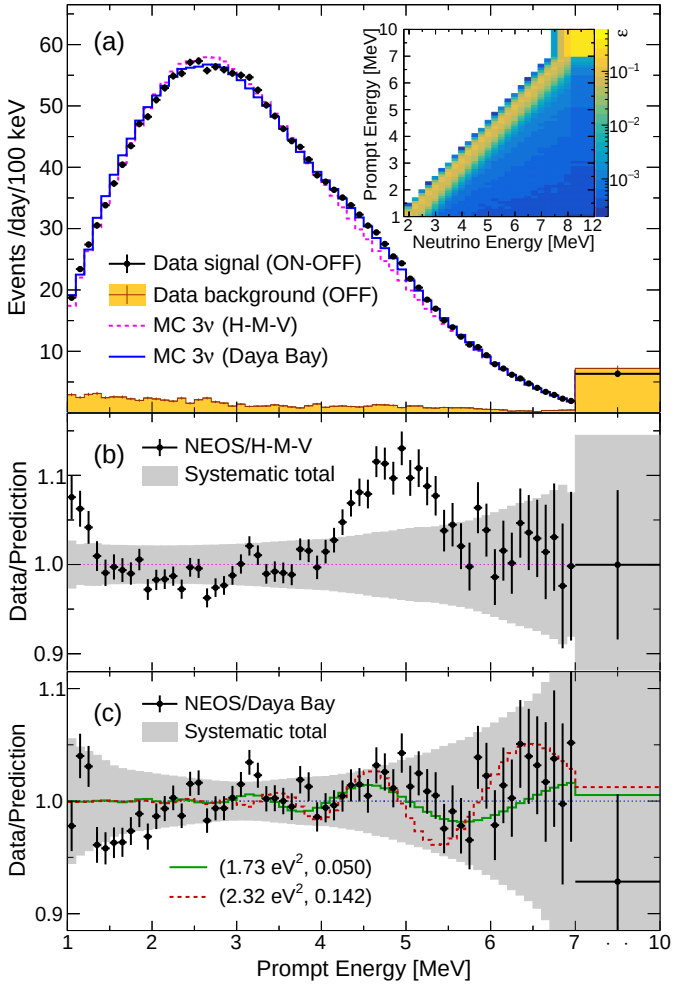

Figure 1.23: (a) The IBD prompt energy spectrum of the NEOS experiment. The last bin is integrated up to 10 MeV. The orange shaded histogram is the background spectrum obtained with reactor OFF data. The detector response matrix in the inset shows the relation between the neutrino energy and the prompt energy. (b) The ratio of the observed prompt energy spectrum to the Huber-Mueller flux prediction weighted by the IBD cross-section with the 3 ν hypothesis. The predicted spectrum is scaled to match the area of the data excluding the 5 MeV excess region. (c) The ratio of the data to the expected spectrum based on the Daya Bay result with the 3 ν hypothesis, scaled to match the whole data area. The solid green line is the expected oscillation pattern for the best fit of the data to the 3+1 ν hypothesis and the corresponding oscillation parameters ($\sin^2 2\theta_{new}$, Δm^2_{new}) is (0.05, 1.73 eV^2). The dashed red line is the expected oscillation pattern for the reactor antineutrino anomaly (RAA) best fit parameters (0.142, 2.32 eV^2). The gray error bands in (b) and (c) are estimated total systematic uncertainties, corresponding to the square roots of diagonal elements of the covariance matrices. [88]

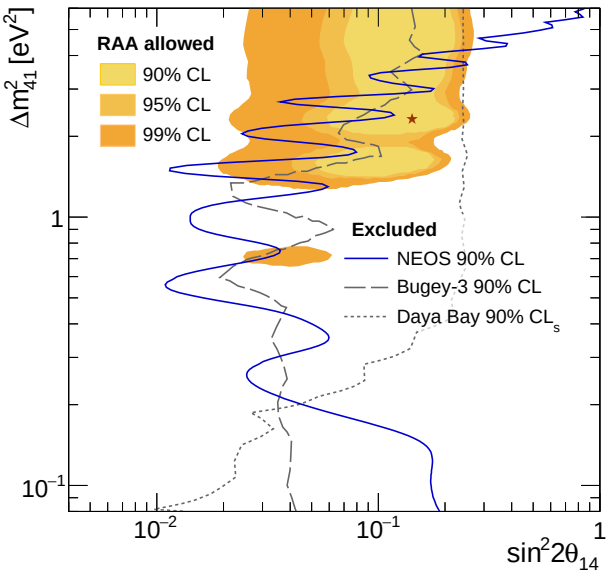

Figure 1.24: Exclusion curves of the NEOS experiment for 3+1 neutrino oscillations in the $\sin^2 2\theta_{14} - \Delta m^2_{41}$ parameter space. The solid blue curve is 90% C.L. exclusion contours based on the comparison with the Daya Bay spectrum, and the dashed gray curve is the Bugey-3 90% C.L. result. The dotted curve shows the Daya Bay 90% C.L. result. The shaded area is the allowed region from the reactor antineutrino anomaly fit, and the star is its optimum point. [88]

consisting of an outer crown of liquid scintillator without Gd and 24 other PMTs. It can detect the 8 MeV gammas from neutron capture on Gd as well as the 511 keV gammas from positron annihilation. The experiment is placed under the ILL water channel and benefits from 65 t of passive shielding. A lead (Pb) and polyethylene (PE) shielding is placed around the detector. An active muon veto is also used.

The energy resolution, measured with a ^{54}Mn calibration source (0.835 MeV γ, is σ_E/E = 9%. The first results have been published using 66 days of reactor on and 138 days of reactor off data [30]. A pulse shape discrimination (PSD) analysis, based on the ratio of the pulse tail charge over the pulse total charge allowed to discriminate antineutrino signals from backgrounds due to electronic or proton recoils for example (see figure 1.26). The PSD distribution of the correlated background induced by cosmic rays is parametrised using reactor off data. It is modeled with multi-gaussian functions for different time and energy bins that correspond to electronic recoils, proton recoils or accidental coincidences. The PSD distribution of reactor ON data is then fitted with this background model plus an additional gaussian for the reactor antineutrino component.

The STEREO experiment measured 396.3 $\pm$ 4.7 $\overline{\nu}_e$ per day with a signal over background ratio S/B = 0.9. They have searched for oscillations in the antineutrino energy spectrum by comparing the energy spectrum of each cell. Figure 1.27 shows that they could exclude a large region of the sterile oscillation parameters including the former best fit value of the reactor anomaly $\sin^2 2\theta_{ee}$ = 0.14 and Δm^2_{new} = 2.4 eV^2 at 97.5 % CL.

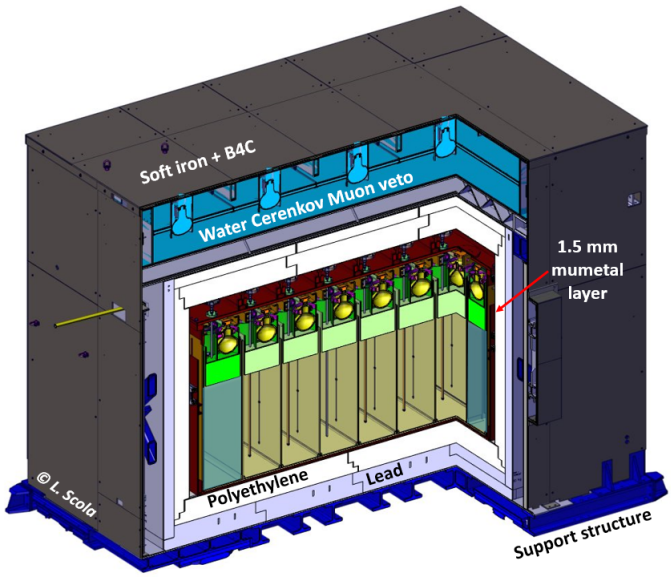

Figure 1.25: The STEREO detector with its 6 cells of Gd-loaded liquid scintillator readout by PMTs in yellow, the different layers of shielding and the muon veto in blue[97].

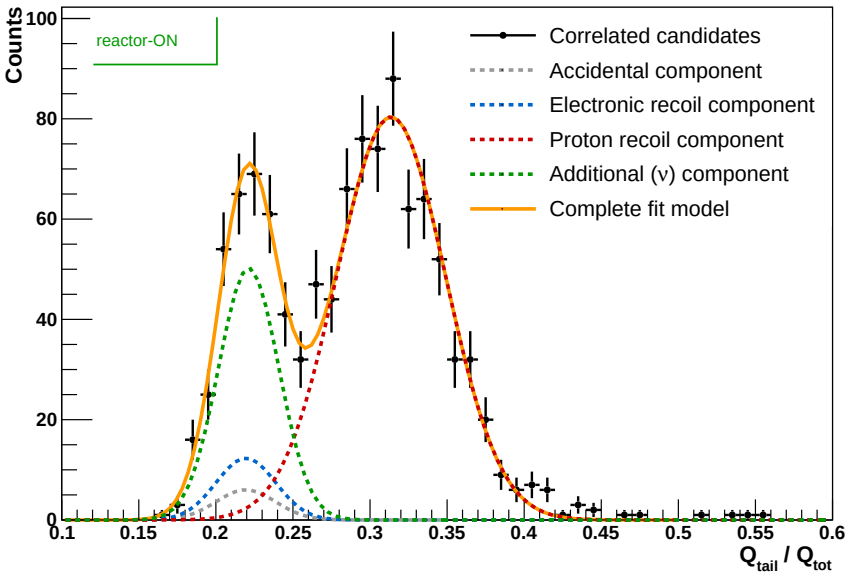

Figure 1.26: Example of pulse shape discrimination of the STEREO experiment for events with reconstructed energy in [3.125,3.625] MeV, collected in 22.8 days of reactor-on. The dashed curves show the components of the neutrino signal (in green) and backgrounds model. [30]

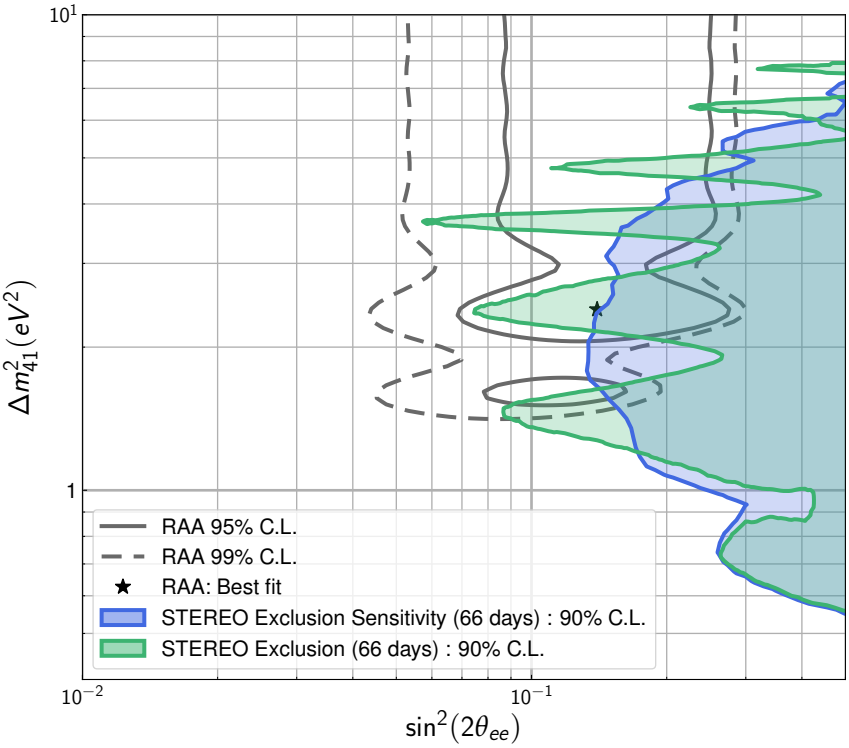

Figure 1.27: Exclusion contour of the oscillation parameters of the STEREO experiment using 66 days of reactor on data [30].

DANSS

DANSS [28] is a Russian experiment located at the industrial Kalinin Nuclear Power Plant. The core of the 3.1 GW_{th} reactor is 3.7 m high and has a diameter of 3.2 m which smears the oscillation pattern. A first prototype DANSSino has already demonstrated the feasibility of this experiment. The DANSS detector is moved to vary the neutrino baseline from 10.7 to 12.7 m thanks to a lifting gear. It uses highly segmented plastic scintillator strips (figure 1.28). The $1 \times 4 \times 100$ cm^3 plastic scintillator strips are made with polystyrene similar to those of the MINOS experiment. The strips are wrapped in thin Gd-containing coat. In each strip, three wavelength shifting optical fibers are glued. The middle one is connected to a silicon photomultiplier (SiPM) and the other two are coupled to a single PMT common for all the fibers of one module (50 parallel strips).

The scintillator strips are laid in two perpendicular directions and held by copper frames, which act also as passive shielding and neutron reflector. This strips are assembled in modules in a total volume of 1 m^3. A passive shielding of lead and borated polyethylene surrounds the detector and an active muon veto with plastic scintillators is used. As the detector is placed under the reactor core, it benefits from a passive shielding of 50 m.w.e that reduces the cosmic background by a factor

6.

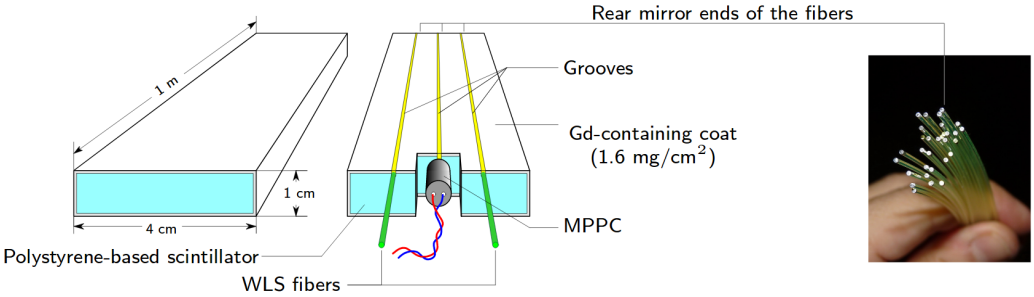

Figure 1.28: A strip of the DANSS detector [28].

The light yield of 38 photo-electrons (PE)/MeV gives an energy resolution of 20.3%. It takes advantage of the spatial and time difference distributions between prompt and neutrons to discriminate IBDs from accidental backgrounds as seen in figure 1.29. DANSS detects around 5000 $\overline{\nu}_e$ per day [29]. The distance of the detector to the reactor is varied to get a relative measurement of the antineutrino flux. Using 9.66×10^5 antineutrino events, they excluded the reactor antineutrino anomaly optimum point with a confidence level of more than 5 σ. The exclusion curves in the $\sin^2 2\theta_{14} - \Delta m^2_{41}$ parameter space are shown in figure 1.30. However, their systematic uncertainties are still being studied.

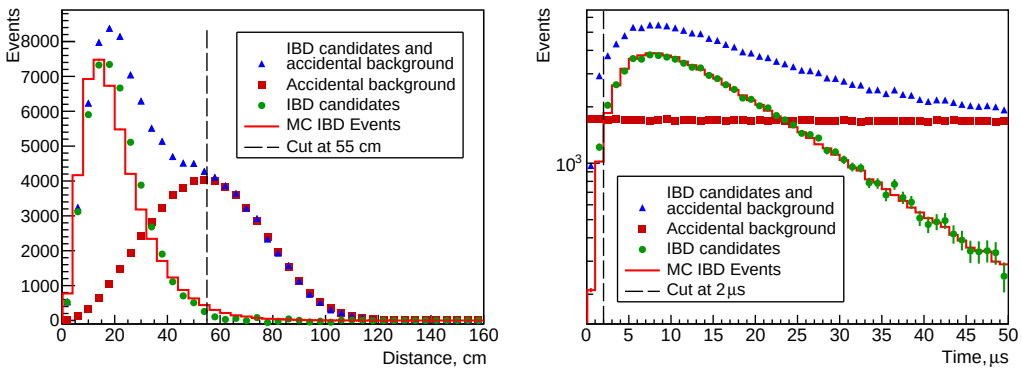

Figure 1.29: *Left:* distance between prompt and delayed reconstructed positions. *Right:* time between prompt and delayed signals. Errors are smaller than sizes of points [29].

PROSPECT

PROSPECT (Precision Reactor Oscillation and Spectum Experiment) is located at the High Flux Isotope Reactor at Oak Ridge National Laboratory (USA) that operates at 85 MW for 24 days cycles [41]. The reactor core has a diameter of 0.435 m and a height of 0.508 m and is highly enriched in ^{235}U (more than 99%).

A movable 4 ton detector was built and placed between 7 and 9 m from the reactor core. The detector uses segmented liquid scintillator doped with ^{6}Li. The

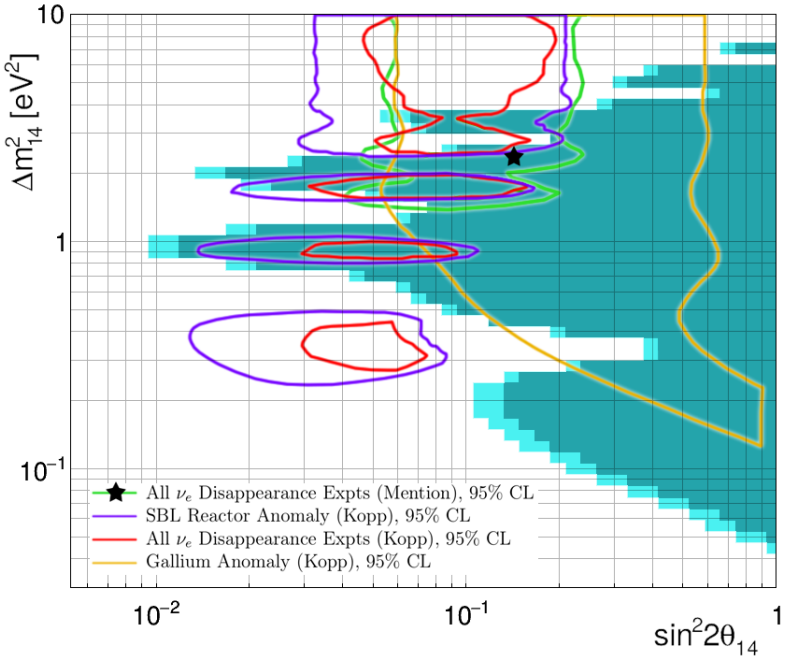

Figure 1.30: Exclusion areas (90 % C.L. in cyan and 95 % in dark cyan) of the DANSS experiment for 3+1 neutrino oscillations in the $\sin^2 2\theta_{14} - \Delta m^2_{41}$ parameter space. Curves show allowed regions from neutrino disappearance experiment, and the star is the best point from the RAA and GA fit [29].

scintillator volume is segmented by optical separators into a two-dimensional array of 154 rectangular segments. Each segmented part of 14.5 × 14.5 × 117.6 cm^3 is readout by PMTs at both end (figure 1.31). The overburden is only 1 m.w.e.

The neutron capture on ^{6}Li produces an α and a tritium. A pulse shape discrimination is used to differentiate neutron and positron signals. It is based on the ratio tail over total of the integral of the waveforms. Their energy resolution is 4.5 % at 1 MeV.

With 33 days of reactor ON data, 24698 ± 277 (stat) IBDs were detected after subtracting accidental and correlated backgrounds [41]. The IBD excess between reactor ON and OFF can be seen in figure 1.32. The signal-to-background ratios for accidentals and correlated are respectively 2.25 and 1.36. The data disfavor the reactor antineutrino anomaly at 98.7% confidence level. The exclusion curves in the $\sin^2 2\theta_{14} - \Delta m^2_{41}$ parameter space are shown in figure 1.33.

SoLid

The SoLid experiment is installed at the BR2 research reactor at Mol in Belgium [16]. A first prototype SM1 (288 kg) took data in 2016. The SoLid phase I detector (1.6 tons) commissioning started in November 2017 and is now taking data. More information on these detectors can be found in chapters 4 to 7.

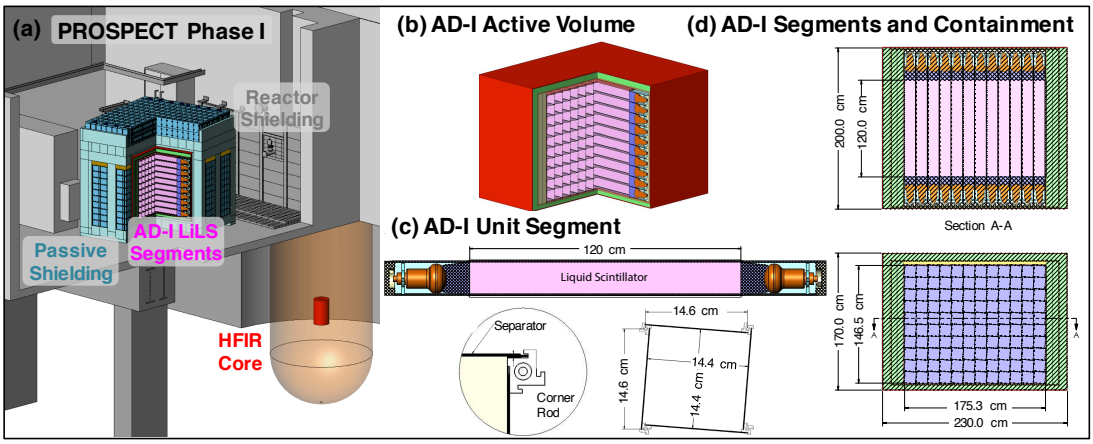

Figure 1.31: The Prospect detector [42].

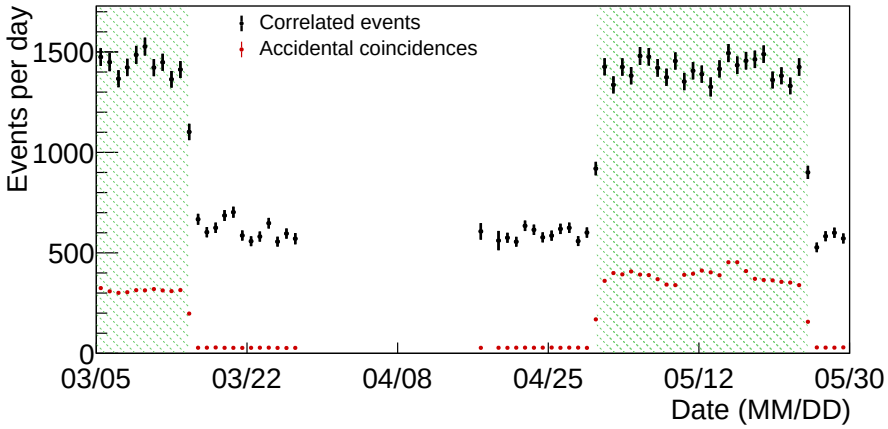

Figure 1.32: Number of daily IBD-like events from the PROSPECT experiment after accidental subtraction (in black) and calculated accidental coincidences (in red). IBD candidate event rates are corrected for time-dependent variations in detector veto and livetime. Shaded regions correspond to reactor-on periods [41].

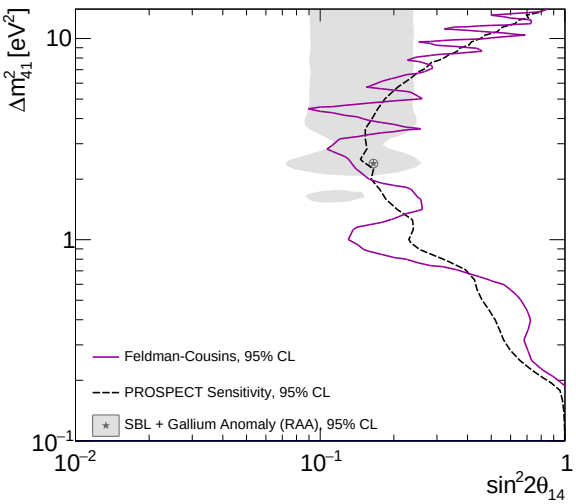

Figure 1.33: Sensitivity and 95 % C.L. sterile neutrino oscillation exclusion contour from the 33 live-day PROSPECT reactor On dataset. The best fit of the Reactor Antineutrino Anomaly is disfavored at 2.2 σ C.L.. [41].

1.2.4 Sterile neutrinos influence on $\beta\beta$ decay search

As we have seen, the search for sterile neutrinos and neutrinoless double beta decay are very active with many experiments addressing neutrino issues. All the open questions we have about neutrinos are related to each other and finding any new piece of information has implications on every experiment. Indeed, the existence of sterile neutrinos would for example dramatically change the interpretation of $0\nu\beta\beta$ decay experiments results.

A fourth sterile neutrino would have huge implications on the neutrino mass issues. Different experimental hints favor a new neutrino mass in the eV range while other known neutrinos would have sub-eV masses. This new neutrino would contribute a lot to the signal searched in the $\beta\beta$ decay experiments. According to [99], it would contribute such that $m_{\beta\beta} \geq 0.02$ eV (95 % C.L.).

As seen previously, the half-life of the $0\nu\beta\beta$ (eq. 1.38), which can be measured with the $0\nu\beta\beta$ decay rate, depends on the effective Majorana mass $m_{\beta\beta}$ (eq. 1.39). This effective mass can also be written:

$$|m_{\beta\beta}| = |m_1 U_{e1}^2 + m_2 U_{e2}^2 e^{i\alpha_2} + m_3 U_{e3}^2 e^{i\alpha_3}| \tag{1.41}$$

We have already seen in figure 1.11 that finding the value of $m_{\beta\beta}$ with double beta decay experiments could help figure out the neutrino mass ordering (normal or inverted hierarchy). A similar plot from Giunti and Zavanin [75] is shown in figure 1.34. In the 3 neutrino mixing scheme, there is a range of m_1 between 2.3 and 6.6 10^{-3} eV for normal hierarchy where there can be a complete cancellation of $m_{\beta\beta}$. In this case, it would be impossible to prove the Majorana nature of the

neutrino with double beta decay experiments. In the case of a 3 + 1 neutrino scheme (i.e. the existence of a fourth sterile neutrino), $m_{\beta\beta}$ has to take into account the new neutrino mass m_4:

$$|m_{\beta\beta}| = |m_1 U_{e1}^2 + m_2 U_{e2}^2 e^{i\alpha_2} + m_3 U_{e3}^2 e^{i\alpha_3} + m_4 U_{e4}^2 e^{i\alpha_4}| \tag{1.42}$$

The prediction of $m_{\beta\beta}$ in function of the lightest neutrino mass is thus altered a lot as we can see in fig 1.35. In the case of normal hierarchy, a new neutrino mass shifts the allowed region to higher $m_{\beta\beta}$ values. The allowed region for the inverted hierarchy is expanded and there is a wide range of values of the lightest mass m_3 for which $m_{\beta\beta}$ is canceled. This would be dramatic for the $0\nu\beta\beta$ decay search. The next generation of double beta decay experiments aims to reach an effective neutrino mass down to 15 meV. This would cover the entire allowed parameter space in the case of the assumption of inverted hierarchy and the existence of only 3 neutrinos. It is thus crucial to know if a new neutrino mass state exists for the ability of double beta decay experiments to reach a conclusion.

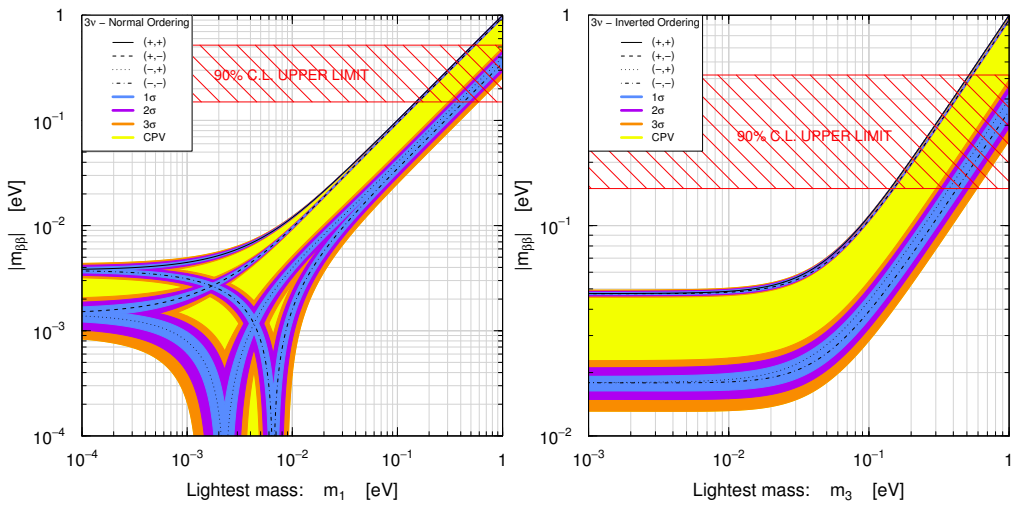

Figure 1.34: Case of 3 ν mixing. *Left:* $m_{\beta\beta}$ as a function of the lightest neutrino mass m_1 in the Normal Hierarchy. *Right:* $m_{\beta\beta}$ as a function of the lightest neutrino mass m_3 in the Inverted Hierarchy. The signs in the legend indicate the signs of $e^{i\alpha_2}$, $e^{i\alpha_3} = \pm 1$ for the four possible cases in which CP is conserved. The intermediate yellow region is allowed only in the case of CP violation. The 90 % confidence limit takes into account KamLAND-Zen results [75].

We have seen how the existence of a new sterile neutrino would impact the $0\nu\beta\beta$ decay search. But we can also see how $0\nu\beta\beta$ decay search can give information on the sterile neutrino search. Indeed, the distribution of $m_{\beta\beta}$ versus the sum of the three neutrino mass: $\Sigma = m_1 + m_2 + m_3$ (figure 1.36) is also shown in [75]. Σ is an interesting variable as it can be measured in both the 3 and 3+1 neutrino schemes with cosmology. There is a wide range of $m_{\beta\beta}$ and Σ in purple in figure 1.36 for which double beta decay experiments and cosmological measurements could show the existence of sterile neutrino given that oscillation experiments have found the neutrino mass hierarchy.

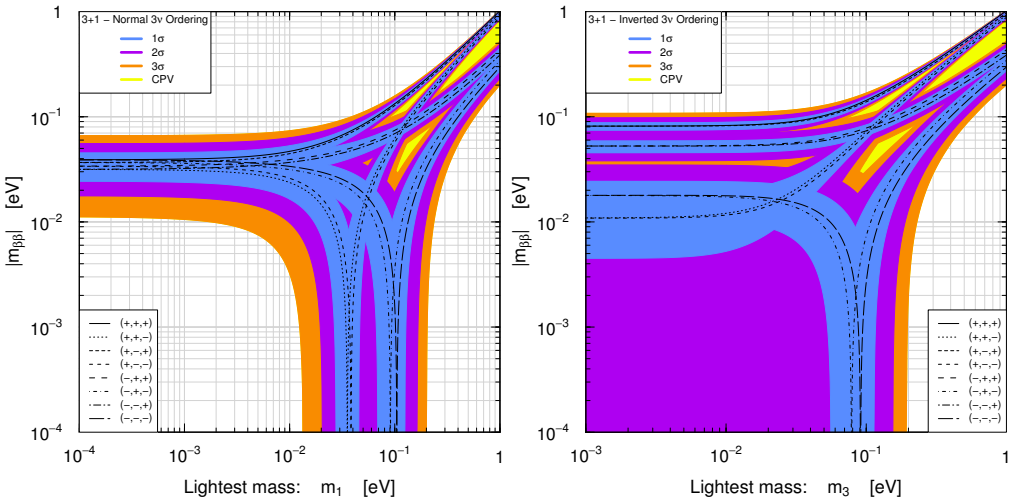

Figure 1.35: Case of 3+1 ν mixing. *Left:* $m_{\beta\beta}$ as a function of the lightest neutrino mass m_1 in the Normal Hierarchy. *Right:* $m_{\beta\beta}$ as a function of the lightest neutrino mass m_3 in the Inverted Hierarchy. The intermediate yellow region is allowed only in the case of CP violation [75].

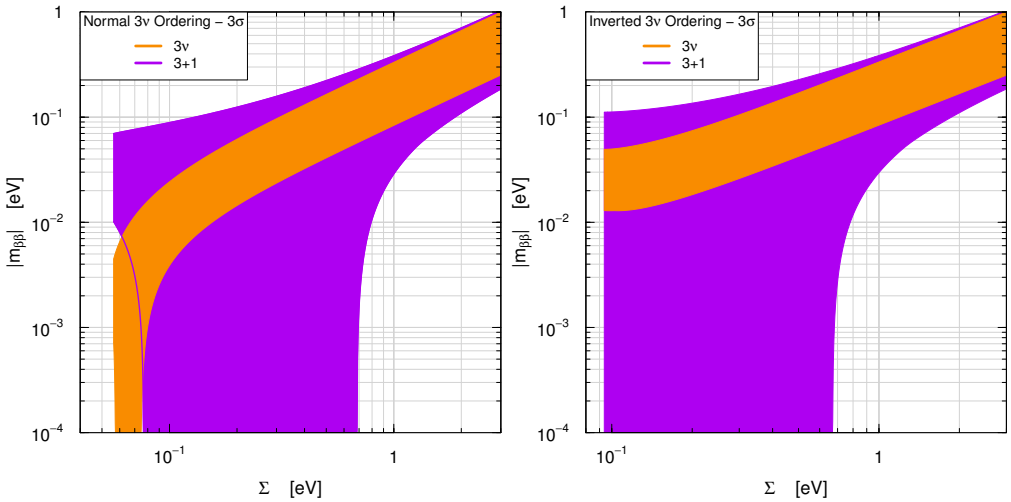

Figure 1.36: Comparison of the 3 ν (in orange) and the 3+1 ν (in purple) mixing. *Left:* the 3σ allowed regions in the Σ–$|m_{\beta\beta}|$ plane for the normal hierarchy *Right:* the 3σ allowed regions in the Σ–$|m_{\beta\beta}|$ plane for the inverted hierarchy [75].

1.2.5 Conclusion

This chapter has shown that many questions remain about neutrinos concerning their oscillation matrix, their masses, their nature or the existence of sterile neutrinos for example. All these questions are entangled. Pushing the limits of our knowledge on one parameter like the existence of a new sterile neutrino brings knowledge on the other parameters searched like the half-life of the $0\nu\beta\beta$ process. This is why working on two very different experiments like SuperNEMO and SoLid at the same time is really interesting to get a better understanding of neutrinos.

Part I

SuperNEMO

Chapter 2

The SuperNEMO demonstrator

2.1 SuperNEMO technology

As explained in the first chapter, the goal of $0\nu\beta\beta$ decay experiments is to determine the nature of neutrinos, either Majorana or Dirac, by searching the $0\nu\beta\beta$ energy peak. A peak in the two electron sum energy spectrum at the $Q_{\beta\beta}$ value, if not due to background, would prove the Majorana nature of the neutrinos. This chapter is about the SuperNEMO demonstrator that is being built at LSM to look for $0\nu\beta\beta$ decays. The detector principle with the tracking and calorimetry technology will be first introduced. Then the main challenges that the experience will face with the background reduction will be presented as well as the simulation and analysis tools that have been developed.

2.1.1 Detection principle

To measure precisely the energy of the two electrons from $0\nu\beta\beta$ decays and remove background efficiently, the NEMO experiments have chosen a tracking and calorimetry technology. The electrons coming from the source foils cross the tracking chamber where their trajectories are reconstructed. They end up in the calorimeter where they deposit all their energy (fig. 2.1). Although the energy resolution and detection efficiency are modest compared to germanium or bolometer experiments, the particle tracking provides a powerful background rejection. In addition, the discrimination between different types of events thanks to the good particle identification, allows us to measure backgrounds in different channels and can help to study $\beta\beta$ decays to excited states.

This kind of experiment allows to separate the source from the detector so any $\beta\beta$ isotope can be studied. The previous NEMO-3 experiment which has run from February 2003 to January 2011 has measured $2\nu\beta\beta$ decay for seven isotopes. For the SuperNEMO demonstrator, 6.23 kg of ^{82}Se will be studied. The mass of isotopes studied with this technology is lower than for experiments using liquid scintillator or liquid TPCs but the flexibility to choose the most interesting isotopes, as long as it can be produced in a foil shape, is a great advantage.

The SuperNEMO demonstrator is currently being built at LSM. The calorimeter and the tracker have been assembled. The electronics commissioning has begun in June 2018 at Manchester. The $\beta\beta$ source foils will be installed in September and the detector will then be closed. The goal of the demonstrator is to take data during 2.5 years to demonstrate that a zero background experiment is feasible before building a bigger experiment with 100 kg of ^{82}Se or ^{150}Nd.

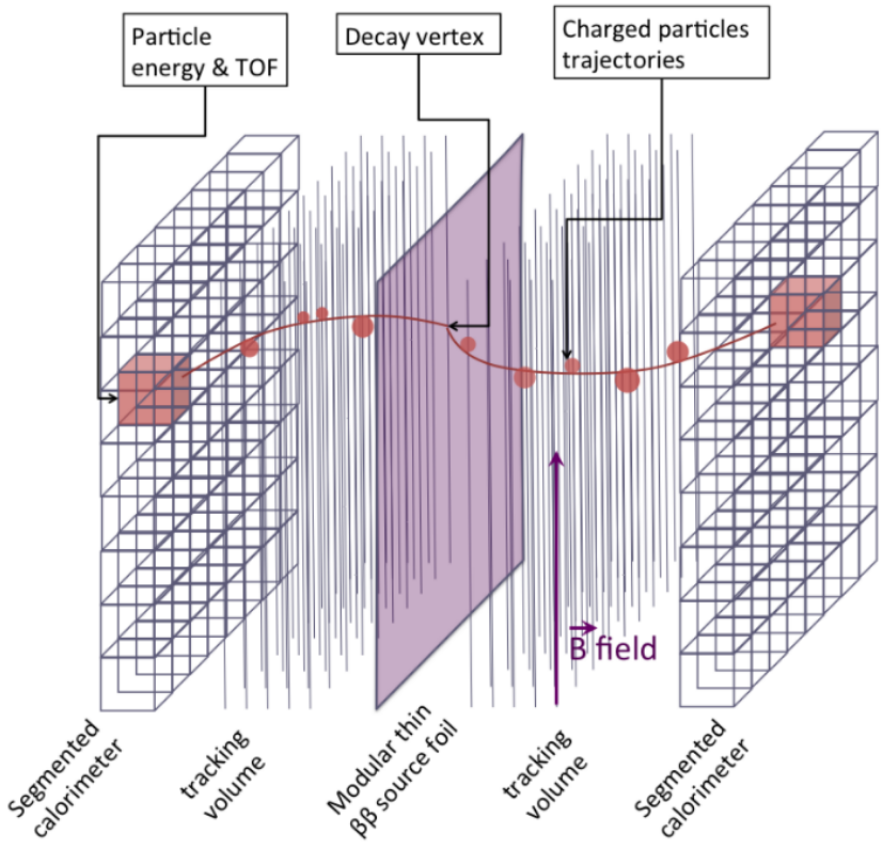

Figure 2.1: Detection principle of SuperNEMO with the tracker and the calorimeter. Two electrons are emitted from the source foil (in purple). Their tracks (in red) are detected in the tracking volume before they deposit their energy in the calorimeter blocks (red cubes).

2.1.2 Mechanical design

The SuperNEMO demonstrator is composed of several parts: the sources, the tracker and the calorimeter arranged as a sandwich as shown in fig.2.2. The source foils are installed at the center of the detector. They are surrounded by the tracker so that it can detect the electron tracks that originate from the foils. The next layer after the tracker is the calorimeter where the electrons deposit all their energies after being tracked. The calorimeter is composed of several blocks of plastic scintillators and PMTs around the tracker.

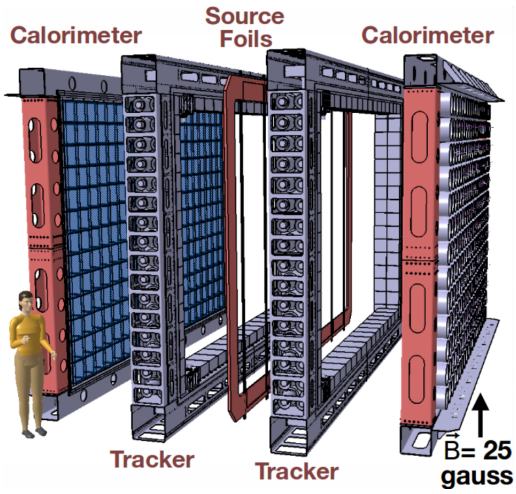

Figure 2.2: Schematic view of the SuperNEMO demonstrator.

2.1.3 The source foils

While in NEMO-3 several $\beta\beta$ isotopes (mainly 7 kg of ^{100}Mo and 1 kg of ^{82}Se) were used to produce different source foils and thus look for $0\nu\beta\beta$ of different isotopes, in the SuperNEMO demonstrator, only ^{82}Se is used to validate the technology. Indeed, ^{82}Se has a high transition energy ($Q_{\beta\beta} = 2.998$ MeV), its enrichment is feasible using standard technique (centrifugation) and it has a high $2\nu\beta\beta$ half-life ($T_{1/2}^{2\nu\beta\beta} = 9.39 \pm 0.17$ (stat) $\pm$ 0.58 (syst) $\times$ 10^{19} years from the NEMO-3 experiment [35]). A second phase with ^{150}Nd should be taken if its enrichment is achievable.

The ^{82}Se is first enriched and purified in Russia via double or quadruple distillation or reverse chromatography. Powders of ^{82}Se are then transformed into source foils. The powder is mixed with a radiopure glue (PolyVinyl Alcohol) and ultra pure water and then smeared between two 12 μm thick Mylar backing films. To dry these demonstrator sources, two techniques are used. The first one is the NEMO-3 technique that uses Mylar perforated by irradiation. However this technique could contaminate the source so a second technique has been developed. In the Laboratory of Annecy le Vieux (LAPP), it has been decided to unmould the foils and cut them into pads. These pads are then sandwiched between two mylar sheets with welding. In the detector, 34 foils of 2.7 m long are placed representing a total mass of ^{82}Se of 6.23 kg.

In addition to these Se foils, it will be shown in this thesis that it would be interesting to install copper foils in the detector, as it was done in NEMO-3. Cu is not a $\beta\beta$ emitter so it allows to control the external background (see chapter 3). The copper foils that will be used in the SuperNEMO demonstrator are 4 NEMO-3 Cu foils of 2500 mm long, 64 mm large and 57.5 μm thick.

2.1.4 The tracker

The tracker allows reconstructing precisely in three dimensions the trajectories of individual electrons. When a charged particle like an electron enters the tracker, it ionizes the gas. The tracker gas is a mixture of He (95%), ethyl alcohol (4%) and Ar (1%). The ionization electrons are then detected in the tracker cells.

The two trackers on each side of the source have a total of 2034 Geiger cells that are 3 m long and divided in 9 layers parallel to the source foils. Each cell is composed of one anode wire at the center with eight ground wires around it. The high electric potential between the anode and the grounded wires makes the ionisation electrons drift towards the anode and create an electron avalanche by ionising more atoms. The Geiger mode is obtained when the avalanches created by the electrons are saturated. A current is created by these moving electrons in the anode which shows in which cell the first charged particle has passed. Other avalanches are created all along the anode wire by de-excitation and recombination UV photons (fig. 2.4). The longitudinal position is obtained with the time needed for these avalanches to reach both ends of the cell. In the SuperNEMO operating conditions, the avalanche is expected to spread through a cell in about 50 μs. They are readout by cathode copper rings placed at each end of the cells (fig. 2.3).

Figure 2.3: Picture of a half tracker module (9 layers of cells $\times$ 113 rows) assembled at the Modane underground laboratory (LSM) before the coupling with the calorimeter on the open side.

The wiring of the cells has been done by a robot in a clean room to automate the process and reduce the risk of contamination by radioactive impurities.

The tracker is isolated from the calorimeter to avoid radon emanation from the PMTs and the outside with a nylon radon-tight film.

2.1.5 The magnetic field

Some positrons can be created in the detector, mostly because of pair creation from high energy gammas emitted after a neutron capture, event thought the neutron shielding should reduce a lot this background. To distinguish more easily the electrons from positrons, it has been decided to use a magnetic field, as in NEMO-3, to

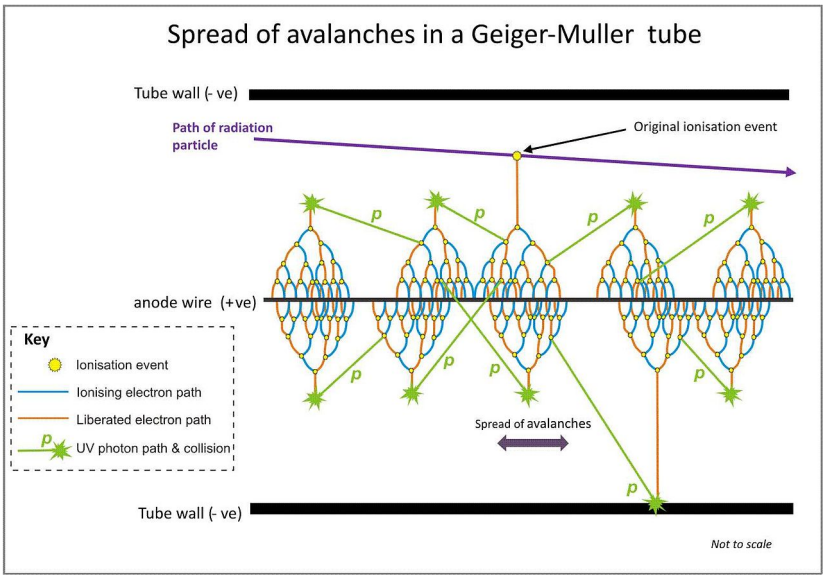

Figure 2.4: A Geiger cell principle: a charged particle ionizes the gas and creates a first avalanche. UV photons from this avalanche create themselves other avalanches. The electrons of the avalanches create a current in the anode wire.

curve the charged particles trajectories. Copper rods recycled from NEMO-3 and reshaped to surround the demonstrator with iron return field plates should provide a 25 G magnetic field. As the PMTs are highly sensitive to the magnetic fields, they are shielded with 3 mm thick pure iron sheets that will disrupt the homogeneity of the magnetic field but it should not have an important impact on the particle identification efficiency according to simulations [56].

2.1.6 The calorimeter

The energy of the electron is the variable used to discriminate between $0\nu\beta\beta$ and $2\nu\beta\beta$, which is an irreducible background, or background from natural radioactivity. Thus it must be known with the highest accuracy achievable. In the SuperNEMO experiment, six calorimeter walls are built around the tracker to measure the particle energies. These walls are made of 712 optical modules (OM) which are composed of a plastic scintillator and a PMT. Two main walls parallel to the source foils and the tracker are 20 OM long and 13 OM tall (fig. 2.5). Two other calorimeter walls of 64 OM are installed on the top and the bottom of the detector to serve as a γ veto and two other walls of 128 OM, called x-walls, cover the sides of the detector.

The plastic scintillator is made of polystyrene (PS) doped with POPOP (1,4-di-(5-phenyl-2-oxazoly)benzène), a wavelength shifter, and pTP (para-terphenyl) to increase the light yield. Charged particles and gammas, thanks to Compton scattering, lose their energy in these blocks via ionization. Thus the scintillator emits photons proportionally to the charged particle deposited energy. The plastic scintillators are carved so that the PMT bulb is coupled with a RTV615 glue to the scintillating blocks (figure 2.6). The main wall PMTs are 8 inch R5912-MOD

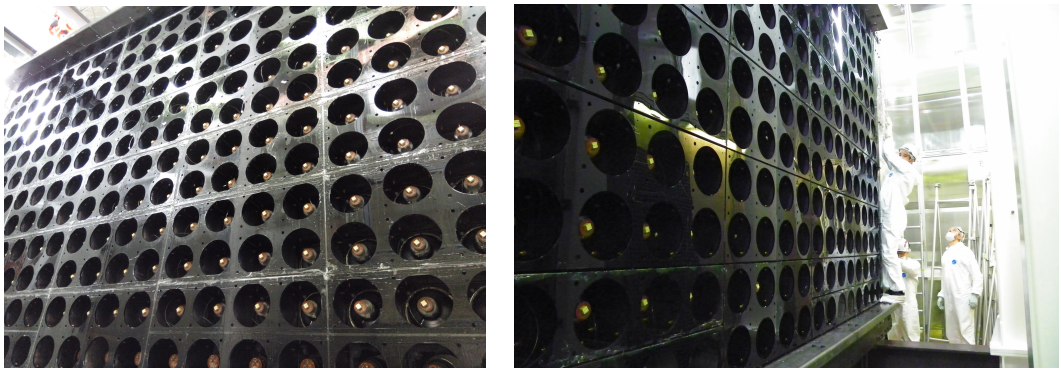

Figure 2.5: Pictures of one of the main calorimeter wall, seen from outside the detector, at the LSM. The back of the PMTs is shown.

Hamamatsu PMTs. The other walls and the first and last raws of the main walls are covered by 5 inch PMTs. These 5 inch optical modules have a lower energy resolution but also a lower probability to detect electrons originating from the source due to their position.

The calorimeter electronics, realised at LAL, will digitize the signals at the 1 GHz sampling frequency so that a pulse shape analysis can be done off-line. The same electronics has been used for the SoLid test bench (chapter 5). The energy will be computed from the charge of the pulses.

The scintillation blocks are wrapped with Teflon on their side to increase the photon collection efficiency and aluminised Mylar on the sides and the front face to further increase the light collection and protect the scintillator against UV photons from the tracker or from other scintillator blocks. This calorimeter has a mean energy resolution (FWHM) of 8.3% at 1 MeV [47].

During my thesis, I got the opportunity to take part to the calorimeter construction at the LSM. I have tested some optical modules before they were installed on the calorimeter walls. A ^{22}Na source that emits two back-to-back 511 keV gammas in coincidence was used to compare the amplitude spectra of the tested OM with a reference OM.

2.1.7 The calibration system

To know well the energy and the time scales of the detector, two different calibration approaches will be used.

A source deployment system will be installed to get an absolute energy measurement with ^{207}Bi sources. They emit electrons at 3 different energies (482 keV, 976 keV and 1682 keV). ^{207}Bi sources will be described in more details in chapter 5 as we have used them for the LAL test bench for the SoLid detector R&D. The sources will be automatically deployed for regular calibration runs and then removed.

Figure 2.6: Picture of an optical module (scintillator in violet with a PMT) seen with UV photons.

A light injection system will also be deployed to calibrate the calorimeter response. Pulses of UV LED light will be regularly injected through optical fibers in every optical module to monitor their gain (fig. 2.7). To check that the light level remains the same, a reference optical module compares the UV LED light to an ^{241}Am source placed close to it. Deviations of the PMT gains due to applied voltage fluctuations can thus be tracked and corrected at the 1% level. This system is also useful to perform time calibration and to check the energy linearity of the PMTs at high energies around the ^{82}Se $Q_{\beta\beta}$.

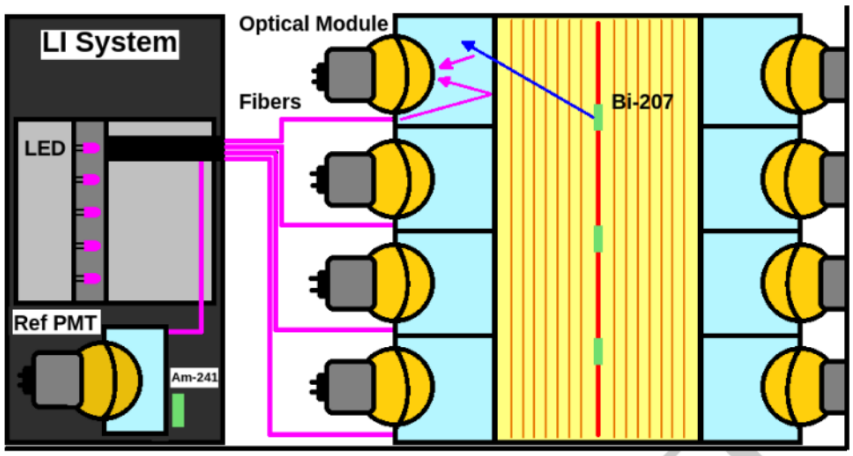

Figure 2.7: Schematic view of the light injection system to calibrate the optical modules of the SuperNEMO demonstrator [102].

2.1.8 Expected sensitity

With 6.9 kg of ^{100}Mo, the NEMO-3 experiment set a limit on the half-life of the $0\nu\beta\beta$ process of $T^{0\nu}_{1/2} > 1.1 \times 10^{24}$ years.

Some of the main expected improvements between NEMO-3 and SuperNEMO are the decrease of the foils contamination in ^{208}Tl and ^{214}Bi, as well as the decrease of radon in the tracker and the improvement of the energy resolution by a factor 2. The sensitivity of the demonstrator and the full detector have been computed considering an energy resolution of 4% FWHM at 3 MeV and the following background activities:

- A(^{208}Tl) < 2 μBq/kg
- A(^{214}Bi) < 10 μBq/kg
- A(^{222}Rn) < 0.15 mBq/m^3

Unfortunately, the ^{208}Tl activity in the source foils has been measured and is around 50 μBq/kg. However, the goal to reduce the energy resolution by a factor 2 compared to NEMO-3 has been achieved thanks to an R&D program. The expected sensitivity of the demonstrator considering an exposure of 17.5 kg.year at 90 % confidence limit is $T^{0\nu}_{1/2} > 6.5 \times 10^{24}$ years. With 100 kg of ^{82}Se, the full-scale SuperNEMO detector should reach a limit after 5 years of data-taking of $T^{0\nu}_{1/2} > 1 \times 10^{26}$ years.

2.2 Backgrounds

2.2.1 Types of background

Several types of backgrounds, mostly due to β emitters isotopes from natural radioactivity, can mimic the $0\nu\beta\beta$ signal. It is very important to know precisely their activity as the $0\nu\beta\beta$ measurement is very difficult because of its very long half-life.

The background is mostly due to the presence of natural radioactive isotopes from the ^{238}U and ^{232}Th decay chains (figure 2.8). The more troublesome isotopes for the search of $0\nu\beta\beta$ are the ones with a Q_β higher than the ^{82}Se $Q_{\beta\beta}$: ^{208}Tl (Q_β = 4.99 MeV) and ^{214}Bi (Q_β = 3.27 MeV).

Backgrounds can be discriminated with their origins:

- Internal background for decays occurring in the source foil
- Radon background for events due to radon contamination in the tracker volume
- External background for decays occurring outside the source and the tracker volume.

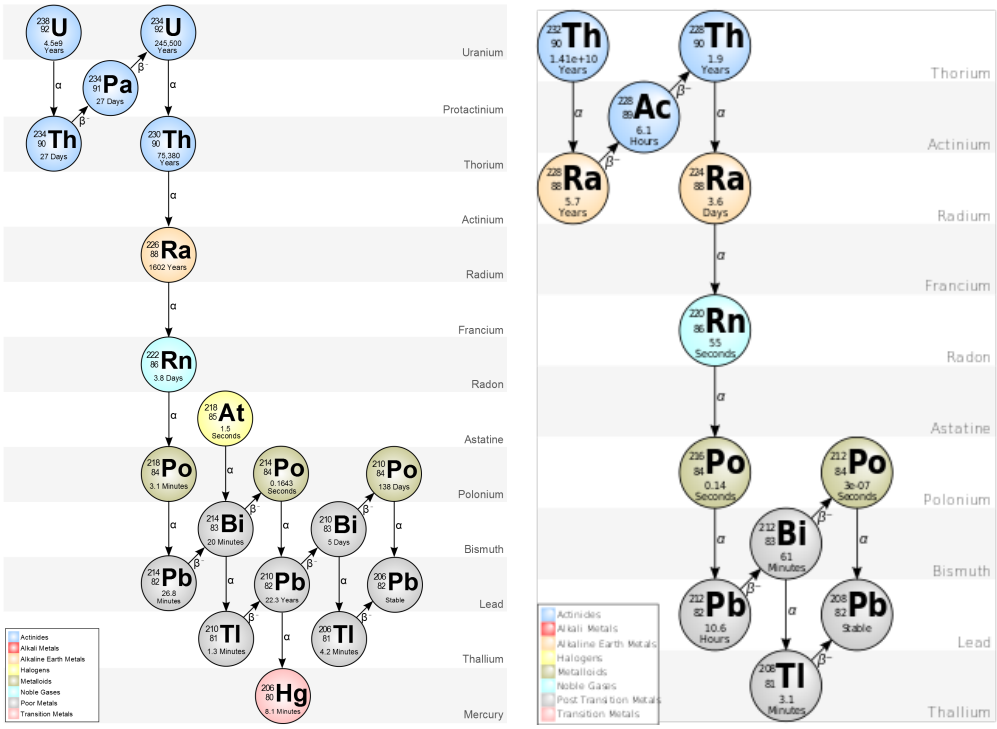

Figure 2.8: ^{238}U (left) and ^{232}Th (right) natural radioactivity decay chains. [2]

Internal background

The internal background events mimic $\beta\beta$ decays in different ways. Starting with a simple β decay event, a second electron can be produced either by internal conversion of a deexcitation γ from the daughter nucleus, or by Möller scattering or Compton scattering in the foils (fig. 2.9).

A way to estimate the ^{214}Bi background which decays via β^- to ^{214}Po (BiPo events) (see fig. 2.8, left) is to use the e$\alpha(\gamma)$ topology. Indeed, the ^{214}Po decays via the emission of an α particle with a half-life of 164 μs. The trigger allows tagging β events followed by α particles so BiPo events are measured via the e$\alpha(\gamma)$ channel and $\beta\beta$ events followed by a delayed α can be removed.

For ^{208}Tl (see fig. 2.8, right), eγ, e$\gamma\gamma$ and e$\gamma\gamma\gamma$ topologies are used as the decay of ^{208}Tl is accompanied by several γ rays.

$2\nu\beta\beta$ decays are themselves an irreducible background to $0\nu\beta\beta$ decays when the two electron sum energy is too close to $Q_{\beta\beta}$. Indeed, the calorimeter energy resolution can be too large to say if these events are in the $0\nu\beta\beta$ energy window. The measurements of the $2\nu\beta\beta$ energy spectrum and rate are thus very important and must be as precise as possible. However, isotopes like ^{40}K, ^{60}Co and ^{234m}Pa in the source foils are a background for this $2\nu\beta\beta$ half-life measurement as shown in the NEMO-3 experiment [33].

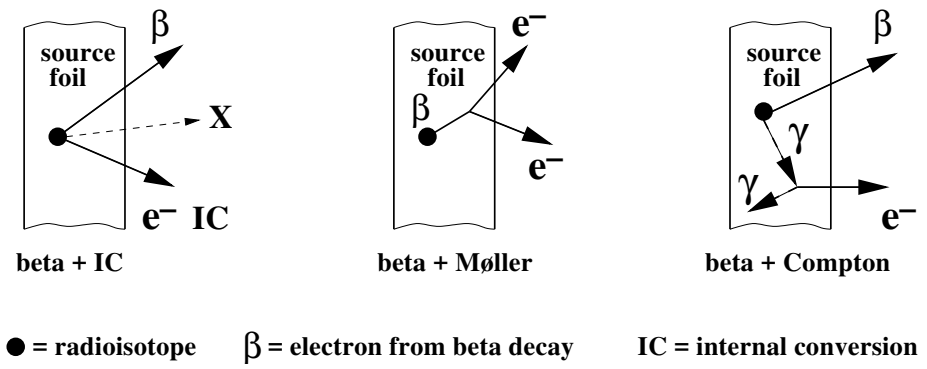

Figure 2.9: Contributions of the internal background in the source foil to the $\beta\beta$ background.

Radon (^{222}Rn)

Radon in the detector is another type of background. It can be outgased in the air from the rock walls of the laboratory or other materials. As it is a highly diffusive gas, it can enter the detector through materials like seals. When ^{222}Rn decays to ^{218}Po (see fig. 2.8, left), the ejected α particle can free several electrons of this last atom transforming it to a positively charged ion. Some of these charged ^{218}Po are neutralized by recombining with negative ions in the gas for example. Many of their daughter nuclei, ^{214}Pb, are deposited on the surface of the cathode wires in the tracking chamber or on the foils surface.

One of the more troublesome progenies of radon (^{222}Rn) that can mimic $\beta\beta$ signals is ^{214}Bi. However, BiPo events can be used to measure the radon activity via the eα channel.

Another source of background due to radon progenies is the β decay of ^{210}Pb to ^{210}Bi. Its end-point Q_β of 1.16 MeV is too low to be an issue for $0\nu\beta\beta$ but it has to be taken into account to get a precise measurement of the $2\nu\beta\beta$ spectrum.

External background

There are different contributions to the external background that can mimic $\beta\beta$ decays:

- External high energy γ emitted by natural radioactivity outside the detector (mostly ^{40}K, ^{214}Bi and ^{208}Tl) although it has been shown in the NEMO-3 experiment that it accounts for $\sim 2\%$ of the external background after cuts were applied thanks to the efficient shielding [32].

- Neutrons coming from cosmic muon spallation or radioactivity in the environment of the detector can produce γ rays via neutron capture. However it has been shown that in the NEMO-3 detector, the neutron background represents only 0.93% of the total background at energies below 4 MeV [32].

- Radioactive contamination of detector material. It is mostly due to the PMT glass, made of silicon dioxide. Despite a selection with HPGe detectors, the contamination in ^{226}Ra, ^{228}Ra and ^{40}K remains important. Their troublesome progenies are ^{214}Bi, ^{208}Tl, ^{228}Ac and ^{40}K. This represented one half of the eγ events observed in NEMO-3 [32].

All these external backgrounds can produce external gamma which can themselves produce 2β-like events by pair creation (with misidentification of the charge), 2 Compton scatterings or one Compton and one Möller scattering in the source foil (fig. 2.10).

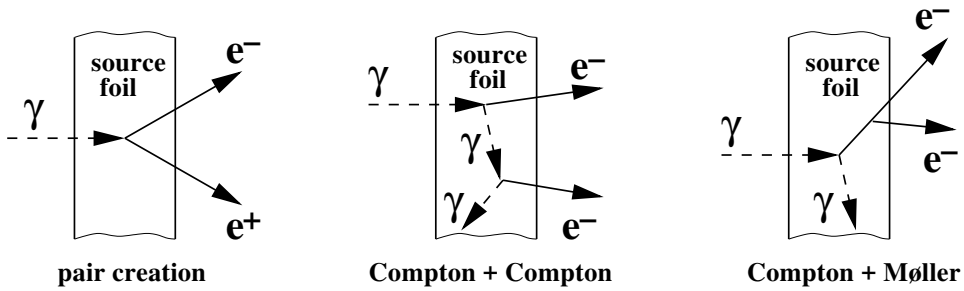

Figure 2.10: Contributions of the γ external background to the $\beta\beta$ background in the source foil

As a consequence, the external gamma ray flux has to be measured precisely. It can be done using the crossing electron channel or the γe-external channel (in opposition to γe-internal events coming from the source foil) (fig. 2.11). This will be studied in more details in chapter 3.

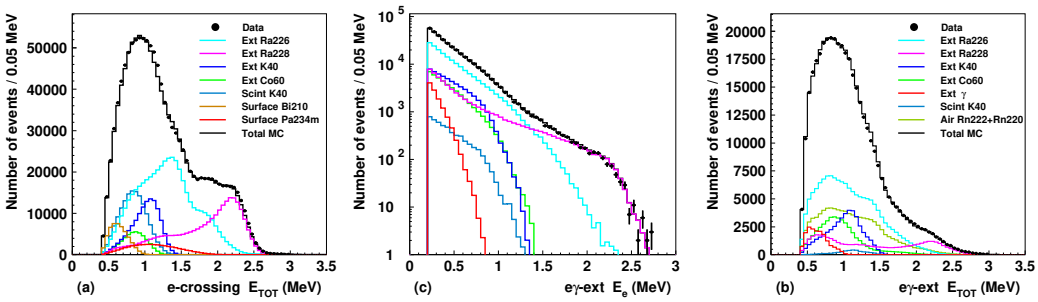

Figure 2.11: Results of the phase 2 fit for the whole NEMO-3 detector: a) energy sum of crossing electron events, b) energy sum of the electron and γ-ray for γe-external events, c) detected electron energy for γe-external events [32].

2.2.2 Background reduction

Radiopurity

To prevent any radioactive contamination in the detector, every material has to be very carefully selected so that it is the most radiopure as possible (activity below

the mBq/kg or μBq/kg). All the material radiopurities have been tested with High Purity Germanium detectors (HPGe).

One of the main challenge was to reduce the PMT glass contamination. A work has been done with Hamamatsu Photonics to reduce this contamination. Ten PMTs from different lots have been crushed by Hamamatsu to measure the radiopurity of the glass and the insulators. Then they have been sent to LSM to cross-check the measurements with HPGe detectors. The total expected activities for 8 and 5 inch PMTs and their insulators can be found in table 2.1. It shows that the radiopurity is better than in NEMO-3 for ^{40}K and ^{226}Ra (which leads to ^{214}Bi) but it is worse for ^{232}Th (that leads to ^{208}Tl) [106].

	SuperNEMO activities (Bq)			NEMO-3 activities (Bq)
isotope	8" PMTs	5" PMTs	total	total
^{214}Bi	141	56	197	324
^{208}Tl	41	3	44	27
^{40}K	417	123	540	1078

Table 2.1: Total activities of the PMTs for SuperNEMO and NEMO-3.

The $\beta\beta$ sources had also to be purified to prevent radioactive contamination. To control the source contamination, the BiPo detector has been built at the Canfranc underground laboratory in Spain. It is made of 2 layers of 40 PMTs and scintillator blocks each that takes the source foils in sandwich. It can detect possible hot spots thanks to the segmentation. The following internal contaminations have been obtained: [92]

- an upper limit of 300 μBq/kg for ^{214}Bi
- a weighted average over different Se foils which gives a measurement of 52 μBq/kg for ^{208}Tl

Radon facility

We have seen that the radon which is highly volatile in the laboratory air can be an issue if it comes in the detector tracker. The radon level in the LSM is around 15 Bq.m^{-3}. The goal is to achieve a radon level inside the detector of 0.15 mBq.m^{-3}.

In NEMO-3, a residual radon contamination had been observed due to leaks in the external shielding joints and calorimeter walls. To reduce this contamination, an anti-radon facility and a tent made of plastic films to isolate the detector have been installed which have reduced the level of radon by a factor 6. A similar system will be used for the SuperNEMO demonstrator. An anti-radon tent made of PMMA panels will surround the detector. To get rid of radon inside the tent emanating mostly through possible leaks or from PMTs, the air inside the tent will be flushed with radon-free air thanks to an anti-radon factory (a charcoal column will trap the radon atoms long enough for them to decay).

Shielding and underground laboratory

To prevent external background contamination, a good shielding of the detector is very important.

The SuperNEMO experiment, like the previous NEMO experiments, takes place at LSM, inside the Frejus tunnel between France and Italy (fig. 2.12). The 1700 m of rock of the mountain above this laboratory is used as a shielding against cosmic rays. It represents 4800 m.w.e which makes it the deepest underground laboratory in Europe. The cosmic ray flux is reduced by a factor more than 10^6 so only 4 cosmic rays per m^2 per day are expected. This very interesting environment is also used for astrophysical, biology or geology experiments.

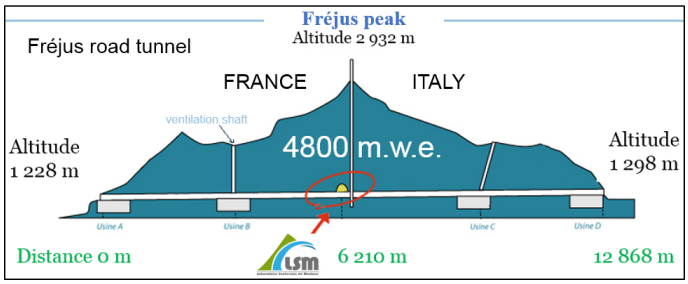

Figure 2.12: Schematic view of the underground laboratory of Modane (LSM).

The cosmic rays are not the only annoying external background. The rocks of the laboratory are also radioactive so the detector needs to be protected against photons and neutrons emitted by them. Shielding made of layers of iron will be placed around the detector against γ rays. Bricks of borated water may be used also against neutrons.

After removing all the possible backgrounds with passive shielding, a precise simulation has to be done to investigate the impact of the remaining background.

2.3 Simulation and analysis tools

2.3.1 Monte-Carlo simulation

A simulation software has been created to investigate the impact of the different backgrounds on the $0\nu\beta\beta$ measurement. Simulations help to assess the detector efficiency.

The software simulation is based on Geant4 [3]. The definition of the primitive detector geometry, the database of the materials, the vertex generator, the kinematics of the radioisotopes are implemented with the C++ library Bayeux. The generator of $\beta\beta$ and other radioactive backgrounds is called Genbb/Decay0 and is implemented in Bayeux. The Bayeux library also takes care of data handling. It

is used by several experiments in nuclear or particle physics. The Falaise package depends on the Bayeux library but is used specifically for the SuperNEMO experiment. It defines the geometry and materials of the SuperNEMO demonstrator as well as the reconstruction algorithms and the analysis tools.

Events are first simulated by Genbb and their vertex is located in the detector by the Bayeux vertex generator. The particles are propagated through the virtual detector with the Geant4 based-model which takes into account possible interactions like scattering, ionisation or Bremsstrahlung. To get a realistic simulation, the detector response has to be taken into account with for example the 8% FWHM energy resolution of the calorimeter at 1 MeV that smears the true simulated energy of the particle. The events are then reconstructed before being analysed. The same software is used for reconstructing and analysing Monte-carlo and recorded data to reduce systematic errors. The simulated data are thus as similar as possible to recorded data.

2.3.2 Analysis chain

Event reconstruction

The data pass through several algorithms to identify the physical event that happened. Tracker hits are grouped in clusters and fitted to reconstruct tracks in the wire chamber. These tracks are then associated with possible calorimeter hits if they exist (fig. 2.13). The tracks are defined as positive or negative depending on the curvature of a positively or negatively charged particle going from the source to the detector under the 25 G magnetic field.

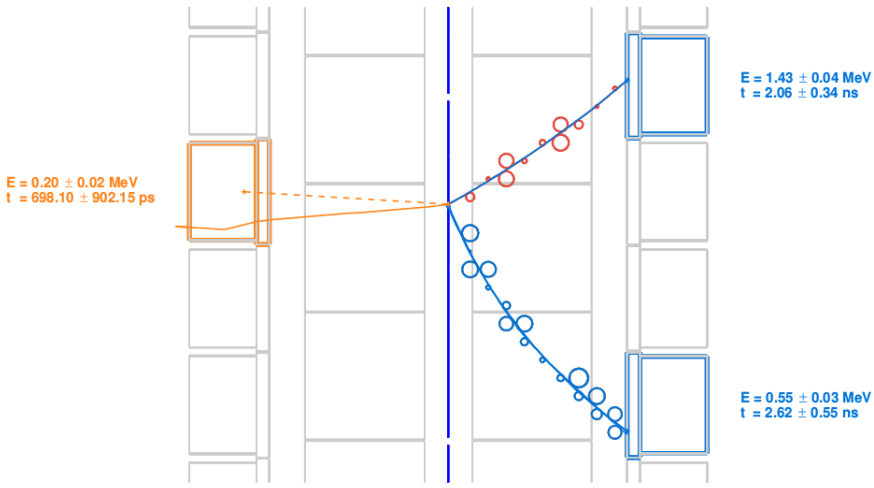

Figure 2.13: A SuperNEMO simulated event with two electron tracks (in blue) and one gamma (in orange) reconstructed. All the particles emerge from the source foil (in dark blue). The electrons are tracked in the wiring chamber. The red and blue circles show the fired cells that were used to reconstruct the electron tracks. The three particles deposit their energy in calorimeter blocks. The gamma particle corresponds to a calorimeter block not associated with a track.

Particle identification

To continue the event reconstruction, particles must be identified in the detector. The following criteria have been used to identify the different particles (fig. 2.14):

- Electrons from the source are negatively curved tracks in association with a calorimeter hit.
- Positrons from the source are positively curved tracks in association with a calorimeter hit.
- Alphas are short straight tracks with no associated calorimeter hit.
- Gammas are one or several calorimeter hits unassociated with any track.

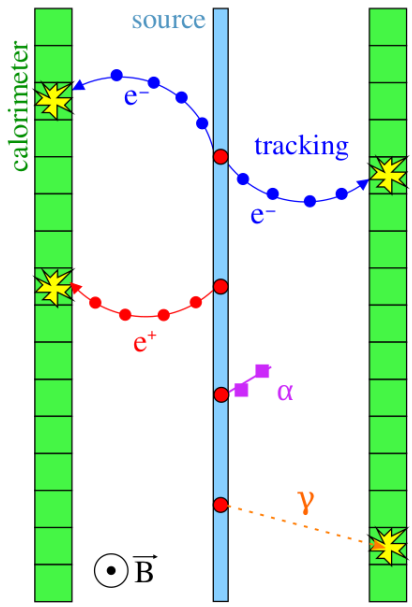

Figure 2.14: Schematic view of the different types of particles interacting in the detector. The electrons (in blue) are negatively curved tracks from the source with at least one calorimeter hit. The positrons (in red) have a similar definition but with positively curved tracks. The alpha particles (in violet) have only very short tracks. The gammas (in orange) are reconstructed if a calorimeter hit is not associated with any track.

Once the particles of an event are identified, they can be assembled to be classified in a channel event like two electrons, a crossing electron, one electron and one or several gammas... All these channels are interesting to study the different backgrounds. The final channel is of course the two electron channel to look for $\beta\beta$ decay.

Variables measured

Thanks to the tracker and the calorimeter, the SuperNEMO experiment has a great advantage compared to the other $\beta\beta$ decay experiment: it has access to the

kinematics of the events. Some variables that can be reconstructed and used for the analysis are:

- The individual energy of the particle deposited in the calorimeter blocks.
- The vertex barycenters, each vertex computed as the extrapolation of the track fit on the source.
- The angle between 2 particles calculated as the angle between the tangent of the 2 track vertices at the extrapolated vertex of origin.
- The internal and external probabilities based on the time of flight (ToF) of the particle for events with two particles that have both an associated calorimeter hit, including one charged particle.

The internal probability is used to measure the probability that two particles come from the source. The external probability tests if one of the particles at least comes from somewhere else. For example, a crossing electron could mimic a $\beta\beta$ event from the source. In that case the curvature of one of the two tracks separated by the source should be different from the $\beta\beta$ events. However, in many cases the curvature can be changed by scattering of the electrons in the wire chamber so the internal probability is very useful to discriminate these kinds of events.

To compute these probabilities, we start with a χ^2 calculation for both hypotheses ($hyp = int$ or ext):

$$\chi^2_{hyp} = \frac{(\Delta t_{meas} - \Delta t_{th})^2_{hyp}}{(\sigma^2_{exp} + \sigma^2_{th})_{hyp}} \tag{2.1}$$

where Δt_{meas} is the time difference between the particles measured by the calorimeter and Δt_{th} is the predicted one, using relativity to compute the traveling time of the particles, which depends on the internal or external hypotheses. σ^2_{exp} and σ^2_{th} are the experimental and theoretical errors. Probabilities are then derived from the χ^2 computation using the error function that transforms a gaussian distribution into a flat distribution between 0 and 1:

$$P(\chi^2_{hyp}) = \frac{1}{\sqrt{2\pi}} \int_{\chi^2_{hyp}}^{+\infty} x^{-\frac{1}{2}} e^{-\frac{x}{2}} \mathrm{d}x \tag{2.2}$$

2.4 Conclusion

It has been seen that the main challenge of the SuperNEMO demonstrator, like other $\beta\beta$ experiments, will be to fight against backgrounds induced by natural radioactivity. Thanks to its tracker and calorimeter detector, several observables will be available to characterize and identify particles. The next chapter will focus on the strategies to measure and reject the external background using simulations.

Chapter 3

External background analysis

3.1 Simulation to study the external background

3.1.1 Motivations of the study

As explained before, $0\nu\beta\beta$ search is so complicated that the background has to be reduced at the maximum and controlled very well. It is first reduced using shieldings and very radiopure materials for the detector construction. However, some backgrounds remain and need to be cut off from the signal searched. This chapter mostly focuses on the external background. In NEMO-3, it was not the biggest background but as the radon and internal backgrounds are expected to decrease for the demonstrator, it could become one of the major issue for SuperNEMO. Although it is expected to be negligible in the energy window of the $0\nu\beta\beta$ decays, it has to be taken into account for the measurement of the $2\nu\beta\beta$ decays. The latter is indeed the most important and irreducible background to $0\nu\beta\beta$ signals. It has thus to be measured as precisely as possible. As $2\nu\beta\beta$ signals covers all energy range from 0 to $Q_{\beta\beta}$, its half-life measurement is more sensitive to the external background.

The external background study shown in this chapter has been made in three steps. The first step studies the possibility to reject the external background in the $\beta\beta$ channel. The second step demonstrates that this background can be measured very precisely. Indeed, the SuperNEMO technology has the advantage to be able to separate the events in different channels using their topologies. Finally, the utility to install copper foils in the detector has been be studied. As copper is very radiopure, it should be sensitive mostly to external background and thus provide an independent way to control it.

3.1.2 Simulations and estimation of the expected backgrounds

Simulation of the external background

As already explained in chapter 2, there are several sources of external background: neutrons coming from cosmic muon spallation, external γ or neutrons emitted by

radioactivity outside the detector and radioactive contamination of detector materials. Unfortunately, the simulation of all these backgrounds would require too much CPU time. Thus for a first estimation of the external background, only the most important contributions detected in NEMO-3 have been simulated during this thesis.

In the NEMO-3 experiment, an external background model has been built to account for the detected events in different channels [33]. In this model, the contributions of the γ ray flux from the surrounding rocks are supposed to be negligible thanks to the shielding but the contributions of the detector components are taken into account. Table 3.1 shows that according to the measurements, the PMTs contamination in ^{40}K, ^{214}Bi and ^{208}Tl are the most important contributions to the external background. The iron shielding is the most radioactive component but as iron can absorb the gammas before they leave the shielding, it does not produce much background in the detector.

Components of NEMO-3	Total activity (Bq)			
	^{40}K	^{214}Bi	^{208}Tl	^{60}Co
Photomultiplier tubes	1078 ± 32	324 ± 1	27.0 ± 0.6	
Plastic scintillators	21.5 ± 0.9			
μ-metal PMT shield				14.6 ± 2.6
Iron petals	100 ± 4	9.1 ± 1.0	3.1 ± 0.5	6.1 ± 1.8
Copper on petals				18.4 ± 0.8
Iron shield		73600 ± 200	484 ± 24	

Table 3.1: Activities of the different components of the external background model in NEMO-3 [33]. Apart from the iron shielding that absorbs the emitted gammas, the PMT contributions are dominant.

For the SuperNEMO demonstrator, the radioactivity of the different components has been measured to make sure it is low enough. Although work has been done with Hamamatsu to lower the activities of the PMT glasses, they are still high enough to become likely the most important contribution to the external background.

As seen in the previous chapter, there are two types of PMTs in the calorimeter: 5 inch and 8 inch PMTs. The total activity of the 5 inch PMTs is lower than for 8 inch PMTs as they are smaller and less numerous. Furthermore, the particles emitted by these 5 inch PMTs have a lower probability to reach the source foils due to their place as it will be seen in section 3.4.1. Thus for most of this work, only backgrounds in 8 inch PMTs have been simulated.
The measured total activity for the 8 inch PMT glass and their insulator, which are the less radiopure components of the PMTs, are the following (with 7% systematic uncertainty):

- A(^{40}K ext) = 417 Bq

- A(^{214}Bi ext) = 140.5 Bq
- A(^{208}Tl ext) = 41.4 Bq

Estimation of the external background contributions

As a first estimation of the external background, ^{40}K, ^{214}Bi and ^{208}Tl contaminations inside the PMT glass have been simulated. The simulations give the detection efficiency of each isotope. The number of events expected can be calculated with 3.1:

$$N_i = A_i \times \epsilon_i \times t \tag{3.1}$$

With A_i the total activity of the isotope i, ϵ_i the detection efficiency of the isotope i and t the running time of the experiment (2.5 years). The detection efficiency is extracted from simulation data by dividing the number of detected events in the channel studied by the number of simulated events.

Simulation of other backgrounds and estimation of their contributions

To compare the impact of the external background due to PMTs with the impact of the other types of backgrounds, simulations of radon and internal backgrounds have also been realised.

The gas of the tracker can be contaminated by ^{222}Rn. When it desintegrates to ^{218}Po, the ejected alpha particle can free several electrons transforming the ^{218}Po into charged ions. Most of their daughter nuclei, ^{214}Pb are deposited at the surface of the cathode wires in the tracking chamber or at the foils surface [33]. This is an issue as there is ^{214}Bi in their decay chain. ^{214}Bi has thus been simulated at the surface of the wires of the tracker. To compute the number of expected events, the formula 3.2 has been used:

$$N_{Rn} = A_{Rn} \times V \times \epsilon_{Rn} \times t \tag{3.2}$$

With A_{Rn} the expected radon activity (150 μBq/m^3), V the tracker volume (15 m^3), ϵ_{Rn} the detection efficiency (extracted from the simulation) and t the running time of the experiment (2.5 years).

The internal background is also troublesome. According to the foil activity measurement done with the BiPo detector [48], there are contaminations of ^{214}Bi and ^{208}Tl inside the foils of the order of:

- A(^{214}Bi int) = 300 μBq/kg (limit obtained with the BiPo detector)
- A(^{208}Tl int) = 52 μBq/kg (weighted average measurement over different Se foils)

Like in NEMO-3, there may be also other contamination in the source foils like ^{234m}Pa and ^{40}K but their activities have not been measured yet.

The number of events expected from the source foil contamination is calculated with 3.3:

$$N_i = A_i \times \epsilon_i \times m \times t \tag{3.3}$$

with A_i the measured activity of the isotope i, ϵ_i the detection efficiency of the isotope i (extracted from the simulation), m the mass of ^{82}Se (6.23 kg), t the running time of the experiment (2.5 years).

Simulation of the $2\nu\beta\beta$ events

The signal interesting in this analysis is the $2\nu\beta\beta$ desintegration of ^{82}Se. These events are themselves background events for the $0\nu\beta\beta$ desintegrations of ^{82}Se so it is important to know well the half-life of $2\nu\beta\beta$ which is impacted by the external background. To know accurately the half-life of $2\nu\beta\beta$ decays, one can calculate it from the number of decays observed. Indeed, the expected number of $2\nu\beta\beta$ for ^{82}Se can be computed this way:

$$N_{2\nu\beta\beta} = \frac{N_A \times ln2 \times \epsilon_{\beta\beta} \times m \times t}{M(^{82}Se) \times T_{1/2}^{2\nu\beta\beta}} \tag{3.4}$$

With N_A the Avogadro number, $\epsilon_{\beta\beta}$ the detection efficiency (extracted from the simulation), m the ^{82}Se mass (6.23 kg), t the running time of the experiment (2.5 years), $M(^{82}Se)$ the mass number of ^{82}Se and $T_{1/2}^{2\nu\beta\beta}$ the half-life. In this work, the goal is to compare the number of external background events expected with the number of $2\nu\beta\beta$ events expected from ^{82}Se so a half-life of $T_{1/2}^{2\nu\beta\beta} = 9.39 \pm 0.17$ (stat) $\pm$ 0.58 (syst) 10^{19} years, that was measured with NEMO-3 [35], has been used. When the experimental data will be available, the number of $2\nu\beta\beta$ events detected will be used to extract a more accurate half-life measurement.

Simulation conditions

The simulation has been run with the Falaise simulation software developed for the SuperNEMO experiment (see part 1.4.1). The detector configuration in this simulation is very close to the reality. The main difference is the use of a uniform 25 G magnetic field in the whole detector as it has not been measured yet. However, it has been proven that it does not change the particle identification significantly [56].

An energy resolution of 8% at 1 MeV (FWHM) and a time resolution of 400 ps at 1 MeV have been used. The energy thresholds have been set to 150 keV for the highest energy electron and 50 keV for the lowest energy electron which correspond to the values planned for the SuperNEMO thresholds.

Two different simulations were performed. One was done putting Se in all the strips of the detector to be as close as possible to the final configuration and evaluate the impact of the external background on the $2\nu\beta\beta$ measurement. Another one was done replacing the selenium by copper in all the strips and removing the mylar backing film. The goal was to evaluate the usefulness to install copper strips

in the detector in order to control the external background, to see if the place of the copper strips would have an impact and to know the number of expected events for different thickness of copper foils.

As the simulation of ^{40}K, ^{214}Bi and ^{208}Tl inside the PMT glass can not be neglected but is very inefficient to create $\beta\beta$-like events in the source foils, it required to simulate hundreds of millions of events. However, the number of events simulated was limited by CPU time. It took several days with hundreds of jobs running in parallel in the Computing Center of Lyon to simulate these events. Still, the statistical error remains important in the following results with only around one hundred of events selected in the interesting channel. To limit this statistical uncertainty, a simulation will be run for the whole collaboration so that more CPU time can be used. The external background has been simulated only for 8″ PMTs. The simulation of external background in 5″ PMTs for copper foils has shown that it could be neglected in a first approximation. The simulations of radon, internal backgrounds and $2\nu\beta\beta$ of Se have also been done. As these ones are much more efficient, the statistical uncertainty due to CPU time limitation was not an issue.

Event selection

Only two types of particles are used in this study: electrons and gammas.

- Electrons are defined as a negatively charged particle track intercepting the foil associated with a hit in a calorimeter block. The charge of the particle is accessible thanks to the curvature of the track in the wire chamber. It is defined as negative if the track turns anti-clockwise when looking at the detector from the top.

- Gammas also deposit energy in the calorimeter blocks but are not visible in the tracker. Thus a gamma is defined as at least one hit in a calorimeter block with no associated track. The timing information is used to associate them with electrons.

For all the electron tracks, a vertex position is extrapolated from the source foil. A requirement on the distance between the different vertex positions of all the tracks of a same events is used. The horizontal distance between the vertices has to be less than 6 cm and the vertical distance less than 7 cm. It has been shown that it keeps 95 % of $\beta\beta$ events from the source.

3.2 External background expected in the 2 electron channel

The $2\nu\beta\beta$ half-life of Se will be measured in the internal two electron (2e-int) channel. Internal refers to the fact that the two electrons should be emitted from the source foil at the same time.

3.2.1 Contributions to the external background

By looking at the external background simulated data in the two electron channel, three types of events have been noticed.

- Two successive Compton scatterings in the foil (figure 3.1).
- A first Compton scattering in the foil from an external gamma releases an electron that undergoes itself a Möller scattering creating another electron (figure 3.2).
- A crossing electron: an external electron can travel trough the detector and cross the foil (figure 3.3). It can be reconstructed in this channel if the curvature of one part of its track is badly reconstructed and the timing badly measured.

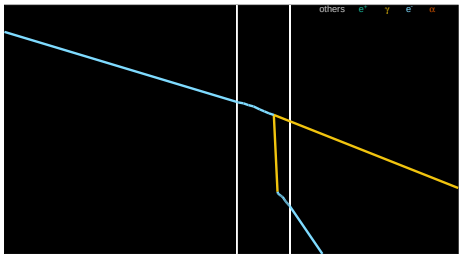

Figure 3.1: Top view of an external gamma (in yellow) arriving on the Cu foil (between the two white lines) releasing two electrons (in blue) by two Compton scattering.

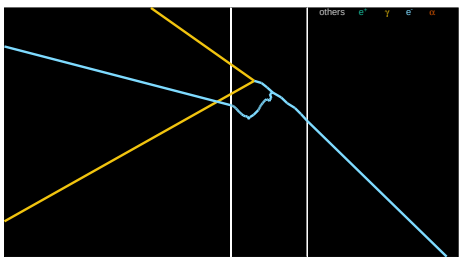

Figure 3.2: Top view of an external gamma (in yellow) arriving on the Cu foil (between the two white lines) releasing one electron (in blue) by Compton scattering. This electron releases itself another electron (in blue) by Möller scattering.

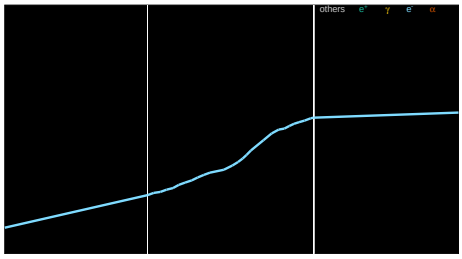

Figure 3.3: Top view of an external electron (in blue) arriving on the Cu foil. It is deviated by a few scatterings before leaving the source and hitting the calorimeter on the opposite side of the source.

The most frequent events in this 2e-int channel are crossing electrons. Using cuts on the internal and external probability, introduced in chapter 2, should reduce these events as their time of arrival on the calorimeter is different.

3.2.2 External and internal probability cuts

The simulation results shown in figure 3.4, requiring only 2 electron tracks with vertex in the source foils, show that the external background, in blue, is the dominant one. Such a level of background would not allow a measurement of Se $2\nu\beta\beta$ signal (S/B = 0.6). However, the tracko-calorimetry technology of the SuperNEMO demonstrator has the great advantage to give access to several variables like the energy, position or detection time of each particle.

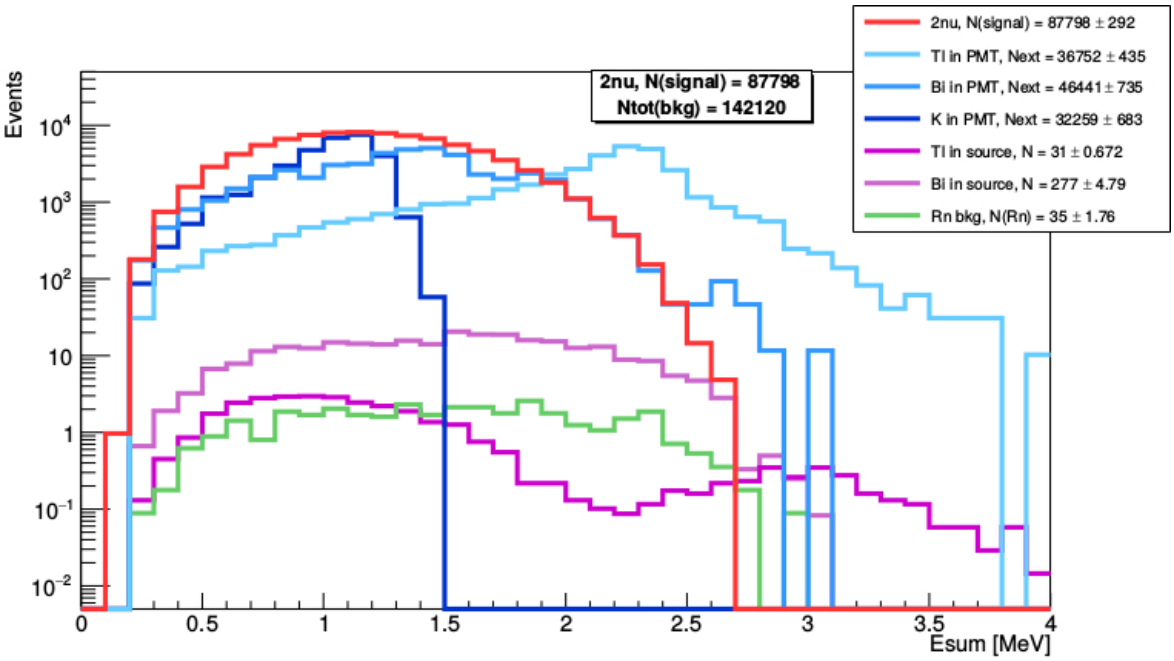

Figure 3.4: Energy spectrum of 2 reconstructed electron events coming from the source foils for different types of background or signal. The number of expected events is given in the legend.

The internal and external probabilities are very useful to distinguish particles coming from the source foils or other parts of the detector. They are thus very suitable to reject external background. In the following, the NEMO-3 selenium analysis cuts have been set [35], in order to check if the background can be measured and controlled efficiently with a similar analysis. An event is considered as internal if its internal probability is above 4% and its external probability is below 1%.

In figure 3.5, where the internal and external probabilities of external background and signal are shown, we can see a clear separation between the two populations. Cuts on these parameters (internal probability > 4% and external probability < 1%), in red in figure 3.5, should improve greatly the signal over background ratio. They keep 87.2% of the $2\nu\beta\beta$ events and remove 97.6% of the external background.

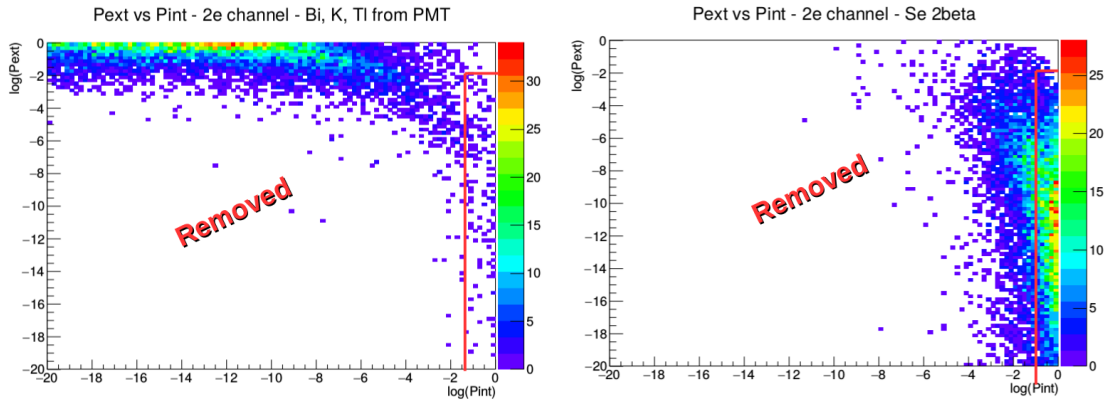

Figure 3.5: External probability vs Internal probability for external background on the left and $2\nu\beta\beta$ of Se on the right. The part in the red rectangle shows the events that are kept after the standard internal and external probability cuts.

Figure 3.6 shows that the external and internal probability cuts have reduced most of the external background although it is still the dominant contribution with 2580 ± 282 events expected. The $2\nu\beta\beta$ signal can be clearly seen with 76899 ± 273 events expected which gives a signal over background ratio S/B = 27 taking into account other background contributions. This is, however, an optimistic S/B as contributions to the internal background from several isotopes are still missing.

3.3 External background measurement

The external background can be observed with much more statistics in other channels than the 2e-int one. It allows to measure the activities of the different isotopes that contribute to this background using equation 3.1 in order to predict the number of external backgrounds expected in the 2e-int channel.

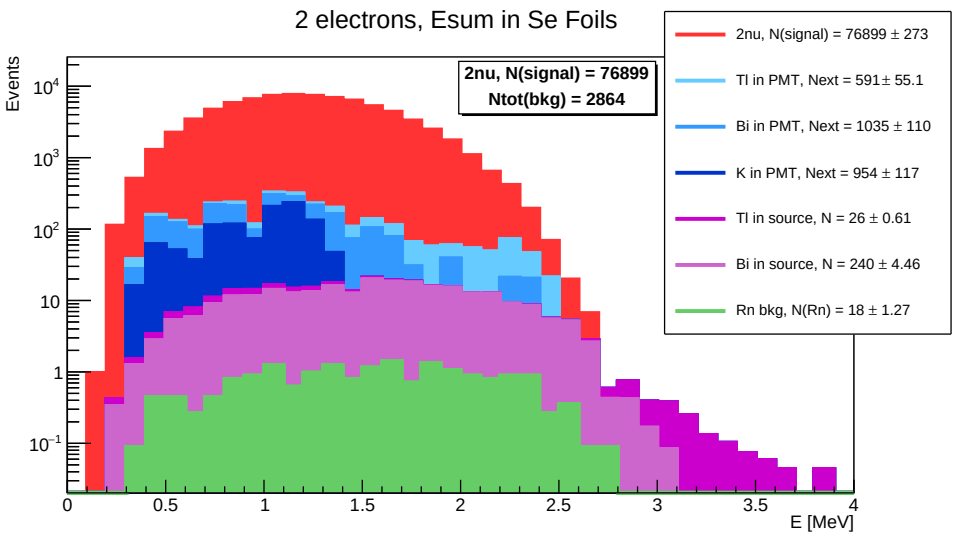

Figure 3.6: Stacked energy spectrum of 2e-int events for different sources of background or $2\nu\beta\beta$ signal after internal and external probability cuts.

3.3.1 The crossing electron channel

The crossing electron channel is used to measure the activities of Tl, Bi and K in the PMT glass. In this section, a study based on simulation will show how sensitive this channel is to these backgrounds.

In the crossing electron channel (figure 3.7), an electron is created via several possible mechanisms like in a Compton scattering of an external γ with the scintillator or a β decay on the surface of the scintillator. This electron deposits part of its energy in the scintillator before crossing the tracker and the source foil to reach another scintillator block where it deposits the rest of its energy.

To tag crossing electrons, two tracks with a compatible vertex on the source foil must have opposite curvature, since this variable is defined for particles originating from the source, and the external probability has to be high enough. Using similar cuts as in NEMO-3, the external probability has to be $> 1\%$ and the internal probability has to be $< 4\%$. In this crossing electron channel, the sum energy is computed using one electron track going from a calorimeter block to a source foil and another one from the source foil to a calorimeter block in the other wall with the same vertex.

The sum energy deposits of the electron is shown in figure 3.8. The external background dominates largely in this channel. It represents 99.97 % of the events. The internal background may increase if all the isotopes are taken into account but it should remain low. Besides, it will be measured accurately in other channels like the single electron channel. Using the shape of the crossing electron energy distribution, the ^{208}Tl contribution can be separated easily from the ^{214}Bi and ^{40}K contributions. With $(1700 \pm 5.9) \times 10^3$ external background events that should be observed after 2.5 years of data taking, the statistical uncertainty on this measurement should be

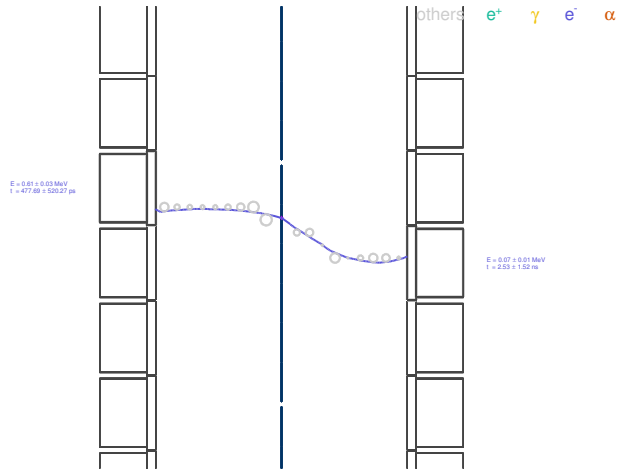

Figure 3.7: Display of a ^{214}Bi event coming from a PMT surface contamination, reconstructed in the crossing electron channel. The ^{214}Bi emits a gamma on the left wall that deposits energy on a calorimeter block (not seen in the figure) and emits an electron by Compton scattering. This electron (violet track) crosses the left part of the tracker and the source foils before reaching another scintillator block on the right.

around 0.08 %. The crossing electron channel will thus be very efficient to measure the external background activities. A precise measurement per strip of selenium could even be performed to get a more accurate background model.

3.3.2 The γe-ext channel

The γe-ext channel (figure 3.9) has also been used in NEMO-3 to measure the external background activities although it can be less efficient than the crossing-e channel as the γ detection efficiency is lower for the electron and it requires a second interaction from the γ in the source foils. In addition, the reconstruction of the energy deposited by the γ is less good than for electrons. This channel is thus used to cross-check the measurements performed in the crossing electron channel. The creation of such events comes from an external photon that deposits some energy in a scintillator block before reaching the source foil. In the source, it creates an electron via Compton scattering for example that will be detected in the tracking chamber and the calorimeter.

To tag γe-ext events, one electron track and one gamma detected in a calorimeter block are required to have a compatible vertex on the source foil and a good external probability. The requirements set on the time of flight variables are: internal probability smaller than 4% and external probability greater than 1%.

The energy sum distribution of the gamma and the electron is presented in figure 3.10 for all the background isotopes simulated and the $2\nu\beta\beta$ of ^{82}Se. It shows that in this channel, the external background represents 99.8 % of the events. It is thus a very interesting channel to measure it. With $(587 \pm 3.7) \times 10^3$ external background events that should be observed after 2.5 years of data taking, the statistical

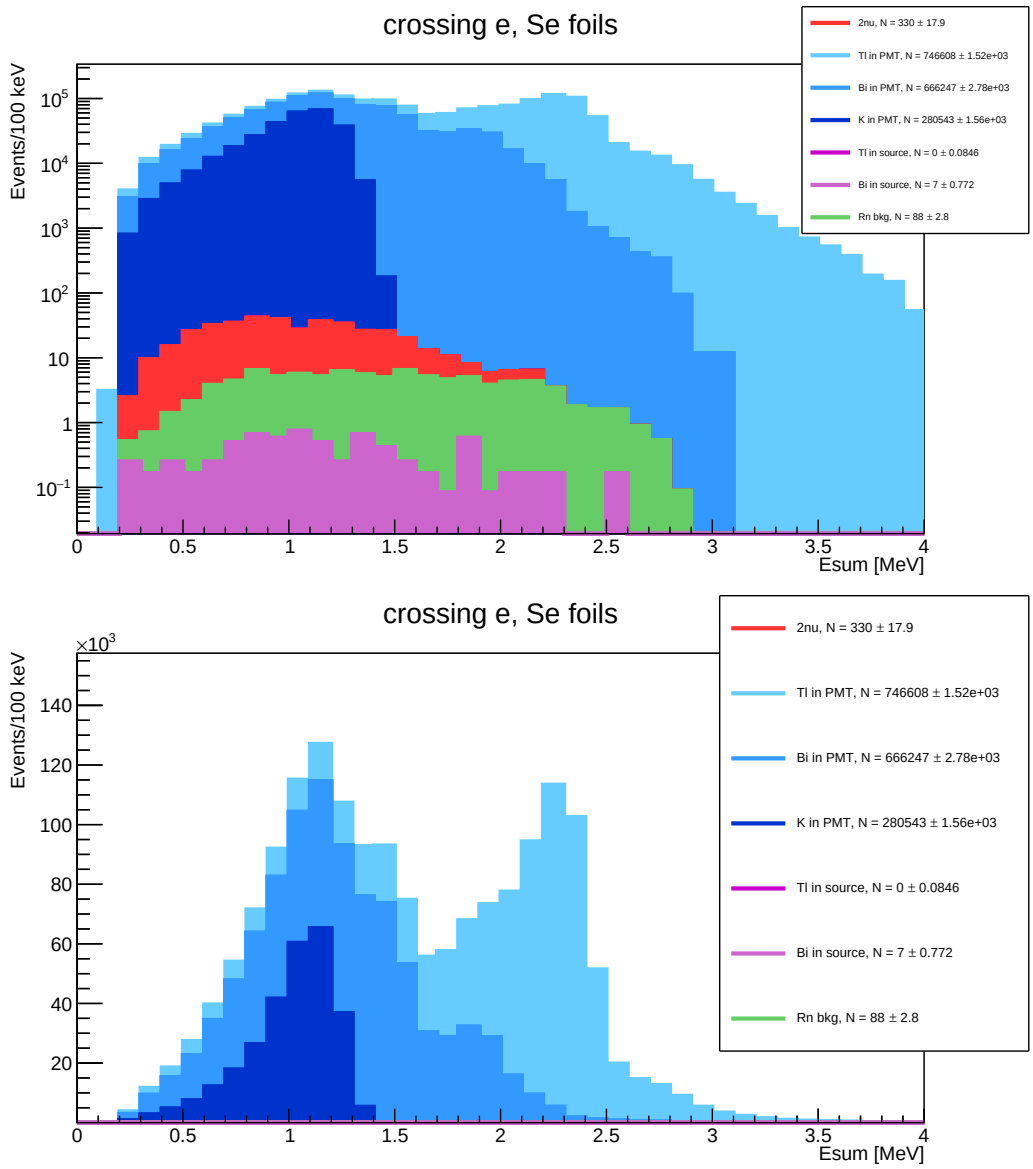

Figure 3.8: Sum energy distribution of the two electron deposits in the calorimeter blocks for the crossing electron channel. *Top:* Logarithmic scale. *Bottom:* Linear scale. The external background isotopes have a dominant contribution compared to the events from the ^{82}Se source or from radon.

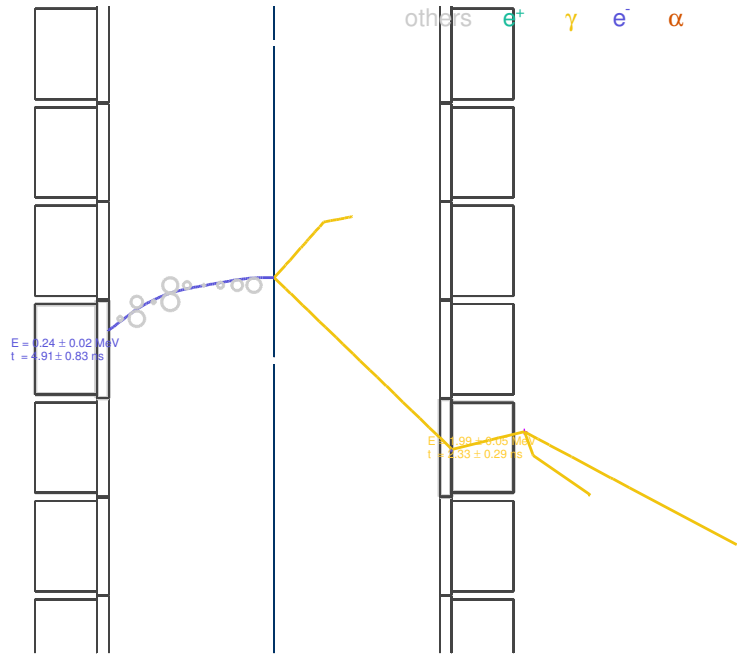

Figure 3.9: Display of a simulated ^{208}Tl event in the PMT glass reconstructed in the γe-ext channel. The ^{208}Tl emits several γ on the right and one of these gammas creates an electron via Compton scattering in the source before leaving the detector on the top.

uncertainty on the measurement of this background should be around 0.13 %.

3.3.3 Impact of the external background of the Se $2\nu\beta\beta$ half-life measurement

As explained previously, the main issue with the external background is its impact on the ^{82}Se $2\nu\beta\beta$ half-life measurement. The latter can be calculated using equation 3.4. $N_{2\nu\beta\beta}$, the number of $2\nu\beta\beta$ events measured, is computed by subtracting the number of background events to the total number of events measured in the 2e-int channel:

$$N_{2\nu\beta\beta} = N_{total} - (N_{int\ bkg} + N_{Rn\ bkg} + N_{ext\ bkg}) \tag{3.5}$$

With N_{total} the total number of events measured in the 2e-int channel and $N_{int\ bkg}$, $N_{Rn\ bkg}$, $N_{ext\ bkg}$ the number of internal, radon and external background events expected in the 2e-int channel. These numbers of background events are obtained by using the activities measured in dedicated channels.

One of the uncertainties on the number of external background events expected in the 2e-int channel is induced by the measurement of the activities of the isotopes contributing to this background. These activities are measured more accurately in the crossing electron channel as seen in section 3.4.1. One of the uncertainty on these activities come from the statistical uncertainty on the number of crossing electron events which is 0.08% according to simulations.

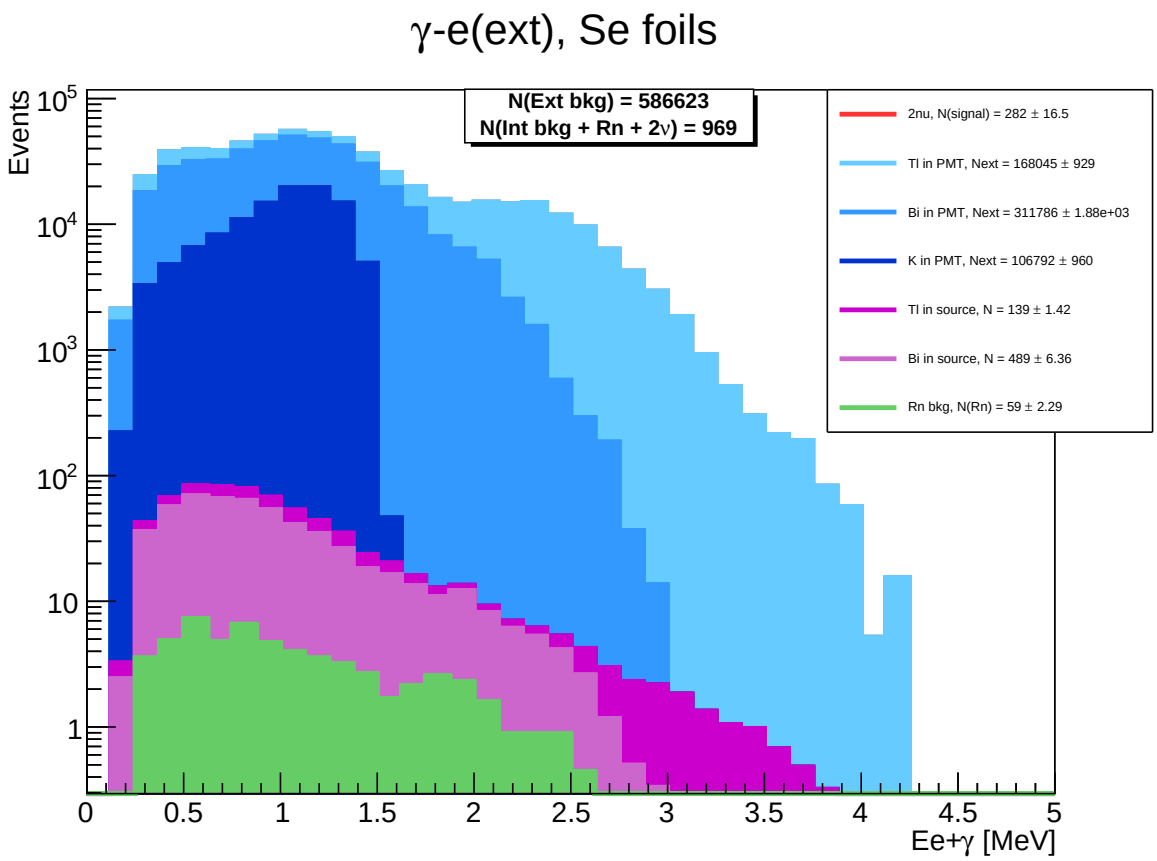

Figure 3.10: Energy sum distribution of the gamma and the electron in the 1e1γ-ext channel. The contributions from the external background isotopes are dominant compared to the events from the source or from radon.

As no data is available yet, a first impact of the external background on the ^{82}Se $2\nu\beta\beta$ half-life measurement can be evaluated using this uncertainty value on the external background measurement. The systematic uncertainty on the ^{82}Se $2\nu\beta\beta$ half-life measurement due to the external background is evaluated with the error propagation method. To make the calculation, the number of expected events $N_{2\nu\beta\beta}$ and $N_{ext\ bkg}$ are taken from the 2e-int distribution presented in figure 3.6. The calculated uncertainty on the number of expected external background events, due to the statistical uncertainty on the measured activities, leads to an error of 0.003% on the ^{82}Se $2\nu\beta\beta$ half-life measurement which is very low. This is of course very optimistic but it shows that the large statistics acquired in the crossing electron and γe-ext channels will allow to reduce the impact of this background on the ^{82}Se $2\nu\beta\beta$ half-life measurement. To be more accurate, the large statistics in these channels will allow to measure the external background for each strip to adapt this uncertainty with the source foil position.

In NEMO-3 [35], the systematic uncertainty on the external background measurement for ^{82}Se was $\pm$10% which is much higher than the statistical uncertainty on the measured activities of the isotopes of 0.08%. Indeed, this takes into account the systematic uncertainty of the fit of the background model to the data and the differences in activities found between different channels.

The total systematic uncertainty for the measurement of the ^{82}Se $2\nu\beta\beta$ half-life was evaluated to be 6.3%. The uncertainty due to the external background activity estimation was 0.6%. The most important systematic uncertainty for this measurement was due to the uncertainty on the detector acceptance, reconstruction and selection efficiency. It was estimated with calibration runs with ^{207}Bi sources whose activities were measured independently with HPGe detectors with a systematic error of 5%. For the SuperNEMO experiment, it should be reduced thanks to a new calibration of the ^{207}Bi sources.

3.4 Control of the external background with copper foils

Copper foils have been used in NEMO-3 in order to control the external background. As the copper is not a $\beta\beta$ emitter, all the events detected from these foils are from internal or external backgrounds or radon. The number of events detected in the 2e-int channel is not high enough to measure the external background accurately but it is an interesting way to control it independently from the internal backgrounds coming from the ^{82}Se foils.
The expected background has been simulated on copper foils to see if they should be efficient to detect enough external background in the SuperNEMO detector in 2.5 years. The goal of this study was also to estimate the best thickness for these Cu foils. The more external background events are detected on these copper foils, the more accurate it is to control it.

3.4.1 Events expected in the two electrons channel in copper foils

To start the simulation, a first approximation of NEMO-3 Cu foil thickness of 63 μm has been used. Copper has been simulated in all the source strips as the possible positions of these foils were to be determined. Then the obtained results have been normalised considering a quantity of 0.41 kg of Cu which corresponds to two strips of Cu in the demonstrator. This is a reasonable quantity compared to the 36 strips of ^{82}Se needed to keep a good sensitivity on the measurement of its $0\nu\beta\beta$ half-life.

The Copper foils are not totally radiopure. Internal backgrounds in the NEMO-3 Cu foils have been measured using the single electron channel. The internal activity of β emitters can be determined by fitting the energy spectra in different channels as it was done in NEMO-3 for the single electron channel (see figure 3.11). The activities measured in NEMO-3 have been considered for this study as the same Cu foils should be used for the demonstrator:

- A(^{214}Bi int) = 0.16 mBq/kg
- A(^{208}Tl int) = 11 μBq/kg
- A(^{40}K int) = 3.7 mBq/kg
- A(^{234m}Pa int) = 1.5 mBq/kg

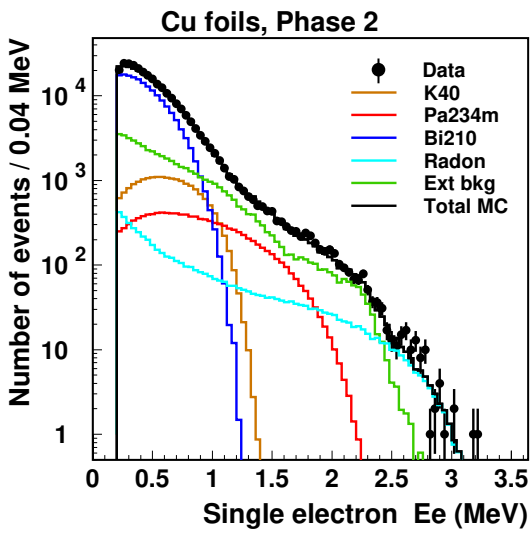

Figure 3.11: Single electron energy spectra for copper in NEMO-3 phase 2 data [33].

The external background has to be controlled in the two electron internal (2e-int) channel as it is the one in which $\beta\beta$ is searched for. An estimation of the internal and radon backgrounds in this channel for the Cu foils has been done. Figure 3.12 shows that radon and thallium contributions can be neglected. After

2.5 years, around 86 events of internal background are expected.

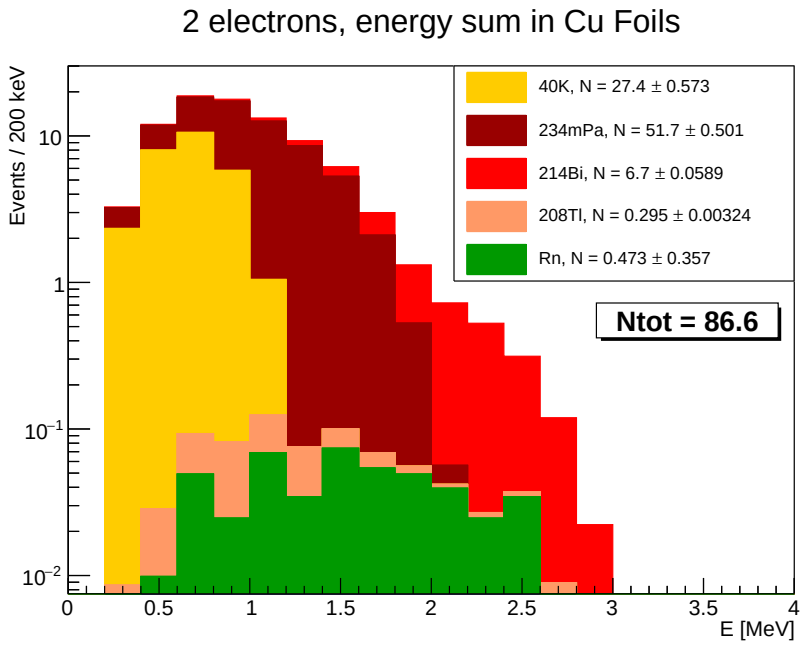

Figure 3.12: Sum energy distribution of the two electrons for the isotopes that contribute the most to the internal background and radon background.

In figure 3.13, the contributions to the external background in the 2e-int channel are shown. As said previously, the 8″ PMT backgrounds dominate largely compared to the 5″ PMT backgrounds. The contributions of the latter can thus be neglected in the external background simulation. In total, 95.6 events of external background are expected in this channel which allows to control it with a statistical uncertainty of around 10%. This number of events is in the same order as the number of internal background events. Fortunately, the measurement of the activities of the Cu foils can be done using other channels as it was seen like the single electron channel. It is thus useful to add Cu foils in the detector as there is some place available, in order to check the validity of the external background model.

3.4.2 Copper foil thickness study

The possibility to increase the Cu foils sensitivity to the external background by increasing their thickness has been investigated. The larger the Cu foil thickness, the higher the probability for an external gamma to undergo Compton scattering or for an electron to undergo Möller scattering. However, an increase of the foil thickness also leads to a decrease of the probability of a particle to escape the foil.

A possibility of stacking several foils together has been considered. Copper foils of thickness of 63, 126, 189 and 252 μm have been simulated. The result in figure 3.14 shows that Cu foils are more sensitive to the external background with a

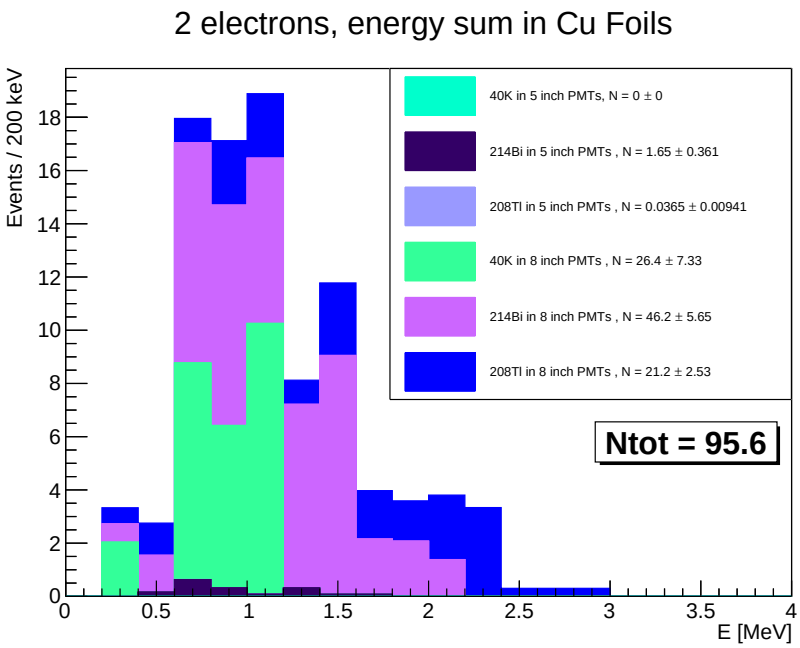

Figure 3.13: Sum energy distribution of the two electrons for all the isotopes that contribute the most to the external background.

thickness of 189 μm. The biggest increase in efficiency is between 63 μm and 126 μm. Thus it was advised to install double or triple thickness Cu foils.

Unfortunately, because of mechanical constraints in the construction, it has been decided to use only one layer of copper foils. Some tests have been done and it showed that it is very difficult to keep several layers together without full gluing. The NEMO-3 Cu foil thickness has been measured more precisely during the preparation of the foils for the demonstrator and is equal to 57.5 μm. As this study shows, it should decrease a bit the sensitivity to the external backgrounds compared to the 63 μm thick Cu foils which has been simulated. Still, these foils should detect around 90 events of external background and thus be sensitive enough to it in the 2e-int channel with a precision of around 10%.

3.5 Conclusion

This work gave a first overview of the impact of the external background in the demonstrator results. With a reduction of the internal and radon backgrounds, it will be much more important than in the previous NEMO-3 experiment. Fortunately, the crossing electron and γe-ext channels used in NEMO-3 analysis will also be useful for the demontrator analysis to measure precisely this external background. A statistical uncertainty of around 0.1% is expected for the measurements of these backgrounds in these channels. Unfortunately, the demonstrator did not start data taking before the end of the thesis so the simulations that I have done will be used for future analysis.

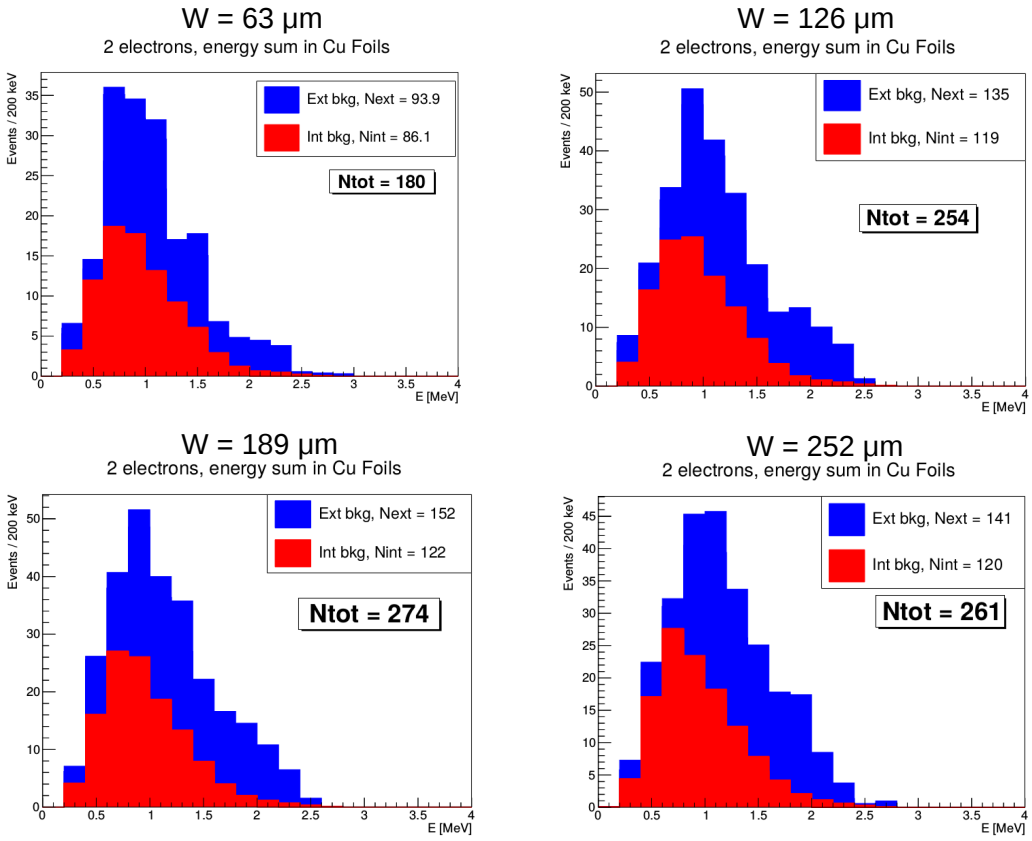

Figure 3.14: Energy sum of the two electrons reconstructed in the 2e-int channel for different thickness (w) of the copper foils.

This work has also been very useful to decide on the utility to install copper foils in the demonstrator. It has shown that in 2.5 years, two strips of NEMO-3 copper foils would be sensitive enough to the external background to control its model independantly from the ^{82}Se internal background model with around 10% of accuracy.

Part II

SoLid

Chapter 4

The SoLid experiment principle and SM1 prototype results

4.1 Introduction

As already presented in chapter 1, several experimental anomalies, including a recent revaluation of the reactor $\overline{\nu}_e$ spectrum, have put our understanding of neutrino oscillations and reactor flux models into question. New measurements at the closest possible distance to a reactor are required to shed light on these questions. To investigate the hypothesis of an oscillation toward a sterile neutrino, detectors must have fine energy and spatial resolution to measure the $\overline{\nu}_e$ flux as a function of distance and energy. The SoLid experiment addresses this issue with a highly segmented detector and an important work on the improvement of the energy resolution.
In this chapter, the SoLid technology will first be presented with its neutrino source and the environmental backgrounds. Then the SM1 prototype that took data just before the beginning of this thesis will be introduced as well as its results.

4.2 Antineutrino source: the BR2 reactor

4.2.1 Antineutrinos from nuclear reactors

In a pressurized water reactor (PWR), the reactor fuel, composed of rods of enriched uranium dioxyde, produces heat by fission. The fission process is self-sustained as the core isotopes fission under a high neutron flux releasing themselves neutrons. To create fissions efficiently, the neutrons have to be moderated. In PWR, the moderator is pressurized water. It also serves as the primary coolant. The pressurized water circulates and transfers the heat to a secondary circuit via a steam generator. The generated steam flows to turbines that spin an electric generator.

Nuclear reactors are huge sources of $\overline{\nu}_e$. A one gigawatt reactor produces around 2×10^{20} $\overline{\nu}_e$ per second. The reactor fuel is composed of fissile elements, mostly ^{235}U, ^{238}U, ^{239}Pu and ^{241}Pu. Each fission can lead to very different fission fragments. The fission products undergo cascades of β^- decays until they reach stability. In average, they undergo three β^- decays, emitting $\overline{\nu}_e$ each time.

The prediction of the $\overline{\nu}_e$ flux from the reactor is necessary to know the number of expected events in the detector. However it is not trivial as it has to take into account each possible fission fragment and β branches. To get the fission rates, a simulation of the neutrons flux inside a detailed 3D model of the BR2 core is run with MCNPX [86]. The MURE code is then used to track the burn-up of the fissile products [100].

There are two possibilities to compute the $\overline{\nu}_e$ spectrum: the summation method or the conversion method.

The summation method is based on individual fission product beta decay summation as presented in eq. 4.1.

$$N_\nu^{emit}(E) = \sum_n Y_n(Z, A, t) \times \sum_i b_{n,i}(E_0^i) P_\nu(E_\nu, E_0^i, Z) \tag{4.1}$$

with n a fission product, i a β-branch of the n fission product, $N_\nu^{emit}(E)$ the number of $\overline{\nu}_e$ expected, $Y_n(Z, A, t)$ the cumulative fission yields obtained from simulations with the MURE code which takes into account the reactor power evolution, $b_{n,i}(E_0^i)$ the branching ratios of the ith β decay branch with endpoint E_0^i and $P_\nu(E_\nu, E_0^i, Z)$ the normalized shape function of each β decay. It requires knowledge on the thousands of β branches involved and the weighting factors of the fission products which is called fission yields. The spectra obtained may lack of accuracy because of the uncertainties on some β decay end-points, the branching ratios or some effects like the impact of weak-magnetism corrections. This leads to systematic uncertainties of the order of 10% [101].

The conversion method relies on the electron spectra obtained at ILL reactor at Grenoble in the 80's. These electron spectra are converted into antineutrino spectra. The number of $\overline{\nu}_e$ emitted with the conversion method is calculated as in equation 4.2:

$$N_\nu^{emit}(E) = \int_0^{t_{run}} \frac{P(t)}{\sum_k \alpha_k(t) E_k} \times \sum_k \alpha_k(t) S_k(E) dt \tag{4.2}$$

with k the fissile isotope (^{235}U, ^{238}U, ^{239}Pu,^{241}Pu), $P(t)$ the reactor power, α_k the number of fissions of the kth isotope at the considered time, E_k its mean energy released per fission and $S_k(E)$ the corresponding $\overline{\nu}_e$ spectra normalized to one fission.
The first part $\frac{P(t)}{\sum_k \alpha_k(t) E_k}$ corresponds to the fission rates computed with MURE. The second part uses $S_k(E)$ which corresponds to the converted $\overline{\nu}_e$ spectra obtained with the revisited conversion of ILL β spectra for ^{235}U and ^{239,241}Pu. For ^{238}U, the recent measurement of its β spectra done by Haag et al. [81] is used. The conversion of β spectra to $\overline{\nu}_e$ spectra is obtained by adjusting with several virtual β branches the measured electron spectra and then convert it to $\overline{\nu}_e$ spectra for each branch using the conservation of energy (equation 4.3):

$$E_{\overline{\nu}_e} = E_{0,b} - E_e \tag{4.3}$$

With $E_{\overline{\nu}_e}$ the antineutrino energy, E_e the electron energy and $E_{0,b}$ the maximum available energy of the branch b.

The two methods are used in the SoLid experiment to cross-check the results.

4.2.2 The BR2 reactor

The antineutrino source of the SoLid experiment is the Belgian Research Reactor 2 (BR2) located at the SCK·CEN research center in Mol, Belgium. It is a research reactor of the type PWR (Pressurized Water Reactor). It is involved in several programs like research on materials or the production of medical isotopes and semi-conductors.

The BR2 reactor operates at an average thermal power of 60 MW. It is active roughly half a year in periods of around a month. The SoLid experiment should benefit of 150 days of reactor on per year during 3 years. This research reactor has several advantages to conduct a sterile neutrino experiment.

- The core provides a very high neutrino flux thanks to its twisted geometry. It is also very compact, compared to power reactors, with a diameter of around 0.5 m and a height of 1 m. This gives a good precision on the emission point of the $\overline{\nu}_e$ compared to the baseline studied of a few meters. It is an advantage because a good resolution on the $\overline{\nu}_e$ travelling distance is necessary to investigate an oscillation towards sterile neutrinos.
- The reactor fuel is highly enriched, at 93.5%, in ^{235}U. Thus the reactor $\overline{\nu}_e$ flux prediction will be easier as contributions from the other fissile isotopes can be neglected.
- The detector can be placed at the same floor as the reactor core and as close as 5.5 m from the latter thanks to the layout of the reactor hall (fig. 4.1). It will also benefit from a very effective shielding against the reactor induced background.

4.3 The IBD reaction

Like most of the experiments that detect antineutrinos from reactors, including the neutrino discovery experiment in 1956, SoLid detection uses the inverse beta decay (IBD). It is the charged current interaction of a $\overline{\nu}_e$ with a proton:

$$\overline{\nu}_e + \mathrm{p} \rightarrow \mathrm{e}^+ + \mathrm{n} \tag{4.4}$$

IBD is the highest cross-section interaction at the reactor neutrinos energy (3 MeV in average). It also allows to measure the $\overline{\nu}_e$ energy. The antineutrino signature

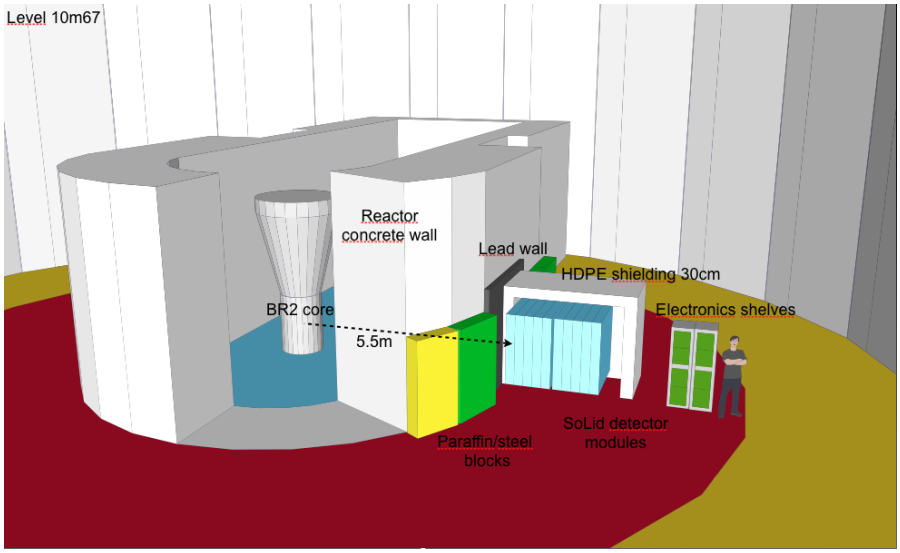

Figure 4.1: Picture of the BR2 reactor and the installation of the SM1 detector in the reactor hall.

from IBD is the detection in time delayed coincidence of a positron and a neutron. As the nuclear recoil can be neglected, the measurement of the positron energy gives a good estimate of the $\overline{\nu}_e$ energy using the formula 4.5

$$E_{\overline{\nu}_e} \sim E_{\mathrm{e}^+} + (m_n - m_p) \tag{4.5}$$

with m_n and m_p the neutron and proton masses.
However, the IBD process can only happen if the $\overline{\nu}_e$ has an energy higher than a relatively high threshold. This threshold value depends on the nucleus on which the $\overline{\nu}_e$ interacts. For hydrogen nucleus, as the proton is considered to be free, the energy threshold can be computed as in equation 4.6:

$$E_{\overline{\nu}_e}^{thresh} = \frac{(m_{e^+} + m_n)^2 - m_p^2}{2m_p} \simeq 1.806 \ \ \mathrm{MeV} \tag{4.6}$$

With m_{e^+}, m_n and m_p the positron, neutron and proton masses.
The detected $\overline{\nu}_e$ energy spectrum is obtained by multiplying the IBD cross section with the reactor $\overline{\nu}_e$ energy spectrum as shown in fig. 4.2.

The positron deposits very quickly its energy inside the detector before annihilating with an electron creating two gammas of 511 keV. The positron and the 2 annihilation gammas are detected within a few nanoseconds. This is called the prompt event of the IBD signal. The energy deposits of the two annihilation gammas can be detected separately from the positron energy deposits thanks to the high segmentation.

The neutron has to thermalise before it can be captured tens of microseconds later. Its signal is called the IBD signal delayed event. Neutrons travel a few cm before being thermalised. The IBD signal is thus very correlated in time and space which is an advantage to reduce backgrounds in segmented detectors.

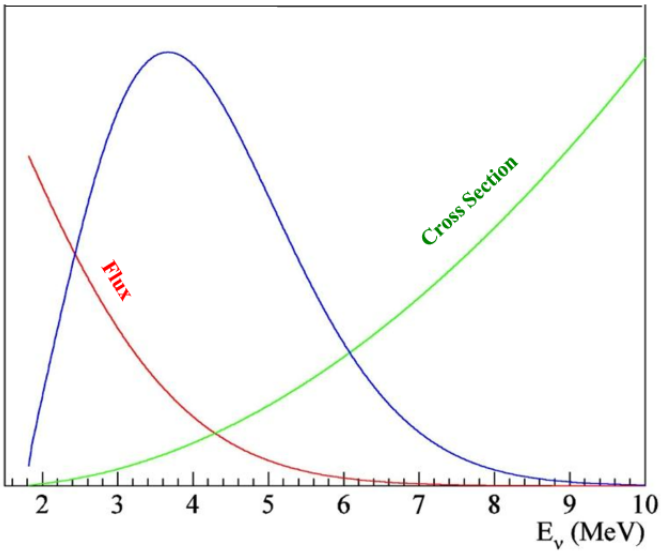

Figure 4.2: The energy spectrum of the detected $\overline{\nu}_e$ in blue that comes from the folding of the IBD cross section in green and the reactor $\overline{\nu}_e$ energy spectrum in red [93].

4.4 The backgrounds

All the processes that can mimic a prompt and a delayed signal in the detector are backgrounds for the experiment. They have different origins, they can come from the reactor, cosmic rays or natural radioactivity.

4.4.1 Cosmic background

Like most of the research reactor experiments, the SoLid detector can not be installed underground. Its overburden is approximately of 10 meters water equivalent. The cosmic-ray background radiations are thus large. Neutrons, muons and hadrons produced in the atmosphere interact in the detector orders of magnitude more frequently than the reactor $\overline{\nu}_e$. Backgrounds can be created by muon spallation (when the collision of a muon with matter expels nucleons) and neutron activation (a stable nuclei captures a neutron and can then decay to a more stable nuclei). A spallation neutron entering the detector can produce a proton recoil that mimic the prompt event before thermalising and being captured tens of microseconds later producing a delayed signal. Slow neutrons are also an issue as they can contribute to the accidental background if a gamma ray is detected in coincidence for example.

4.4.2 Reactor background

Many particles are emitted from the reactor core, in addition to neutrinos, but fortunately, their fluxes are attenuated by the reactor pool. Yet some of them can reach the detector and interact in it. The most troublesome reactor backgrounds are fast neutrons and high energy gammas. The latter can also be produced by activation from the reactor fast neutrons on materials.

4.4.3 Natural radioactivity

Natural radioactivity can induce background in the detector. The ^{6}Li sheets used to detect neutrons could contain ^{214}Bi contamination. The ^{214}Bi comes from the ^{238}U chain and is also a background for the SuperNEMO experiment. When ^{214}Bi decays to ^{214}Po, it can emit an electron with a $Q_\beta = 3.27$ MeV which corresponds to possible IBD prompt energy. The ^{214}Po then decays towards ^{210}Pb with a half-life of 163.6 μs by emitting an α particle. This can reproduce the neutron capture scintillation signal in the ^{6}LiF:ZnS(Ag). The ^{214}Po half-life is similar to the neutron thermalisation and capture time and the α emitted with an energy of 7.69 MeV can excite the ZnS. These ^{214}Bi decays background are called BiPo in the following.

4.4.4 Background measurement

The backgrounds can be either accidentals or correlated. For accidental background, the prompt and the delayed events have different origins. For the correlated background, however, they have the same origin.

Because of the high rate of singles (i.e. events not correlated with other events) like gamma rays or muons, there is a high probability to find an electromagnetic (EM) single in time coincidence with a ZnS signal. These accidentals events have to be measured precisely. Their topology is different from IBD signals: they are more separated in space and have often lower prompt energy. The accidentals may vary a lot depending on the reactor operations. It has to be measured for each data taking period. An off-time window method is used to measure their rate. The delayed signal (neutron signal) timestamp is shifted by a time window (1 μs for example) so that the prompt and the delayed signals can not be correlated (fig. 4.3). A negative time window can also be used by looking for a neutron signal before the prompt event.

The correlated background is due to prompt and delayed events produced via the same mechanism. The dominant contribution to this background is expected to be fast neutrons which produce proton recoils during thermalisation. The correlated cosmic background is measured using data from reactor off periods. The accidentals for this period have also to be subtracted using the previous off-time window method. The fast neutrons from the reactor are neglected as they are slowed down by 50 cm of water from the reactor pool and the concrete wall. A normalization factor has to be applied to these data in order to match the correlated background

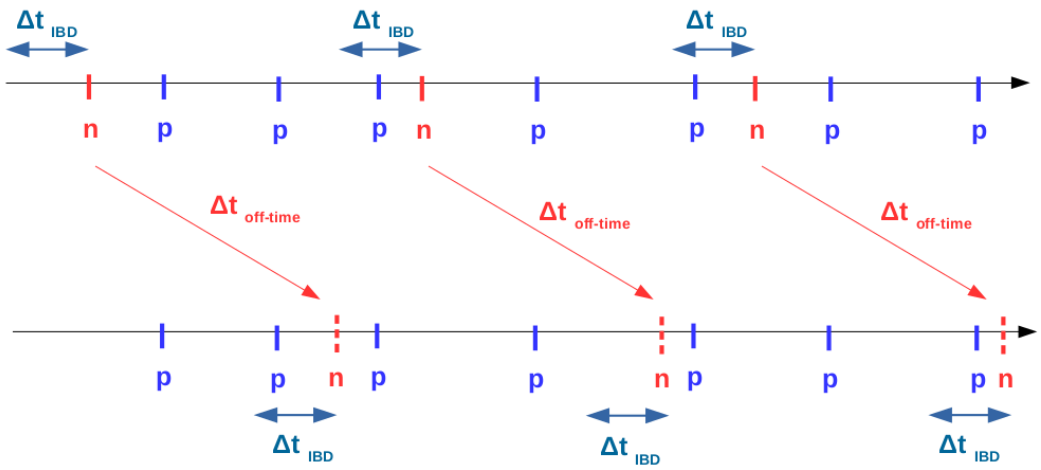

Figure 4.3: Illustration of shifted time window method to measure accidental background. Top: example timeline of prompt (in blue) and neutron (in red) events. Bottom: The timestamp of the neutron is delayed by $\Delta t_{off-time}$ so that coincidences that are formed within Δt_{IBD} are not correlated anymore.

for reactor on data. It depends on the pressure variations in the atmosphere for example as pressure affects the muon or fast neutron rates.

4.5 SoLid technology

The main features of the SoLid technology are the high segmentation and the use of 2 separate solid scintillators to detect the neutron and ionising particles. To achieve this, the SoLid detector is made of thousands of Polyvynil-Toluene (PVT) cubes with thin sheets of ^{6}LiF:ZnS(Ag) laying in one or two sides of each cube. The PVT scintillator is sensitive to ionising particles while the ^{6}LiF:ZnS(Ag) scintillator is sensitive to neutrons (fig. 4.4). Tyvek wrapping is used to isolate cubes from each other in order to know where the interactions took place and to improve light collection. The scintillating light is brought by wavelength shifting optical fibers crossing the cubes to Silicon Photon Multiplier (SiPM).

4.5.1 Scintillator detection principle

The PVT scintillator is used to detect ionising particles such as positrons, electrons, gammas or muons. It also serves as a proton target for IBD interactions and an effective moderator for neutrons. The PVT has the advantage to have high light yield and optical transparency.
The cubes are made of ELJEN Technology EJ-200 PVT based plastic scintillator and have a side of 5 cm. To place the optical fibers for light extraction, square grooves are cut in the sides of the cubes.

The positron interaction in the PVT gives a sharp electromagnetic (EM) signal (tens of ns). It deposits most of its energy in the cell where the IBD interaction took place. The positron annihilates quickly with an electron producing two 511 keV γ. These γ often deposit their energy in cubes away from the positron cube. A simulation study has shown that around 30 % of annihilation gammas have a Compton interaction in the same cell where annihilation occurred. In many cases, the positron energy can thus be reconstructed independently of the γ energies thanks to the high segmentation.

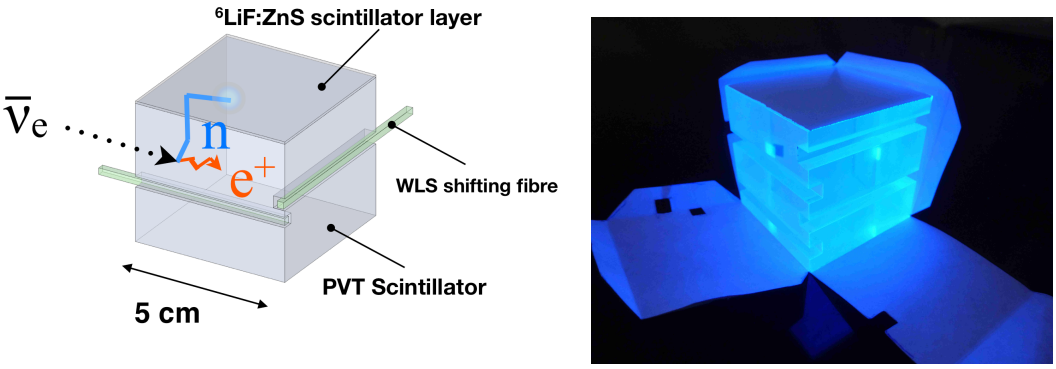

Figure 4.4: *Left:* Schematic of a neutrino interaction inside a SoLid cube. *Right:* Picture of the two scintillators under UV light: the PVT cube and the ^{6}LiF:ZnS(Ag) sheets with their Tyvek wrapping.

The ^{6}LiF:ZnS(Ag) scintillators from Scintacor are used to detect neutrons via the breakup reaction 4.7:

$$n +^6 \mathrm{Li} \rightarrow \alpha +^3 \mathrm{H} \tag{4.7}$$

The ^{6}LiF:ZnS(Ag) scintillators have a square surface of 5×5 cm and a thickness of 250 μm. The α and ^{3}H particles can travel a few tens of μm and thus excite surrounding ZnS grains. This produces scintillation light in the ZnS(Ag). Neutrons are likely to be detected in a neighbouring cell of the IBD interaction as they have to thermalise in the PVT before they react efficiently with ^{6}Li.

The two scintillators have different signal shapes: the ZnS(Ag) scintillation signal is longer in duration (tens of μs) than the PVT signal and its waveform shows several peaks. The neutron capture produces a high density of ionisation energies that lead to a large population of excited states that deexcites to the ground state with many different transitions. This signal shape difference between the two scintillators allows distinguishing neutrons from electronic scintillation signals with pulse-shape discrimination using the ratio of integral over maximum amplitude of the waveforms (fig. 4.5).

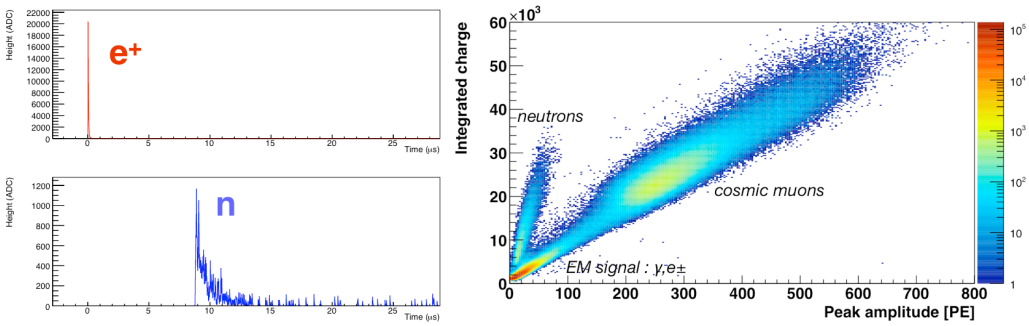

Figure 4.5: Example of an IBD signal with the positron and the neutron signals in time delayed coincidence. A pulse shape discrimination allows one to distinguish easily the neutron and the positron signals.

4.5.2 Wavelength shifting optical fibers

The SoLid technology uses wavelength shifting optical fibers to extract the light from the scintillators. The scintillating photons of both scintillators are emitted with a wavelength in the blue visible spectrum around 420 nm. They are captured by optical fibers after internal reflections inside the PVT cube. The Tyvek wrapping around the cube enhance light collection by reflecting photons and avoids light leakage to neighbouring cubes. The incident light from the wavelength shifting optical fibers is re-emitted as green photons. The wavelength is shifted to change the refraction angle in order to keep the light in the fiber.

Each cube is coupled to two or four fibers depending on the SM1 or Phase I detector. The fibers are in the horizontal and vertical direction in order to localise the signals in specific cubes. The fibers are readout by Silicon Photon Multipliers at one end. To decrease the light loss, the other end of the fiber is covered with a reflective material.

4.5.3 Silicon photomultipliers

The sensors that readout the scintillating light are MPPCs (Multi-Pixel Photon Counter) also known as SiPM (Silicon Photon Multiplier) from Hamamatsu. The SiPMs employed are Hamamatsu S12572-050 [82]. They can perform single photon counting. They are formed of an array of 60×60 avalanche photo-diodes within an active area of 3×3 mm^2. The photo-diodes are connected in parallel with a quenching resistor for each one. These resistors are used to limit the signal current and decrease it quickly.

The avalanche photo-diodes operate in Geiger mode. An over-voltage (the difference between the set voltage and the break-down voltage), is applied to the sensor to create a depletion region without charge carriers. When incident photons enter the photo-diode silicon, they may create electron-hole pairs in the depletion region.

These electrons and holes move towards the respective P-doped or N-doped regions. The charge carriers collide with atoms when travelling in the crystal lattice. The resultant ionisation creates more electron-hole pairs that can cause further ionisation resulting in a divergent pixel avalanche. The signal amplitude is discretised as it depends on the number of pixels that have been triggered. The gain of the SiPM reflects the number of charge carriers per incident photon. It is linear with the over-voltage.

SiPMs represent several advantages:

- They have a fast response
- They are relatively cheap. Given the high segmentation of the detector, many sensors are required so it is important that their price is not too important.
- They do not require high voltages
- They have a high photon detection efficiency (PDE) with a peak sensitivity at a wavelength around 400 - 500 nm. The PDE can be increased by increasing the over-voltage. For 12572-050P SiPMs, the PDE is around 25% for an over-voltage of 1.5 V (fig. 4.6).

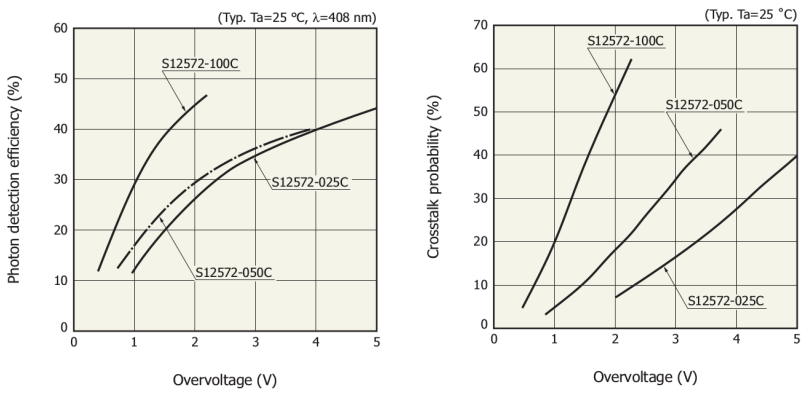

Figure 4.6: *Left:* Photon detection efficiency vs over-voltage for 3 different sensors. SoLid SiPMs are S12572-050. Right: Cross-talk probability vs over-voltage.

Some effects can however influence the SiPM signals:

- The cross-talk (fig. 4.6) is a phenomenon that happens when a pixel is fired by another pixel even though no incident photon crossed it. It is due to an electron from the avalanche that emits a UV photon which travels to another pixel thus firing it. It increases artificially the signal amplitude by $\sim 10\%$ and degrades the energy resolution.
- The quenching is due to two photons arriving one after the other on the same pixel. The second photon can not increase the signal amplitude. The photon counting is thus falsified. However, due to the low number of photons arriving from the SoLid detector, it can be neglected.

- Dark counts come from thermal agitation of electrons that create a pixel avalanche. This effect is random and very high for SiPMs (typically 1000 kHz at 20°C). It depends on the over-voltage and the temperature so the phase I detector has been cooled down to decrease it.

4.6 SoLid sensitivity

To study SoLid sensitivity to the neutrino experiment anomalies, and the existence of a sterile neutrino, a software, SoLid Oscillation analysis framework (SoLO), has been developed. It generates signal and backgrounds to make an oscillation analysis.

In the study performed with SoLo, the reactor is considered to run at 60 MW and only $\overline{\nu}_e$ from the dominant ^{235}U isotopes are taken into account. It is assumed that the signal to background ratio (S:B) will be equal to 3 and the IBD detection efficiency will be 30%. The background shape is taken from SM1 data. In this simulation, the SoLid detector has a mass of 1.6 tons and a relative energy resolution $\sigma_E = 14\%/\sqrt{E_{vis}}$ with E_{vis} the detected energy.

The IBD candidate events are binned in energy and in distance. The measured number of events is fitted with a model of signal, that assumes oscillations towards a sterile neutrino, and background. A gaussian χ^2 that compares the measurement with the fit is then minimized for various $\sin^2(2\theta_{ee})$ and Δm^2_{41} values. The exclusion regions for 150 and 450 days of reactor on are shown in fig.4.7. The 95 % confidence limit (C.L.) are shown in brown for 150 days of reactor on data (around 1 year) and in dashed black line for 450 days of reactor on data (around 3 years). The black solid line is the 3σ line for 450 days of reactor on data. The global best fit point from experimental anomalies is within the exclusion region.

4.7 SM1 prototype

The goal of the prototype SoLid Module One (SM1) was to demonstrate the feasibility of the technology. The SM1 detector had a scintillator mass of 288 kg and was in direct line of sight with the center of the reactor core at a distance of 6 m. Its commissioning started in early 2015 while the reactor was operational at nominal power of 60 MWth. After a few days of data taking, the reactor shut down for 1.5 year for an overhaul of its Beryllium fuel core matrix. Long reactor off runs were taken to study the background as long as some calibration runs.

4.7.1 SM1 mechanical design

The SM1 detector was composed of 9 planes of 16 × 16 cubes. Each 2304 PVT cube had one ^{6}LiF:ZnS(Ag) scintillator sheet placed on the face perpendicular and closest to the reactor. The cubes and the ZnS sheet were wrapped in DuPont Tyvek of 75 g/m^2. They were all coupled to two perpendicular fibers so each plane had 32 fibers (16 verticals and 16 horizontals) to bring the scintillating light to

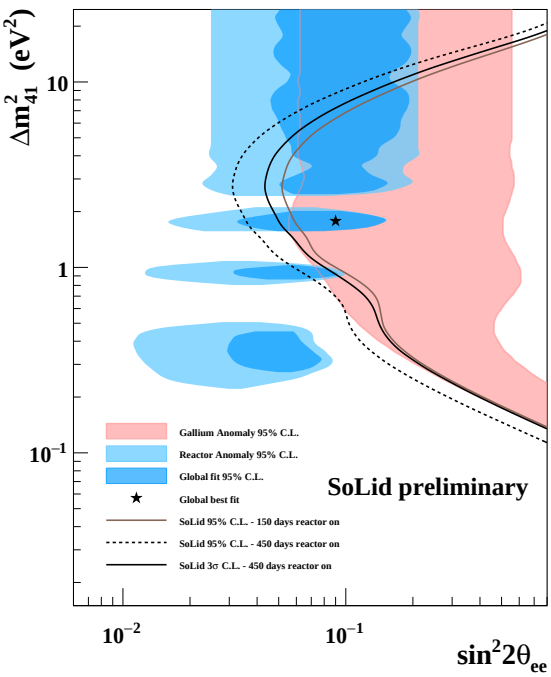

Figure 4.7: SoLid sensitivity plot.

SiPMs. The fibers were single clad wavelength shifting fibers of type BCF-91A from Saint-Gobain. Each plane of cubes sat in an aluminium frame. High Density Polyethylene (HDPE) bars of 2 cm were used between the aluminium frame and the cube array to compensate for cube misalignment and to reflect escaping neutrons (fig. 4.8). Sheets of HDPE with 2 mm thickness were also placed on each face of the plane. Holes in the HDPE bars and the aluminium frame allowed the fibers to go outside the frame so that SiPM could be attached to them. The SiPMs, Hamamatsu S12572-050P, were coupled to the fibers with optical grease. A thin aluminium tape covered the other end of the fibers to reflect the light. The position of aluminium tape and SiPM (bottom or top for example) are alternated from a fiber to another to increase the detector uniformity. The 9 planes were stacked together perpendicularly to the reactor neutrinos direction (fig. 4.9). A passive shielding of 9 cm thick HDPE surrounded the detector. The detector was protected from the reactor backgrounds by the concrete reactor pool wall and an additional 20 cm lead wall.

4.7.2 SM1 electronics readout

In the SM1 detector, each 288 fibers was coupled to one SiPM. Custom analogue front-end boards (AFE) coupled to a front-end trigger board with an FPGA formed the read-out system. One AFE was coupled to the 32 SiPMs of one plane in order to digitise and amplify the signals. The analogue signals from the SiPM were digitised at a rate of 65 MHz. The waveforms readout lasted for 256 samples, i.e.

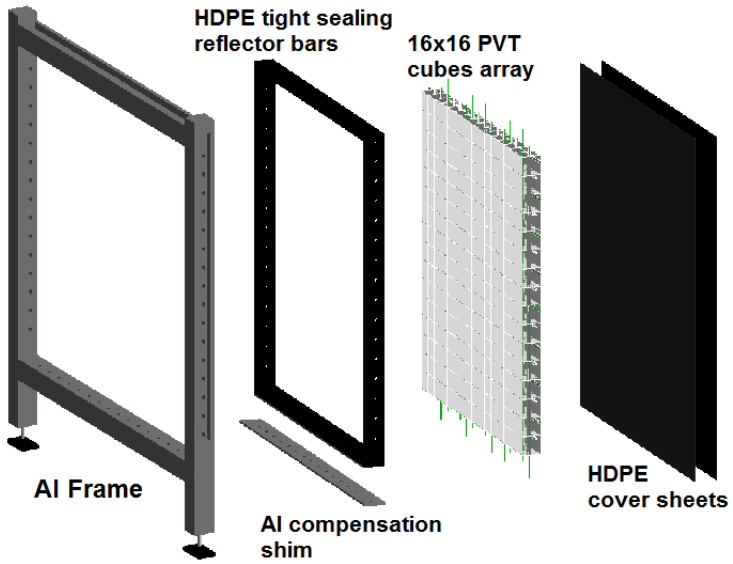

Figure 4.8: Picture of a decomposed plane of SM1. The 16 × 16 PVT cubes with Li sheets form the detection plane. Optical fibers (in green) cross the cubes array. HDPE bars all around the cubes array reflect neutrons. The planes lay in aluminium frames and are covered with HDPE sheets.

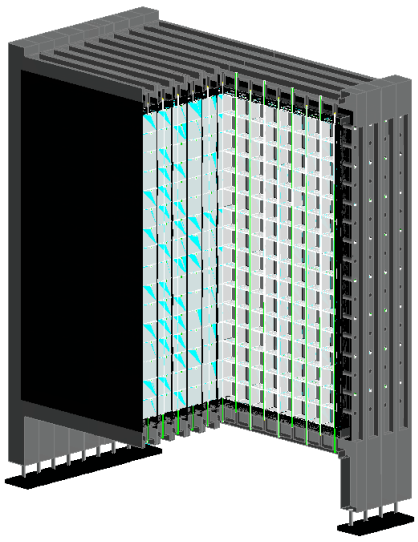

Figure 4.9: Picture of the SM1 detector with its 9 planes

4.096 μs. The first 25 samples were prior to the trigger time. It allowed to study the structure of the ZnS signal to discriminate neutrons from EM events. The AFE also provided a programmable bias voltage for each SiPMs. It was necessary to get the same photon detection efficiency for all the sensors as they had different breakdown voltages. The SiPM over-voltage was set at 1.5 V to get a photon detection efficiency of around 25%. The cross-talk probability was measured to be 18%. The SiPMs were equalised online at the level of 20%. Further offline calibration allowed to have a better detector uniformity with an achieved RMS of 3%. The dark count rate was evaluated to be of 0.5 MHz per channel.

A coincidence threshold trigger required coincidence between 2 fibers in a same plane within 48 ns. To get a manageable data rate, the amplitudes of the two channels had to be above a threshold of 6.5 SiPM photo-avalanches (PA) resulting in an average energy cut-off of roughly 500 keV.

4.7.3 Event reconstruction

There are three types of objects reconstructed in SM1: electromagnetic signals (EM) cubes, neutron cubes and muon tracks.

EM cubes

An EM cube signal requires a coincidence between one horizontal and one vertical fiber. The amplitude of these PVT signals is proportional to the energy deposited in the reconstructed cube. The amplitude of each peak is corrected from variations in the light detection efficiency, the gains of the channels and the attenuation effects in the optical fibers.

Neutrons

The neutrons interactions in the ^{6}LiF:ZnS(Ag) scintillator can be distinguished from EM signals in the PVT with pulse shape discrimination. The integral over amplitude ratio (IoA) of the waveforms is used to distinguish the two scintillation types. For each channel the IoA is corrected by the ratio of its mean value over the median of all values across the detector. The PID (Particle Identification) variable used to identify neutrons is then computed by adding the corrected IoA of both vertical and horizontal channels. Examples of PID distributions with two peaks well separated can be seen in figure 4.10. An AmBe neutron calibration source shows that neutron rich data have PIDs at high values. Reactor on, off and ^{60}Co runs are depleted in neutrons and show lower PIDs. Signals with a PID > 10 are considered as neutron signals and those with a PID < 10 are considered as electromagnetic (EM) signals.

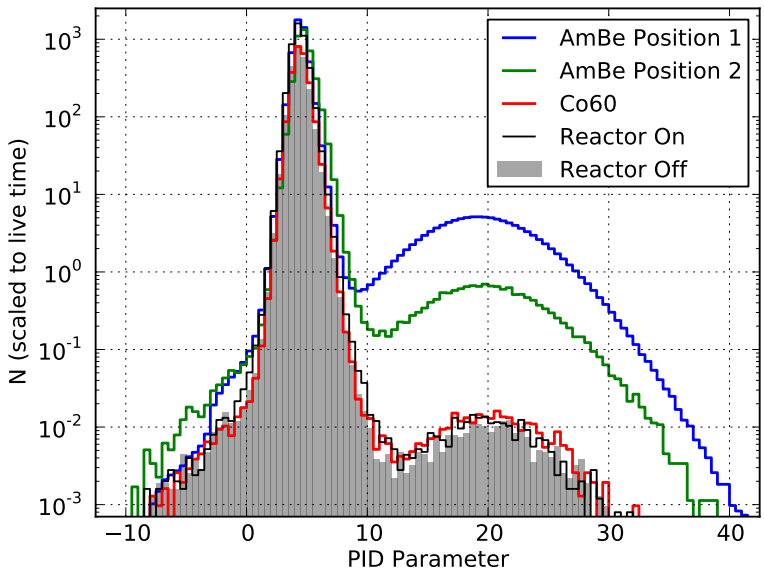

Figure 4.10: Neutron discrimination plot for several data sets. The reactor ON, OFF and ^{60}Co (black, grey and red) runs are depleted in neutrons. The AmBe calibration data (blue and green) have an increased neutron rate compared to the other data sets.

Muons

Muons can be tracked easily thanks to the high segmentation of the SM1 detector (fig. 4.11). Muon tracks are used for calibration as their pathlength through each cube can be reconstructed.

It is very important to tag muons efficiently since muon spallation can be an important background for IBD reconstruction. Crossing muons are tagged as events for which more than 8 MeV was deposited in the PVT. According to simulation, it represents 93% of muons crossing the detector. For the remaining low energy deposits by muons, it has been shown that half of them involve at least one outer edge cube of the detector. The outer layer of cubes is thus used as a veto region.

4.8 SM1 results

4.8.1 Neutron detection study

Neutron capture efficiency

In order to know the number of detected IBD events, the neutron detection efficiency, ϵ_n, had to be measured. It depends on the neutron capture probability on ^{6}Li (ϵ_{Li}) and the neutron signal detection probability (ϵ_{det}):

$$\epsilon_n = \epsilon_{Li} \times \epsilon_{det} \tag{4.8}$$

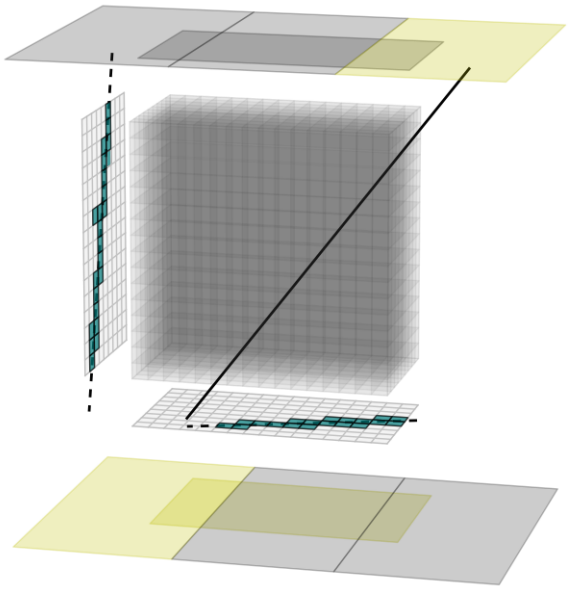

Figure 4.11: Example of a muon track in SM1 prototype. The blue squares show the clusters of triggered channels in the two SiPM arrays. The black straight line shows the result of the linear regression to reconstruct the positions of the cubes in which the muon deposited energy.

The neutron capture probability on ^{6}Li (ϵ_{Li}) is a function of the thickness of the ^{6}LiF:ZnS(Ag) screen and the ^{6}Li to ZnS ratio. This efficiency is raised by the fact that a neutron can cross the same screen several times through multiple scattering on protons of PVT cubes. However, it can also be captured on the hydrogen of the PVT or escape the detector through air gaps. The neutron capture efficiency has been estimated using Geant4 and MCNPX simulations to:

$$\epsilon_{Li} = 52.01 \pm 0.53(stat) \pm 3.06(syst)\% \tag{4.9}$$

The scintillation in the ZnS(Ag) screen produces up to 175 000 optical photons per neutron capture. However lots of these photons are lost due to attenuation in the screen, light losses in the wavelength shifting optical fibers or absorption in the PVT. In the end, around a hundred of photons distributed in over tens of microseconds reach the SiPM.

The neutron signal detection probability depends on the trigger efficiency and the off-line reconstruction efficiency. It has been estimated using calibration data with neutrons from an AmBe source. ϵ_{det} is computed as the ratio of the number of neutrons identified in each cube per the expected number of neutrons from simulation. The average value for cubes across the detector gives:

$$\epsilon_{det} = 5.51 \pm 0.02(stat) \pm 1.21(syst)\% \tag{4.10}$$

This was much less than expected. The final neutron detection efficiency is thus:

$$\epsilon_n = 2.87 \pm 0.65\% \tag{4.11}$$

To understand this low neutron detection efficiency, a test bench has been built [16]. A PVT cube with a ^{6}LiF:ZnS(Ag) screen was coupled to a PMT on the opposite face of the screen. The scintillating light was also readout by 8 cm long wavelength shifting fiber with an attached SiPM. The PMT signal was used as a trigger to get a nearly unbiased neutron amplitude spectrum. The result is the red curve in figure 4.12. A substantial part of the events are below 3 PA amplitude. The blue curve shows the neutron amplitude spectrum when using the SM1 trigger condition. The coincidence threshold trigger had to be set high enough to get a manageable data rate because of SiPM dark noise for example. It can be seen, however, that it decreases a lot the neutron detection efficiency. Furthermore, the required time delayed coincidence of 48 ns between fibers in X and Y was too strict and the light yield not high enough. A more complex triggering method that exploits the neutron waveform properties has thus been implemented for the Phase I detector. In addition, the light yield has been increased thanks to R&D done during my PhD thesis (see chapter 5).

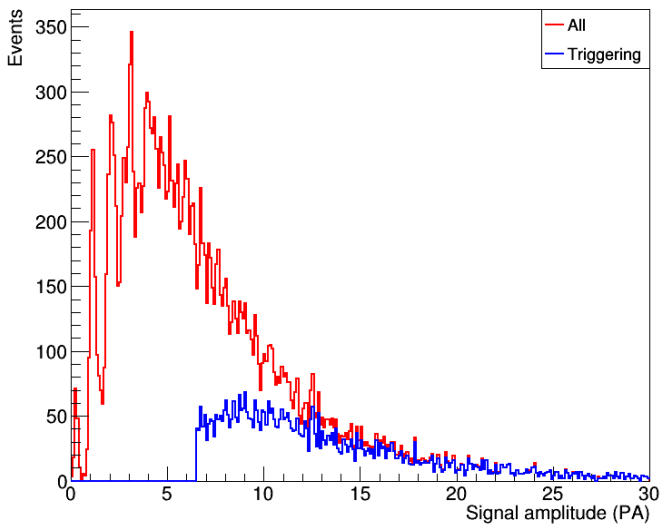

Figure 4.12: Neutron peak amplitude distribution from SiPM coupled to a fiber and a cube cell. The red curve has been obtained by triggering on a PMT signal. The PMT is directly coupled to a PVT cell on the opposite face of the ^{6}LiF:ZnS(Ag) screen. The blue distribution has been obtained by using the SM1 trigger conditions.

Neutron thermalisation and capture time

The neutron thermalisation and capture time, τ_n, represents the time needed for a neutron to thermalise by scattering before being captured by a ^{6}LiF:ZnS(Ag). It has been estimated using AmBe sources. The prompt event is defined as a proton recoil and the delayed event is the neutron capture on ^{6}Li. The measurement result gave $\tau_n = 91.56 \pm 1.07$ μs which is in agreement with the Geant4 simulation value

of $\tau_n = 91.45 \pm 0.94$ μs .

To decrease the neutron capture time in the Phase I detector, it has been decided to add a second ^{6}LiF:ZnS(Ag) screen for each cube. According to simulations, it will increase the neutron capture efficiency on ^{6}Li up to 66% and decrease the mean capture time down to 65 μs.

4.8.2 Light yield and energy resolution

The PVT cubes have been calibrated on site using crossing muons. The track length of the muons in each cube can be obtained by fitting the muon track through the detector with a straight line as shown in fig. 4.11. Thanks to the high segmentation of the detector, it has been shown with simulations comparisons that the precision of reconstructing the pathlength through a cube is around half a centimeter. The ratio of the integral of the waveform over the reconstructed pathlength is computed and corrected for each channel (fig. 4.13). It can be compared to the theoretical value for a minimally ionising muon in the PVT, 1.776 MeV/cm, in order to calibrate all the cubes in energy.

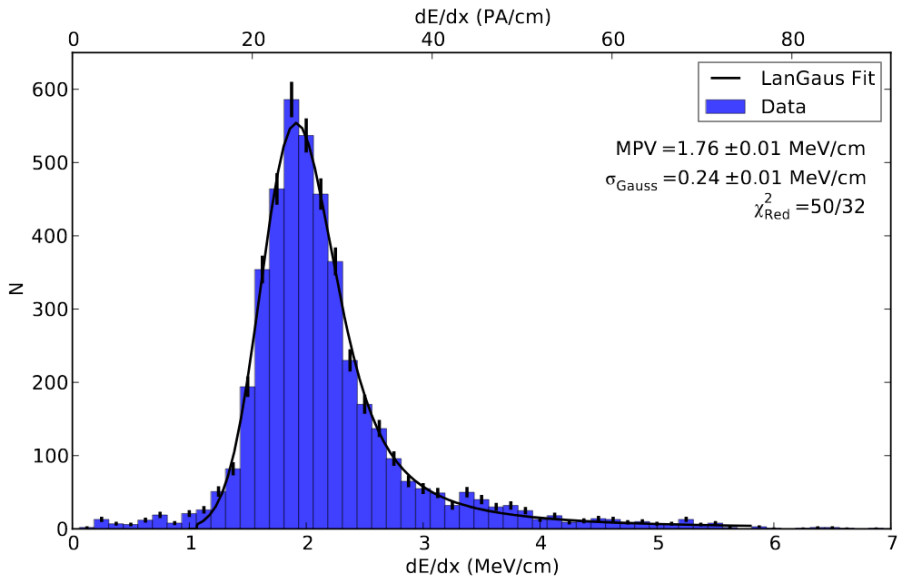

Figure 4.13: dE/dx distribution for a single cube after one day of data taking (reactor off). The top scale uses the number of SiPM pixel avalanches, and the bottom scale shows the energy scale per length from comparisons with simulation .

The measured light yield was in average 12 PA per fiber and per MeV of energy deposited in the same cube. This corresponds to an energy resolution of 20% for 1 MeV electrons.

4.8.3 Detector response

Several types of events induced by backgrounds are easily detectable and can be used to check the detector response and the object reconstruction.

After muon events

Michel electrons are high energy electrons created by a stopping muon that decays in the detector. They are identified in the detector by selecting a tagged muon followed by an EM event with $E_{vis} > 3.5$ MeV within a [1, 26] μs time window. To estimate the accidental background, a shifted time window of 1 ms is used. After the subtraction of the flat accidental background, the muon lifetime is measured by fitting the $\Delta t_{\mu e}$ with an exponential function (fig. 4.14). The value found is $\tau_\mu = 2.281 \pm 0.002$ $(stat)$ ± 0.052 $(syst)$ μs. The good agreement with the theoretical values (2.197 μs) [25] demonstrates the efficicency of the time reconstruction.

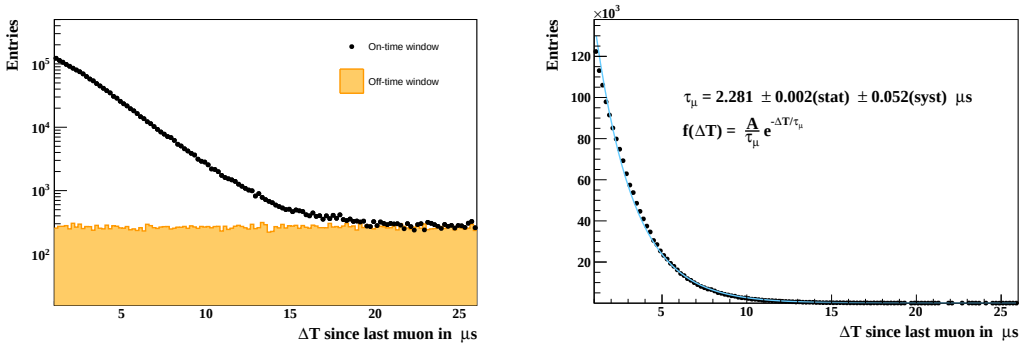

Figure 4.14: *Left:* Distributions of the time difference between a muon and a Michel electron for the on-time (black dots) and off-time (yellow) windows. *Right:* The muon lifetime is fitted using an exponential function after accidental subtraction.

Spallation neutrons constitute a background induced by muons. They are identified as a neutron following a tagged muon in a time window of [1, 1001] μs. A shifted time window of 1 ms is used to estimate the accidental background. By fitting the result obtained in fig. 4.15 with an exponential and a flat background, the neutron capture time is found to be $\tau_n = 89.81 \pm 2.63$ $(stat)$ μs. It is in agreement with the simulation and AmBe calibration values. It validates the time synchronisation of the detector readout as well as the particle identification.

BiPo events

BiPo can be identified by selecting events with a prompt and a neutron in the same cube, a time difference between neutron and prompt smaller than 1 ms and a prompt energy greater than 0.6 MeV and smaller than 3 MeV. After applying a muon veto cut, the distribution of Δt between prompt and neutron can be fitted with two exponentials plus a constant (fig. 4.16). The first exponential corresponds to fast neutron contamination and the constant corresponds to the accidental rate.

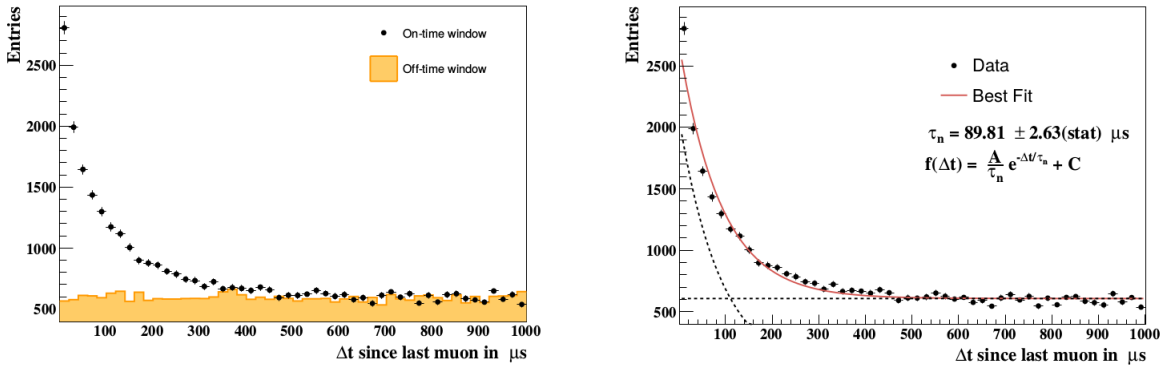

Figure 4.15: Distribution of the time difference between a muon and a neutron for the on-time (black dots) and off-time (yellow) windows. By fitting the distribution with an exponential and a flat distribution, the obtained neutron capture time found is: $\tau_n = 89.81 \pm 2.63(stat)\mu$s

The second exponential corresponds to the BiPo decays. After the fit, the second exponential gives a ^{214}Po half-life of 167 $\pm$ 34 μs which is consistent with the expected value of 164.3 μs.

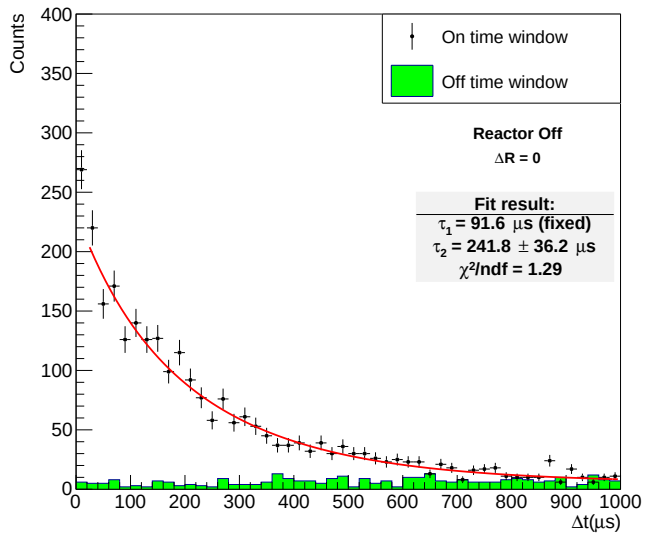

Figure 4.16: Distribution of the time difference between a prompt and a neutron for the on-time (black dots) and off-time (green) windows. By fitting the distribution with two exponentials and a flat distribution, the fraction of BiPo events can be measured and compared to the fraction of cosmic or spallation neutrons.

4.8.4 IBD search

IBD event selection

IBD-like interactions in the detector are tagged as an EM cube followed by a neutron cube in delayed time coincidence. To select specifically IBD interactions and reject backgrounds, several cuts have been applied.

Two types of background, accidentals and correlated, have been measured in order to study the efficiency of the IBD cuts to reduce them. The accidental rates and energy spectrum depend on the reactor operations. An off-time window analysis allows to measure the accidental background for reactor on and off conditions. It has been assumed that the correlated background does not change regarding the reactor operation by considering that no fast neutrons are induced by the reactor operating at full power thanks to the shielding. Thus it is estimated using reactor Off data.

Using the previous studies on the neutron capture time, the time difference between the prompt and the neutron Δt was required to be < 220 μs. To take advantage of the high segmentation of the detector, cuts on the distance between the prompt and the neutron have also been set: $\Delta r =]0, 2]$ cubes. Furthermore, a multiplicity cut requiring that the prompt is localised in maximum 2 cubes side by side is used. As lots of background events have low energies, the prompt energy E_{prompt} has to be within [1, 8] MeV. A muon veto is finally set. The time between any IBD candidate and any muon, $\Delta t_{IBD-\mu}$ must be > 250 μs. The efficiency of these cuts to reduce background is shown in fig. 4.17. The preselection data set contains coincidence pairs using timing information alone. All these cuts allow to reduce the accidental background by almost a factor 100 and the correlated background by a factor 10. According to the IBD event simulation, the relative signal efficiency is 57% (without taking into account the neutron detection efficiency).

Unfortunately, because of the small reactor On data set (50 hours) and the low neutron detection efficiency, only 10 $\pm 1(stat)$ $\overline{\nu}_e$ events were expected to be observed which is too low compared to the number of background events. The prompt energy distribution for the accidentals and correlated backgrounds as well as for the IBD simulated events are shown in fig. 4.18. The number of observed events is 10 $\pm$ 18 with a signal over background ratio of 1:30.

Correlated background components

The different correlated background contributions have been measured with the 578 hours of data reactor off by using the same cuts to select IBD events except for the distance between the prompt and the neutron. The accidentals were estimated by using a negative time window of -450 μs and their contribution was substracted. The distance between neutron and EM cubes (ΔR) distribution was fitted using the simulated shapes for the combined atmospheric and spallation neutron background (FN) and the BiPo background to estimate the fraction of each correlated back-

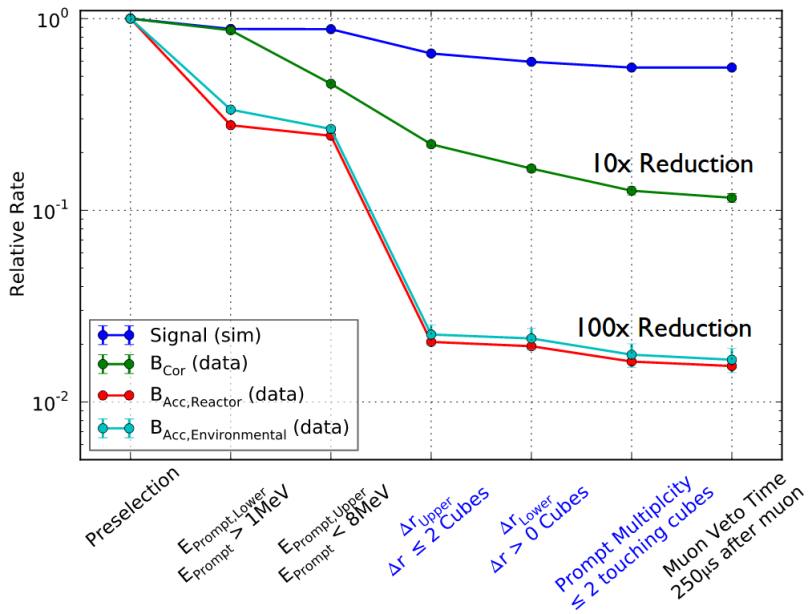

Figure 4.17: Signal and Background relative rates for each selection cut applied sequentially. The relative rates are obtained by normalising to the number of EM-neutron signals pairs reconstructed in delayed time coincidence. The topological cuts in blue are applied last.

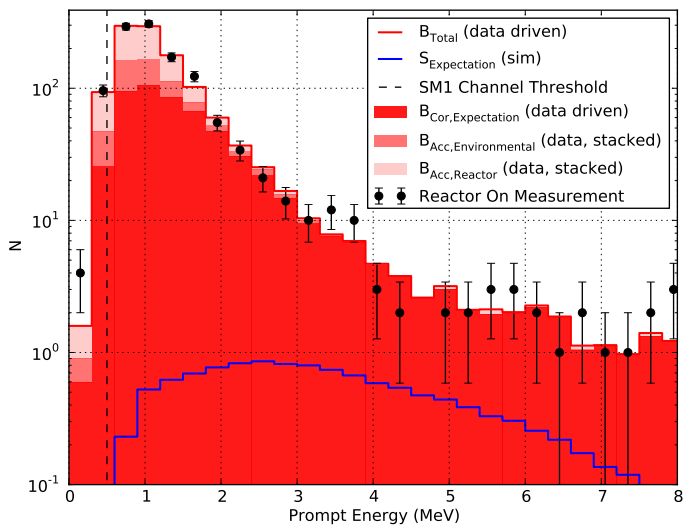

Figure 4.18: Comparison between data and background model for the prompt energy distribution of selected IBD candidates. The backgrounds for accidentals and correlated are obtained with respectively reactor on and reactor off data. The IBD events spectrum from simulation is shown in blue.

ground. By selecting events with $\Delta R = [1, 2[$ cubes, it was found that atmospheric and spallation neutrons are the dominant correlated background for the IBD event selection (fig. 4.19). With the BiPo, they contribute to about 82 % to the total number of IBD like events.

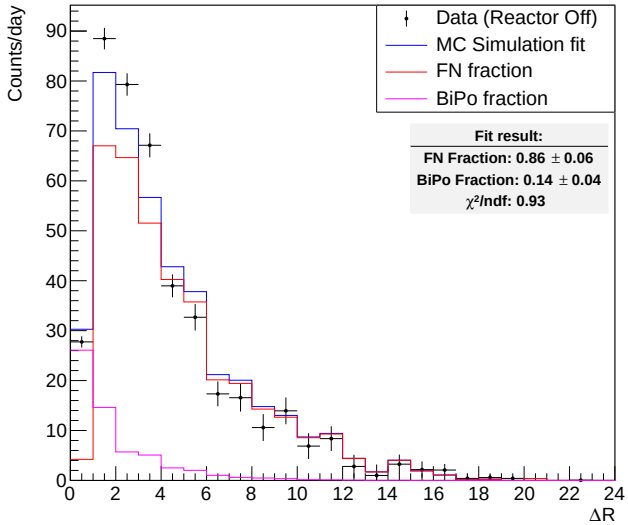

Figure 4.19: Comparison between data and background model for the prompt energy distribution of selected IBD candidates.

4.9 Conclusion

The first prototype detector SM1 has shown very interesting features, the particle identification and the segmentation of the detector have been very helpful to reject backgrounds.

At the beginning of my thesis, I have been involved in SM1 analysis to study the spatial distribution of the backgrounds and IBD cuts. I have also performed a cosmogenics search (^{9}Li and ^{12}B) that has shown that the SM1 detector was not sensitive enough to these backgrounds compared to the accidental rate.

To improve the energy resolution for SoLid phase I, an R&D program has started at LAL to test different designs of the detector cells in order to increase the light yield. This increase would also allow to lower the detection threshold to get a more efficient neutron trigger and improve the background rejection. Furthermore, a better detector uniformity would be helpful.

Chapter 5

Optimization of the light yield for SoLid phase I

5.1 Introduction

The initial goal of the test bench built at LAL was to test polystyrene scintillators from the previous NEMO-3 experiment to see if they could be used instead of buying new PVT scintillators for SoLid phase I. This test bench was also a convenient way to run several tests to look for improvements of the light yield. Indeed, in SM1, the energy resolution was 20% at 1 MeV (26 photo-avalanches (PA) per cube). For SoLid phase I, the goal was set to 14% at 1 MeV requiring to detect at least 50 PA per cube. To do so, the light yield had to be increased by a factor two.

The experience of the LAL group in the NEMO experiments has inspired the test bench setup we have built. Indeed, the trigger system used is similar to the trigger system of an electron spectrometer [98] used for the NEMO-3 and SuperNEMO experiments to qualify the plastic scintillators. The use of a ^{207}Bi source was also motivated by the regular deployment of this source to perform energy calibrations in the NEMO detectors.

In this chapter, the test bench setup will first be presented. Then the data analysis strategy and the results we have obtained to improve the light yield will be explained. Finally, the proposed configuration for the SoLid detector will be described as well as the control of the cube production.

5.2 Test bench setup

Our test bench is composed of four parts (figure 5.1): a radioactive source, an external trigger, the SoLid type scintillator and the electronics. It has been designed to be as flexible as possible in order to test various configurations for the SoLid scintillator cubes: wrapping, position and type of fibers, effect of the ZnS neutron screen, machining and cleaning of the cubes, SiPMs and fiber reflectors...

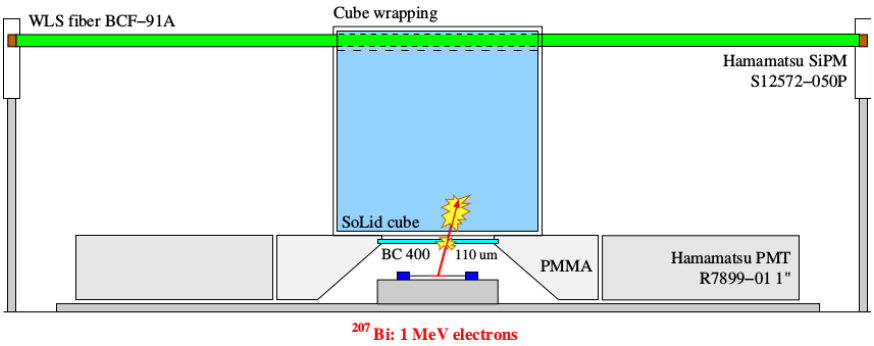

Figure 5.1: Schematic description of the scintillator test setup in the standard configuration used for most of the measurements. The calibration source, the PMTs and the scintillator cube are mounted on a rail in order to allow their translation all along the fiber.

5.2.1 The ^{207}Bi source

The detected reactor antineutrino spectrum extends from 1.8 to 8 MeV so a ^{207}Bi source is suited to study the energy resolution of SoLid cubes as it produces mono-energetic electrons at the same energy scale, around 1 MeV. We use a 37 kBq ^{207}Bi source which decays almost exclusively through electron capture to excited states of ^{207}Pb (figure 5.2) [49]. The decay is followed by ^{207}Pb deexcitation with γ-ray emission. Some of the gammas produced can convert in K, L or M shell conversion electrons (table 5.1). Most of these conversion electrons have an energy of 976 keV with 7.1 % probability, 1050 keV with a 1.8 % probability or 1060 keV with a 0.4 % probability. Regarding our energy resolution, we expect to observe only 1 peak at 995 keV average energy in our test bench. A second lower energy peak could be observed around 500 keV but it is less frequent and it is drowned in the Compton background of 1 MeV gammas.

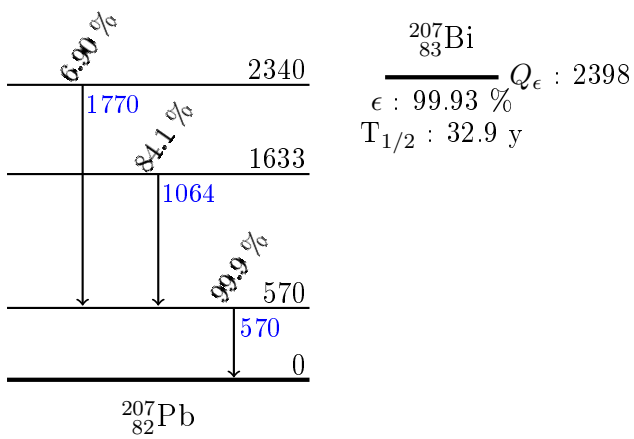

Figure 5.2: ^{207}Bi decay scheme to excited states of ^{207}Pb (from [49]). The energies are given in keV.

The ^{207}Bi source emits mainly gammas so an external trigger system is needed to select only the 1 MeV electrons entering the cube.

Table 5.1: Main internal conversion electrons emitted by the deexcitation of ^{207}Pb after ^{207}Bi decays (from [49]).

Transition	**Shell**	**Energy (keV)**	**Probability (%)**
$570 \rightarrow 0$	K	482	1.5
	L	555	0.43
	M	566	0.12
$1633 \rightarrow 570$	K	976	7.1
	L	1049	1.8
	M	1060	0.44
	N	1063	0.12

5.2.2 The external trigger system

An external trigger (figures 5.4 and 5.3) is used to trigger only on the 1 MeV conversion electrons and not on all the gammas from the source which are more frequent than conversion electrons and do not give a clear energy peak because of Compton interactions.

This external trigger is made of a thin scintillator BC 400 with a thickness of 110 μm, 2 light-guides in PMMA and 2 photomultiplier tubes (PMTs) from Hamamatsu (R7899-01 1") (figure 5.4). The optical coupling is ensured by optical grease (BC 630) between the thin scintillator and the light-guides and by an optical epoxy silicone rubber compound (RTV 615) between the light-guides and the PMTs. The electrons coming from the source are detected in the thin scintillator before entering the cube to be tested. No external background is expected as there is almost no trigger when we remove the source. This system has been designed to minimize the distance between the source and the scintillator in order to increase the source solid angle and reduce the energy loss by the electrons before entering the scintillator cube. We trigger in coincidence between the 2 PMTs at -5 mV.

Figure 5.3: The external trigger with the thin scintillator in the middle and the ^{207}Bi source .

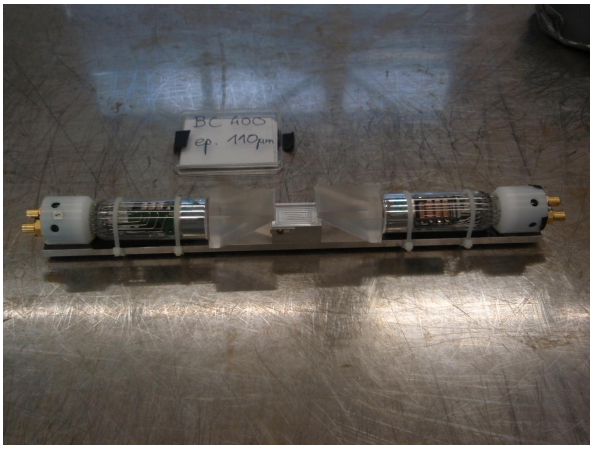

Figure 5.4: The 2 PMTs and the light-guides of the external trigger .

As shown in figure 5.5, without external trigger, the 1 MeV peak (around 40 PA) in the energy spectra (in blue) is drowned in the gamma spectra. Requiring trigger from the thin scintillator (in magenta), we select mostly 1 MeV electrons. The external trigger system can also be used as a veto (in cyan) to look at gamma response of the SoLid cubes. Gammas interact in the whole volume of the scintillator cube while electrons are contained in less than 1 cm^3 in front of the source. The Compton edge of the 1 MeV gammas can also be fitted. Less than 2% difference between the Compton edge fit and the 1 MeV peak fit is observed. It can thus be concluded that both interactions produce the same light yield as the systematic errors are around 5%. However, to test light yield improvements, the test bench has to be sensitive to small light yield variations so the electron 1 MeV peak is more suited than the gammas Compton edge.

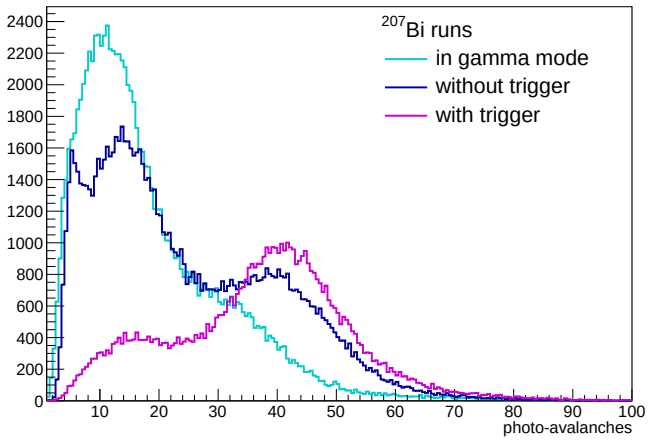

Figure 5.5: Comparison of the energy spectrum registered by the 2 SiPMs in different trigger modes. In blue is the spectrum in coincidence with the 2 SiPMs only, in magenta the spectrum in coincidence with the small scintillator and in cyan using the small scintillator as an electron veto. The 1 MeV peak can be seen around 40 PA.

5.2.3 The scintillator detector

The test bench is designed to study SoLid scintillator cubes and to make transformations in order to test light yield improvements very easily. It is a much more simple SoLid-like detector with only one cube. To be as close as possible to the SoLid detector, the light is guided by optical fibers to SiPMs. It allows us to study also the propagation of the light to the SiPMs and to look for improvements.

The detector (figure 5.1) is composed of:

- a cube wrapped in Tyvek with or without ZnS sheets
- one or several optical squared fibers with a length of about 90 cm and a width of 3 mm (we tested single clad and multi clad fibers: BCF-91A)
- one or two Hamamatsu SiPM (S12572-050P) at the end of the fibers (or mirrors, depending on the configurations we want to study).

The scintillator cubes and the triggering system are both mounted on a rail and can be moved with a light tight manual jack from outside the black box (figures 5.6 and 5.7). A support allowed to install a row of 16 cubes above the rails. With this design, the external trigger and the source could be translated along the fibers to measure the light attenuation as a function of the cube position along the fiber.

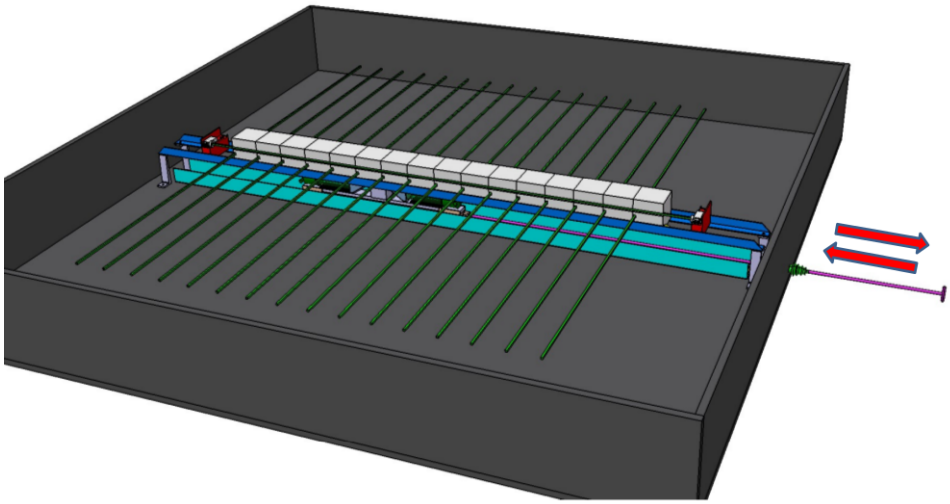

Figure 5.6: Picture of the test bench setup designed at LAL. The external trigger with the source is mounted on rails (in white) and can translate under the scintillator cubes (in grey) with their optical fibers (in green). The light is readout at the end of the fibers by SiPMs fixed in the red supports.

The detector had to be installed in the dark. We have built a black box made of black polyethylene with a volume of 120 x 120 x 15 cm^3 to be able to install optical

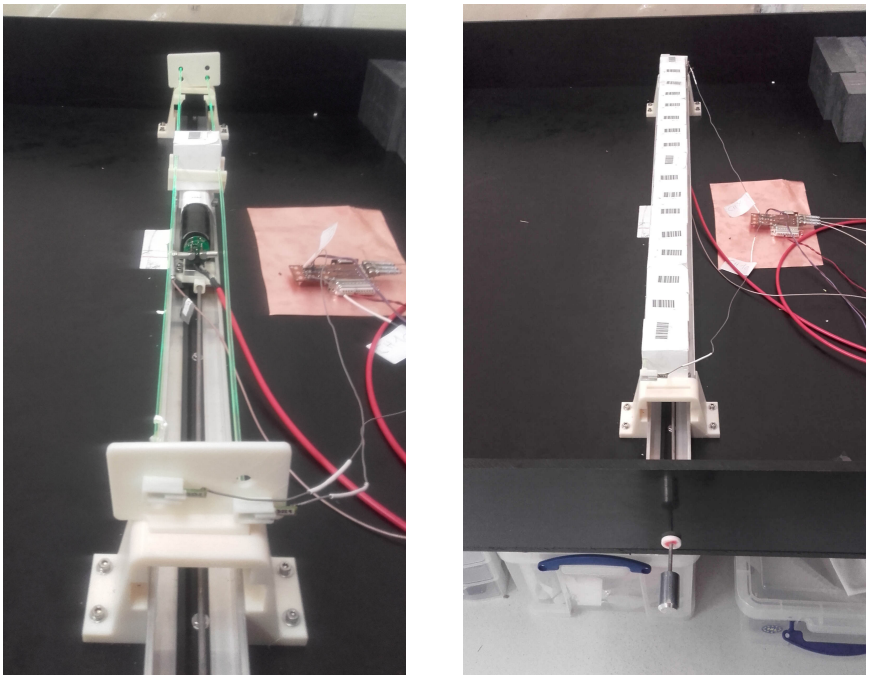

Figure 5.7: Pictures of the test bench setup. *Left*: a single cube with 2 fibers, *Right*: a row of cubes. The external trigger (PMTs) and the source can be moved thanks to the rails by pulling the jack.

fibers in 2 perpendicular directions as in SoLid.

Most of the measurements were taken with the same setup called standard setup (figure 5.1). It uses the external trigger and the ^{207}Bi source. The SoLid type detector in this standard configuration is composed of one cube, one multi-clad fiber and two SiPMs (one at each end of the fiber).

5.2.4 Electronics and Acquisition

The photo-detectors selected for SoLid are the Hamamatsu SiPMs S12572-050P with a photon detection area of 3×3 mm^2. These SiPMs (like in SM1) were soldered on custom-made PCBs installed in 3D printing supports also used to maintain the optical fiber. The optical contact between the SiPM and the fiber is ensured by optical grease (BC 630). The power supply and signal collection of the photo-detectors are provided by a single mini-coaxial cable per SiPM (figure 5.8).

The SiPM electronics board is a prototype board to supply voltage to the SiPM, amplify and shape the output signal. Two power supplies (EA-PSI 6150-01) are used to supply this board (figure 5.9). They have a resolution of 10 mV and a stability of 5 mV which is important to get stable measurements with SiPMs. One power supply is set at 5 V to amplify the signal and the other one is set to put an over-voltage of 1.5 V. An over-voltage of 1.5 V is used like in SM1 to maximize the SiPM gain and minimize the dark count rate. With this setup, the same voltage must be

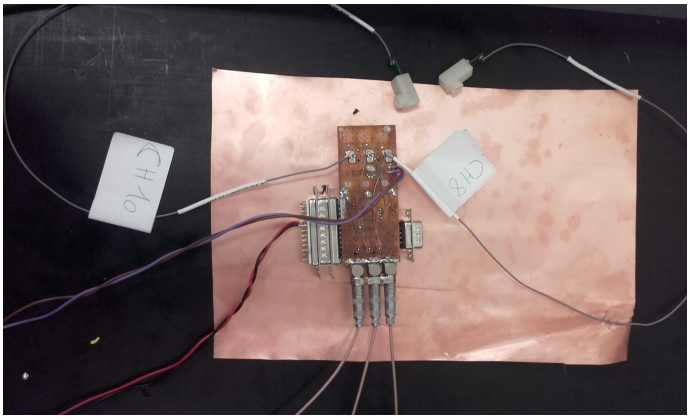

Figure 5.8: Picture of the SiPMs in their white support to maintain the fiber with their electronics board.

provided to the two SiPMs. We have selected the two photo-detectors to have close operating voltages: 67.40 and 67.46 V. We define the voltage as the good regime for the first one (instead of an average) in order to allow comparison with data sheets at least for this detector. The two PMTs of the external trigger are supplied with one high voltage power supply (Ortec 556) at -1400 V.

An electronic sampling board from the SuperNEMO experiment is used for the acquisition of the amplified SiPM signal and external trigger PMT signals. The WaveCatcher ASIC-based waveform digitizer module developed at LAL has 16 channels which digitise up to 3 GS/s over 1024 samples. It has an average noise of 0.7 mV RMS. Given the amplifiers and the single photo-avalanche signal amplitude, this noise is not negligible for the measurements but working with the charge of the pulses instead of amplitude gives good enough precision. We use 1.6 GS/s to have a good return to the baseline after the pulses.

5.2.5 Simulation of energy losses of the electrons

The energy deposited in the cube by the electrons has been simulated in order to determine the mean energy of the ∼1 MeV conversion electron peak from the ^{207}Bi source and to compute the energy losses in the thin triggering scintillator and the wrapping of the cubes. The setup has been simulated (figure 5.10) using the Bayeux [4] software developed for the simulation of the SuperNEMO experiment [46] and GEANT 4 [3].

This simulation indicates that only ∼25 keV (figure 5.11, left) is lost on average by the electrons in the triggering scintillator. This fraction of the mean electron energy (∼3 %) is negligible compared to the energy resolution of the SoLid scintillators at 1 MeV: ∼14% for SoLid and ∼20 % for SM1. The conversion electrons from the 570 and 1064 keV transitions (doubled by the K and L atomic shells) are visible on the right plot of figure 5.11 where no detector energy resolution has been applied. Applying these energy resolutions to the simulation one can see in figure

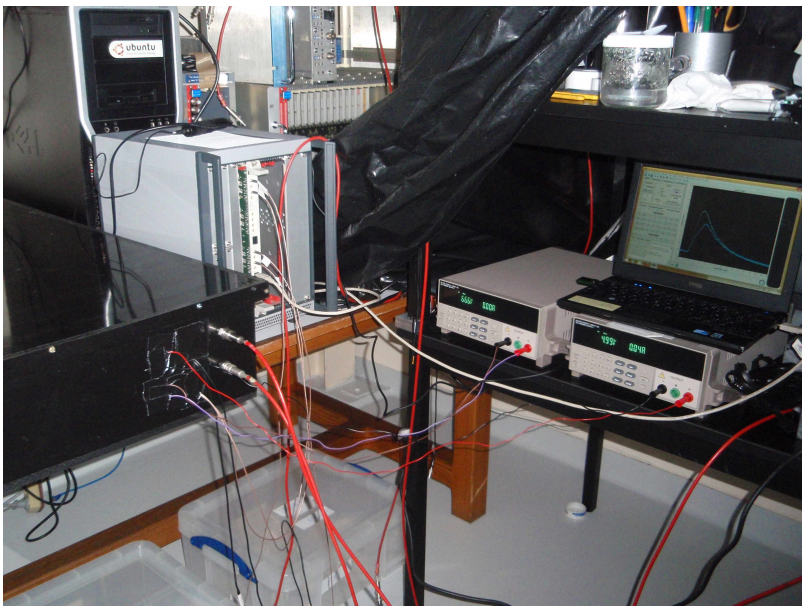

Figure 5.9: Picture of the electronics of the test bench. On the right there are two power supplies for the SiPM with the computer to acquire the data. In the middle we can see the acquisition board and the black box with the setup on the left

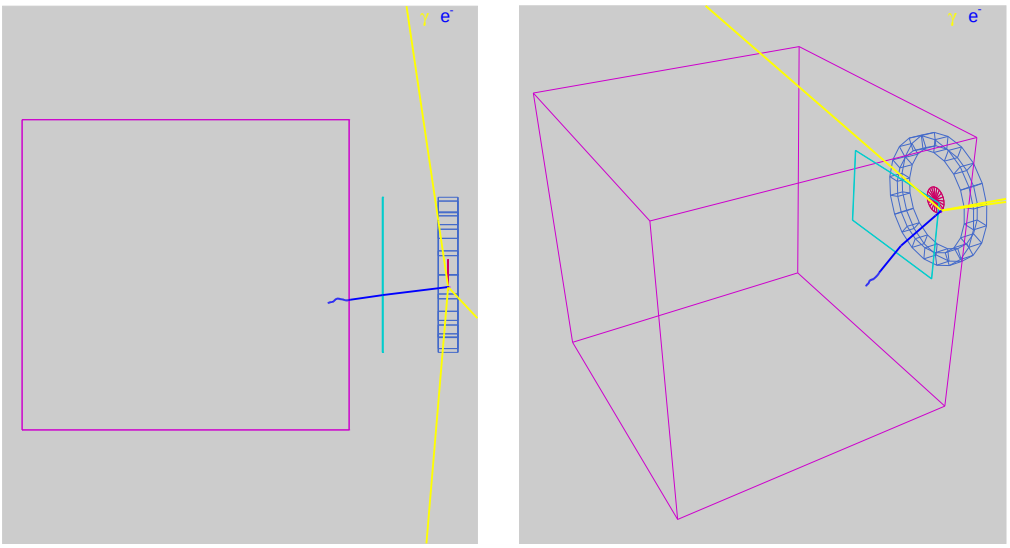

Figure 5.10: Display of a simulated event with one conversion electron (blue track) and three gammas (yellow tracks) emitted by the active area (dark red) of the calibration source. The conversion electron is detected both by the thin trigger scintillator (cyan) and the SoLid scintillator cube (magenta).

5.12 that the double peak structure disappears. It can also be seen that the smaller peak around 500 keV is no longer visible over the Compton background of the 1064 keV gamma ray. There is hence no chance to observe both conversion electron energy peaks in our setup.

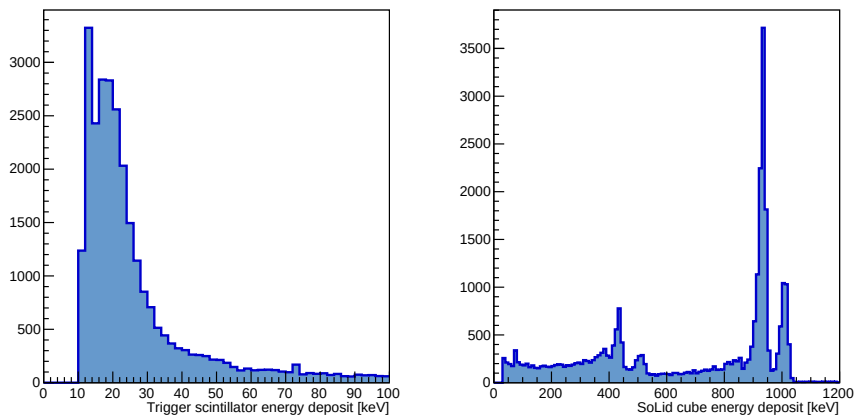

Figure 5.11: Simulated energy deposition by the ^{207}Bi conversion electrons in the trigger thin scintillator (left) and in the SoLid cube (right) wrapped in thick Tyvek (270 μm). The conversion electrons from the 570 and 1064 keV transitions are visible on the right plot where no detector energy resolution has been applied.

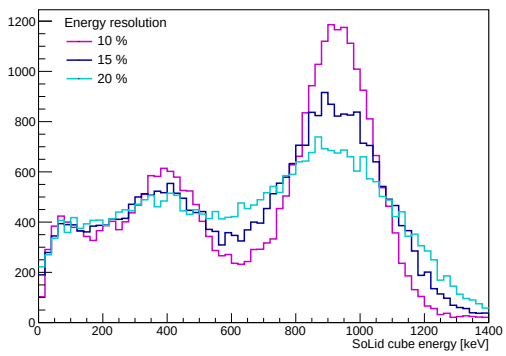

Figure 5.12: Simulated energy deposition by the ^{207}Bi conversion electrons in the SoLid cube wrapped in 270 μm thick Tyvek after applying 3 energy resolution values $\sigma_E/E = 10, 15, 20$ %.

Different cube wrappings have been tested to improve the light reflectivity in SoLid cubes. It will be explained in section 5.4.2 that the Tyvek revealed to be the most suitable material to wrap the scintillators. In the simulation of this setup it has been added as a uniform material of a given thickness and density around the cubes. However Tyvek as a non-woven product consisting of HDPE fibers is quite non-uniform in thickness. In table 5.2 the properties of SM1 and SoLid Tyvek sheets are presented. The ranges are estimates given by the producer DuPont based on individual specimen measurements. These different values have been simulated to estimate the electron energy losses before entering the scintillator cube as shown

in the left plot of figure 5.13. The average density value is used to get a reference peak position to be compared to the measured values.

Table 5.2: Properties of the Tyvek sheets from DuPont datasheets. The density is computed by ourselves from the average thickness and weight.

Sample	**Reference**	**Weight** ($g\,m^{-2}$) average [range]	**Thickness** (µm) average [range]	**Density** ($g\,cm^{-3}$) average
SM1 Tyvek	DuPont 1073D	75 [72 - 78]	205 [135 - 275]	0.366
SoLid Tyvek	DuPont 1082D	105 [101.5-108.5]	270 [190 - 350]	0.389

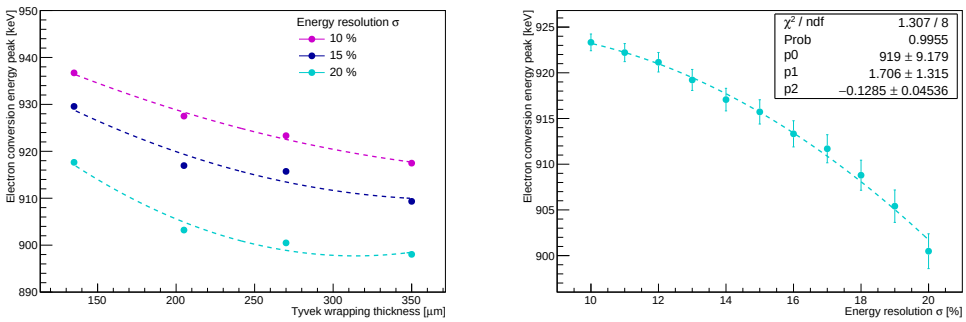

Figure 5.13: *Left*: fitted value of the simulated ^{207}Bi energy peak of SoLid cube wrapped in Tyvek as a function of Tyvek thickness after applying energy resolution corrections ($\sigma_E/E = 10, 15, 20$ %). *Right*: variation of the fitted peak value as a function of energy resolution for 270 µm Tyvek. The graph is fitted with a second order polynomial function.

Figure 5.13 right shows that the energy losses are also of the order of few tens of keV. The difference in peak positions as a function of energy resolution is certainly due to the averaging of different portions of lower energy events seen before the electron peak. For SM1 wrapping with 20 % energy resolution, the peak is expected around 900 keV and around 915 keV for SoLid with 15 % energy resolution. These values will be our references to convert our light-yield results at 1 MeV.

The function fitted on the right plot of figure 5.13 will be used at each measurement to determine the energy peak position as a function of the energy resolution measured. One can also note here that the strong non-uniformity of Tyvek should not disturb the measurements (the electron source can face different thicknesses of Tyvek because of this non-uniformity) since the mean energy peak position is changing of only ∼1 % in these ranges.

5.3 Data measurement processing

Before taking measurements, there are several effects that have to be taken into account. It includes correction from temperature, SiPM cross-talk and pedestal.

5.3.1 Correction from temperature

Before supplying the SiPMs with the correct over-voltage, the latter needs to be corrected from temperature variations. Indeed, the SiPM gain is temperature dependent. A thermometer inside the black box (EL-USB-TP-LCD) records the temperature every minute. Before taking a measurement, we correct the over-voltage with the formula:

$$V_{OP} = V_{BR} + V_{OV} - 0.060 \times (25 - t) \tag{5.1}$$

where V_{OP} is the operating voltage, V_{BR} the breakdown voltage given by the producer for a gain of 1.25×10^6 at 25°C, V_{OV} the over-voltage selected for SoLid (1.5 V for example) and using the temperature t in °C given by our probe at the start of the measurements.

As the setup is in an air-conditioned room, the temperature variations in half a day are not very high. The maximum temperature variation noticed in 24 hours was of the order of 2°C. Given that the room temperature is around 19±1°C, the voltage correction is about 0.3-0.4 V. The ^{214}Bi source has a high activity so a measurement takes only a few minutes. A serial of measurements for a given comparison takes place then in a few hours and the temperature variations should be negligible. This is verified by reference measurements at the beginning and the end of the series.

5.3.2 Correction of pedestal

Before taking a measurement, we have also to check the pedestal. Since we are able to set the pulse position in our 640 ns acquisition window we have kept around 100 ns to compute the pedestal before the pulse. The WaveCatcher system is calibrated before taking measurements so the baseline is well centered at zero. We have tested the difference between the average pedestal measured in this pre-pulse window or during internal trigger runs and the pedestal value remains within 1σ. The pedestal value is typically around 0.1 V·ns while the ^{207}Bi peak is around 2.5 V·ns in a single channel.

5.3.3 Correction from cross-talk

After each measurement, another correction has to be taken into account: the SiPM cross-talk. Optical cross-talk occurs in SiPMs when, during the primary avalanche multiplication some photons are emitted and start secondary avalanches in one or more neighbor cells. A single avalanche emits few tens of photons and the cross-talk probability is high when no optical barrier (metallic trench) is implemented. This is not the case of SoLid's generation photo-detectors so the cross-talk probability is rather high (few tens of percent). In our case we are only interested in the direct (i.e. simultaneous) cross-talk since we work in coincidences with several SiPMs.

To correct the measurements from SiPMs pixel cross-talk, a dark count rate run is taken for each SiPM in a black box, triggering with a low threshold on each SiPM, each day. In figure 5.14, the first single avalanche peaks are visible in these dark count rate runs. The crosstalk probability is computed as the ratio of dark count hits exceeding a threshold of 1.5 PA, to those exceeding a threshold of 0.5 PA, so by calculating the ratio of the integral of the charge spectrum above 1.5 PA over the integral of the charge spectrum above 0.5 PA (figure 5.14).

$$\text{crosstalk} = \frac{\int(\text{spectrum } > 1.5\text{PA})}{\int(\text{spectrum} > 0.5\text{PA})} \tag{5.2}$$

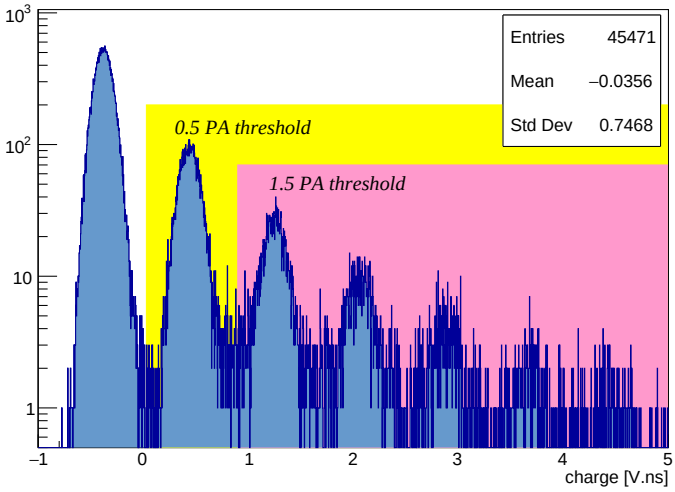

Figure 5.14: Determination of the direct cross-talk probability using dark count events. The first peak is the pedestal given by the internal trigger and the following peaks correspond to 1, 2, 3... photo-avalanches.

The average cross-talk probability has been measured at 17 ± 1 % (statistical only) at 1.5 V over-voltage.

The cross-talk probability is increasing with the over-voltage since the gain increase produces more carriers that can produce photons. In our case we could be interested to increase the over-voltage and thus the gain and the photon detection efficiency to have more light yield. We have measured the cross-talk as a function of the over-voltage. The result is presented in figure 5.15 where we can observe cross-talk probabilities increasing quickly from 10 to 60 % from 1.0 to 3.0 V.

5.3.4 Pulse reconstruction

From the WaveCatcher acquisition, we get a data file with the digitisation points of the pulses with a sampling period of 625 ps. After comparing the charge and the

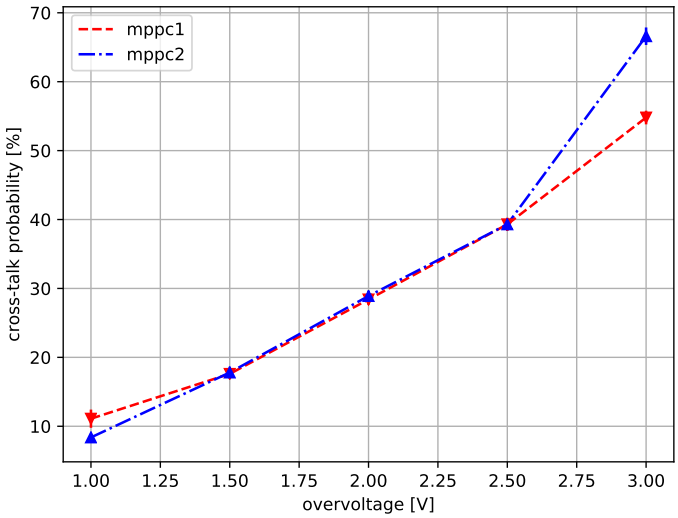

Figure 5.15: Variations of cross-talk probability for the two SiPMs as a function of over-voltage.

maximum amplitude of pulses for energy considerations, it seems that the resolution is better for charge, because of the baseline noise. To calculate the charge of each pulse, the maximum amplitude is identified and we integrate the amplitudes around this maximum from 50 ns before to around 190 ns after (figure 5.16). This point is not exactly at the end of the pulse (which is hard to identify because of the noise) for high amplitude pulses but it avoids noise fluctuations. Variable integration windows as a function of the pulse amplitude have also been tested but since no improvements were seen, the simplest method was kept.

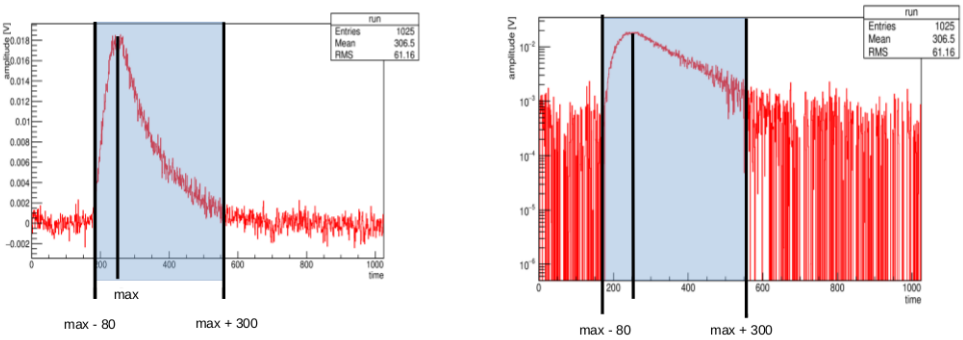

Figure 5.16: The same pulse on a linear scale on the left and on a logarithmic scale on the right. We calculate the charge of the pulses by integrating betwen 80 samples before the maximum (50 ns) and 300 samples after the maximum (190 ns).

5.3.5 Conversion from pulse charge to photo-avalanches

The posibillity to see single photo-avalanche peaks at low energy is used to convert the charge of the pulses in photo-avalanches. The procedure is the following (figure 5.17):

1. Look for the maxima bins of each of the first single photo-avalanche peaks and then fit each peak around its maximum with a gaussian.

2. The charges of these maxima are reported in a graph as a function of the number of single photo-avalanches.

3. Fit this graph with a linear function. The slope coefficient gives the conversion factor between the charge of the pulses and the number of PA. We neglect a possible constant term due to pedestal subtraction, it should have no impact for 20-30 PA peaks at 1 MeV.

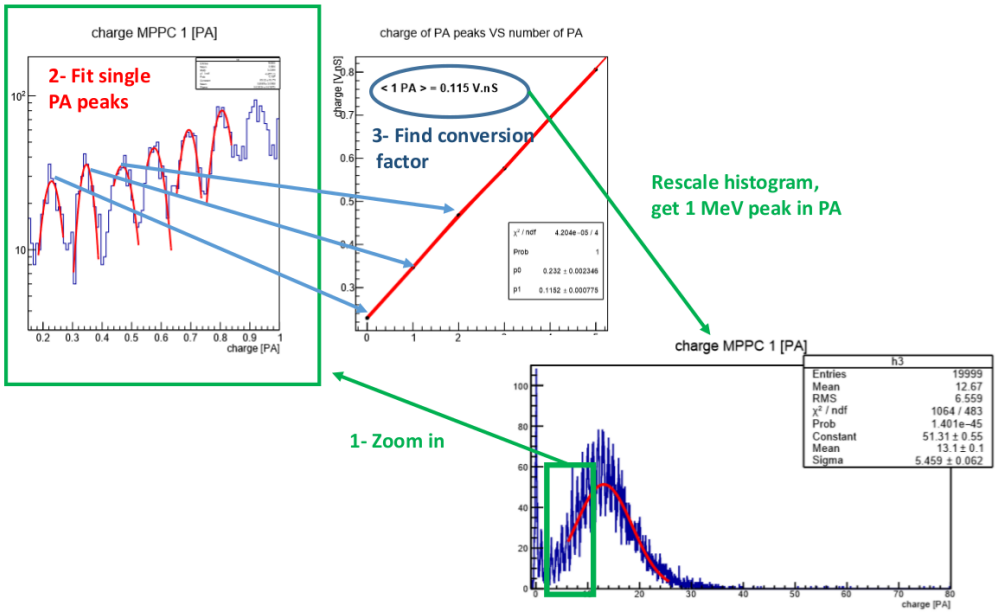

Figure 5.17: The procedure to convert charge in photo avalanches: we look for the single PA peaks by zooming in the 1 MeV peak. We find the conversion factor to rescale the spectrum with the 1 MeV peak.

5.3.6 Fit of the conversion electron peak

After rescaling histograms so that the pulse charges are in PA, we need to get the number of PA at 1 MeV. The following procedure is thus used:

1. Sum the charges of the pulses (in PA) of both SiPMs for every event.

2. Plot the charge spectrum of the sum of the 2 SiPMs signals in PA and see the 1 MeV peak in photo-avalanche.

3. Fit the 1 MeV peak of SiPM 1, SiPMs 2 and of the sum of both SiPM with gaussians, the means of these fits give the number of photo-avalanches detected for 1 MeV electrons.

4. Plot also for each event the charge of SiPM1 vs the charge of SiPM2 to check that the correlation factor is correct.

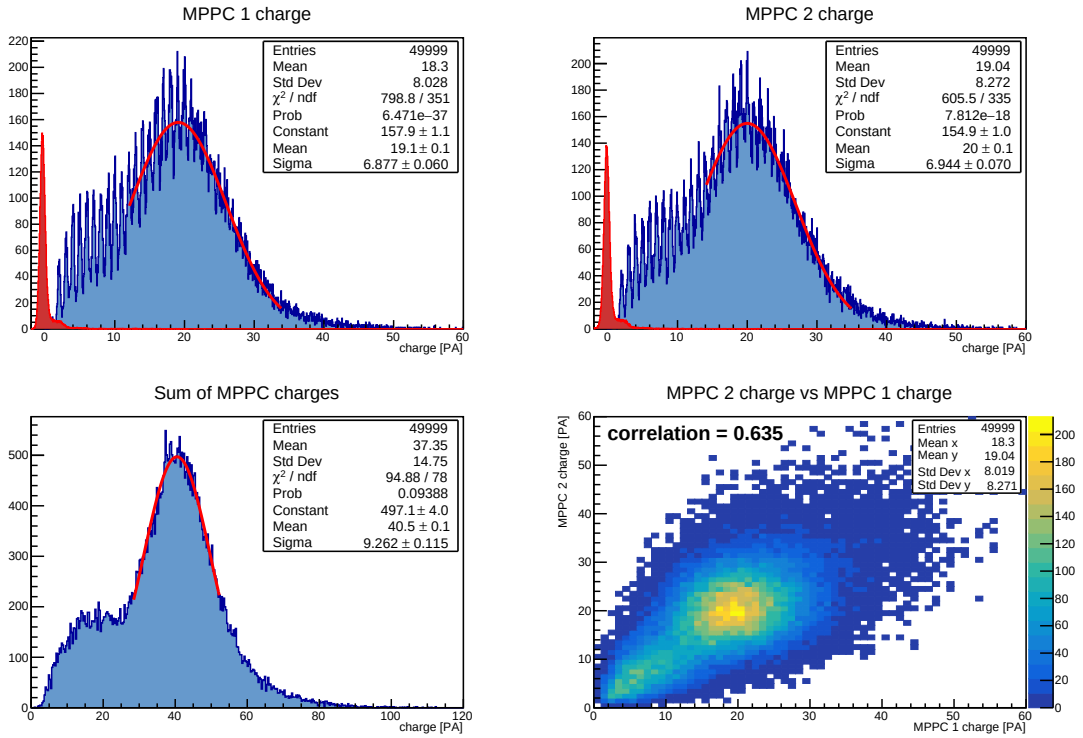

Figure 5.18: Result of the measurement after the calibration procedure. On top is shown the two calibrated charge spectra in PA for each SiPM with the Gaussian fit (in red are also presented the pedestal spectra after calibration). Bottom left is the sum of the 2 SiPM charges and the right one shows the correlation between them.

5.3.7 Measurement uncertainties

As a large amount of events is acquired for each measurement (between 20000 and 50000 most of the time), the statistical uncertainties are not significant. For a measurement with 20000 events, the statistical error on the mean of the Gaussian function that fits the 1 MeV peak is only 0.2%. Our systematic uncertainties are much larger so for the following we will not consider the statistical uncertainties anymore.

The systematic uncertainties can have two origins: the setting up of a measurement or the analysis of the data. The last one should be dominated by the final fit of the sum of the SiPM signal distribution. This gaussian fit has been tested in different ranges and binnings on a reference measurement. The variations of the

starting and stopping fitting point in reasonnable ranges give less than 2 % variation in the fitted mean position. The fit quality is always very good in these ranges with $\chi^2/NDF \approx 1$. The histogram binning before the fit has also been tested and show even smaller variations of the mean value (≈1 %).

The setting up of the experiment can introduce different sources of uncertainty like the source positioning, the cube rotation, small curving or twisting of the fibers, the voltage setting... To control these systematics, we always take a reference measurement with the same setup, cube and fibers. These reference measurements have been done at different moments with different temperature and voltage settings. Thus comparing their results gives a good estimation of the systematic uncertainties. The variations in photo-avalanches measured for 32 of these reference measurements is shown in figure 5.19. We find on average 40.3 PA for the 1 MeV peak and a standard deviation of 2.3 which corresponds to about 5 %.

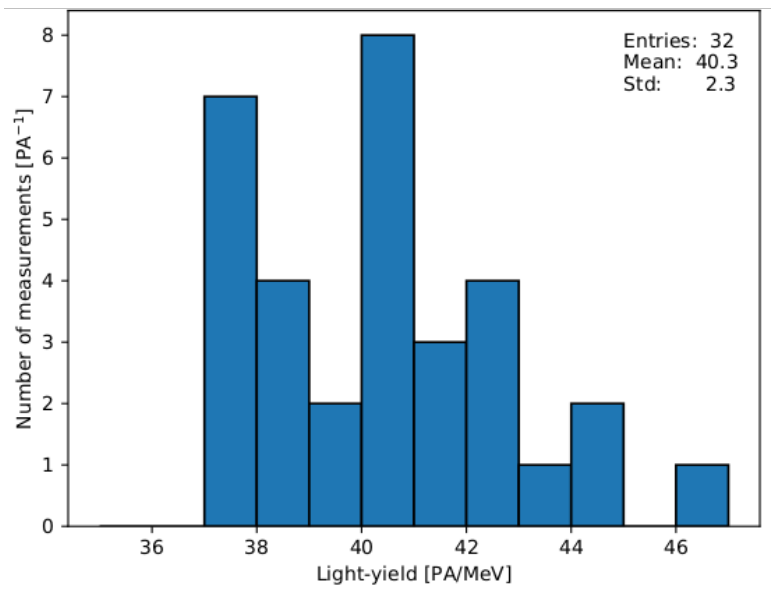

Figure 5.19: Light yield measurements performed at different moments for the same reference setup. The standard deviation of this distribution is taken as a measure of the systematic uncertainty.

As this study should take into account all the systematic uncertainties, the 5% error is used as our error on the light yield measurements.

5.4 Light collection study

With the test bench, we have started to look for improvements of the light yield using different materials used to build the detector. We have tested different scintillators, optical fibers or wrappings for example.

Most of the time, the numbers given in the following are averages over several measurements. All these measurements are corrected from the 17% cross-talk probability. If the contrary is not written, the results given are the sum of PA of both SiPMs in the standard setup. The measurements presented in the same table have been done the same day, at the same temperature and the same voltage to reduce the systematic uncertainties. There might be some small differences in light yield for similar measurements between different tables because they have been done at different days, but they are always consistent.

5.4.1 Scintillating material

Having a good light yield for the scintillating cube is very important to get a good estimation of the antineutrino energy. In SM1, the cube scintillator used was polyvinyltoluene (PVT with reference EJ-200) since it is one of the best plastic scintillator in terms of light yield (∼10000 photons/MeV) and it has good timing properties (2.1 ns decay time).

As more scintillator was needed to build the SoLid detector, an idea was to reuse some polystyrene based scintillator with PTP as primary fluor and POPOP as wavelength shifter available at LAL from the NEMO-3 experiment [38]. It is expected to give ∼8000 photons/MeV.

To compare both SM1 and NEMO-3 scintillators, we have machined NEMO-3 scintillators (PS cubes) that were bigger ($\sim 10 \times 10 \times 10$ cm^3) so that their shape was similar to SM1 cubes ($5 \times 5 \times 5$ cm^3 with grooves for fibers). Different cubes have been measured several times. In figure 5.20 the average measurement of each cube is presented. They are classified in 2 groups depending if they are PVT cubes from SM1 or polystyrene cubes machined from NEMO-3 scintillators.

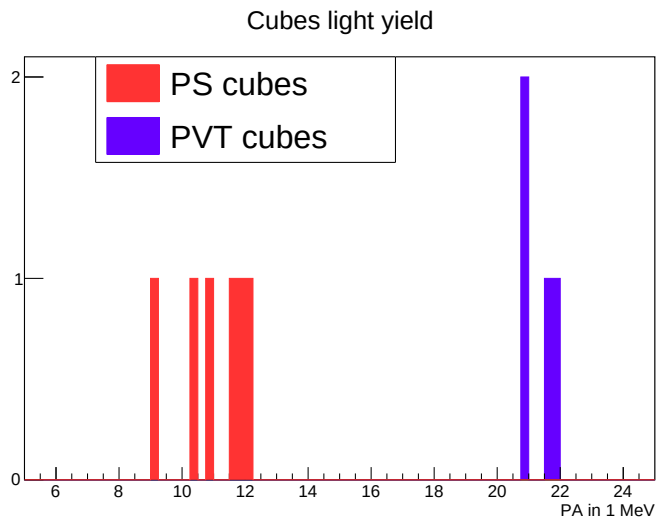

Figure 5.20: Measurement of the number of PA for PVT and polystyren (PS) cubes.

There are differences in light yield between the PS cubes from LAL that can be explained by different POPOP and PTP concentrations. PS cubes have 50 % less light yield than PVT cubes. A 20 % difference only was expected, but it might be due to different polishing, or to the fact that POPOP concentration was adapted to the bigger size of the PS blocks which was not optimal for SoLid size scintillators. It was decided not to use NEMO-3 cubes but to order new PVT cubes for SoLid phase I.

Concerning the cube scintillator, we have also investigated the cleaning. We have shown that cleaning the cubes by hand with water, soap and a rag could increase the light yield by 25%. A cleaning procedure for cubes and fibers has been set up for the SoLid construction.

The surface roughness influence on light yield has also been tested. It has been measured with a roughness meter. For SM1 cubes the surface roughness average was around 0.44 μm. For SoLid phase I, the scintillator cube machining has been improved to optimize the surface quality. The average roughness of the new PVT cubes was around 0.04 μm. The test bench measurements have shown that this led to an increase of light yield of 10 %.

5.4.2 Cubes wrapping

A way to increase the light yield of the detector is to wrap cubes with a better reflector. SM1 cubes were isolated optically by Tyvek wrapping. We have tested different wrapping for the SoLid detector.

To check some possible systematic effects, a first test has been conducted about the looseness of the Tyvek wrapping. We have not seen any consequence of a looser Tyvek on the light yield so this should not be a source of uncertainty for the measurements.

We have first tried to improve the reflectivity by increasing the number of SM1 Tyvek wrapping layers around a cube (figure 5.21). As a ZnS sheet is used in SoLid which absorbs photons on one face of the cube, we did the measurements with ZnS (in red) and without ZnS (in orange). It is shown that adding one layer of Tyvek improves well the light collection but the improvements with more layers is smaller. As there are more than 12000 cubes to wrap for the SoLid detector, it is not efficient to use several layers of Tyvek. However this test shows that the reflectivity of SM1 wrapping can be improved with better reflectors.

We have tested several types of reflectors (see table 5.3) including Teflon, well-known as one of the best reflective material for scintillators, thicker Tyvek, and other materials found in the laboratory like aluminised mylar or paper. The results are shown in table 5.3. As expected, the 0.2 mm thick Teflon tape (80 g.m^{-2}) is the best one as it improves the light yield by 31% compared to SM1 Tyvek. However this soft tape is not convenient at all to wrap thousands of cubes so it can not

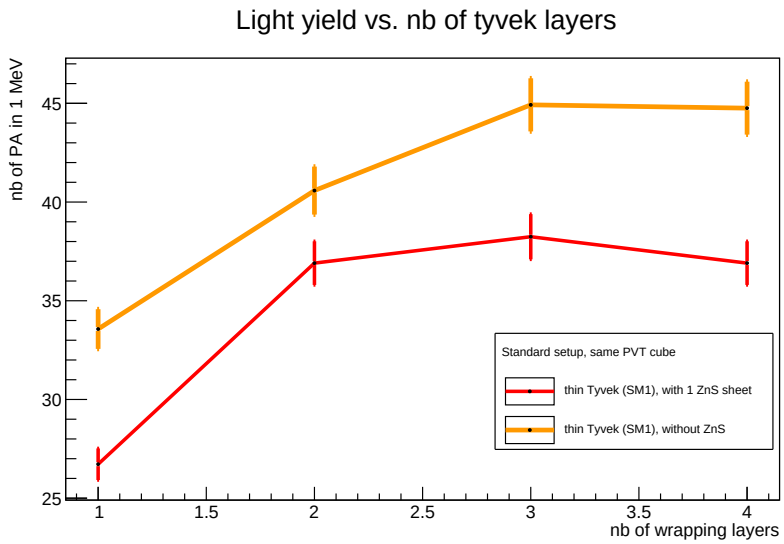

Figure 5.21: Light yield for different number of SM1 tyvek layers. The error bars correspond to the 5 % systematic errors.

be used for SoLid. Paper and aluminised mylar are not as good as Tyvek. Using the thicker Tyvek from DuPont does improve the light yield by 9%. For the SoLid detector, thicker Tyvek has been ordered (105 g.m^2). We have tested it and seen that it improves the light yield by 10%.

5.4.3 ^{6}LiF:ZnS(Ag) neutron screens

The SoLid neutron screen is a ^{6}LiF:ZnS(Ag) scintillator with a surface of 5×5 cm^2 and a thickness of 250 μm. In SM1, there was one screen per cube. To improve the neutron detection efficiency and decrease the neutron capture time, it was decided to put 2 neutron screens in each cube for SoLid phase I. However, these screens are not as reflective as Tyvek so we have tested the effect of the neutron screens on the cube light yield to check that it would not decrease too much by adding more neutron screens.

To investigate the influence of the number of neutron screens placed around the plastic scintillator we have measured the light yield of a SoLid cube adding consecutively neutron screens up to 3 to quantify the light attenuation. Table 5.4 shows that 12 % of light is lost by adding 2 neutron screens. However the decrease is 8 % when only one neutron screen is added while it is ∼4% when the second one is added. This seems to be due to the fact that the second neutron screen has been placed along the fiber. Indeed, adding the third screen not along the fiber gives again 8 % light-yield loss. In conclusion the light loss in the final detector with two neutron screens instead of one like in SM1 is limited to 12% thanks to the fact that one of the two neutron sheets will go all along an optical fiber between the PVT scintillator and the Tyvek instead of covering a full face.

wrapping		PA in 1 MeV	$\frac{\text{measurement}}{\text{SM1 thin Tyvek}}$
SM1 thin Tyvek (75 g.m^2)		33.6	1
Thick Tyvek (118 g.m^2)		**36.7**	**1.09**
Thin aluminised mylar		18.8	0.56
Teflon		**44**	**1.31**
Paper		22.2	0.66

Table 5.3: light yield for different wrapping materials.

ZnS position		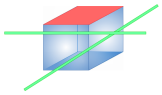	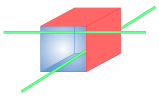	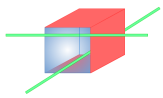
PA per MeV	33.6	30.9	29.6	27.1
variation to no screen [%]	-	-8.0	-11.9	-19.3

Table 5.4: Light yield for an increasing number of neutron screens (in red).

The first neutron screens used in SM1 and in a part of SoLid phase I were very fragile (SM1 ZnS and Solid ZnS - old production in table 5.5). A new generation of screens (Solid ZnS - new production in table 5.5) was produced for the rest of SoLid construction with a better substrate (plastic backing MELINEX 339). We have tested different screens used for the SoLid detector to see if the ^{6}LiF:ZnS(Ag) fabrication has an impact on the plastic scintillator light collection. To be closer to the SoLid design and to increase the effect, we have used two neutron screens for these measurements. The results are shown in table 5.5. Given our uncertainties, there is almost no influence of the neutron screen fabrication techniques to the plastic scintillator light collection. This is understandable since only the substrate which is toward the Tyvek has been modified. These 3 types of screens have been used for SoLid detector construction. In order to limit the effect of a slightly lower light yield and the fragility of SM1 ZnS, the oldest ZnS from SM1 production have been used in the outer layer of the SoLid detector. The detector uniformity should thus be preserved.

ZnS type	SM1 ZnS	SoLid ZnS - old production	SoLid ZnS - new production
PA per MeV	27.2	29.9	29.8

Table 5.5: Light yield for different type of neutron screens. We do not see any change within our 5% uncertainties.

5.4.4 Optical fibers

Optical wavelength shifting fibers are used to bring scintillation light to the SiPMs. We have tested some possible systematic errors due to the positioning of the fibers on the cubes grooves. The fiber grooves in the SoLid scintillator cubes have been set to 5 mm for the 3 mm squared fibers. The goal is to facilitate the fiber insertion once the frame is assembled. Indeed, pilling up the cube machining tolerances could prevent the fiber to go through. The consequence of that is some possibilities for the fiber to move in the free space. We have measured different exagerated positioning effect of the fibers relatively to the cube to quantify the strength of the results.

First the rotation of the fiber along its axis has been tested. When rotating the fiber with an angle of 45°, 90°, -45°, we see an effect of less than 4% difference in light yield compared to the 0° position. This is within the systematic uncertainties so this effect seems negligible.

SoLid optical fibers are produced by Saint-Gobain which was the only producer able to make double clad squared fibers of 3×3 cm^2 well adapted to the SiPM dimensions. At the time of SM1 prototype construction, only single clad fibers were available. As we managed to get double clad fibers from Saint Gobain after SM1 construction, we have tested the differences in light collection and attenuation between single clad and double clad fibers to figure out whether it would be worth

to change the fibers. Thanks to the rails in the setup, we were able to translate the whole trigger and detector setup (^{207}Bi source, external trigger and cube) along the fiber. We could thus measure the attenuation along the fibers. We have fitted the different measurement points along the fiber with the following function 5.3:

$$f(x) = C \times e^{\frac{-x}{l_0}} \tag{5.3}$$

with l_0 the attenuation length and C the capture coefficient.

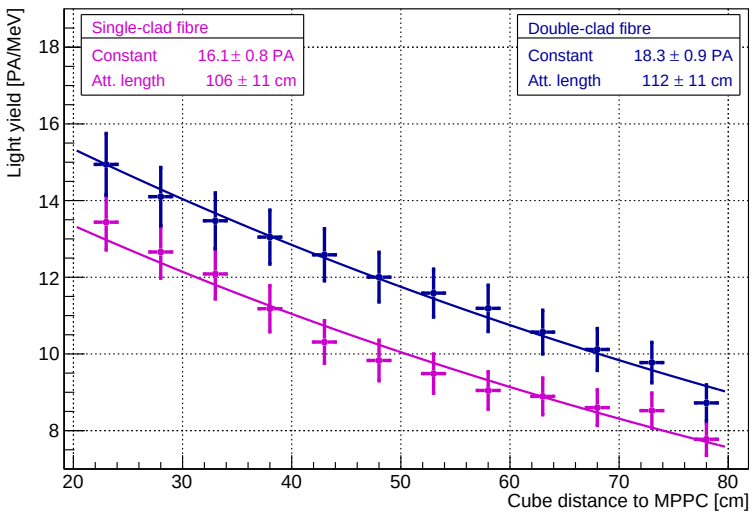

Figure 5.22: Light attenuation along a single-clad fiber (as in SM1) and a multi-clad fiber. The attenuation is fitted with the function 5.3 with two parameters: C, constant, and l_0, att. length.

We see that the multi-clad fibers can bring more light to the SiPMs than the single-clad fibers. The capture coefficient C is 14% higher (18.3 for double-clad instead of 16.1 for single-clad) which means that the double-clad fibers can trap more photons. Thus it has been decided to use double-clad fibers for the SoLid phase I detector.

5.4.5 Mirrors

Mirrors are installed at one end of the fibers to reflect the light to the SiPM which is at the other end. In SM1, aluminum sticky mirrors were used. For SoLid, we have considered using aluminised mylar mirrors. These mirrors could be attached to the fiber with a 3D printed connector instead of gluing it. Using a mirror should not improve the light collection from the cube or the attenuation length of the fiber but it has an impact on the reflectivity at the end of the fiber so the attenuation can thus be fitted by the following function 5.4:

$$f(x) = C \times (e^{-x/l_0} + re^{\frac{-(2\times 92-x)}{l_0}}) \tag{5.4}$$

With f the light yield in PA/MeV, x the distance from the SiPM, l_0 the attenuation length (in cm), r the reflectivity coefficient and C the capture coefficient. The fiber length is 92 cm.
Several measurements have been taken along the same fiber and cube with a mirror from SM1 and an aluminised mylar mirror. The capture coefficient C and the attenuation length l_0 of the fitting fuction 5.4 have been fixed according to the properties of the double-clad fiber that was used for this measurement. As we can see in figure 5.23, using an aluminised mylar mirror does increase the light detected by the SiPM as the reflectivity measured for the aluminised mylar mirror is 0.98 while the one of SM1 mirror is 0.73.

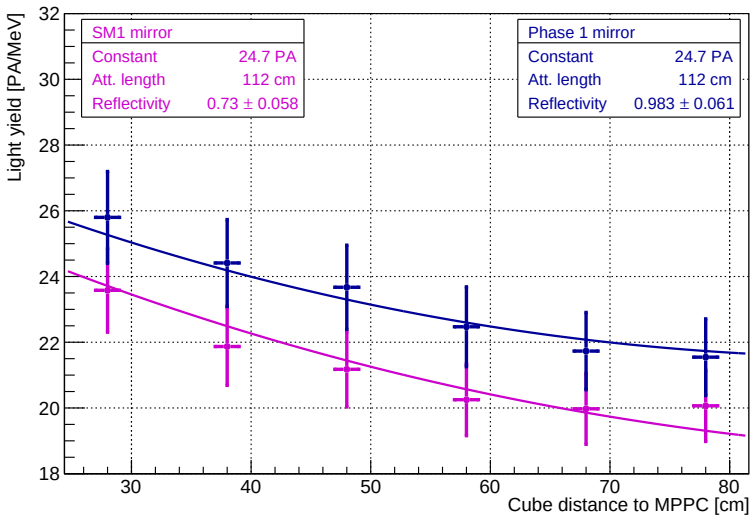

Figure 5.23: Comparison between SM1 mirror and aluminised mylar mirror at the end of a multi-clad fiber. The fit is done by fixing the capture coefficient and the attenuation length of the fiber to compare the reflectivity only.

5.5 Configuration study

5.5.1 Optical fiber configuration

There are several ways to improve the light yield. We have first tested several detector materials and another way was to investigate the detector configuration: the optimal number of fibers and their positioning. Several options were possible to collect the light from the scintillator through the fibers. It was of course mainly constrained by the cost of the material, electronic channels, and the ease to build the detector. In SM1 two squared 5×5 mm^2 grooves at the surface of the cube was chosen to receive the two 3×3 mm^2 fibers with one SiPM and one mirror at each end. It was convenient for machining and easy for detector integration in planes.

For SoLid we have tested other possibilities that could be more efficient like having the fiber going through the cube to have more scintillating material surrounding

the fiber. We have tested cubes with circular holes going through the scintillator and observed indeed 10 % increase in light yield. But considering the machining time, cost and possible local heating (that could damage scintillating properties) during drilling for this cube design, this solution was not selected.

After deciding to keep the fibers on the cube side, we have tried to find the optimal number of fibers that should be attached to each cube. To do so, we have measured the light yield of one cube in the standard configuration (with 1 fiber and 2 SiPMs at each end of the fiber). Then we have added fibers around this cube and we kept measuring the light yield of the same fiber. We have found with the results in table 5.6 that increasing the number of fibers decreases the light yield per fiber (down to 60% from 1 to 4 fibers) but it increases the light yield per cube (up to 240% from 1 to 4 fibers). This is because there is a finite amount of scintillating photons created which is divided between the number of fibers available. However increasing the number of fibers increases the probability to collect photons.

number of fibers			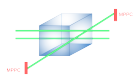	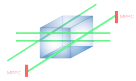
PA per MeV per fiber	33.1	27.6	24.1	19.8
PA per MeV per cube	33.1	55.2	72.3	79.0

Table 5.6: Light yield for an increasing number of fibers. Increasing the number of fibers decreases the light yield per fiber but it increases the light yield per cube.

For SoLid construction we were limited by the number of SiPMs because of electronics cost. It has been decided to use two SiPMs per channel instead of just one like in SM1. So four SiPMs were available per cube. We could either keep SM1 design with 2 fibers per cube and double readout per fiber, one SiPM at each end of the fiber, or we could use four fibers per cube with one SiPM and one mirror at each end of the fiber. With this work we have shown first that mirrors allowed to reduce the number of photons lost in the fibers and second that using four fibers per cube instead of two could increase the light yield per cube by 140% while the relatively small decrease of light yield per fiber would not be a problem. It has thus been decided to use four fibers per cube with one mirror and one SiPM at each end of the fiber.

5.5.2 Comparison between SM1 and SoLid configurations

After all these tests, several changes have been decided to improve the light yield and the neutron detection efficiency of the SoLid detector compared to SM1:

- use PVT cubes
- use a thicker Tyvek wrapping

- use 2 neutron screen sheets per cube
- use double-clad fibers
- put aluminised mylar mirror at the end of the fibers
- use four fibers per cube instead of two

We have tried to make a comparison of the light yield expected for SM1 and for SoLid according to test bench measurements. To do so, we have used the closest configurations to the SM1 and Solid phase I detectors as possible.

For the SM1 configuration we have used a SM1 cube with one SM1 neutron screen, SM1 Tyvek, two single-clad fibers with one SiPM and one SM1 mirror at each end. We have done several measurements with the cube at different distances from the SiPMs. Then we have extrapolated this measurements for a whole plane using the measured attenuation length.

For the SoLid configuration, we have used a SoLid cube with 2 neutron screens from SoLid, a SoLid thick Tyvek, 4 double-clad fibers used for the detector construction with one aluminised mylar mirror and one SiPM at each end. As we could plug only two SiPMs for each measurement, we have repeated the measurement twice with the four fibers, changing only the SiPM positions for the two measurements.

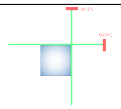	SM1-like setup: 18.6 PA/MeV
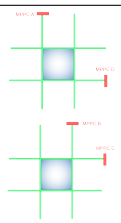	SoLid-like setup: 51.6 PA/MeV

Table 5.7: Light yield (PA/MeV/cube) for a configuration close to the SM1 detector (*top*) and close to the SoLid phase I detector (*bottom*). The cube is installed at the center of the fibers. The SoLid phase I like measurements have been done in two times by changing the SiPM positions.

The results are shown in table 5.7. At this point, we can already compare extrapolation of SM1-like test bench measurements to SM1 detector light yield. As seen in the previous chapter, after calibrating SM1 detector with muon, the light yield was found to be 24 PA/MeV per cube. This is more than what is measured with the test bench. Possible explanations to the fact that we measure less light than SM1 (and SoLid as we will see later) detectors are the differences of setup and electronics. However, this difference is likely dominated by the main change between our test bench and the real-size detectors: the number of cubes. Some light can be lost in the neighboring cubes but picked up by the fiber if there is a

whole row of cubes around it. Measurements have thus been done with a whole row of cubes. They show that the light yield increases by 12 % if there is a row of 16 cubes instead of just one cube along a fiber. With the SoLid-like setup, the light yield increases by a factor 2.8 (51.5 PA/MeV) which is a great improvement.

The extrapolated maps for a whole plane could be made using these measurements (table 5.7) and the attenuation length previously measured for SM1 fibers and mirrors (figure 5.24) and SoLid phase I fibers and mirrors (figure 5.25). The first thing that we see is the improvement of the uniformity of the detector. The maximum light yield difference between cubes is 43% in the SM1-like configuration while it decreases to only 6% for SoLid phase I configuration. This is mostly due to the fact that we are using four fibers with alternated readout instead of two. According to the extrapolation of the test bench measurements, the light yield per cube for SoLid phase I detector should be increased by 2.8. We will see later that this factor is very close to the improvement factors found after SM1 and SoLid calibrations.

The studies made with the test bench have been very successful. With all the improvements found, an average light yield of 52.3 PA/MeV was expected for SoLid phase I detector which corresponds to an energy resolution of 14 %.

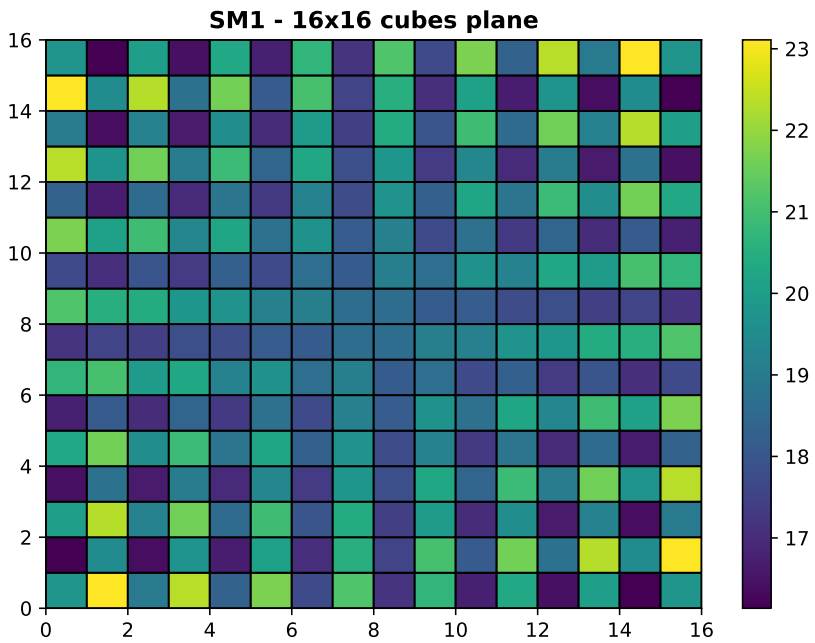

Figure 5.24: Map of SM1 light yield (number of PA per MeV per cube) extrapolating test bench measurements. The average light yield is 18.9 PA/MeV with a maximal difference of 43 %.

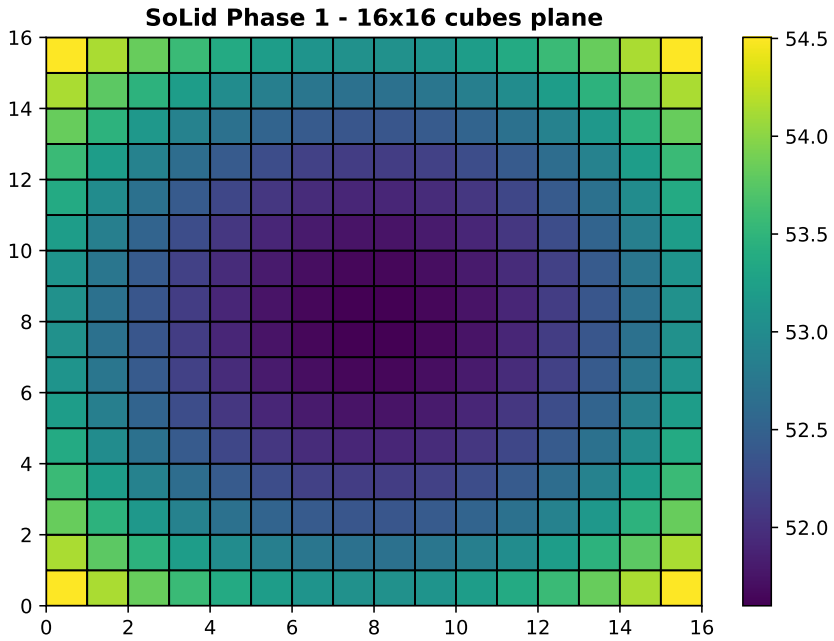

Figure 5.25: Map of SoLid light yield (number of PA per MeV per cube) extrapolating test bench measurements. The average light yield is 52.3 PA/MeV with a maximal difference of only 6 %.

5.6 SoLid cube production performance

After conducting a fruitful R&D for the SoLid detector, the test bench has also been helpful to control the cube production for the detector construction. We have tested several cubes along the construction in the standard configuration with the same Tyvek and same fiber in order to check that their light yield is similar enough to avoid a large non-uniformity of the detector. In figure 5.26, we see that cubes from different batches are quite uniform, their light yield lies within two sigma deviation and most of them are within one sigma.

Optical fibers are another component for which uniformity could be tested with the test bench. All the optical fibers were produced by Saint-Gobain at the same time. The production is expected to be very uniform. We have tested few samples with our setup but we could not see real differences even if the attenuation lengths mentioned from these samples could differ up to 20 %. As we have shown with our setup we are not precise enough in measuring the attenuation length. We have also tested some fibers that were rejected during the detector assembly because they were showing some localized defaults. In our test setup we didn't see bad results with these fibers.

5.7 Conclusion

The test bench built at LAL to investigate the light yield of SoLid detector has been very useful. It has helped us a lot to understand better the detector and several

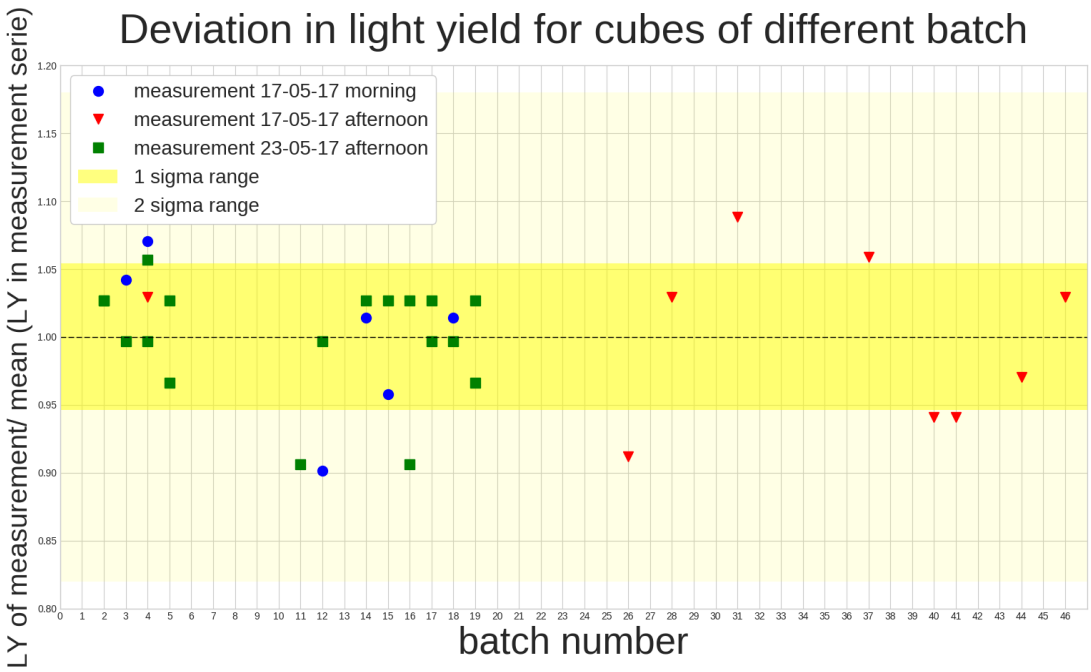

Figure 5.26: Light yield deviation for cubes of different batch for the SoLid detector construction. Points represent the number of PA measured for a cube divided by the average number of PA for a whole measurement serie.

improvements have been found for the phase I-like using four double-clad fibers, thicker Tyvek or aluminised Mylar mirror.

I have been involved a lot in the building of the test bench and its commisionning. I have written all the programs to analyse the data and done many of the measurements to test improvements of the light yield and the construction materials.

The effects of these improvements have been quantified and it was found that it is reasonable to expect an energy resolution of 14 % for phase I. In the next chapter, the construction of the SoLid phase I detector will be described as well as its performance. This work has been published on ArXiv [17] and is being reviewed to be published in JINST.

Chapter 6

SoLid phase I detector

6.1 Introduction

The SoLid phase I detector is a new detector that took advantage of the experience gained from the SM1 prototype detector, the R&D done in England to increase the neutron detection efficiency and at LAL to increase the light yield as seen in chapter 5. The detector has been built in 2017 at Ghent University and was then moved to the BR2 reactor site. It started data taking for commissioning in December 2017.

In this chapter, the design and the characteristics of the SoLid detector will first be presented. Then the different calibrations and the data taking campaigns will be described.

6.2 Mechanical design

The SoLid phase I detector is around five times larger than the SM1 detector. It is made of 5 modules of 10 planes. Each plane is an array of 16 $\times$ 16 cubes. The total fiducial mass is 1.6 tons.

To increase the light yield, as seen in chapter 5, some changes have been done on the detection cells. They are still composed of a PVT cube (EJ-200 PolyVinyl-Toluene) of 5 cm width. There are, however, two ^{6}LiF:ZnS(Ag) sheets to detect neutrons per cell on two faces of each cube instead of one (figure 6.1). These Li sheets have also been rigidified with a plastic backing (MELINEX 339). The cubes are wrapped in a thick Tyvek of 105 g.cm^{-2}. The PVT cubes have four grooves to increase the number of fibers from two in SM1 to four in phase I. The 92 cm long fibers are wavelength shifting double-clad fibers from Saint-Gobain. One extremity of each fiber is connected to a SiPM with optical grease and the other is connected to an aluminised Mylar mirror with a 3D printed plastic connector. The SiPMs employed are still Hamamatsu S12572-050 devices with a photon detection efficiency of 35% and a typically dark count rate of 1000 kHz at room temperature [82].

The cubes array lay in an aluminum frame with four polyethylene tight sealing reflector bars. To improve the neutron reflection, the bar thickness has been in-

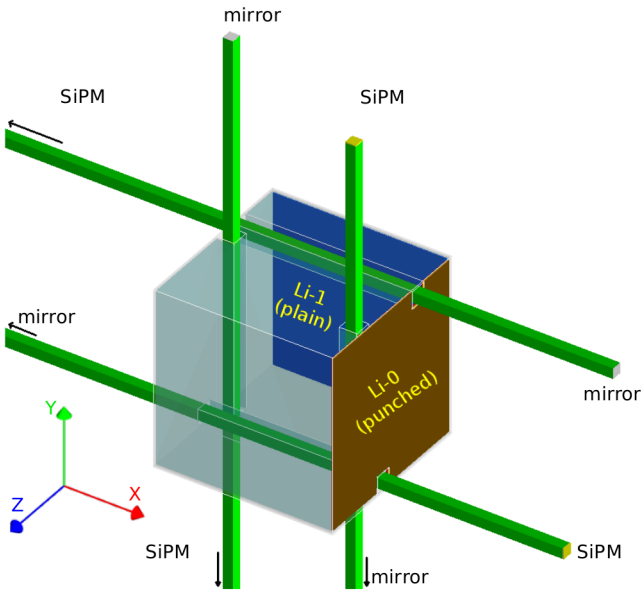

Figure 6.1: Schematic view of a cube in the SoLid phase I detector.

creased to 5 cm. Tyvek sheets wrap each face of the planes (figure 6.2).

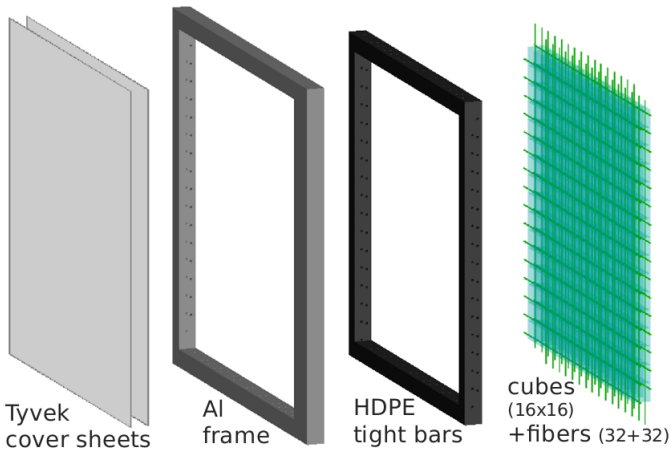

Figure 6.2: Schematic view of a plane in the SoLid phase I detector.

The detector has been installed inside a container where the 5 modules are movable on a rail system. The external size of the container is $244 \times 259 \times 385\ \mathrm{cm}^3$. In order to decrease the SiPM dark count rate by one order of magnitude, the detector is cooled down to 11°C.
Different shielding have been used against backgrounds induced by cosmic rays or the reactor. A water wall was built all around the container. It consists of poyethylene (PE) tanks filled with water. The water wall is 50 cm thick and 3.4 m high. A 50 cm thick PE ceiling has been installed on top of the container (figure 6.3)

and 10 cm thick PE plates below. The back of the water wall was completed at the beginning of 2018, after the first December data taking period in order to get access to the detector during the commissioning. There are also 2 mm thick cadmium sheets inside the container that absorb residual thermal neutrons. Finally, a lead wall between the detector and the reactor core has been built.

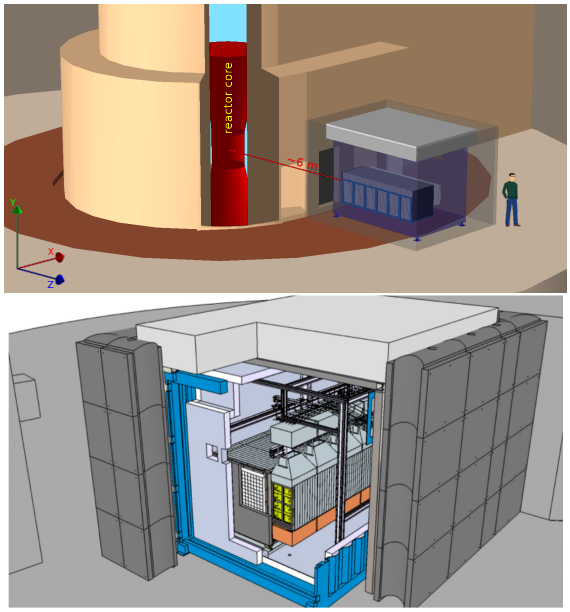

Figure 6.3: Schematic views of the SoLid phase I detector inside the container which is surrounded by the water wall (grey) and the polethylene ceiling.

6.3 Electronics and trigger

The readout electronics of each plane are placed in electronic boxes located on sides of the frames. The readout system is composed of two parts: the analog front-end and the digital front-end. The analog front-end provides the bias voltage to the SiPMs. It shapes and amplifies the signals with a band-pass filter. The signals are then sampled and processed by the digital board's components. The trigger is implemented on a Field-Programmable Gate Array (FPGA) chip included in the digital front-end.

For the phase I detector, 3200 SiPMs are used and have to be equalised. To set precisely the voltage of all SiPMs, a first global voltage is applied per analog board. As the SiPM breakdown voltages vary within a large range, an additional voltage per channel that can vary in a range of 3.8 V is set. To set this accurate voltage, a voltage scan is first performed iteratively to fit single PA peaks in order to measure the over-voltage value for each channel. An over-voltage of 1.5 V was used for the first data until April. Then it has been increased to 1.8 V. Almost all the channels (99 %) are operational and their gains vary within 1.4 % after equalisation (figure

6.4).

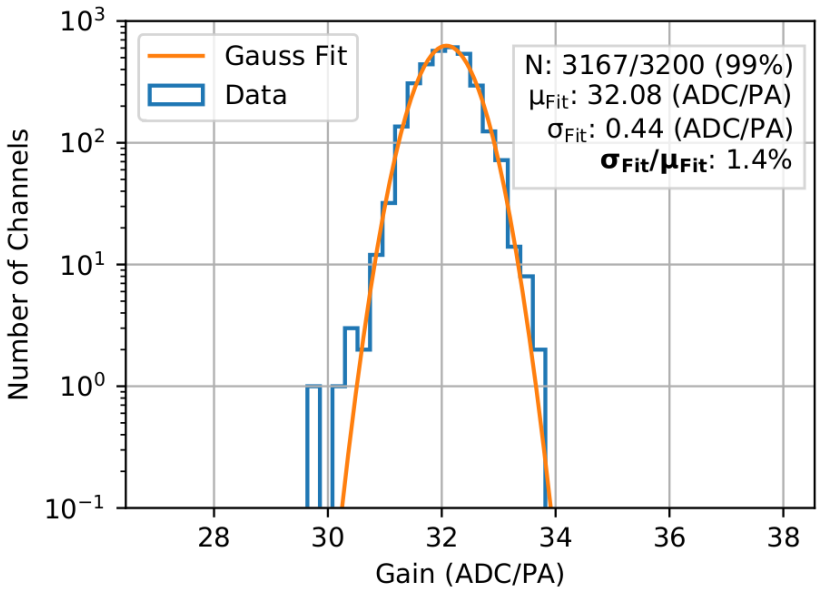

Figure 6.4: Gain of the detector SiPMs after equalisation.

Each channel digitises waveforms with 14 bit resolution at a rate of 40 MHz. With 3200 SiPMs to record data, the high data rate that comes out of the FPGAs to the online software has to be controlled with zero-suppression and efficient triggers. A zero suppression is applied to reduce the data rate depending on the trigger type. It allows recording only parts of the signal waveforms above a certain threshold. Three types of triggers are implemented in parallel for SoLid phase I. The firmware has been updated in April and some trigger conditions have changed so only the trigger logic is explained in this part, the precise conditions for each data set will be given in the analysis part.

- The first one is a random trigger to monitor SiPMs. It reads all channels during 6.4 μs at a rate of 0.5 Hz.

- The second one is a threshold trigger set at about 2 MeV which is used to tag muons. Once this trigger happen, all the channels are readout during 12.8 μs with a zero-suppression of 1.5 PA.

- The last trigger is set to detect neutrons if a minimum number of peaks are detected within a sliding time window (figure 6.5). The zero-suppression is lowered for a local time window to the neutron in order to increase the neutron reconstruction efficiency. A buffer of several hundreds of μs around the neutron is used to register EM signals in $\pm$ 3 planes around the neutron. This trigger is used to tag IBD events like the one presented in figure 6.6.

With these triggers, the data rate is around 1.5 TB/day. The neutron trigger and reconstruction efficiency is 79 ± 3 % which is much better than for SM1.

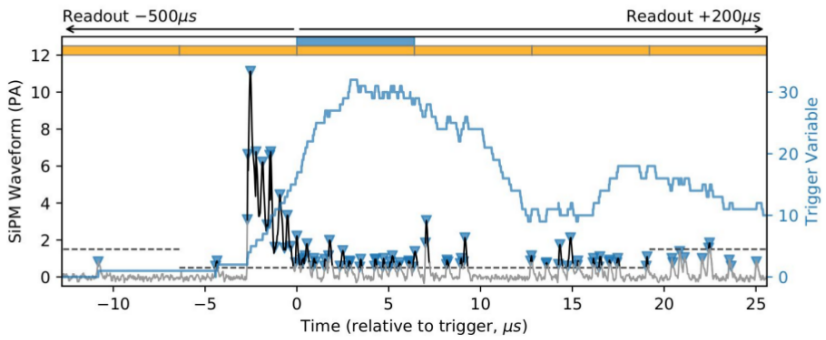

Figure 6.5: Example of a neutron triggered waveform (black). The number of peaks over threshold (PoT) is represented in blue and used to trigger on neutron events. All signals in the ±6 planes around the neutron are readout for several hundreds of μs. The zero-suppression threshold (horizontal dashed lines) is lowered for a time window around the neutron.

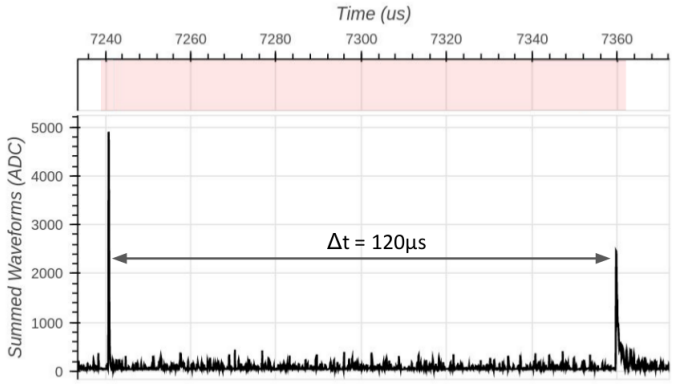

Figure 6.6: An example of IBD candidate signal.

6.4 Construction planning

The phase I detector has been built at Ghent University. The construction started at the end of 2016. The 12800 cubes machined by a company have been washed, weighed and wrapped with Li sheets manually. All the cube informations were registered in a database to simulate accurately the proton content of the detector (figure 6.7). After being wrapped, cubes were assembled in aluminum frames and PE bars (figure 6.8). The position of each cube has been carefully recorded. The fibers were then inserted inside the grooves before SiPMs and mirrors were fixed at their extremities. The plane construction ended with the cabling of all SiPMs and the closing of the aluminum frames. Each plane has been calibrated with radioactive sources at Ghent in order to fix possible issues with channels like bad contacts

between fibers and SiPMs.

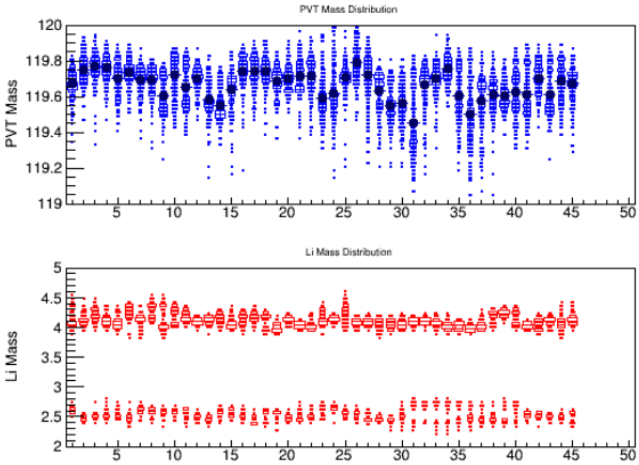

Figure 6.7: Masses in grams of PVT cubes (in blue) and Li sheets (in red) for each detector plane. The Li sheets with lower masses had been produced for SM1. They have been put at the edges of each plane.

The first four modules have been shipped to BR2 in October 2017. The fifth module was delayed because of a batch of Li sheets that was defective and had to be replaced, and the electronics that had to be completed. Most of the shielding with the PE roof and the left and right water walls have been installed in November. The fifth module was completed and brought to BR2 at the beginning of 2018. The back water wall and the lead wall in front of the reactor core have been completed at the beginning of April.

6.5 Individual cube calibration

Two types of calibrations with different goals have been performed with two different automated systems at Ghent University and in-situ at the BR2 reactor.

Each detector plane has been first calibrated at Ghent University during the construction of the detector. The goal was to check the quality of the response of each cube in the detector in order to identify possible defects and fix them.

Calibration campaigns have then been run on the BR2 site. EM calibrations have been done to get the EM signal energy calibration constants. Neutron calibrations have also been performed to measure the neutron signal detection and reconstruction efficiency.

The calibration of the SoLid detector is very challenging as each of the 12800 cubes has to be calibrated at the 2% level for the energy scale and at the 3% level for the neutron capture efficiency.

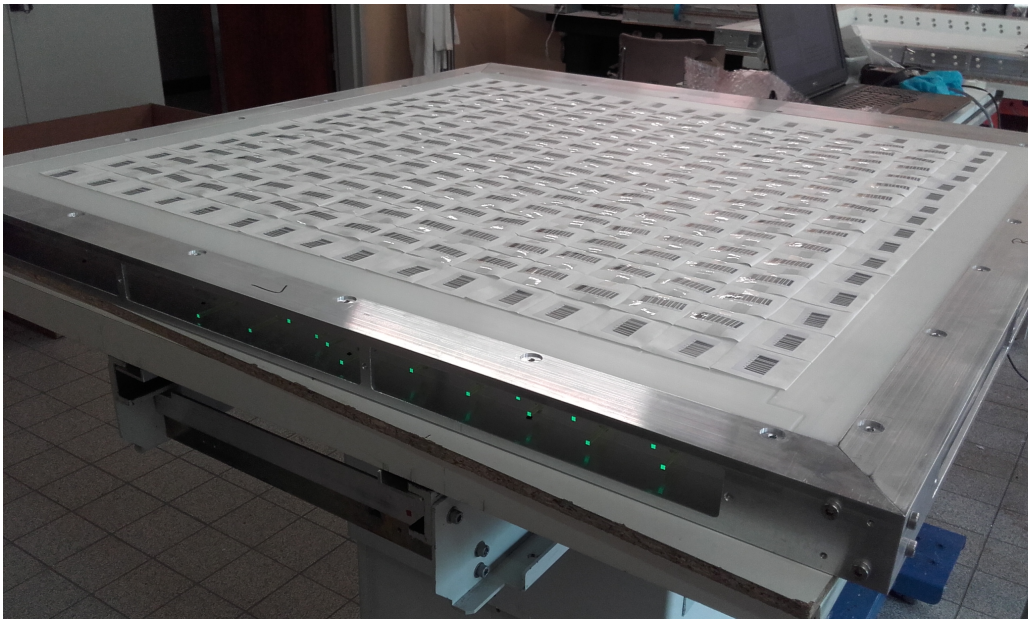

Figure 6.8: Picture of a plane being assembled (*top*) and a module being installed inside the container (*bottom*).

6.5.1 Calibration at Ghent with Calipso

A preliminary calibration during the detector construction was performed at Ghent University. This calibration was used for quality assurance purposes and allowed early identification of defective components. Furthermore, it provided a good knowledge of the detector response before the installation at BR2.

A robot, called Calipso, has been built to carry out this calibration. It allowed placing automatically radioactive gamma and neutron sources in front of each cube (figure 6.9).

It took around one day to calibrate a full frame. All the 50 planes have been calibrated before being installed in the container. Minor construction problems have been identified and fixed.

Figure 6.9: Picture of the Calipso robot with a frame installed to be calibrated. The source is located in the black box in the red square. The electronic box is on the right of the plane.

EM calibration

A ^{22}Na source has been used to calibrate EM signals and thus check the PVT cubes. This source emits two 511 keV gammas back-to-back together with a 1.27 MeV gamma in about 90.3% of its decays. While one of the two 511 keV gammas was used to start an external trigger, the Compton edge of the 1270 keV gamma interaction in the cubes of the detector could be fitted to measure the light yield (figure 6.10). The 4.4 MeV gammas from an AmBe source, as well as the 2.2 MeV gammas from neutron capture on hydrogen, have also been exploited to check the energy scale linearity of the PVT cubes.

The energy scale has been assessed with two independent approaches. The first one uses the Kolmogorov-Smirnov method to compare the calibration data with Geant4 Monte-Carlo simulation. The Monte-Carlo distributions are rescaled and smeared by a light yield and an energy resolution. The second one performs an analytical fit to extract the calibration constants. It computes a probability density function (pdf) based on Klein-Nishina cross-section [90] and fit the calibration data with this pdf to find the Compton edge and the energy resolution. Both methods agree at the 1 % level.

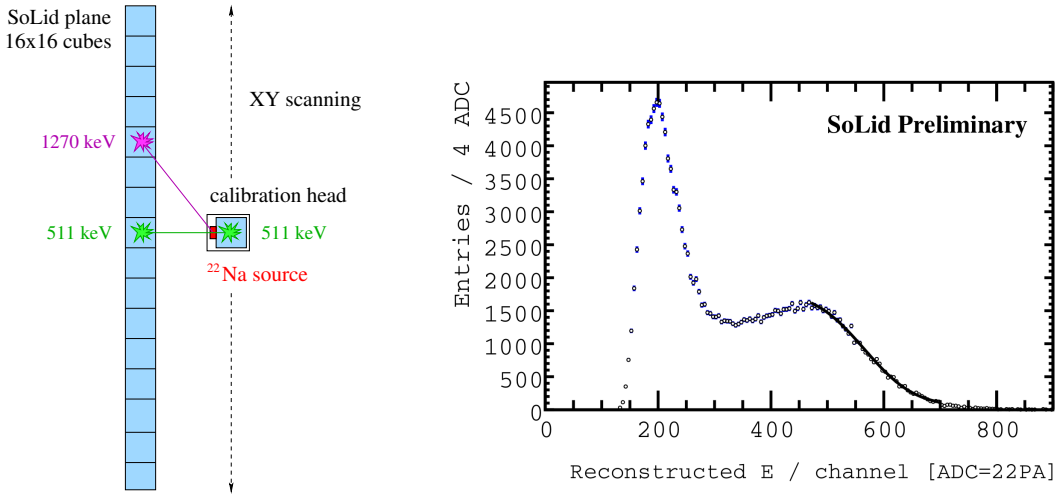

Figure 6.10: *Left*: schematic of the ^{22}Na calibration system on Calipso. One of the 511 keV gammas is used to trigger and the 1270 keV gamma Compton edge is measured on the SoLid plane. *Right*: the ^{22}Na energy spectrum measured in a cube of the SoLid detector. The first peak around 200 ADC is due to the 511 keV gammas and the compton edge around 500 ADC corresponds to the 1270 keV gammas.

This calibration has shown that all the frames are very uniform in light yield (figure 6.11). A preliminary average light yield of 87.3 PA/MeV/cube was estimated before cross-talk subtraction which exceeds SoLid requirements and the test bench results. Comparing AmBe and ^{22}Na calibrations for a same cube has demonstrated that the energy scale is linear (figure 6.12).

Neutron calibration

AmBe and ^{252}Cf sources with polyethylene collimator have been employed to study the neutron signals from the Li sheets. The sources were placed in 25 positions per plane. The calibration data have been compared to Geant4/MCNPX predictions. In addition, in order to have a comparison independent from the simulation, a relative measurement among all the planes was realized. During this calibration campaign, it was observed that one batch of ^{6}LiF:ZnS(Ag) was worse than the others, thus it has been replaced, and one cube over the 12800 cubes had a missing Li sheet that has been added afterward (figure 6.13). The average neutron detection efficiency was around 66 % and is uniform between planes (figure 6.14).

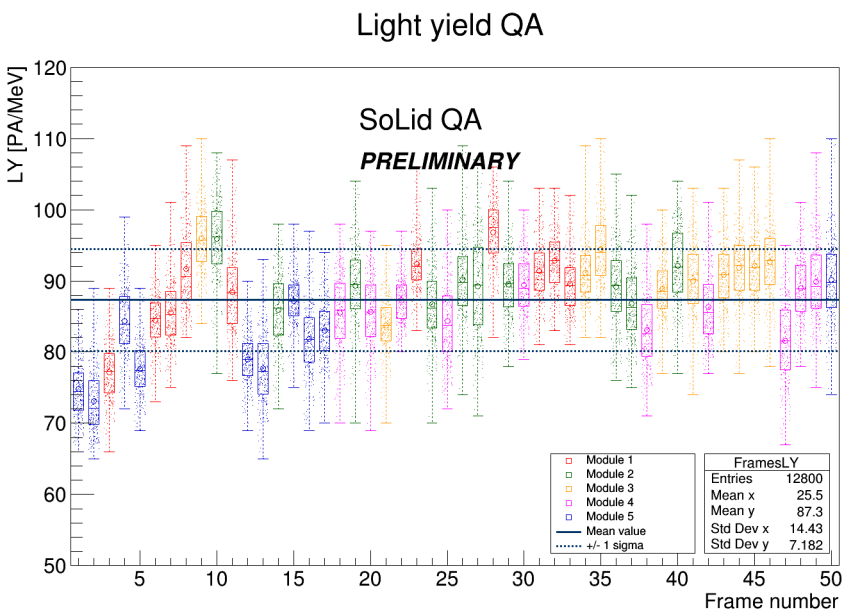

Figure 6.11: Average number of PA/MeV/cube (not corrected from cross-talk) for each frame obtained with a ^{22}Na calibration source installed on the Calipso robot. A frame represents 16 × 16 cubes.

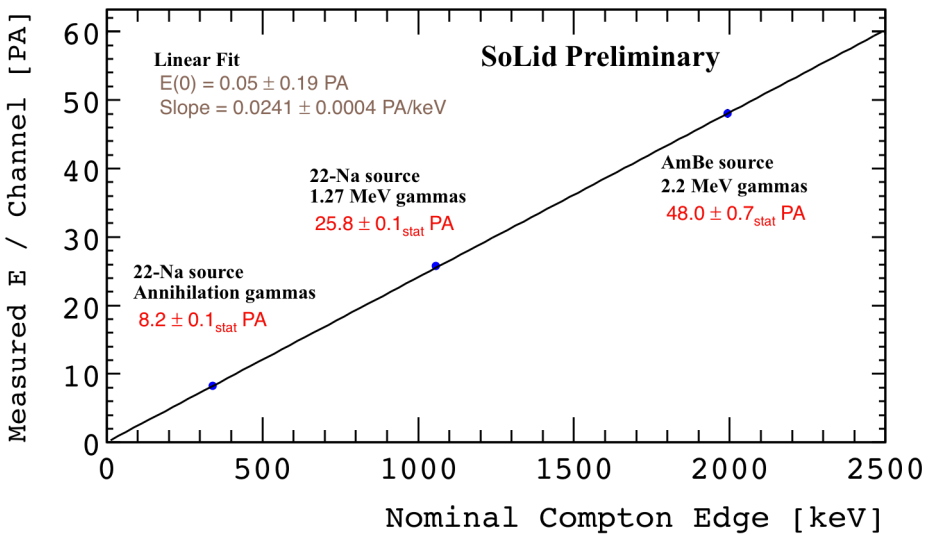

Figure 6.12: Validation of the linearity of the energy scale by comparing the calibration constants obtained with AmBe and ^{22}Na sources.

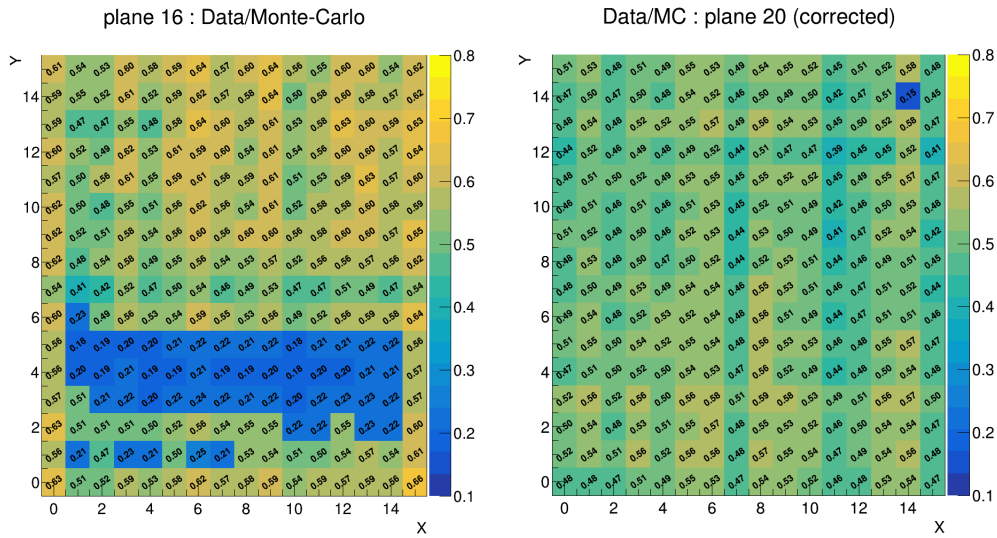

Figure 6.13: Neutron detection efficiency for each cube computed by comparing calibration data with a ^{252}Cf source and simulation. On the left, the bad batch of Li sheets is clearly visible as well as the cube with a missing Li sheet on the right. These defective batch and cube have been replaced.

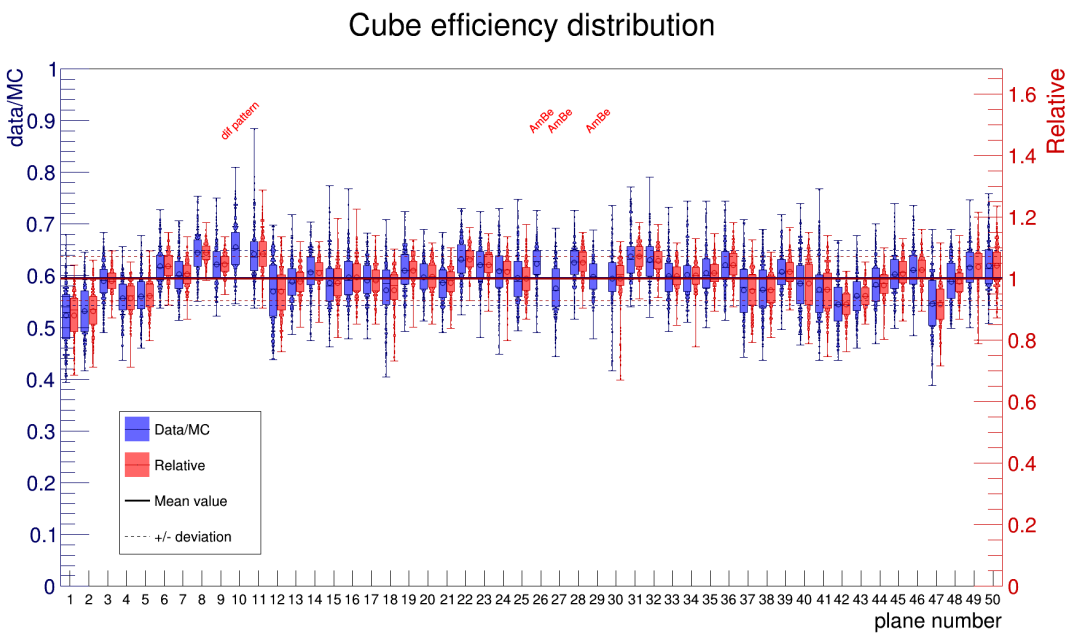

Figure 6.14: Average neutron detection efficiency per plane

6.5.2 Calibration on site with CROSS

To calibrate regularly the detector on site, another robot, named CROSS, has been built. It sits above the detector planes and mechanically opens gaps between sets of ten planes to move the sources inside. Nine positions per gap have been used (figure 6.15).

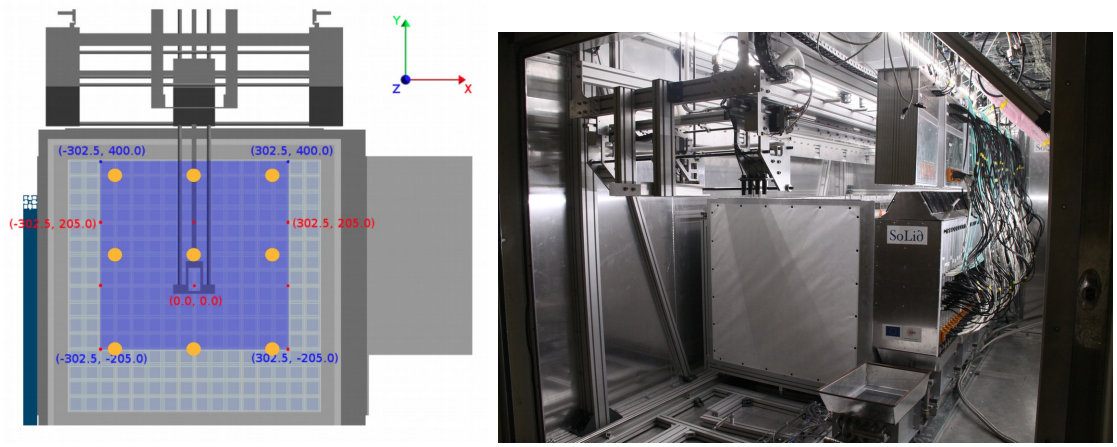

Figure 6.15: *Left*: Schematic view of the CROSS robot and the different source positions (yellow dots). *Right*: and its picture inside the container.

The first calibration campaign on site happened in March 2018 and lasted for 11 days. Three radioactive sources were used: ^{22}Na to calibrate EM signals, AmBe and ^{252}Cf to calibrate neutron signals.

EM calibration

To calibrate in energy the EM signals for each cube, the Compton edges at 1.057 MeV from the 1.270 MeV gammas of ^{22}Na have been fitted. The AmBe source was also used as it emits 4.438 MeV gammas with a Compton edge at 4.198 MeV. The two methods, Kolmogorov and analytical fit from pdf have been employed to extract calibration constants.

The ^{22}Na data give an average light yield of 77.1 PA/MeV/cube without cross-talk subtraction (figure 6.16). The 10 % lower value compared to Calipso results can come from temperature effects, or different over-voltage settings. The cubes energy calibration was also performed with the AmBe source and it gave a light yield of 76.9 PA/MeV/cube. An excellent agreement is thus observed between calibrations at 1.27 MeV and at 4.4 MeV which confirms the linearity of the energy response. The whole detector has been calibrated in energy with uncertainties at the 3 % level.

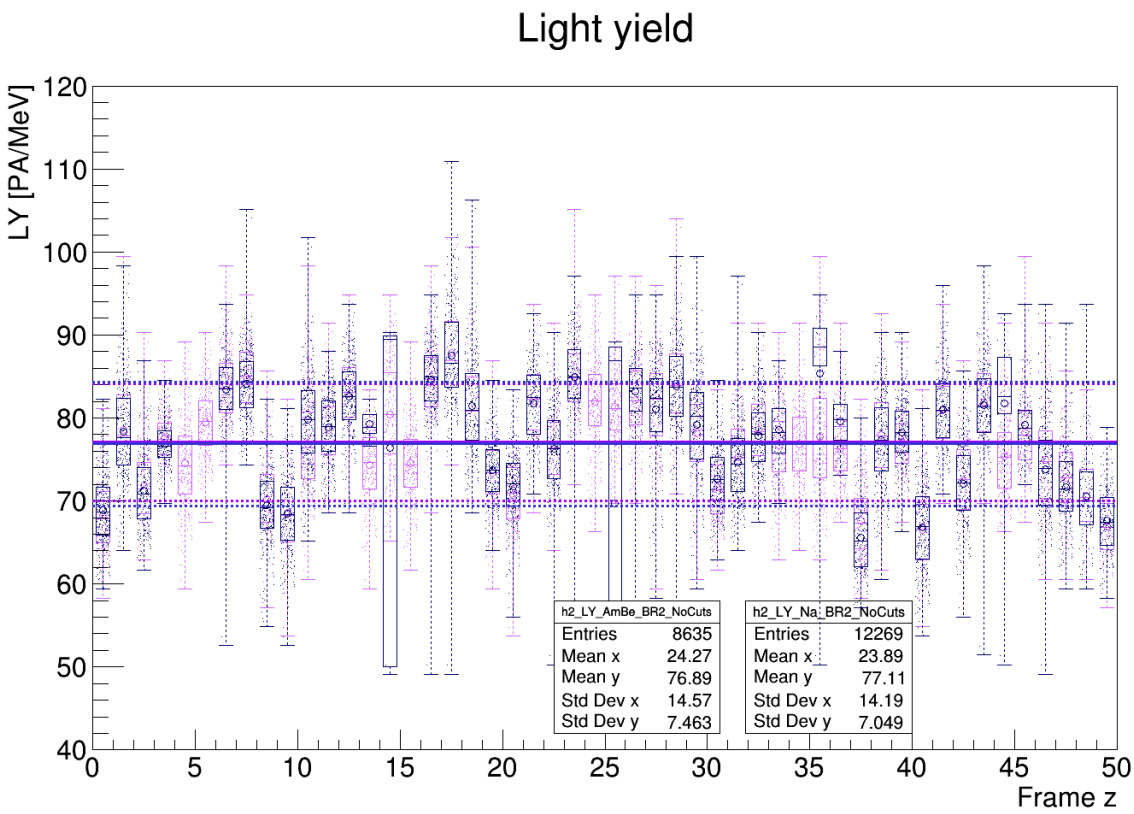

Figure 6.16: Average number of PA/MeV/cube (not corrected from cross-talk) for each frame obtained with a ^{22}Na calibration source (in violet) and an AmBe source in (dark blue) installed on the CROSS robot.

Neutron calibration

AmBe and ^{252}Cf sources have been used for neutron calibration. Monte-Carlo simulations have been run to compare the neutron reconstruction efficiency with calibration data in each cube for each position of the sources. The neutron reconstruction efficiency takes into account the neutron trigger probability and the off-line reconstruction efficiency that will be explained in more details later. It was measured per cube with a statistical error of 2.5 % and is greater than 75 % (figure 6.17). The statistical error will decrease with the next calibration campaigns. The increase in neutron detection efficiency compared to Calipso calibration results is due to changes in the neutron trigger: the number of peaks over threshold required, the zero-suppression and the over-voltage have been optimised.

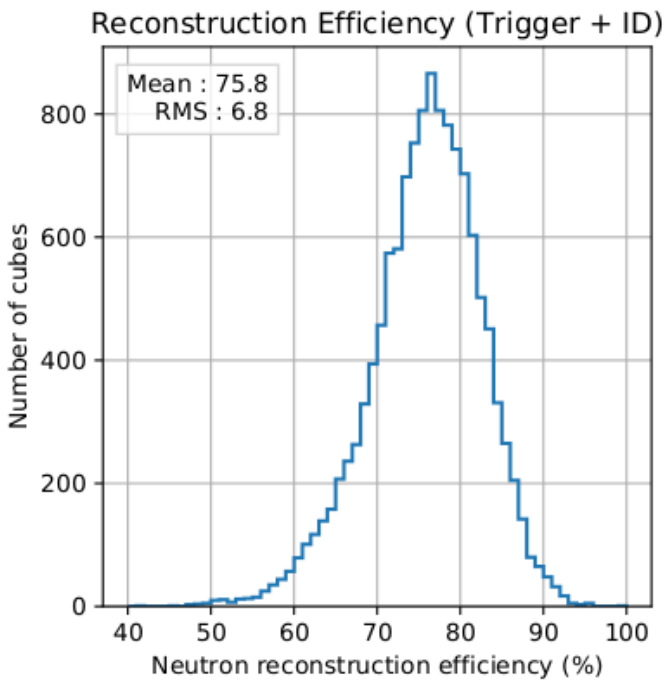

Figure 6.17: Neutron reconstruction efficiency from calibration campaigns with CROSS.

6.6 Data taking campaigns

Since the installation of the detector at BR2, data have been taken during 3 reactor cycles in December 2017, February and May 2018 (table 6.1). The comissioning of the detector has been finished in February 2018.
The periods between cycles when the reactor turned off have been used to run calibration campaigns with radioactive sources, record reactor Off data to understand the environmental backgrounds and update the firmware in March.
The data taking is monitored remotely. The trigger rates and SiPM variables are very stable for both reactor On and Off (figure 6.18). An issue with humidity increasing in the container has been solved by flushing the container with compressed

air.
In 2018, 6 reactor cycles are expected to provide around 150 days of reactor On data.

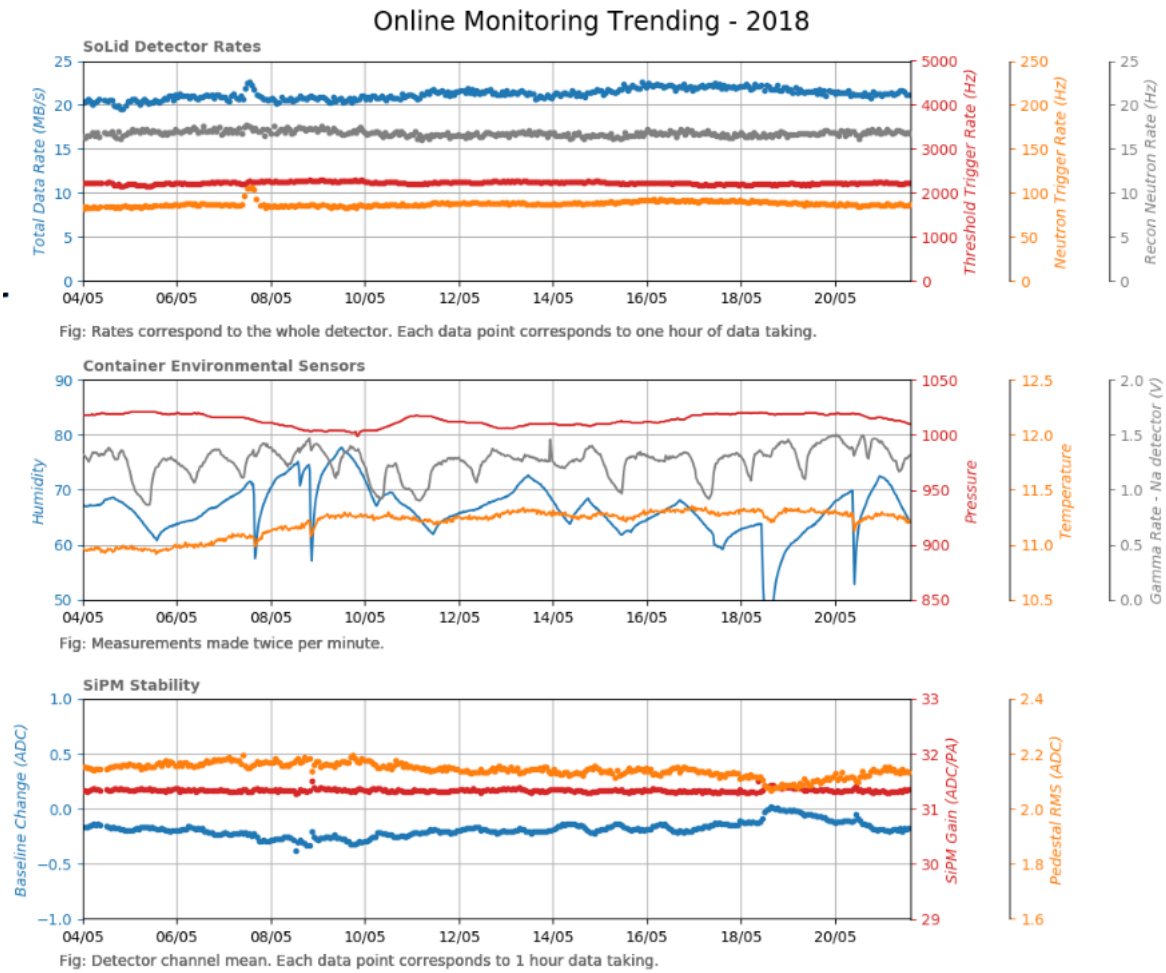

Figure 6.18: Online monitoring of the SoLid phase I detector in 2018. On top, the different trigger rates were very stables. In the middle, the environmental sensors inside the container show low variations of the pressure and the temperature. However, the humidity has varied a lot so compressed air has been flushed in the container to decrease it. In the bottom, the SiPM gains and pedestal were very stable over time.

6.7 Conclusion

The SoLid detector design, although similar to SM1, has been improved in order to increase the light yield and the neutron detection efficiency. The first calibration campaigns have shown that great improvements have been made since the SM1 prototype. In the next chapter, a first IBD analysis with this detector will be presented.

Dates	02/12/17 12/12/17	12/12/17 25/12/17	06/02/18 25/02/18	26/02/18 01/03/18	19/03/18 28/03/18	25/04/18 22/05/18	23/05/18 11/06/18
data type	ON	OFF	ON	OFF	Calibration	ON	OFF

Table 6.1: Data taken since the detector commissioning. The reactor status is indicated by ON and OFF.

Chapter 7

SoLid phase I data analysis

7.1 Introduction

In this chapter, a preliminary analysis of the first SoLid phase I data will be presented. Some work has first been done to reconstruct properly the different physical objects to tag IBD events and backgrounds. These objects include electromagnetic (EM) cubes, neutron cubes, muon veto cubes and muon tracks. The object reconstruction has been studied with the commissioning data from December 2017. After introducing all the cuts to select IBD-like events, a search for these events will be presented.

7.2 SoLid phase I data taking

The data sets have already been presented at the end of last chapter. Here we focus on the December 2017 and May 2018 data used for this analysis.

The first December commissioning data were taken with only 4 modules. The back of the water wall shielding was not completed either. These data have been used to start studying the object reconstruction.

The reactor On data from February were taken with the fifth module and the full water wall shielding. However, they have not been analysed yet as the hardware has been improved in April. The data taken in the following period were thus of a better quality.

The reactor On data from May have been used to search for IBD events. They were taken with the full detector and an improved hardware. Indeed, the SiPM over-voltage was raised from 1.5 to 1.8 V to increase their gains and photon detection efficiencies. The minimum number of peaks over threshold for the neutron trigger was increased from 9 to 17 thanks to the SiPM gain increase and the peak finder trigger was lowered from 1.5 PA to 0.5 PA. The IBD buffer size around a neutron signal was also increased from [-380, 100] μs to [-500, 200] μs. In the following work, it can be noticed that the accidentals are measured in a shorter negative time window than the correlated. This is due to the asymmetric IBD buffer size

that was made to keep more correlated events for the data analysis.

As the object reconstruction study was done with December data, it does not take into account all the advantages acquired by the improved trigger for May data.

7.3 Object reconstruction

7.3.1 Saffron analysis software

The SoLid Analysis Framework (Saffron2) is dedicated to the reconstruction and analysis of SoLid data. It is a standalone C++ code.

From DAQ binary files consisting of a collection of samples, Saffron2 emulates the triggers and reconstructs different objects: waveforms, peaks and more sophisticated objects like electromagnetic (EM), neutron, muon cubes or muon tracks. It can also apply calibration constants to the reconstructed objects.

Saffron2 uses a buffer structure to process DAQ data. The reconstruction is performed over a processing cycle. A cycle is defined as a set of data with no gap in the trigger rate of more than 3 ms. The data from a cycle in a file are loaded into memory and reconstructed. Saffron2 first loads binary files to parse waveforms and merge them. The data are then time ordered. Peaks are searched by looking for local maxima in the waveforms. A peak threshold is set at 200 adc (around 300 keV) to reduce the noises due to dark rate for example. The peaks from different channels are then grouped in a time cluster of 80 ns to form an event (a channel is defined as the signals from one SiPM attached to one fiber). Events are the basic reconstructed objects of Saffron2. They are used then to reconstruct EM cubes and muons. Neutrons are reconstructed independently as explained in the next section.

7.3.2 Neutron reconstruction

A dedicated neutron trigger has been implemented as explained previously. Neutrons are also reconstructed offline with the Saffron2 software.

To reconstruct neutrons, a first step is to emulate the neutron trigger on the reconstructed peaks. This is done by determining for each available sample from the emulated neutron trigger, the number of peaks in the previous 6.4 μs time window. A block of 6.4 μs is kept if it has a minimum number of peaks over threshold (PoT), for example more than 17 peaks above 0.6 PA for May data. The number of PoT computed on a neutron waveform is shown in green in figure 7.1. All the blocks in time coincidence or continuous to each other are grouped. Once a channel with a neutron waveform is found, other channels that can form a neutron cube are searched. First, if a neutron waveform is found in the parallel channel that belongs to the same cube, it is added to the neutron cube. All the orthogonal channels in the same plane are then parsed to find the pair of channel with the highest PoT value within $\pm$ 6.4 μs. A neutron cube is thus a collection of neutron waveforms in

2 to 4 channels that form a same cube. The amplitude and integral of each channel are then computed.

The neutron signal amplitude is the maximum sample in a [-12.8, 0] μs window where 0 μs corresponds to the maximum PoT time. The neutron signal integral is computed in the range [-0.225, 12.575] μs with the reference time being the time of the peak with maximum amplitude (figure 7.1).

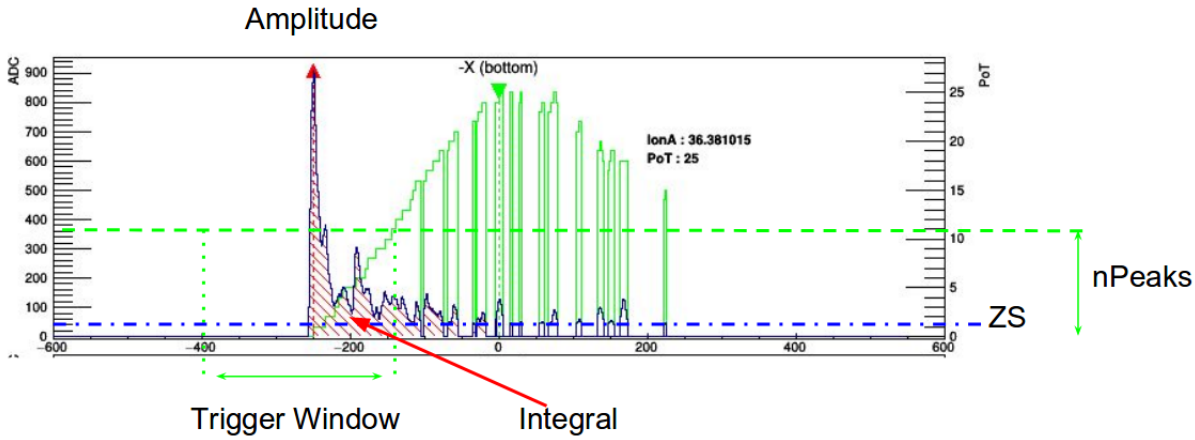

Figure 7.1: Neutron signal reconstruction from a waveform that passed the neutron trigger. The X axis represents the time in samples of 25 ns. The integral is shown in red sripes. The zero-suppression (ZS) is shown in blue. The number of peaks over threshold within a sliding time window of 6.4 μs is represented in green.

The ratio integral over amplitude (IonA) is computed to reject misidentified neutrons. Neutron candidates with a IonA that do not pass the condition from equation 7.1 or with an amplitude higher than 10000 adc are rejected as shown in figure 7.2. The neutron time is computed as the mean value of the two closest times of maximum amplitude for orthogonal channels that constitute the cube.

$$\text{IonA} < 10 + 0.005 \times \text{Amplitude} \tag{7.1}$$

7.3.3 Muon reconstruction

Two types of muon objects are reconstructed in Saffron2: muon tracks and muon veto cubes.

Muon tracks consist of events with at least 8 horizontal channels and 8 vertical channels. An example can be seen in figure 7.3. The energy of the event, corresponding to the sum amplitude of the peaks of the event converted from adc to MeV, must be above 3 MeV. The channel positions are fitted with straight lines to reconstruct the 3D coordinates of the tracks. The tracks that are within a single plane can not be fitted because of ambiguities to reconstruct cubes but they are

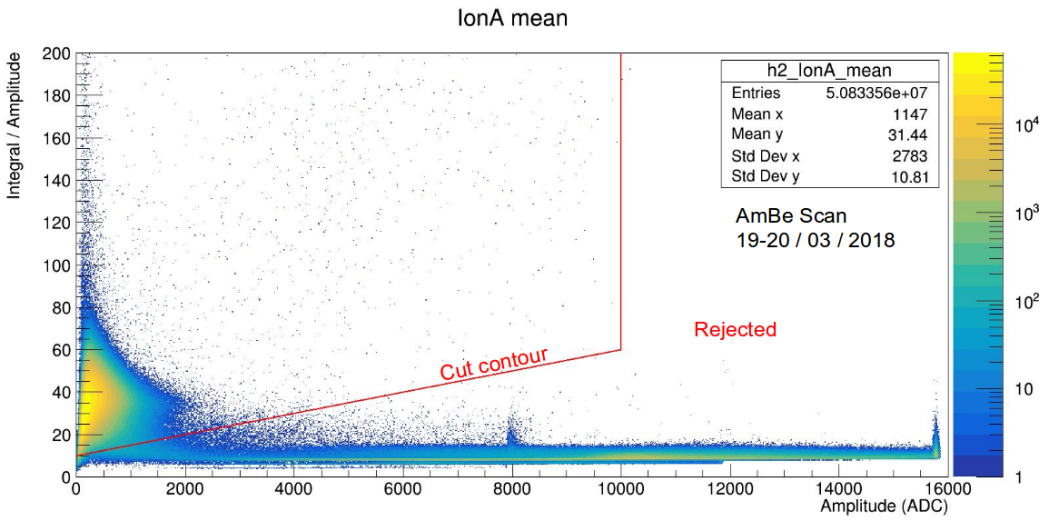

Figure 7.2: Neutron signal selection based on the ratio of the signal integral over amplitude vs the amplitude (IonA) with AmBe calibration data.

tagged for the muon veto. The rate of muon tracks varies between 203 and 221 Hz in the data.

To identify clipping muons, a muon cube object has been introduced. They consist of cubes with 2 horizontal and 2 vertical channels with at least one channel at the edge of the detector and a total amplitude above 4 MeV. Cubes in the outer layer with a total amplitude above 8 MeV are also tagged as muon cubes. These objects have a higher efficiency to tag muons than tracks but a lower purity as high energy γ can also be tagged. The muon tracks and cubes have a tagging efficiency of 94.9% according to simulations.

The muon rate has been compared to pressure variations. As seen in figure 7.4, a clear correlation of the muon rate with pressure is visible as expected. Indeed, an increase of pressure leads to higher probability for a muon to be absorbed in the atmosphere.

7.3.4 EM cube reconstruction

EM cubes are reconstructed within an event of 80 ns as explained in section 7.3.1. For each peak that has not been associated to a cube yet, a peak in an orthogonal channel of the same plane is looked for. If a peak is found, it creates a new cube. All the remaining peaks in the event in channels with the same X, Y and Z positions are added to this cube. This cube reconstruction algorithm recreates thus all possible cubes in an event. The next section is a study of the cube reconstruction performance.

The cube energy is given by the sum amplitude of all the channels belonging to this cube. The gain equalisation and the calibrations have already been presented

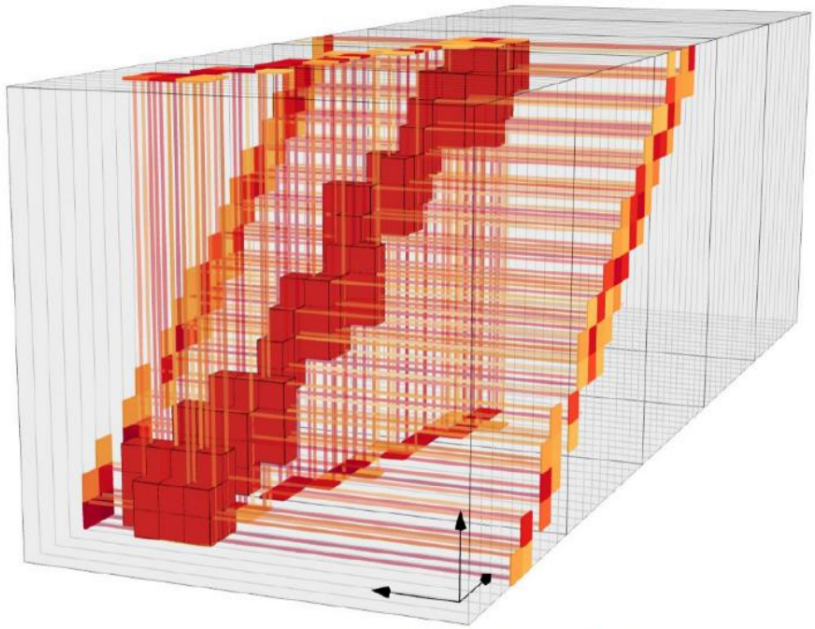

Figure 7.3: Example of reconstructed muon track.

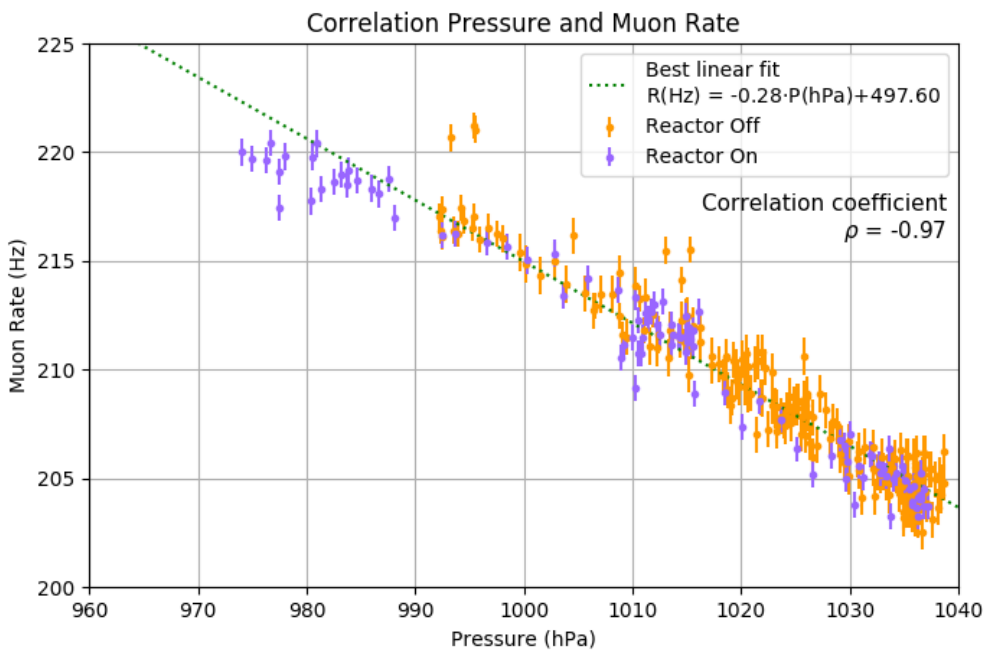

Figure 7.4: Reconstructed muon rate vs pressure for reactor On (in violet) and reactor Off (in orange) data.

in chapter 6. To scale the energy in adc into MeV, a constant gain of 32 adc/PA for May data is applied. It is measured using random trigger runs. An average calibration constant of 77 PA/MeV, obtained from calibration with CROSS, is used to convert the cube energy into MeV. A more precise cube per cube calibration will be implemented soon.

7.4 EM cubes reconstruction cuts

7.4.1 Cube reconstruction performance

As all possible cubes within an event are reconstructed, several cubes can be misreconstructed and artificial (i.e. non physical) cubes can be created due to ambiguities as shown in figure 7.5. Cubes misreconstruction can come from two peaks from the same channel added to a same cube while they come from two different cubes along this channel (orange cubes in figure 7.5). This would lead to a misreconstruction of the energy. Artificial cubes are created by peaks from different cubes in the same plane and the same event that are assembled together to form another cube (red cubes in figure 7.5). A study of commissioning data from December to improve the cube reconstruction is presented in the following.

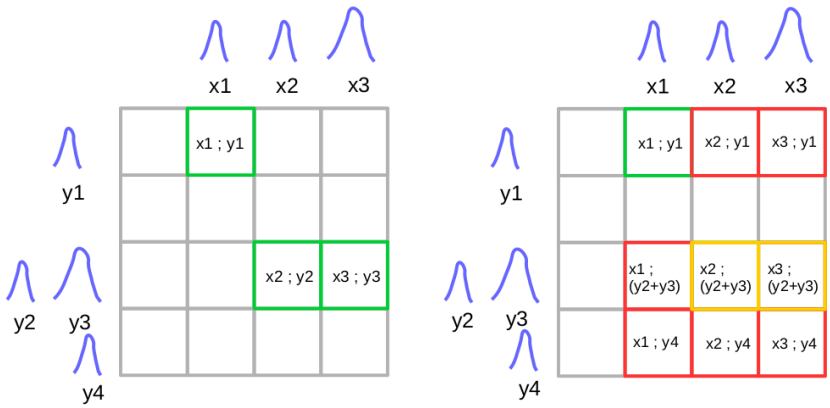

Figure 7.5: *Left*: cubes with physical signals. The peak number 4 can be due to noise like dark count. *Right*: reconstructed cubes. The green cube is well reconstructed. The orange cubes are physical cubes whose total amplitude is misreconstructed. The red cubes are artificial cubes that were reconstructed by Saffron2 algorithm but that are not physical. The drawing are simplified considering only 2 channels per cubes instead of 4.

The number of peaks per channel and the number of fibers (i.e. channels) per cube has first been studied. Figure 7.6 shows that most of the cubes have the same number of peaks and fibers which means that the misreconstruction issues shown in orange in figure 7.5 are rare. However, one can notice that many cubes are reconstructed with 2 or 3 fibers. These cubes are likely to be artificial cubes.

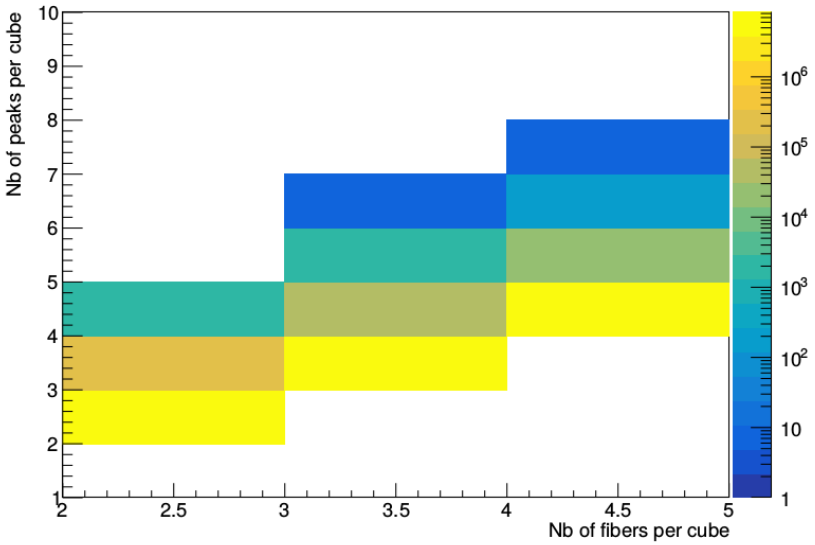

Figure 7.6: Number of peaks associated to the same reconstructed cube as a function of the number of fibers associated to this cube.

Figure 7.7 shows the minimum of the peak amplitudes for cubes depending on the number of channels that form the cubes. This figure demonstrates that the detector is sensitive to single photo-avalanche peaks and that cubes with low number of fibers also have a very low minimum amplitude. Such low amplitude signals are likely to be due to noise like SiPM dark counts. This motivated the 200 adc peak threshold to reconstruct cubes for the first data analysis and the rejection of cubes with less than 4 fibers.

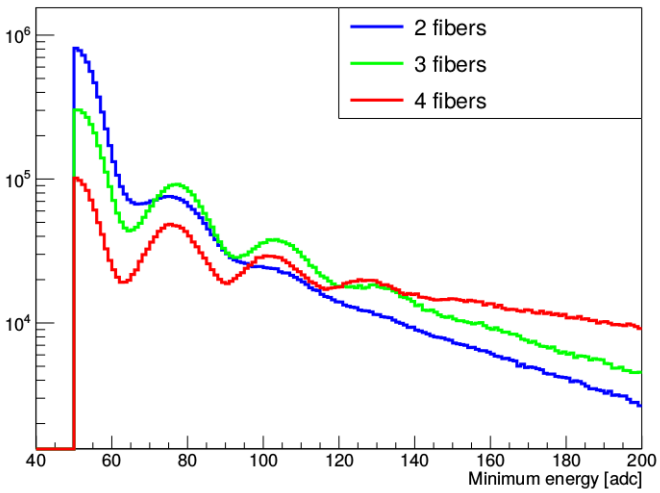

Figure 7.7: Distribution of the peak amplitude (in adc) of the channel with minimum energy for each reconstructed cube for different numbers of fibers (i.e channels) per reconstructed cubes.

7.4.2 Asymmetry cut

To furthermore reject artificial cubes created because of ambiguities in the cube reconstruction, an energy asymmetry variable has been introduced. The asymmetry is computed as in equation 7.2:

$$A = \frac{E_{av}(hor) - E_{av}(ver)}{E_{av}(hor) + E_{av}(ver)} \tag{7.2}$$

.

With $E_{av}(hor)$ the average energy (converted from peak amplitude) of horizontal channels and $E_{av}(ver)$ the average energy of vertical channels.

Physical cubes should have similar peak amplitudes so the energy asymmetry should be low. Figure 7.8 shows the energy asymmetry for cubes with different number of fibers. The histogram that represents cubes with 2 fibers, in blue, shows bumps at asymmetries below 0.7. These are due to very low amplitude signals assembled with each other for which single PA peaks are well distinguished. It demonstrates that the energy asymmetry variable is not efficient to remove very low amplitude signals which is why the peak threshold has been set at 200 adc.

In these figures, it can also be seen that cubes with 3 or 4 fibers present a peak at very high asymmetry, above 0.8, which is even more important for 3 fiber cubes and is very likely due to misreconstructed cubes. The asymmetry should thus be useful to remove ambiguities as physical cubes have only low asymmetry values as it will be demonstrated in section 7.4.4. Cubes with an energy asymmetry above 0.7 have been removed.

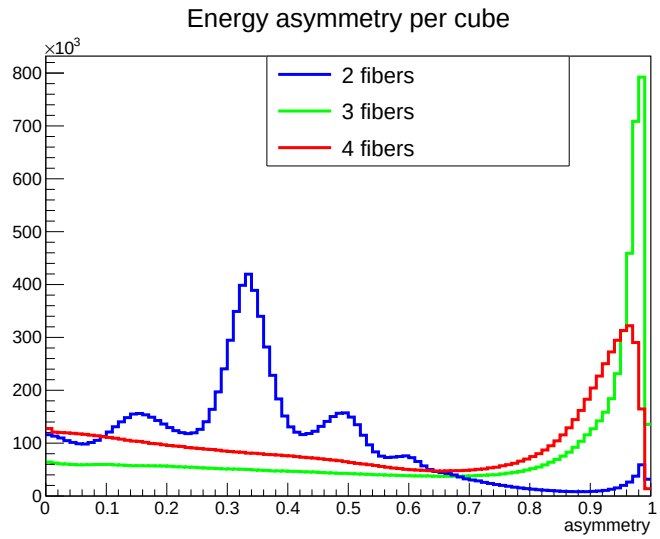

Figure 7.8: Energy asymmetry distribution for cubes with a different number of fibers.

7.4.3 Multiplicity cuts

The first reconstruction cuts that are set to select EM cubes are thus: a minimum peak energy of 200 adc (around 300 keV), signals on the 4 fibers, and an energy asymmetry below 0.7. Although it reduces a lot the number of artificial cubes, a multiplicity cut is then required to avoid creating several EM-neutron pairs with different EM signals from the same physical event.

For this first analysis, it has been decided to keep events with only one reconstructed EM cube with energy above 1 MeV. It allows to have cubes with energy below 1 MeV in the same event but prevent from linking 2 prompt candidates with energy above 1 MeV of the same event with the same neutron. However in the future, the cube multiplicity within a same physical event will be used to discriminate between IBD signals and backgrounds. It could allow for example to tag IBD events by detecting the two annihilation gammas at 511 keV in different cubes from the one where the positron annihilated.

7.4.4 Validation of the cuts with AmBe data

In order to understand the efficiency of the asymmetry variable to distinguish physical and artificial cubes, the 4.4 MeV gammas in the AmBe calibration data have been used. In the energy spectrum (figure 7.9) obtained during the AmBe calibration campaign, the Compton edge of the 4.4 MeV gammas can be seen around 300 PA. To select these gammas, only the cube in front of the source has been kept and an energy cut requires the minimum cube energy to be above 1.5 MeV.

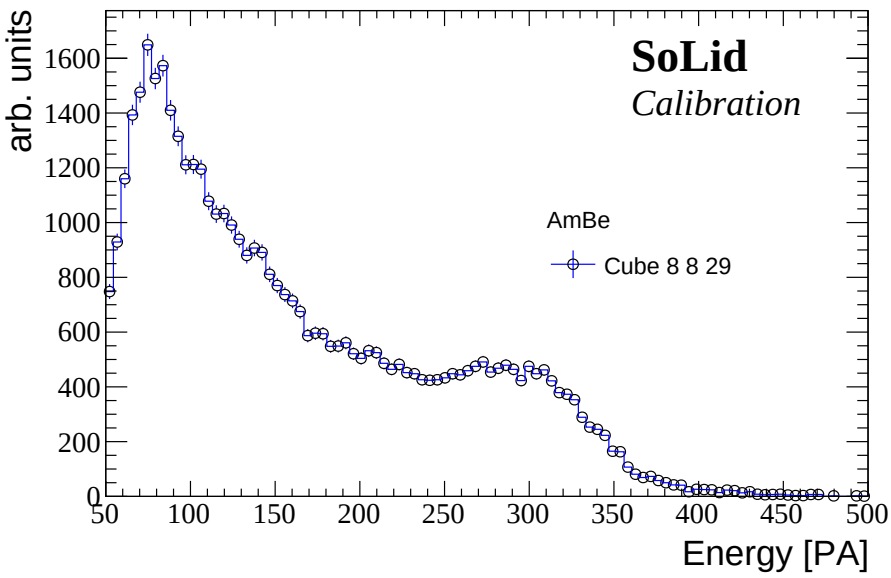

Figure 7.9: Energy distribution in PA for a cube in front of the AmBe source.

The asymmetry distribution in figure 7.10 is peaked at 0 and shows that most

of these physical events have an asymmetry below 0.6. It demonstrates that an asymmetry cut at 0.7 has no impact on physical events and is thus justified to remove most of the artificial cubes.

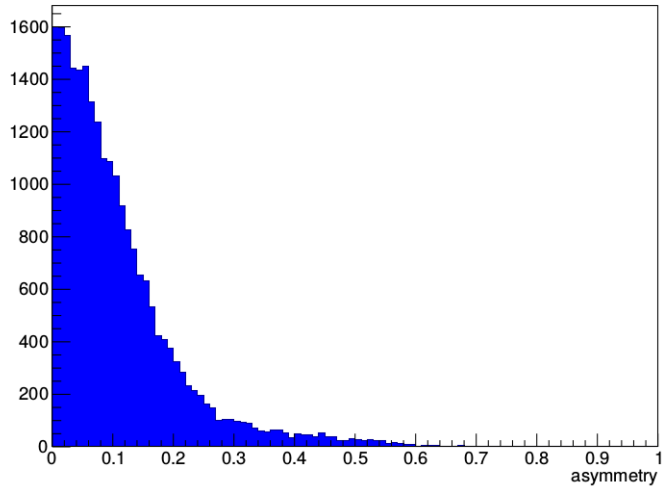

Figure 7.10: Energy asymmetry distribution for the cube in front of the AmBe source with a minimum energy of 1.5 MeV.

As the AmBe calibration source emits neutrons in coincidence with 4.4 MeV gammas, neutron and EM cubes with an energy above 2 MeV detected within 300 μs are paired. The time difference between the delayed and the prompt signal is shown in figure 7.11. The accidental contribution, in green, is measured by searching neutron events in the 100 μs before the EM signals. The distribution is fitted with two decreasing exponentials plus a constant (equation 7.3):

$$f(\Delta t) = c_1 \times exp(-\frac{\Delta t}{\tau_1}) + c_2 \times exp(-\frac{\Delta t}{\tau_2}) + c_{acc} \tag{7.3}$$

The constant term c_{acc} is fixed with the fit of the accidental distribution. The time constants extracted from the fit are $\tau_1 = 11.1 \pm 2.9$ μs and $\tau_2 = 66.7 \pm 1.0$ μs. It is consistent with the expected values from AmBe calibration simulations presented in figure 7.12: $\tau_1 = 12.9 \pm 0.7$ μs and $\tau_2 = 67.96 \pm 0.15$ μs. This demonstrates the good reconstruction of EM and neutron cubes.

7.5 IBD cuts study with simulation data

To start a first analysis of SoLid data and look for IBD signals, some preliminary studies have been performed on simulation data. A set of preliminary cuts has been defined.

The SoLid phase I detector has been simulated using the GEANT4 software. IBDs were generated uniformly in the whole detector. A preliminary readout simulation has also been used to get simulation data as similar as possible to the detector

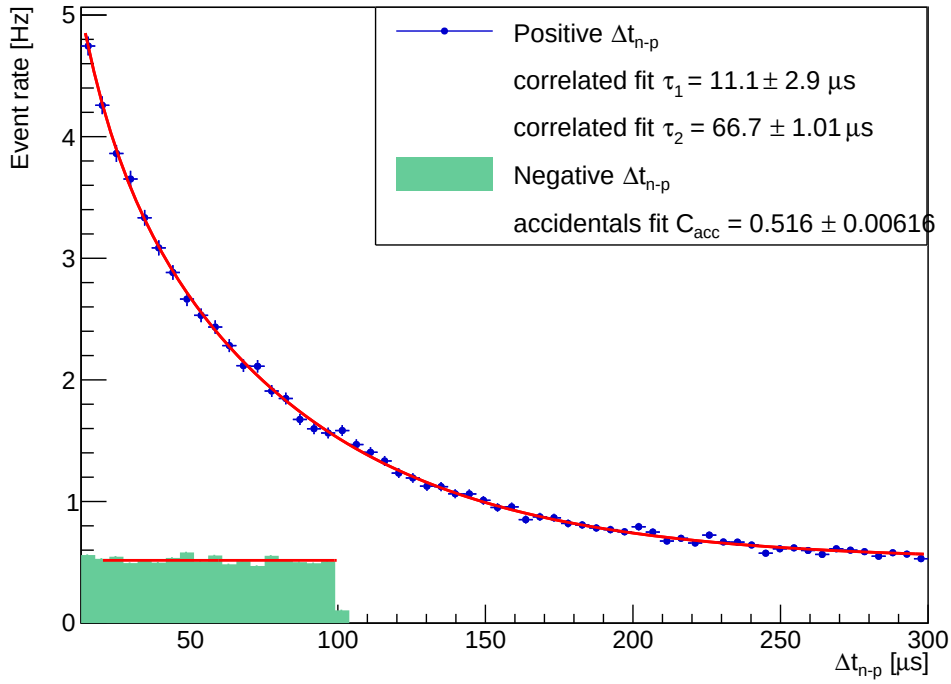

Figure 7.11: Distribution of the time difference between the neutron and the prompt for AmBe calibration data. The green filled histogram shows the accidental distribution obtained by selecting neutrons before the prompts. For convenience, the accidentals negative time window is plotted in the positive time window. The blue points show the correlated events. The distribution is fitted with two decreasing exponentials (with time constants τ_1 and τ_2) plus a constant (obtained from the fit of the accidentals C_{acc}).

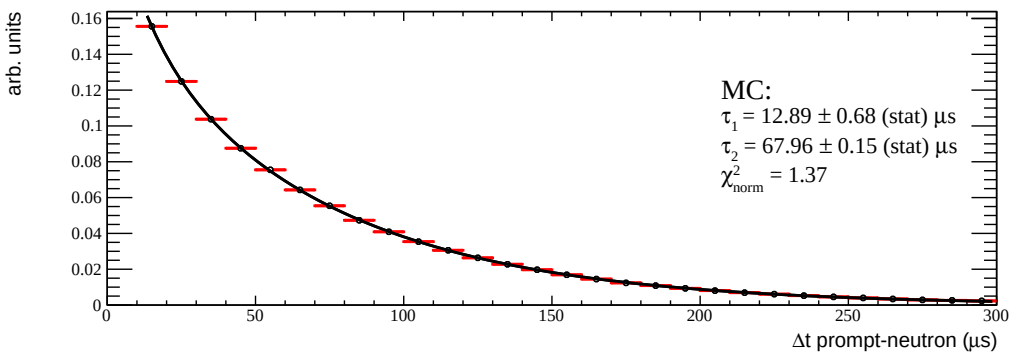

Figure 7.12: Distribution of the time difference between the neutron and the prompt for AmBe simulations. The distribution is fitted with two decreasing exponential with time constants τ_1 and τ_2.

data. The readout simulation converts the energy depositions from the GEANT4 simulation to waveform signals taking into account various effects like scintillation time characteristics, losses due to the fiber attenuation, the SiPM quantum efficiency, the probability for a photon to miss the SiPM surface... The number of photo-avalanches is also increased with the cross-talk, after-pulses and dark counts. The SiPM pulse shapes are tuned to match the amplitude and integral spectra. Only the simulated signals that pass the trigger conditions are kept.

EM cubes that passed the reconstruction cuts have been paired with the reconstructed neutron cube of the same IBD generated event. Figure 7.13 shows that the distribution of the delayed time between prompt and neutron can be fitted with 2 decreasing exponentials with time constants $\tau_1 = 13.3 \pm 2.3$ μs and $\tau_2 = 63.7 \pm 0.5$ μs. This is quite consistent with the neutron thermalisation and capture times found with AmBe data. Removing events with a time difference above 100 μs should keep 80 % of the IBD events.

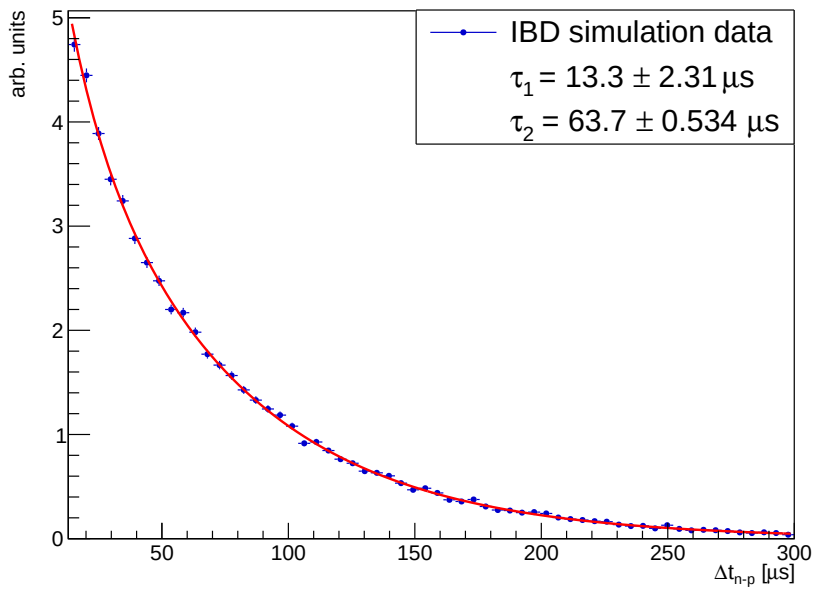

Figure 7.13: Time difference between a reconstructed neutron cube and a reconstructed EM cube for IBD simulations. The distribution is fitted with two decreasing exponential with time constants τ_1 and τ_2.

The distance between the prompt and the neutron is also shown on figure 7.14 and figure 7.15. It demonstrates that the fine segmentation of the SoLid detector is useful to set strict cuts on these variables as the IBD signals are very localised. An asymmetry can be seen on the ΔZ and ΔX distributions. It is due to the position of the two Li sheets in the cube. By requiring ΔX = ΔY = [-2,2] cubes, ΔZ = [-2,3] cubes and ΔR = [0,3] cubes, with ΔR the distance reconstructed in 3 dimensions, 96% of the IBD events are kept. The asymmetry in Z is justified by the boost of

the neutron due to the reactor antineutrino flux direction.

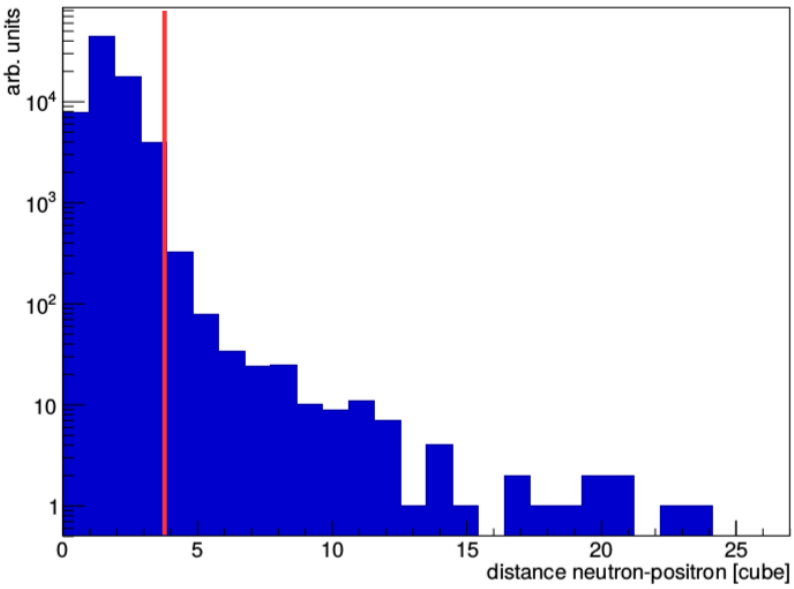

Figure 7.14: Distance between a reconstructed neutron cube and a reconstructed EM cube expressed in cube units for IBD simulation data. The red line represent the IBD cut.

The energy distribution of the simulated prompt signal is shown in figure 7.16. A maximum energy cut has also been studied. Keeping only prompts with an energy below 3000 adc which corresponds to 6.5 MeV keeps 99.6% of the simulated IBD events. These first cuts may not be optimized but are used as a starting point for a preliminary analysis. They keep 76% of simulated IBD events.

7.6 BiPo background study

7.6.1 BiPo search

BiPo is a background from ^{238}U natural radioactivity described in chapter 5 that contaminated ^{6}LiF:ZnS sheets in SM1. While the electrons and gammas emitted by the ^{214}Bi decay to ^{214}Po have an energy up to the end-point $Q_\beta = 3.27$ MeV and can thus mimic a prompt interaction in the PVT, the α emitted in the ^{214}Po decay to ^{210}Pb can mimic a neutron signal in the Li sheet.

A search for BiPo contamination has been done in the December commissioning data. In addition to the reconstruction cuts, several dedicated cuts have been used to look for BiPo events. Pairs of EM and neutron cubes have been done by requiring, like in SM1 analysis, the prompt and the neutron signals to be in the same cube. The prompt energy had to be above 1 MeV and below 3 MeV to get a

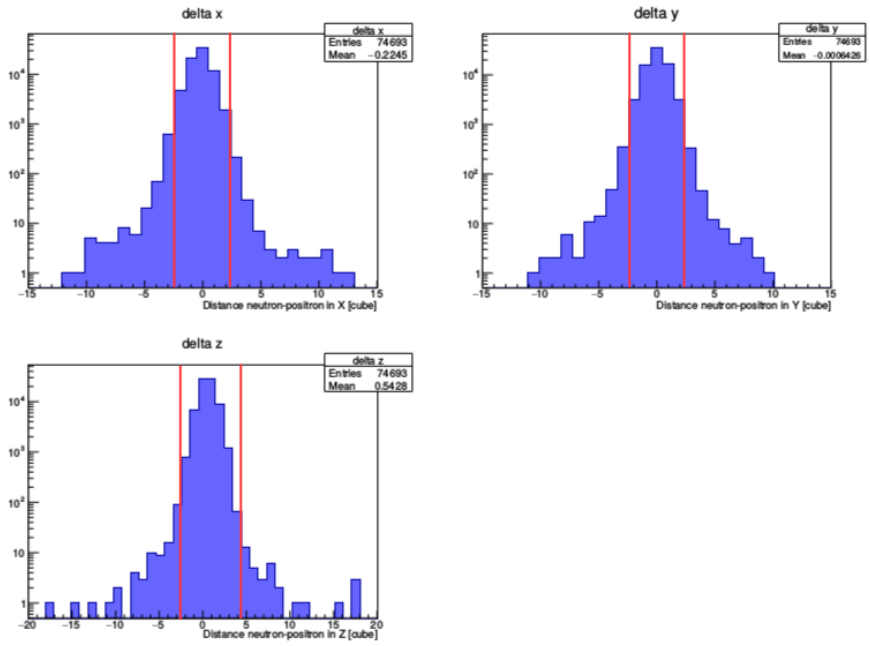

Figure 7.15: Distance in X, Y and Z between a reconstructed neutron cube and a reconstructed EM cube expressed in cube units for IBD simulation data. The asymmetry in X and Z is due to the Li sheets positions and the direction of the reactor antineutrino flux for Z. The red lines represent the IBD cuts.

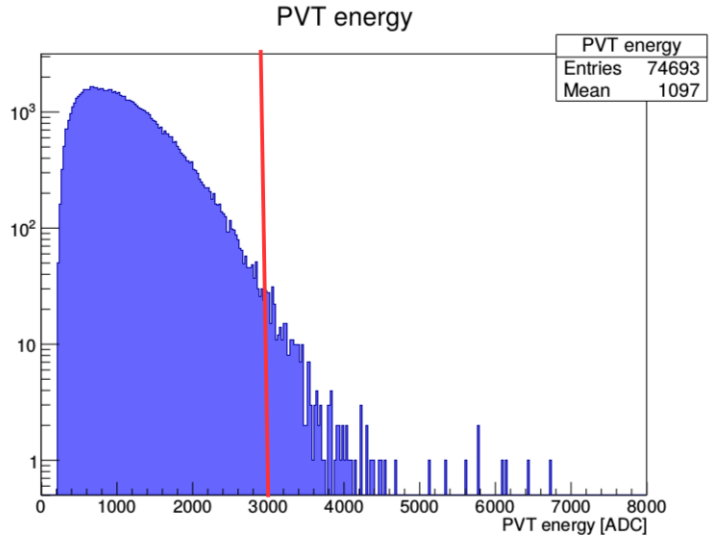

Figure 7.16: Prompt energy distribution in adc from IBD simulations.

clear BiPo signal. Neutron signals were searched in a time window of [-100, 300] μs around the prompt as the ^{214}Po half-life is $T_{1/2}^{^{214}Po} = 163.6 \pm 6$ μs.

Figure 7.17 shows the distribution of the time difference between the prompt and the delayed signal for the BiPo selection data. These distributions have been fitted with equation 7.4 in order to check if the BiPo half-life could be measured. This would be indeed an indication for BiPo contamination in the Li sheets of the SoLid detector.

$$f(\Delta t) = c_1 \times exp(-\frac{\Delta t}{\tau_n}) + c_2 \times exp(-\frac{\Delta t}{\tau_2}) + c_{acc} \tag{7.4}$$

The first exponential in equation 7.4 fits the contribution of fast neutron events with the neutron thermalisation and capture time τ_n measured previously as τ_2 in equation 7.3. The first exponential of equation 7.3 was neglected as τ_1 is small compared to the fit range values between 20 and 300 μs. The constant c_{acc} corresponds to the accidental distribution. It is fitted for negative Δt_{n-p} above 100 μs. The fit parameters are thus c_1, c_2 and τ_2. Both values of τ_2 are consistent for data reactor On and Off. The measured value of τ_2 is $\tau_2 = 250 \pm 20$ μs which gives a ^{214}Po half-life $T_{1/2}^{^{214}Po} = \tau_2 \times ln2 = 173 \pm 14$ μs. This is consistent with the expected value.

This good measurement of the ^{214}Po half-life shows that there is BiPo contamination in the Li sheets so work will have to be done to discriminate these events from the IBD signals. It also demonstrated that the object reconstruction, particularly the position and time of EM and neutron cubes, is working well.

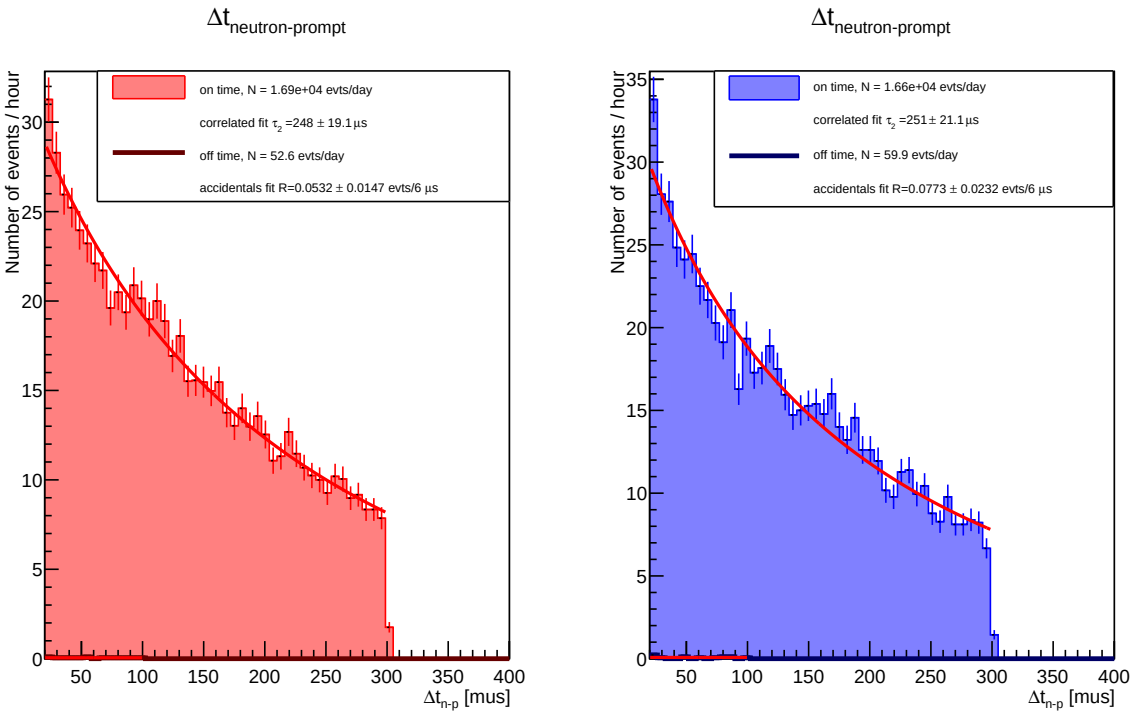

Figure 7.17: Time difference between delayed and prompt signals for the BiPo event selection. On the right the search is done with reactor On data and on the left with reactor Off data. The distributions are fitted with equation 7.4 in order to measure the ^{214}Po half-life. The accidentals are fitted in the range $\Delta t_{n-p} < 100\mu s$ with a constant. They are selected using a negative time window.

7.6.2 BiPo removal

BiPo events have been simulated in the Li sheets. It has been shown that most of BiPo interactions remain in the same cube as most of the time, the electron emitted in the ^{214}Bi decay deposits the largest part of its energy in the PVT cube close to the Li sheet where the disintegration takes place. By removing events with prompt and neutron interacting in the same cube (i.e. ΔR = 0), the BiPo contribution can be reduced by 73% while IBD events are only reduced by 15%.

To remove the BiPo background even more, a minimum energy cut can be set. The maximum prompt energy deposit by BiPo events is 3.27 MeV. However, removing IBD-like events below this energy would reduce the signal too much. According to a preliminary analysis of simulations, cutting events with a prompt energy below 2.8 MeV is a good compromise to remove most of the BiPo events as it decreases the number of BiPo events by 91% while the number of IBD events is reduced by 27 % compared to a minimal energy cut at 2 MeV.

Li sheets scintillation light is currently under study to remove the BiPo background using pulse-shape discrimination. Indeed, for BiPo the α energy is greater than for IBD neutron capture on ^{6}Li.

7.7 Study of background from after-muon events

To avoid selecting muon induced background, a veto on IBD-like events after reconstructed muons has been studied and optimised.

Using the reactor Off data, IBD-like events were formed with previous IBD cuts: ΔR_{n-p} =]0; 3] cubes, $\Delta X_{n-p} = \Delta Y_{n-p}$ = [-2; 2] cubes, ΔZ_{n-p} = [-2; 3] cubes, Δt_{n-p} = [0; 100] μs. Different time windows between muons and neutrons have been tested to reject IBD-like events after muons. A negative time window between neutron and muons has been used to subtract the accidentals. Figure 7.18 shows the fractional excess of IBD-like events for different muon veto times in blue. A good compromise between muon-induced background rejection efficiency and dead time has been found using a muon veto time of 200 μs. The same veto time has been used between two neutron cubes to remove neutrons induced by cosmic rays.

7.8 Search for IBD events

IBD-like events have been searched for reactor On and OFF data. 18 days of reactor On and 7 days of reactor Off data have been used. The following cuts, discussed previously, have been set:

- $A_p < 0.7$ (prompt asymmetry cut)
- Only one prompt with energy above 1 MeV per event
- E_p = [2.8, 6.5] MeV

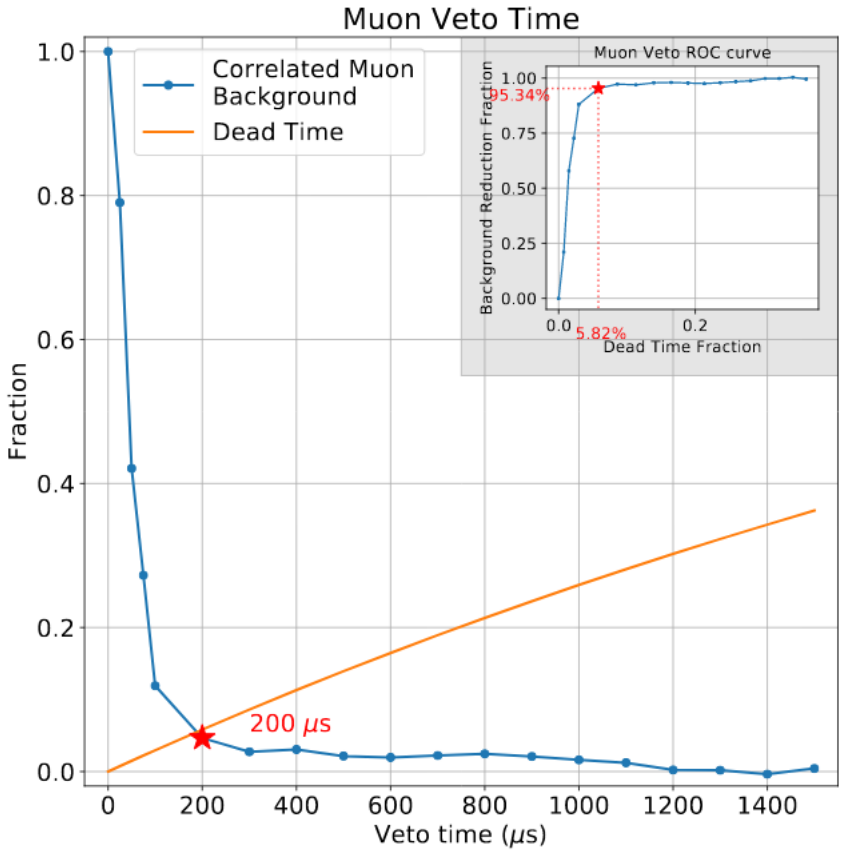

Figure 7.18: Fraction of after-muon IBD-like events remaining when using different muon veto times (in blue) and fraction of dead-time induced by these muon veto time (in orange). It has been chosen to use a muon veto time of 200 μs to remove muon induced background by 95.34% and limit the dead time to 5.82%.

- ΔR_{n-p} =]0, 3] cubes
- ΔX_{n-p}, Y_{n-p} = [-2, 2] cubes
- ΔZ_{n-p} = [-2, 3] cubes
- Δt_{n-p} = [0, 100] μs
- $\Delta t_{n-\mu} > 200$ μs
- $| \Delta t_{n-n} | > 200$ μs

Figure 7.19, top, shows the number of events per day selected with these cuts after subtracting the accidentals. The accidental distribution, shown on the bottom plot, is obtained using a negative time window of 100 μs. An excess of around 172 IBD-like events per day on average appears between reactor On (in blue) and reactor Off (in pink) data. For reactor On data, 35578 IBD-like events were found between the 5th and the 21st of May while for reactor Off data, 13442 IBD-like events were found between the 23rd and the 29th of May.

The distributions of the time difference and distance between neutrons and prompts for reactor On (in red) and reactor Off (in blue) are shown in figure 7.20 along with the prompt energy distribution. The excess seems consistent with IBD simulation distributions but it is not statistically significant enough to perform a precise comparison.

To compute accurately the IBD excess, the spectra for reactor On and OFF have to be carefully normalised. One parameter to take into account is the pressure. The pressure variations are plotted at the middle of figure 7.19. It has been shown in section 7.3.3 that the muon rate, and thus muon induced backgrounds, vary with pressure. However, it has also been shown that BiPo is a background from natural radioactivity present in the SoLid detector and it can not be scaled according to pressure variations. Some work is ongoing to understand accurately the contributions of the different backgrounds and how to rescale rigorously the reactor On and reactor Off histograms in order to show an IBD excess.

7.9 Conclusion

The commissioning data from December 2017 have been useful to work on the EM, neutron and muon cube reconstruction. The AmBe calibration data demonstrated that the EM and neutron cube reconstruction works well. As the ^{214}Po half-life can be fitted well in the data, it proves again that the objects are well reconstructed but it also indicates that the Li sheets are contaminated with BiPo events.

A preliminary analysis of SoLid data acquired in May 2018 has been done. The cuts set in this analysis are strict in order to understand the events selected. An excess of 172 IBD-like events per day has been seen when comparing reactor On and reactor Off data. However more statistics is required, the backgrounds have to be

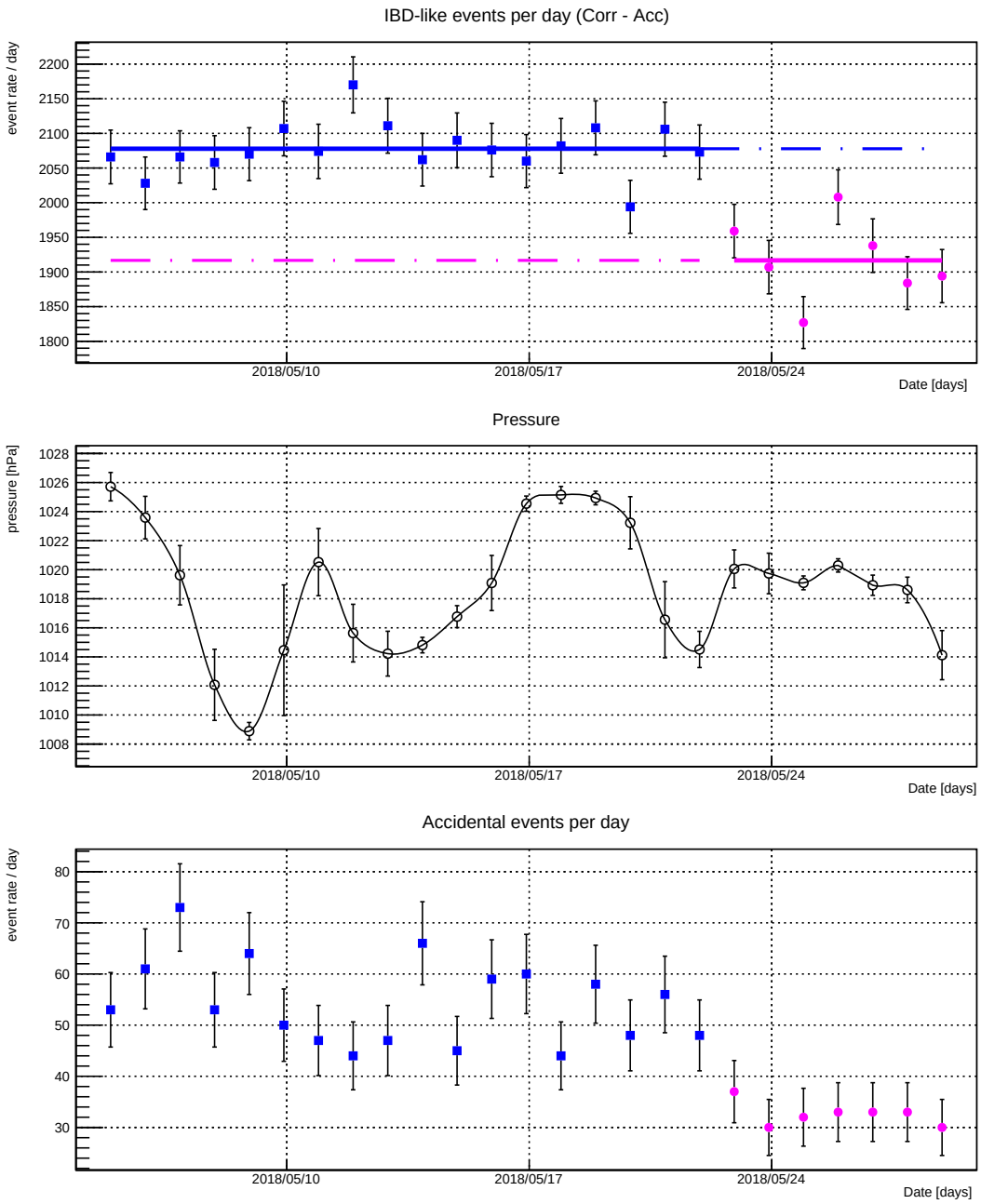

Figure 7.19: *Top*: IBD-like event rate per day. The accidentals (obtained with negative time-window) are subtracted from the correlated (obtained with positive time-window). Reactor On data are shown in blue, reactor Off data are shown in pink. *Middle*: average pressure per day. *Bottom*: accidental rate per day.

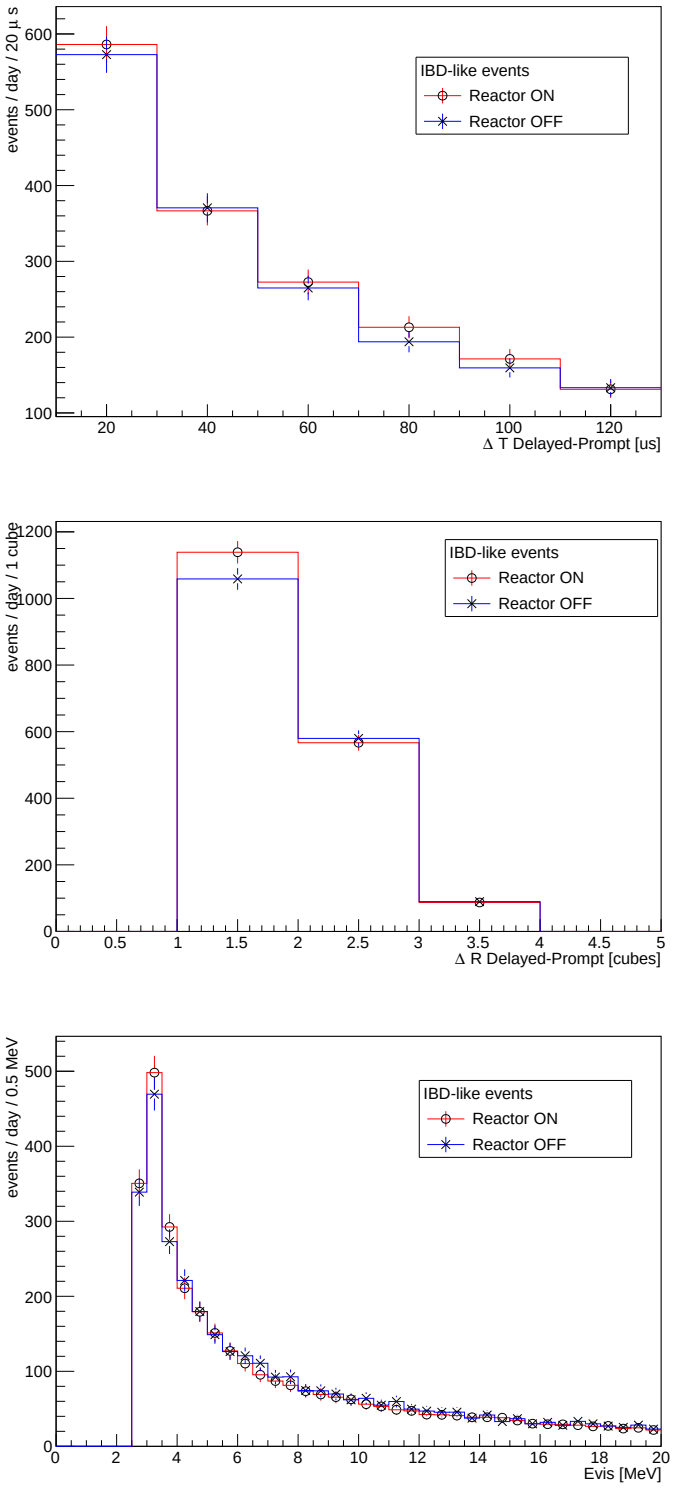

Figure 7.20: Distributions of neutron and prompt pairs passing IBD selection cuts after subtraction of accidentals for reactor On data in red and reactor Off data in blue. *Top*: time difference between neutron and prompt. *Middle*: distance between neutron and prompt. *Bottom*: prompt energy.

reduced and work has to be done on the renormalisation of reactor On and Off data.

More sophisticated object reconstructions are being studied to discriminate better IBD and background events. Instead of reconstructing all possible cubes, including artificial cubes for which strict cuts are required to remove them, the use of clusters of fibers is under investigation. Some work is being done also to reconstruct the 2 annihilation gammas to better tag the IBD events. As explained previously, a pulse shape discrimination of the Li sheet scintillation signals is also being studied to remove BiPo events.

Conclusion

Neutrino physics is a fascinating field full of mysteries that challenges our knowledge of particle physics. Detecting and understanding neutrinos interactions can teach us a lot about the Universe. Many exciting new results should be produced in the coming years in the search of neutrinoless double beta decay or sterile neutrinos. To get these results, huge efforts are provided by physicists to build great neutrino detectors with the state-of-the-art technologies.

During this thesis, I got the opportunity to take part to the construction of two fascinating neutrino experiments: SuperNEMO and SoLid. Their technologies and their environments are very different so it was really interesting to understand how such big detectors of the infinitely small are built.

The SuperNEMO demonstrator, with its tracking and calorimetry technology, should determine the feasibility of such an experiment with more than 100 kg of ^{82}Se to search for neutrinoless doube beta decay. A huge work has been done to select only radiopure materials and to shield the detector against radioactivity. The remaining external background from the PMT radioactivity has been studied. I have shown that if the internal and radon backgrounds are reduced as expected, this external background could be one of the main contributions to measure the $2\nu\beta\beta$ half-life of ^{82}Se. Fortunately, the SuperNEMO technology allows tagging events in different channels and the crossing electrons or the γe-ext channels should help to measure these backgrounds with a statistical uncertainty of 0.1%. In order to predict the efficiency of copper foils to provide an independent measurement of the external background, I have also done simulations of copper instead of ^{82}Se foils in the detector. With this study, it was decided to install two strips of copper which should provide a measurement of the external background with a statistical uncertainty of around 10%.
The ^{82}Se source foils should be installed in the demonstrator in September 2018, just before its closing. First commissioning data should thus be taken at the end of this year without the shielding. The demonstrator sensitivity on the $0\nu\beta\beta$ half-life should be $T^{0\nu}_{1/2} > 6.5 \times 10^{24}$ taking into account an exposure of 17.5 kg.year.

The SoLid experiment searches for sterile neutrinos with a very segmented detector installed at a few meters from the BR2 reactor core in Belgium. The first prototype, SM1, demonstrated that this technology is useful to discriminate cosmic backgrounds or BiPo events from IBD signals.
In order to get a better energy resolution for the phase I detector, we have built a

test bench at LAL to try several improvements like changing the materials or the configuration of the detector. Following the test bench studies, it has been decided to use thicker Tyvek wrapping, aluminised Mylar mirror at one end of each fiber, double-clad fibers and 4 fibers per cube instead of 2. These improvements were expected to increase the light yield by a factor 2.8 and thus reach the target energy resolution of 14% at 1 MeV.
The SoLid detector has been built in 2017. It was installed at BR2 in November 2017 and started taking commissioning data the following months. A first calibration has shown that the light yield has been increased by approximately a factor 3 reaching thus a value of 77 PA/MeV/cube without cross-talk subtraction. I have studied the event reconstruction using December commissioning data. To remove artificial cubes created by ambiguities when assembling fibers to reconstruct the signals, an asymmetry variable was used. A study of AmBe calibration data and a search for ^{214}Bi decays from the ^{238}U chain have demonstrated that the electromagnetic and neutron cubes are well reconstructed. However, it has also shown that the ^{6}Li:ZnS sheets are contaminated with ^{238}U. A preliminary search for IBD-like events has been done on data from May using strict cuts to understand the reconstructed signals. It presents as excess of IBD-like events for reactor On data. However, due to important cosmic and BiPo backgrounds and the lack of statistics, the excess distributions could not be properly normalised and compared to simulation data.
The SoLid detector is now taking data for the next 3 years. Analysis tools are being developed to remove backgrounds. A pulse shape discrimination of ZnS scintillation signals is under study and should help to remove BiPo events. Work is also ongoing to detect the 2 annihilation gammas from the positrons of the IBD signals.
The hunt for sterile neutrinos has started and SoLid, as well as other reactor experiments, should provide soon very exciting results.

Résumé

Les neutrinos sont les particules fondamentales de matière les plus abondantes dans l'univers. Leur existence a été prédite en 1930 par Pauli pour expliquer la continuité du spectre bêta. Ils ont été détectés pour la première fois en 1956 par Reines et Cowan en utilisant le processus de désintégration bêta inverse. Depuis lors, plusieurs expériences ont tenté de percer leurs mystères. On sait aujourd'hui qu'ils n'interagissent que par interaction faible, ils sont donc difficiles à détecter, et qu'ils peuvent osciller entre trois saveurs leptoniques. Cependant, de nombreuses questions perdurent sur leur masse, leur nature ou encore l'existence de neutrinos stériles. Cette thèse appréhende ces deux dernières questions à l'aide de deux expériences différentes : SuperNEMO et SoLid.

Le but de l'expérience SuperNEMO est de rechercher la nature du neutrino, c'est-à-dire s'il pourrait être sa propre anti-particule (particule de Majorana) ou non (particule de Dirac). Pour cela, on cherche à détecter des doubles désintégrations bêta sans émission de neutrinos ($0\nu\beta\beta$) car ce processus n'est possible que si les neutrinos sont des particules de Majorana. Pour rechercher ce type de désintégration, on mesure l'énergie des 2 électrons émis lors des désintégrations double bêta. L'observation d'un pic à l'énergie de transition signerait l'observation de $0\nu\beta\beta$. Ces expériences doivent avoir une exposition (masse d'isotope $\times$ temps) importante, une résolution en énergie optimale et le moins de bruits de fond possible. La diminution des bruits de fond se fait en sélectionnant pour le détecteur des matériaux très peu radioactifs, en le protégeant avec un blindage important et en l'installant en laboratoire souterrain pour le protéger des rayons cosmiques. Le choix de l'isotope double bêta se fait en fonction de la technologie de détecteur et en cherchant à avoir l'énergie de transition et le temps de demi-vie de la $2\nu\beta\beta$ ainsi que le facteur de phase et les éléments de matrice nucléaire pour la $0\nu\beta\beta$ maximaux. Plusieurs expériences recherchent actuellement la $0\nu\beta\beta$ avec des techniques très différentes: GERDA avec des diodes semi-conducteurs, CUORE avec des bolomètres, KamLAND-ZEN avec du scintillateur liquide, EXO-200 avec une TPC ou encore les expériences NEMO avec une technologie associant traqueur et calorimètre. Cette dernière technique est la seule qui permet de détecter les traces individuelles de chacun des deux électrons et de mesurer leur énergie.

Des feuilles sources de l'émetteur double bêta ^{82}Se seront installées au centre du démonstrateur SuperNEMO qui est actuellement en construction au Laboratoire Souterrain de Modane. Ce détecteur est composé d'une chambre à fils de 2034 cellules pour détecter les traces des deux électrons émis lors des désintégrations

et d'un calorimètre pour mesurer leurs énergies (figure 7.21). Le calorimètre est composé de 712 modules optiques associant un photomultiplicateur (PMT) à un scintillateur plastique en polystyrène. Un champs magnétique de 25 G servira à courber les traces des particules dans la chambre à fil pour mesurer leur charge. Le démonstrateur SuperNEMO, avec une exposition de 17.5 kg.ans, devrait être sensible à $T^{0\nu}_{1/2} > 6.5 \times 10^{24}$ ans. Avec 100 kg de ^{82}Se, le détecteur complet SuperNEMO devrait atteindre après 5 ans de prise de données une limite de $T^{0\nu}_{1/2} > 1 \times 10^{26}$ ans.

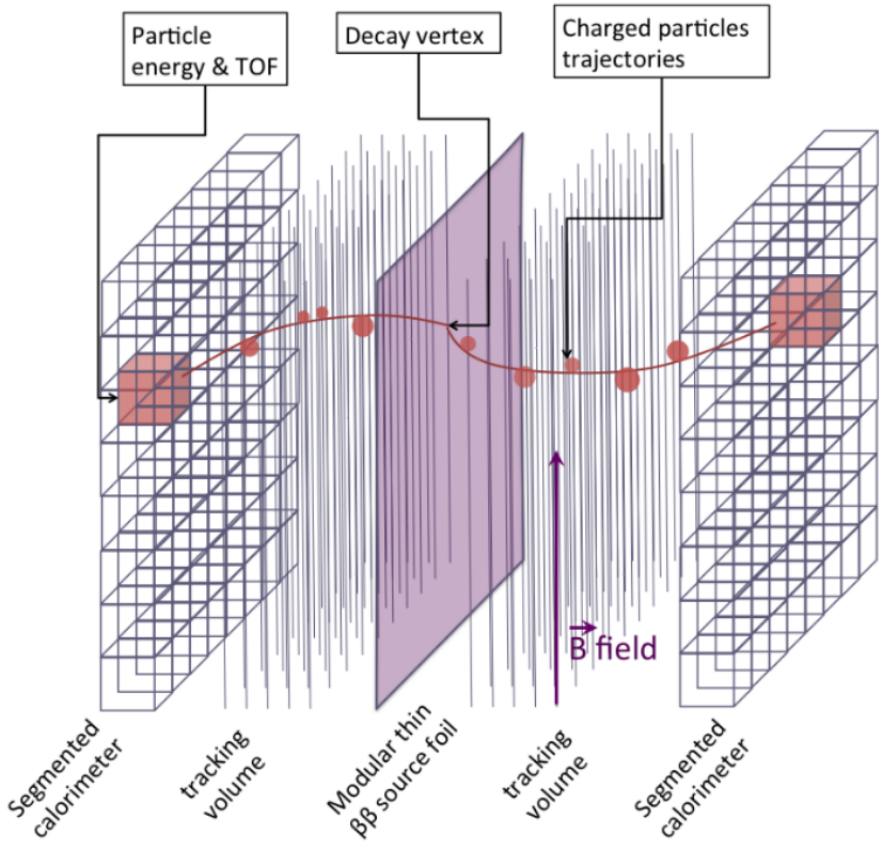

Figure 7.21: Principe de détection de l'expérience SuperNEMO avec le traqueur et le calorimètre. Deux électrons sont émis par la feuille source (en violet). Leurs traces (en rouge) sont détectées dans la chambre à fils avant qu'ils déposent leur énergie dans les blocs de calorimètre (cubes rouges).

Dans cette thèse, des simulations des différents bruits de fonds ont été faites pour comprendre leur impact sur la mesure de l'énergie des électrons issus de la double désintégration bêta du ^{82}Se. Les isotopes les plus problématiques sont notamment le ^{214}Bi et le ^{208}Tl qui font partie des chaînes de désintégration de l'^{238}U et du ^{232}Th à cause de leur grande énergie de transition. Des bruits de fond internes provenant de la source $\beta\beta$, du radon et des bruits de fond externes provenant du verre des PMTs, ont été simulés. L'analyse de cette thèse porte sur le bruit de fond externe qui peut contaminer la mesure de la $2\nu\beta\beta$ qui elle même impacte la mesure de la $0\nu\beta\beta$. En utilisant des coupures basées sur le temps de vol des particules, on peut tester

l'hypothèse que les particules viennent de la source ou des parties plus périphériques du détecteur. En utilisant les même coupures que pour l'expérience NEMO-3, on peut rejeter 97.6% du bruit de fond externe en gardant 87.2% des événements de $2\nu\beta\beta$. Le bruit de fond issu de la contamination des verres de PMTs représentera ainsi 3.4% des événements de $2\nu\beta\beta$ ce qui permettra une mesure précise de cette dernière (figure 7.22).

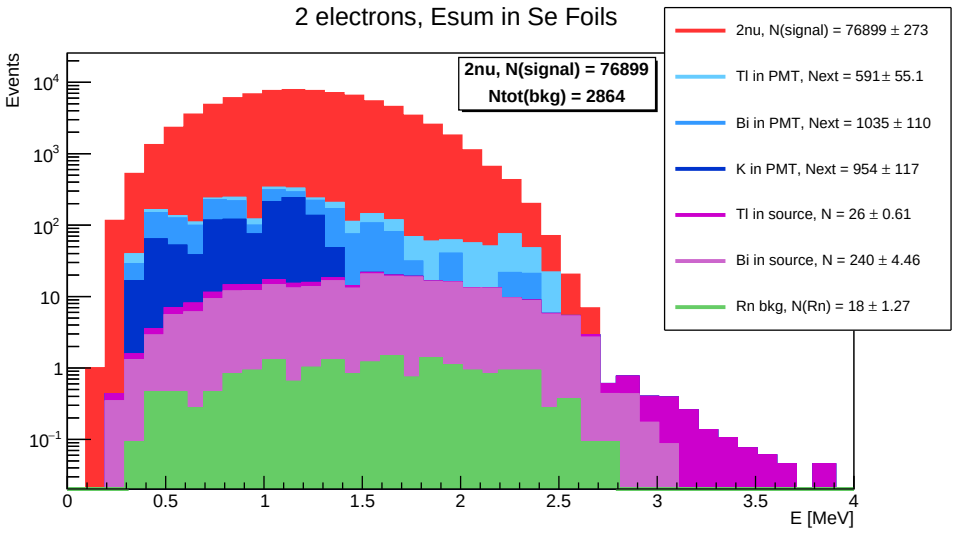

Figure 7.22: Distributions empilées de la somme des dépôts d'énergie des deux électrons dans les blocs des calorimètres dans le canal 2 électrons internes pour différentes sources de bruits de fond ou de signal $2\nu\beta\beta$ du ^{82}Se après les coupures de probabilités interne et externe.

Il est montré que la radioactivité du verre des PMTS pourra être mesurée après 2.5 ans dans le canal d'analyse électron traversant avec une incertitude statistique de 0.08% (figure 7.23) et dans le canal γ-électron externe avec une précision statistique de 0.13%. Des feuilles de cuivre ont aussi été simulées à la place des sources de ^{82}Se pour montrer qu'elles peuvent aider à contrôler le bruit de fond externe efficacement. Suite à ces travaux, il a été décidé d'installer des feuilles de cuivre de l'expérience NEMO-3 parmi les sources de ^{82}Se. Elles devraient permettre de contrôler le bruit de fond externe avec une incertitude statistique de l'ordre de 10%.

La deuxième expérience sur laquelle porte cette thèse est l'expérience SoLid qui recherche l'existence de neutrinos stériles. Plusieurs anomalies expérimentales ont été observées: des excès de ν_e et $\overline{\nu}_e$ pour les expériences LSND et MiniBOONE qui détectaient des neutrinos issus d'accélérateurs, les expériences au gallium SAGE et GALLEX qui ont observé un déficit de ν_e lors de leur calibration et des déficits de $\overline{\nu}_e$ d'expériences qui détectaient des neutrinos issus de réacteurs. Elles pourraient être expliquées par des oscillations d'antineutrinos de réacteurs vers des neutrinos stériles pour un Δm^2 de l'ordre d'1 eV^2. Plusieurs expériences tentent d'observer ce type d'oscillations de $\overline{\nu}_e$ de réacteurs à seulement quelques mètres du cœur telle que STEREO, PROSPECT, DANSS ou SoLid. Ces expériences doivent avoir une bonne résolution en énergie et une bonne sensibilité sur la position du vertex d'interaction en utilisant des détecteurs segmentés par exemple. Elles doivent également rejeter

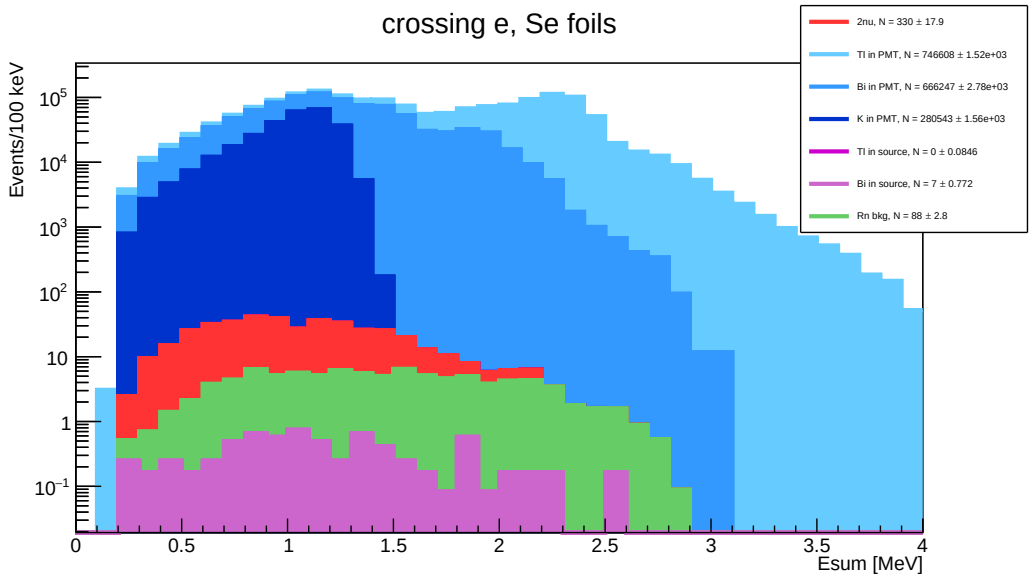

Figure 7.23: Distributions de la somme des dépôts d'énergie des deux électrons dans les blocs des calorimètres dans le canal électron traversant. Le bruit de fond externe a une contribution largement dominante par rapport aux événements provenant de la source de ^{82}Se et du radon.

efficacement le bruit de fond principalement cosmique.

Le détecteur SoLid cherche à mettre en évidence un signal d'oscillation auprès du réacteur BR2 en Belgique en mesurant le flux d'antineutrinos en fonction de leur énergie et de la distance parcourue, grâce à une grande segmentation. La détection des $\overline{\nu}_e$ de réacteur se fait par désintégration bêta inverse. L'interaction d'un antineutrino se traduit donc par l'émission en coïncidence d'un positron et d'un neutron. Les positrons sont détectés dans des cubes de plastique scintillant en PVT de 5 cm de côté et les neutrons sont détectés de manière retardée par des feuilles de ^{6}LiF:ZnS posées sur chacun des cubes (figure 7.24). L'analyse de la forme des pulses permet de distinguer les événements électromagnétiques, des événements neutroniques grâce à l'utilisation de ces deux scintillateurs (figure 7.25).

Un premier prototype, SM1, a montré l'intérêt de cette technologie notamment pour discriminer les bruits de fonds. Les principaux bruits de fonds viennent des muons et neutrons cosmiques et de contaminations en ^{214}Bi. A cause de statistiques limitées dues à l'interruption du réacteur pendant plus d'un an et d'une faible efficacité de détection des neutrons, SM1 n'a pas permis de rechercher des oscillations de neutrinos. Pour la construction du détecteur SoLid, afin d'améliorer la détection des neutrons et la sensibilité du détecteur aux oscillations de neutrinos, un objectif de diminuer la résolution en énergie de 20% à 14% à 1 MeV a été fixé.

Une partie des travaux de cette thèse a consisté à développer et exploiter un banc de test afin d'optimiser la collection de lumière du détecteur pour améliorer la résolution en énergie de SoLid. Ce banc de test consiste en un détecteur type SoLid avec un seul ou une rangée de cubes (figure 7.26). Un système de 2 PMTs permet-

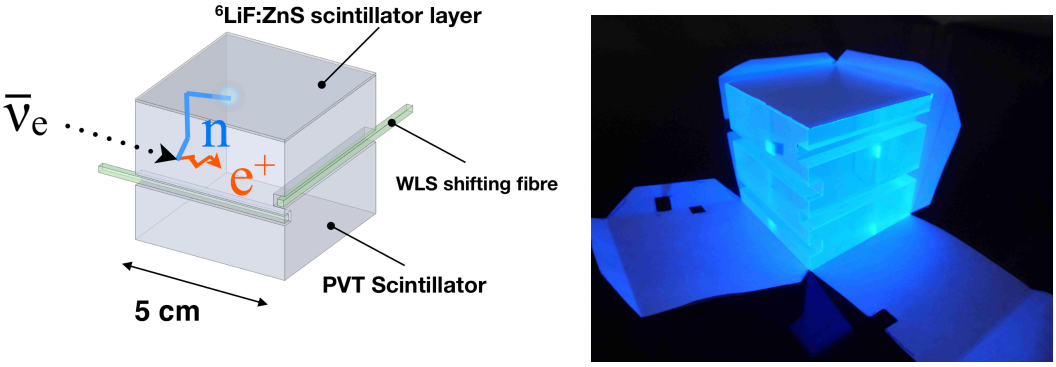

Figure 7.24: *Gauche:* Schéma d'une intéraction d'un neutrino dans un cube de SoLid. *Droite:* Image des deux scintillateurs sous une lumière UV: le cube de PVT et les feuilles de ^{6}LiF:ZnS(Ag) avec leur emballage en Tyvek.

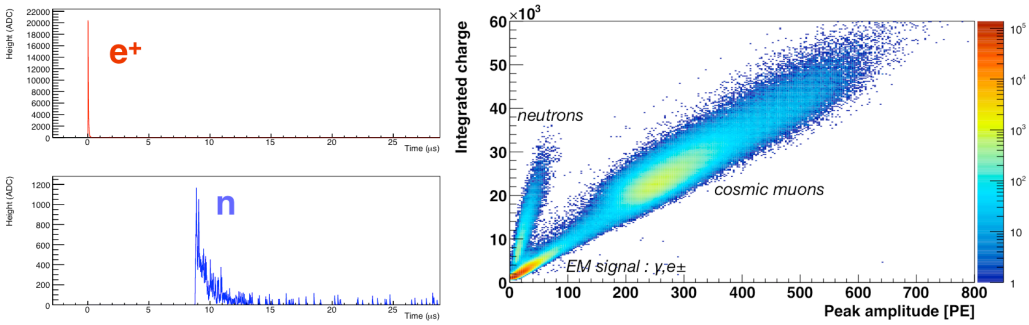

Figure 7.25: Exemple d'un événement de désintégration bêta inverse avec les signaux positron et neutron en coïncidence retardée. Une discrimination basée sur la forme des signaux permet de distinguer les neutrons des positrons.

tait de déclencher l'acquisition sur les signaux des électrons d'1 MeV d'une source de ^{207}Bi. En testant différents matériaux comme les cubes scintillants, l'emballage réflecteur, les fibres optiques, les miroirs au bout des fibres et différentes configurations du détecteur en faisant varier le nombre de feuilles de ^{6}LiF:ZnS, le nombre de fibres ou leur position, les mesures sur le banc de test ont montré qu'une résolution en énergie de 14% pouvait être atteinte pour le détecteur SoLid. Les améliorations proposées ont été prises en compte dans la construction du détecteur SoLid qui s'est achevée en 2017.

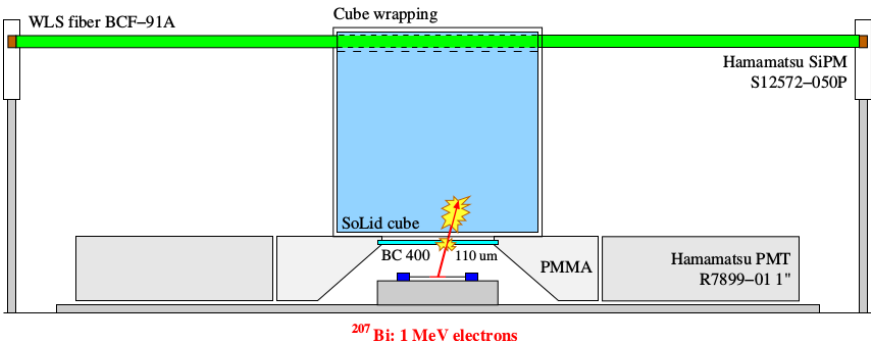

Figure 7.26: Description schématique du banc de test. La source de calibration, les PMTs et le cube de scintillateur sont montés sur des rails pour leur permetre de glisser le long de la fibre.

Les premières données de Décembre 2017 avec un blindage et un détecteur incomplets ont été utilisées dans cette thèse pour étudier la reconstruction des objets: neutrons, muons et cubes électromagnétiques. L'analyse de la reconstruction des cubes a montré que des coupures strictes sur l'énergie, le nombre de fibres par cube et l'asymétrie en énergie étaient nécessaires afin d'enlever les cubes artificiels. L'étude des données de calibration avec une source d'AmBe et les simulations de désintégration bêta inverse dans le détecteur ont validé ces premières coupures. Une contamination en ^{214}Bi a également été mise en évidence. L'analyse des données acquises en Mai avec le réacteur allumé et éteint et des coupures préliminaires strictes ont montré un excès d'événements corrélés similaires à des désintégrations bêta inverses lorsque le réacteur est allumé (figure 7.27).

De nouveaux algorithmes sont en cours de développement afin d'améliorer la reconstruction des objets et la réjection du bruit de fond. La figure 7.28 présente la sensibilité de l'expérience SoLid après 3 ans de prise de données, si le ratio signal sur bruit de fond de 3 est atteint avec une efficacité de détection des événements de désintégration bêta inverse de 30%.

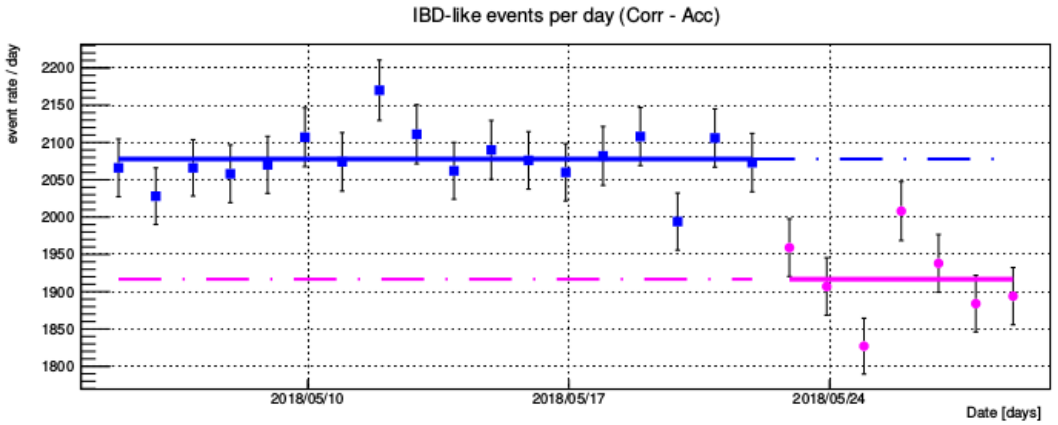

Figure 7.27: Taux d'événements similaires à des désintégrations bêta inverses. Le taux d'accidentels est soustrait au taux d'événements corrélés. Les données réacteur allumé sont montrées en bleu, les données réacteur éteint sont montrées en rose.

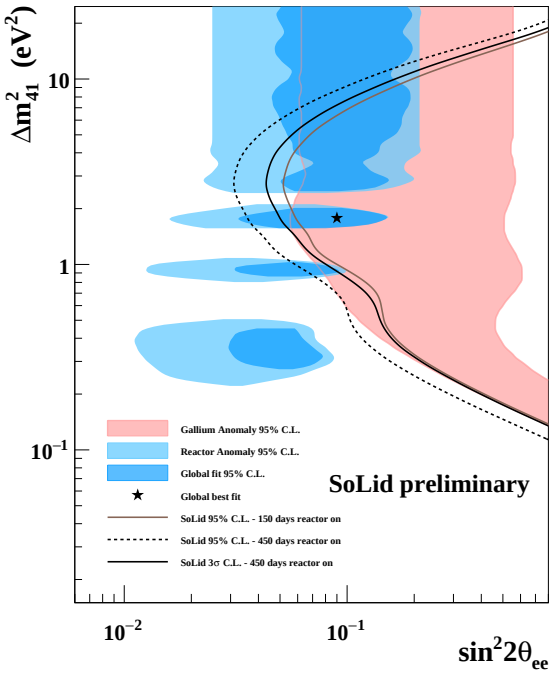

Figure 7.28: Diagramme de sensibilité de l'expérience SoLid après 1 an (150 jours) et 3 ans (450 jours) de prise de données pour un ratio Signal sur bruit de 3 et une efficacité de détection des événements de désintégration bêta inverse de 30%.

Bibliography

[1] http://pdglive.lbl.gov/Particle.action?node=S067&init=0.

[2] http://metadata.berkeley.edu/nuclear-forensics/Decay20Chains.html.

[3] http://geant4.cern.ch.

[4] http://github.com/BxCppDev/Bayeux.

[5] M. G. Aartsen et al. "Measurement of Atmospheric Neutrino Oscillations at 6-56 GeV with IceCube DeepCore". In: (2017). arXiv: 1707.07081 [hep-ex].

[6] M. G. Aartsen et al. "Measurement of Atmospheric Neutrino Oscillations with IceCube". In: *Phys. Rev. Lett.* 111.8 (2013), p. 081801. DOI: 10.1103/PhysRevLett.111.081801. arXiv: 1305.3909 [hep-ex].

[7] K. N. Abazajian et al. "Neutrino Physics from the Cosmic Microwave Background and Large Scale Structure". In: *Astropart. Phys.* 63 (2015), pp. 66–80. DOI: 10.1016/j.astropartphys.2014.05.014. arXiv: 1309.5383 [astro-ph.CO].

[8] A. I. et al. Abazov. "Search for neutrinos from the Sun Using the Reaction ^{71}Ga(ν_e, e$^-$)^{71}Ge". In: *Physical Review Letters* 67 (1991), pp. 3332–3335.

[9] J. N. et al. Abdurashitov. "Results from SAGE (The Russian-American Gallium Solar Neutrino Experiment)." In: *Physical Letters* 328B (1994), pp. 234–248.

[10] K. Abe et al. "Indication of Electron Neutrino Appearance from an Accelerator-produced Off-axis Muon Neutrino Beam". In: *Phys. Rev. Lett.* 107 (2011), p. 041801. DOI: 10.1103/PhysRevLett.107.041801. arXiv: 1106.2822 [hep-ex].

[11] K. Abe et al. "Solar Neutrino Measurements in Super-Kamiokande-IV". In: *Phys. Rev.* D94.5 (2016), p. 052010. DOI: 10.1103/PhysRevD.94.052010. arXiv: 1606.07538 [hep-ex].

[12] S. Abe et al. "Precision Measurement of Neutrino Oscillation Parameters with KamLAND". In: *Phys. Rev. Lett.* 100 (2008), p. 221803. DOI: 10.1103/PhysRevLett.100.221803. arXiv: 0801.4589 [hep-ex].

[13] Y. Abe et al. "Direct measurement of backgrounds using reactor-off data in Double Chooz". In: *Physical Review D* 87.1, 011102 (Jan. 2013), p. 011102. DOI: 10.1103/PhysRevD.87.011102. arXiv: 1210.3748 [hep-ex].

[14] Y. Abe et al. "Improved measurements of the neutrino mixing angle θ_{13} with the Double Chooz detector". In: *JHEP* 10 (2014). [Erratum: JHEP02,074(2015)], p. 086. DOI: 10.1007/JHEP02(2015)074, 10.1007/JHEP10(2014)086. arXiv: 1406.7763 [hep-ex].

[15] Y. Abe et al. "Indication of Reactor $\bar{\nu}_e$ Disappearance in the Double Chooz Experiment". In: *Phys. Rev. Lett.* 108 (2012), p. 131801. DOI: 10.1103/PhysRevLett.108.131801. arXiv: 1112.6353 [hep-ex].

[16] Y. Abreu et al. "A novel segmented-scintillator antineutrino detector". In: *JINST* 12.04 (2017), P04024. DOI: 10.1088/1748-0221/12/04/P04024. arXiv: 1703.01683 [physics.ins-det].

[17] Y. Abreu et al. "Optimisation of the scintillation light collection and uniformity for the SoLid experiment". In: *Submitted to: JINST* (2018). arXiv: 1806.02461 [physics.ins-det].

[18] Y. Abreu et al. "Performance of a full scale prototype detector at the BR2 reactor for the SoLid experiment". In: *Submitted to: JINST* (2018). arXiv: 1802.02884 [physics.ins-det].

[19] P. Adamson et al. "Combined analysis of ν_μ disappearance and $\nu_\mu \to \nu_e$ appearance in MINOS using accelerator and atmospheric neutrinos". In: *Phys. Rev. Lett.* 112 (2014), p. 191801. DOI: 10.1103/PhysRevLett.112.191801. arXiv: 1403.0867 [hep-ex].

[20] Sanjib Kumar Agarwalla, Suprabh Prakash, and Wei Wang. "High-precision measurement of atmospheric mass-squared splitting with T2K and NOvA". In: (2013). arXiv: 1312.1477 [hep-ph].

[21] M. Agostini et al. "Improved Limit on Neutrinoless Double-β Decay of ^{76}Ge from GERDA Phase II". In: *Phys. Rev. Lett.* 120.13 (2018), p. 132503. DOI: 10.1103/PhysRevLett.120.132503. arXiv: 1803.11100 [nucl-ex].

[22] A. Aguilar-Arevalo et al. "Evidence for neutrino oscillations from the observation of anti-neutrino(electron) appearance in a anti-neutrino(muon) beam". In: *Phys. Rev.* D64 (2001), p. 112007. DOI: 10.1103/PhysRevD.64.112007. arXiv: hep-ex/0104049 [hep-ex].

[23] A. A. Aguilar-Arevalo et al. "Observation of a Significant Excess of Electron-Like Events in the MiniBooNE Short-Baseline Neutrino Experiment". In: (2018). arXiv: 1805.12028 [hep-ex].

[24] Q. R. Ahmad et al. "Direct evidence for neutrino flavor transformation from neutral current interactions in the Sudbury Neutrino Observatory". In: *Phys. Rev. Lett.* 89 (2002), p. 011301. DOI: 10.1103/PhysRevLett.89.011301. arXiv: nucl-ex/0204008 [nucl-ex].

[25] K.A. Olive et al. "Particle Data Group". In: *Chin. Phys.* C38 (2014).

[26] J. B. Albert et al. "Search for Neutrinoless Double-Beta Decay with the Upgraded EXO-200 Detector". In: (2017). arXiv: 1707.08707 [hep-ex].

[27] C. Alduino et al. "The projected background for the CUORE experiment". In: *Eur. Phys. J.* C77.8 (2017), p. 543. DOI: 10.1140/epjc/s10052-017-5080-6. arXiv: 1704.08970 [physics.ins-det].

[28] I. Alekseev et al. "DANSS: Detector of the reactor AntiNeutrino based on Solid Scintillator". In: *JINST* 11.11 (2016), P11011. DOI: 10.1088/1748-0221/11/11/P11011. arXiv: 1606.02896 [physics.ins-det].

[29] I Alekseev et al. "Search for sterile neutrinos at the DANSS experiment". In: (2018). arXiv: 1804.04046 [hep-ex].

[30] H. Almazán et al. "Sterile neutrino exclusion from the STEREO experiment with 66 days of reactor-on data". In: (2018). arXiv: 1806.02096 [hep-ex].

[31] Feng Peng An et al. "Measurement of electron antineutrino oscillation based on 1230 days of operation of the Daya Bay experiment". In: *Phys. Rev.* D95.7 (2017), p. 072006. DOI: 10.1103/PhysRevD.95.072006. arXiv: 1610.04802 [hep-ex].

[32] J. Argyriades et al. "Measurement of the background in the NEMO 3 double beta decay experiment". In: *Nucl. Instrum. Meth.* A606 (2009), pp. 449–465. DOI: 10.1016/j.nima.2009.04.011. arXiv: 0903.2277 [nucl-ex].

[33] J. Argyriades et al. "Measurement of the background in the NEMO 3 double beta decay experiment". In: *Nucl. Instrum. Meth.* A606 (2009), pp. 449–465. DOI: 10.1016/j.nima.2009.04.011. arXiv: 0903.2277 [nucl-ex].

[34] E. Armengaud et al. "LUMINEU: a search for neutrinoless double beta decay based on $ZnMoO_4$ scintillating bolometers". In: *J. Phys. Conf. Ser.* 718.6 (2016), p. 062008. DOI: 10.1088/1742-6596/718/6/062008. arXiv: 1601.04989 [nucl-ex].

[35] R. Arnold et al. "Final results on ^{82}Se double beta decay to the ground state of ^{82}Kr from the NEMO-3 experiment". In: (2018). arXiv: 1806.05553 [hep-ex].

[36] R. Arnold et al. "Measurement of the double-beta decay half-life and search for the neutrinoless double-beta decay of ^{48}Ca with the NEMO-3 detector". In: *Phys. Rev.* D93.11 (2016), p. 112008. DOI: 10.1103/PhysRevD.93.112008. arXiv: 1604.01710 [hep-ex].

[37] R. Arnold et al. "Results of the search for neutrinoless double-β decay in ^{100}Mo with the NEMO-3 experiment". In: *Phys. Rev.* D92.7 (2015), p. 072011. DOI: 10.1103/PhysRevD.92.072011. arXiv: 1506.05825 [hep-ex].

[38] R. Arnold et al. "Technical design and performance of the NEMO 3 detector". In: *Nucl. Instrum. Meth.* A536 (2005), pp. 79–122. DOI: 10.1016/j.nima.2004.07.194. arXiv: physics/0402115 [physics].

[39] Roger Arnold et al. "Measurement of the Double Beta Decay Half-life of ^{130}Te with the NEMO-3 Detector". In: *Phys. Rev. Lett.* 107 (2011), p. 062504. DOI: 10.1103/PhysRevLett.107.062504. arXiv: 1104.3716 [nucl-ex].

[40] V. N. Aseev et al. "An upper limit on electron antineutrino mass from Troitsk experiment". In: *Phys. Rev.* D84 (2011), p. 112003. DOI: 10.1103/PhysRevD.84.112003. arXiv: 1108.5034 [hep-ex].

[41] J. Ashenfelter et al. "First search for short-baseline neutrino oscillations at HFIR with PROSPECT". In: (2018). arXiv: 1806.02784 [hep-ex].

[42] J. Ashenfelter et al. "The PROSPECT Physics Program". In: *J. Phys.* G43.11 (2016), p. 113001. DOI: 10.1088/0954-3899/43/11/113001. arXiv: 1512.02202 [physics.ins-det].

[43] Ali Ashtari Esfahani et al. "Determining the neutrino mass with cyclotron radiation emission spectroscopy—Project 8". In: *J. Phys.* G44.5 (2017), p. 054004. DOI: 10.1088/1361-6471/aa5b4f. arXiv: 1703.02037 [physics.ins-det].

[44] Ali Ashtari Esfahani et al. "Determining the neutrino mass with cyclotron radiation emission spectroscopy—Project 8". In: *J. Phys.* G44.5 (2017), p. 054004. DOI: 10.1088/1361-6471/aa5b4f. arXiv: 1703.02037 [physics.ins-det].

[45] D. M. Asner et al. "Method of Fission Product Beta Spectra Measurements for Predicting Reactor Anti-neutrino Emission". In: *Nucl. Instrum. Meth.* A776 (2015), pp. 75–82. DOI: 10.1016/j.nima.2014.09.076. arXiv: 1403.0107 [physics.ins-det].

[46] A. S. Barabash. "SuperNEMO double beta decay experiment". In: *J. Phys. Conf. Ser.* 375 (2012), p. 042012. DOI: 10.1088/1742-6596/375/1/042012. arXiv: 1112.1784 [nucl-ex].

[47] A. S. Barabash et al. "Calorimeter development for the SuperNEMO double beta decay experiment". In: *Nucl. Instrum. Meth.* A868 (2017), pp. 98–108. DOI: 10.1016/j.nima.2017.06.044. arXiv: 1707.06823 [physics.ins-det].

[48] A. S. Barabash et al. "The BiPo-3 detector for the measurement of ultra low natural radioactivities of thin materials". In: *JINST* 12.06 (2017), P06002. DOI: 10.1088/1748-0221/12/06/P06002. arXiv: 1702.07176 [physics.ins-det].

[49] Be, M. et al. *Table of Radionuclides*. Bureau International des Poids et Mesures, 2010.

[50] R. Becker-Szendy et al. "A Search for muon-neutrino oscillations with the IMB detector". In: *Phys. Rev. Lett.* 69 (1992), pp. 1010–1013. DOI: 10.1103/PhysRevLett.69.1010.

[51] G. Bellini et al. "SOX: Short distance neutrino Oscillations with BoreXino". In: *JHEP* 08 (2013), p. 038. DOI: 10.1007/JHEP08(2013)038. arXiv: 1304.7721 [physics.ins-det].

[52] H. A. Bethe and R. F. Bacher. "Nuclear physics". In: *Reviews of Modern Physics* 88.8 (1936), pp. 82–229.

[53] G. Boireau et al. "Online Monitoring of the Osiris Reactor with the Nucifer Neutrino Detector". In: *Phys. Rev.* D93.11 (2016), p. 112006. DOI: 10.1103/PhysRevD.93.112006. arXiv: 1509.05610 [physics.ins-det].

[54] Mathieu Bongrand. "Results of the NEMO-3 Double Beta Decay Experiment". In: *22nd Rencontres de Blois on Particle Physics and Cosmology Blois, Loire Valley, France, July 15-20, 2010.* 2011. arXiv: 1105.2435 [hep-ex]. URL: https://inspirehep.net/record/899326/files/arXiv:1105.2435.pdf.

[55] Thomas Brunner and Lindley Winslow. "Searching for $0\nu\beta\beta$ decay in ^{136}Xe – towards the tonne-scale and beyond". In: (2017). arXiv: 1704.01528 [hep-ex].

[56] S. Calvez. "Dvelopment of reconstruction tools and sensitivity of the SuperNEMO detector". PhD thesis. Universite Paris Sud, 2017.

[57] J. Chadwick. "The intensity distribution in the magnetic spectrum of beta particles from radium (B + C)". In: *Verh. Phys. Gesell.* 16 (1914), pp. 383–391.

[58] J.H. et al. Christenson. "Evidence for the 2Π Decay of the K_2^0 Meson". In: *Physical Review Letters* 13 (1964), pp. 138–140.

[59] Joao A. B. Coelho, W. Anthony Mann, and Saqib S. Bashar. "Nonmaximal θ_{23} mixing at NOvA from neutrino decoherence". In: *Phys. Rev. Lett.* 118.22 (2017), p. 221801. DOI: 10.1103/PhysRevLett.118.221801. arXiv: 1702.04738 [hep-ph].

[60] J. M. Conrad and M. H. Shaevitz. "Sterile Neutrinos: An Introduction to Experiments". In: (2016). arXiv: 1609.07803 [hep-ex].

[61] R. Davis. "Attempt to Detect the Antineutrinos from a Nuclear Reactor by the Cl37(nu, e-)A37 Reaction". In: *Physical Review* 97 (Feb. 1955), pp. 766–769. DOI: 10.1103/PhysRev.97.766.

[62] R. Davis et al. "Search for Neutrinos from the Sun". In: *Physical Review Letters* 20 (1968), pp. 1205–1209.

[63] Double Chooz collaboration et al. "Muon capture on light isotopes in Double Chooz". In: *ArXiv e-prints* (Dec. 2015). arXiv: 1512.07562 [nucl-ex].

[64] G. Drexlin et al. "Current direct neutrino mass experiments". In: *Adv. High Energy Phys.* 2013 (2013), p. 293986. DOI: 10.1155/2013/293986. arXiv: 1307.0101 [physics.ins-det].

[65] Tibor J. Dunai and Nathaniel A. Lifton. "The Nuts and Bolts of Cosmogenic Nuclide Production". In: *Elements* 10.5 (2014), pp. 347–350. ISSN: 1811-5209. DOI: 10.2113/gselements.10.5.347. eprint: http://elements.geoscienceworld.org/content/10/5/347.full.pdf. URL: http://elements.geoscienceworld.org/content/10/5/347.

[66] S. R. Elliott et al. "Initial Results from the MAJORANA DEMONSTRATOR". In: 2016. arXiv: 1610.01210 [nucl-ex]. URL: https://inspirehep.net/record/1489627/files/arXiv:1610.01210.pdf.

[67] C. D. Ellis and W. A. Wooster. "The Average Energy of Disintegration of Radium E". In: *Nature* 119 (1927), pp. 563–567.

[68] Paola Ferrario. "The NEXT double beta decay experiment". In: *PoS* EPS-HEP2017 (2017), p. 105. DOI: 10.22323/1.314.0105. arXiv: 1710.03022 [physics.ins-det].

[69] A. Franklin. *Are There Really Neutrinos?* Perseus Publishing, 2000.

[70] A. Franklin. *Are There Really Neutrinos?* Perseus Publishing, 2000.

[71] A. Gando et al. "Reactor On-Off Antineutrino Measurement with KamLAND". In: *Phys. Rev.* D88.3 (2013), p. 033001. DOI: 10.1103/PhysRevD.88.033001. arXiv: 1303.4667 [hep-ex].

[72] A. Gando et al. "Search for Majorana Neutrinos near the Inverted Mass Hierarchy Region with KamLAND-Zen". In: *Phys. Rev. Lett.* 117.8 (2016). [Addendum: Phys. Rev. Lett.117,no.10,109903(2016)], p. 082503. DOI: 10.1103/PhysRevLett.117.109903, 10.1103/PhysRevLett.117.082503. arXiv: 1605.02889 [hep-ex].

[73] S. Gariazzo et al. "Light sterile neutrinos". In: *J. Phys.* G43 (2016), p. 033001. DOI: 10.1088/0954-3899/43/3/033001. arXiv: 1507.08204 [hep-ph].

[74] S. Gariazzo et al. "Updated Global 3+1 Analysis of Short-BaseLine Neutrino Oscillations". In: *JHEP* 06 (2017), p. 135. DOI: 10.1007/JHEP06(2017)135. arXiv: 1703.00860 [hep-ph].

[75] C. Giunti and E. M. Zavanin. "Predictions for Neutrinoless Double-Beta Decay in the 3+1 Sterile Neutrino Scenario". In: *J. Phys. Conf. Ser.* 718.6 (2016), p. 062074. DOI: 10.1088/1742-6596/718/6/062074. arXiv: 1511.03838 [hep-ph].

[76] Carlo Giunti and Marco Laveder. "Statistical Significance of the Gallium Anomaly". In: *Phys. Rev.* C83 (2011), p. 065504. DOI: 10.1103/PhysRevC.83.065504. arXiv: 1006.3244 [hep-ph].

[77] A. de Gouvea et al. "Working Group Report: Neutrinos". In: *Proceedings, 2013 Community Summer Study on the Future of U.S. Particle Physics: Snowmass on the Mississippi (CSS2013): Minneapolis, MN, USA, July 29-August 6, 2013.* 2013. arXiv: 1310.4340 [hep-ex]. URL: https://inspirehep.net/record/1260555/files/arXiv:1310.4340.pdf.

[78] A. de Gouvea et al. "Working Group Report: Neutrinos". In: *Proceedings, 2013 Community Summer Study on the Future of U.S. Particle Physics: Snowmass on the Mississippi (CSS2013): Minneapolis, MN, USA, July 29-August 6, 2013.* 2013. arXiv: 1310.4340 [hep-ex]. URL: https://inspirehep.net/record/1260555/files/arXiv:1310.4340.pdf.

[79] C. Gunti and C. W. Kim. *Fundamentals of neutrino physics and astrophysics.* Oxford University Press, 2007.

[80] Becquerel H. "On the rays emitted by phosphorescence". In: *Compt. Rend. Hebd. Seances Acad. Sci.* 122.8 (1896), pp. 420–421.

[81] N. Haag et al. "Experimental Determination of the Antineutrino Spectrum of the Fission Products of ^{238}U". In: *Phys. Rev. Lett.* 112.12 (2014), p. 122501. DOI: 10.1103/PhysRevLett.112.122501. arXiv: 1312.5601 [nucl-ex].

[82] Hamamatsu. "Datasheet MPPC (multi-pixel photon counter) S12572-025, -050, -100C/P". In: (2015).

[83] A. Heijboer and for the ANTARES collaboration. "Reconstruction of Atmospheric Neutrinos in Antares". In: Aug. 2009. arXiv: 0908.0816 [astro-ph.IM].

[84] Patrick Huber. "NEOS Data and the Origin of the 5 MeV Bump in the Reactor Antineutrino Spectrum". In: *Phys. Rev. Lett.* 118.4 (2017), p. 042502. DOI: 10.1103/PhysRevLett.118.042502. arXiv: 1609.03910 [hep-ph].

[85] Patrick Huber. "On the determination of anti-neutrino spectra from nuclear reactors". In: *Phys. Rev.* C84 (2011). [Erratum: Phys. Rev.C85,029901(2012)], p. 024617. DOI: 10.1103/PhysRevC.85.029901,10.1103/PhysRevC.84.024617. arXiv: 1106.0687 [hep-ph].

[86] S. Kalcheva et al. "Reactor Core Simulations for Determination of the Antineutrino Spectrum for the SoLid Experiment at BR2 Reactor". In: *Proceedings M&C 2017 (Jeju, South Korea)* (April 16-20, 2017).

[87] Y. J. Ko et al. "Sterile Neutrino Search at the NEOS Experiment". In: *Phys. Rev. Lett.* 118.12 (2017), p. 121802. DOI: 10.1103/PhysRevLett.118.121802. arXiv: 1610.05134 [hep-ex].

[88] Y. J. Ko et al. "Sterile Neutrino Search at the NEOS Experiment". In: *Phys. Rev. Lett.* 118.12 (2017), p. 121802. DOI: 10.1103/PhysRevLett.118.121802. arXiv: 1610.05134 [hep-ex].

[89] K. Kodama et al. "Observation of tau neutrino interactions". In: *Phys. Lett.* B504 (2001), pp. 218–224. DOI: 10.1016/S0370-2693(01)00307-0. arXiv: hep-ex/0012035 [hep-ex].

[90] N. Kudomi. "Energy calibration of plastic scintillators for low energy electrons by using Compton scatterings of γ rays". In: *Nuclear Instruments and Methods in Physics Research Section A: Accelerators, Spectrometers, Detectors and Associated Equipment* 430.1 (1999), pp. 96 –99. ISSN: 0168-9002. DOI: https://doi.org/10.1016/S0168-9002(99)00200-4. URL: http://www.sciencedirect.com/science/article/pii/S0168900299002004.

[91] T. D. Lee and C. N. Yang. "Question of Parity Conservation in Weak Interactions". In: *Phys. Rev.* 104 (1956), pp. 254–258.

[92] P. Loaiza. "BiPo measurements of LAPP enriched Se foils". In: *DocDB* 4382 (2017).

[93] Haoqi Lu. "Reactor antineutrino experiments". In: *Int. J. Mod. Phys. Conf. Ser.* 31 (2014), p. 1460283. DOI: 10.1142/S201019451460283X. arXiv: 1403.0731 [hep-ex].

[94] L. Grodzins M. Goldhaber and A. W. Sunyar. "Helicity of Neutrinos". In: *Phys. Rev.* 109 (1958), pp. 1015–1017.

[95] Michele Maltoni and Alexei Yu. Smirnov. "Solar neutrinos and neutrino physics". In: *Eur. Phys. J.* A52.4 (2016), p. 87. DOI: 10.1140/epja/i2016-16087-0. arXiv: 1507.05287 [hep-ph].

[96] L. Manzanillas. "Development of the source calibration system of the STEREO experiment and search for sterile neutrinos at ILL". PhD thesis. Université Grenoble Alpes, 2016.

[97] L. Manzanillas. "STEREO: Search for sterile neutrinos at the ILL". In: *ArXiv e-prints* (Feb. 2017). arXiv: 1702.02498 [physics.ins-det].

[98] C. Marquet et al. "High energy resolution electron beam spectrometer in the MeV range". In: *JINST* 10.09 (2015), P09008. DOI: 10.1088/1748-0221/10/09/P09008.

[99] G. Mention et al. "The Reactor Antineutrino Anomaly". In: *Phys. Rev.* D83 (2011), p. 073006. DOI: 10.1103/PhysRevD.83.073006. arXiv: 1101.2755 [hep-ex].

[100] O. Meplan. "MURE, MCNP utility for reactor evolution". In: *Tech. Rep. LPSC* 0912 (2009).

[101] Th. A. Mueller et al. "Improved Predictions of Reactor Antineutrino Spectra". In: *Phys. Rev.* C83 (2011), p. 054615. DOI: 10.1103/PhysRevC.83.054615. arXiv: 1101.2663 [hep-ex].

[102] T. Le Noblet. "Background studies and design optimisation of the SuperNEMO demonstrator module Search for $2\nu\beta\beta$ and $0\nu\beta\beta$ decays of 116Cd into the excited states of 116Sn with NEMO-3". PhD thesis. Universite Grenoble Alpes, 2017.

[103] Igor Ostrovskiy and Kevin O'Sullivan. "Search for neutrinoless double beta decay". In: *Mod. Phys. Lett.* A31.18 (2016), p. 1630017. DOI: 10.1142/S0217732316920048, 10.1142/S0217732316300172. arXiv: 1605.00631 [hep-ex].

[104] Stephen Parke. "What is Δm^2_{ee} ?" In: *Phys. Rev.* D93.5 (2016), p. 053008. DOI: 10.1103/PhysRevD.93.053008. arXiv: 1601.07464 [hep-ph].

[105] W. Pauli. *Letter to physicits at Tubingen.* cited in Franklin 2000, p. 71, December 14, 1930.

[106] F. Perrot. "Radiopurity measurements for 8" PMTs and preliminary budget for SN demonstrator". In: *DocDB* 4263 (2017).

[107] B. Pontecorvo. "Electron and Muon Neutrinos". In: *Sov. Phys. JETP* 10 (1960), pp. 1236–1240.

[108] F. Reines and C. L. Cowan. "The Neutrino". In: *Nature* 178 (1956), pp. 446–449.

[109] P. F. de Salas et al. "Status of neutrino oscillations 2017". In: (2017). arXiv: 1708.01186 [hep-ph].

[110] S. H. Seo et al. "Spectral Measurement of the Electron Antineutrino Oscillation Amplitude and Frequency using 500 Live Days of RENO Data". In: (2016). arXiv: 1610.04326 [hep-ex].

[111] Seon-Hee Seo. "New Results from RENO and The 5 MeV Excess". In: *AIP Conf. Proc.* 1666 (2015), p. 080002. DOI: 10.1063/1.4915563. arXiv: 1410.7987 [hep-ex].

[112] Fred L. Wilson. "Fermi's Theory of Beta Decay". In: *Am. J. Phys.* 36.12 (1968), pp. 1150–1160. DOI: 10.1119/1.1974382.

[113] C. S. Wu et al. "Experimental Test of Parity Conservation in Beta Decay". In: *Phys. Rev.* 105 (1957), pp. 1413–1414.

[114] K. Zuber. *Neutrino Physics*. Istitute of Physics Publishing, 2004.

université PARIS-SACLAY | ÉCOLE DOCTORALE PHENIICS

Titre: Physique du neutrino avec les expériences SoLid et SuperNEMO

Mots clés: Neutrinos, Détecteurs, Oscillations, Double désintégration bêta

Résumé: Les neutrinos sont les particules fondamentales de matière les plus abondantes dans l'univers. Ils ont été détectés pour la première fois en 1956. Depuis lors, plusieurs expériences ont tenté de percer leurs mystères. Ils n'interagissent que par interaction faible, ils sont donc difficiles à détecter. On sait aujourd'hui qu'ils ont une masse très faible, et qu'ils peuvent osciller entre trois saveurs leptoniques. Cependant, de nombreuses questions perdurent sur leur masse, leur nature ou encore l'existence de neutrinos stériles. Cette thèse appréhende ces deux dernières questions à l'aide de deux expériences différentes : SuperNEMO et SoLid.

Le but de l'expérience SuperNEMO est de rechercher la nature du neutrino, c'est-à-dire s'il est sa propre anti-particule (particule de Majorana) ou non (particule de Dirac). Pour cela, on cherche à détecter des doubles désintégrations bêta sans émission de neutrinos car ce processus n'est possible que si les neutrinos sont des particules de Majorana. Des feuilles sources de l'émetteur double bêta ^{82}Se seront installées au centre du démonstrateur SuperNEMO qui est actuellement en construction au Laboratoire Souterrain de Modane. Ce détecteur est composé d'une chambre à fils pour détecter les traces des deux électrons émis lors des désintégrations et d'un calorimètre pour mesurer leurs énergies. La mesure de la double désintégration bêta sans émission de neutrinos est très compliquée car si ce processus existe, il est extrêmement rare. Par conséquent, un travail important est fait pour réduire le bruit de fond des rayons cosmiques ou de la radioactivité naturelle.
Dans cette thèse, des simulations des différents bruits de fonds ont été faites pour comprendre leur impact sur la mesure de l'énergie des électrons issus de la double désintégration bêta du ^{82}Se. Il est montré que la radioactivité du verre des photomultiplicateurs ne sera pas négligeable mais qu'elle pourra être mesurée précisément dans certains canaux d'analyse. Des feuilles de cuivre ont aussi été simulées à la place des sources de ^{82}Se pour montrer qu'elles peuvent aider à contrôler le bruit de fond efficacement. Suite à ces travaux, il a été décidé d'installer des feuilles de cuivre parmi les sources de ^{82}Se.

La deuxième expérience sur laquelle porte cette thèse est l'expérience SoLid qui cherche à prouver l'existence de neutrinos stériles. Plusieurs anomalies expérimentales pourraient être expliquées par des oscillations d'antineutrinos de réacteurs vers des neutrinos stériles. Le détecteur SoLid cherche à mettre en évidence un signal d'oscillation auprès du réacteur BR2 en Belgique en mesurant le flux d'antineutrinos en fonction de leur énergie et de la distance parcourue, grâce à une grande segmentation. La détection des antineutrinos de réacteur se fait par désintégration bêta inverse. L'interaction d'un antineutrino se traduit donc par l'émission en coïncidence d'un positron et d'un neutron. Les positrons sont détectés dans des cubes de plastique scintillant en PVT et les neutrons sont détectés par des feuilles de ^{6}LiF:ZnS posées sur chacun des cubes.
Un premier prototype, SM1, a montré l'intérêt de cette technologie notamment pour discriminer les bruits de fonds. Une partie des travaux de cette thèse a consisté à développer et exploiter un banc de test afin d'optimiser la collection de lumière du détecteur pour améliorer la résolution en énergie de SoLid. En testant différents matériaux et différentes configurations du détecteur, les mesures sur le banc de test ont montré qu'une résolution en énergie de 14% pouvait être atteinte pour le détecteur SoLid (contre 20% pour le prototype SM1). Les améliorations proposées ont été prises en compte dans la construction du détecteur SoLid qui s'est achevée en 2017. Une analyse des premières données du détecteur est également présentée pour montrer la sensibilité de SoLid à la détection des antineutrinos de réacteur.

université PARIS-SACLAY | ÉCOLE DOCTORALE PHENIICS

Title: Neutrino physics with SoLid and SuperNEMO experiments

Keywords: Neutrinos, Detectors, Oscillations, Double beta decay

Abstract: Neutrinos are the most abundant fundamental particles of matter in the Universe. They were detected for the first time in 1956. Since then, several experiments have tried to unveil their mysteries. They only interact weakly so they are difficult to detect. It is known that their masses are very low and that they can oscillate between three leptonic flavours. However, several questions remain about their masses, their nature or the existence of sterile neutrinos. This thesis addresses the last two questions with two different experiments: SuperNEMO and SoLid.

The goal of the SuperNEMO experiment is to understand the nature of neutrinos, whether it is its own antiparticle (Majorana particle) or not (Dirac particle). This is investigated by searching for neutrinoless double beta decay as this process is possible only if neutrinos are Majorana particles. Source foils of the double beta emitter ^{82}Se are installed at the center of the SuperNEMO demonstrator which is being assembled at the Modane Underground Laboratory. This detector is composed of a wire chamber to detect the tracks of the two electrons emitted in the decays and a calorimeter to measure their energies. Neutrinoless double beta decay measurement is very difficult because if this process exists, it is extremely rare. An important work has thus to be done to decrease backgrounds from cosmic rays or natural radioactivity.
In this thesis, different backgrounds have been simulated to understand their impact on the measurement of the energy of the two electrons from ^{82}Se double beta decay. It is shown that radioactivity from photomultipliers glasses will not be negligible but it will be possible to measure it precisely in dedicated channels. Copper foils have also been simulated in the source strips to demonstrate that they can help to control efficiently the backgrounds. Following this work, it has been decided to install copper foils in addition to ^{82}Se foils.

The second experiment investigated in this thesis is the SoLid experiment which is looking for the existence of sterile neutrinos. Several experimental anomalies could be explained by oscillations of reactor antineutrinos toward sterile neutrinos. The SoLid detector is looking for an oscillation signal at the Belgian BR2 reactor by measuring the antineutrino flux as a function of their energy and their traveling distance thanks to a fine segmentation. The reactor antineutrinos are detected via inverse beta decay. The antineutrino interaction signal is thus the emission in coincidence of a positron and a neutron. Positrons are detected by plastic scintillator cubes in PVT and neutrons are detected by ^{6}LiF:ZnS sheets placed on 2 faces of each cube. A first prototype, SM1, has demonstrated the advantages of this technology, particularly to discriminate backgrounds. A part of the work of this thesis consisted in developing and exploiting a test bench to optimize the light collection of the detector in order to improve the energy resolution of the SoLid detector. By testing different materials and configurations, the test bench measurement demonstrated that an energy resolution of 14% can be achieved for SoLid phase I, while it was 20% for the SM1 prototype. The improvements proposed have been taken into account for the SoLid detector construction that was achieved in 2017. An analysis of the first detector data is also presented to show SoLid sensitivity to reactor antineutrino detection.

Université Paris-Saclay
Espace Technologique / Immeuble Discovery
Route de l'Orme aux Merisiers RD 128 / 91190 Saint-Aubin, France